

RICE UNIVERSITY

**Transport of Surfactant and Foam in Porous Media for
Enhanced Oil Recovery Processes**

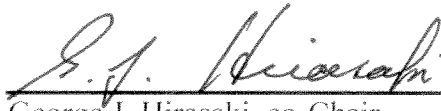
by

Kun Ma

A THESIS SUBMITTED
IN PARTIAL FULFILLMENT OF THE
REQUIREMENTS FOR THE DEGREE

Doctor of Philosophy

APPROVED, THESIS COMMITTEE



George J. Hirasaki, co-Chair
Professor, Department of Chemical and
Biomolecular Engineering



Sibani Lisa Biswal, co-Chair
Assistant Professor, Department of
Chemical and Biomolecular Engineering



Clarence A. Miller
Professor, Department of Chemical and
Biomolecular Engineering



Helge M. Gonnemann
Assistant Professor, Department of Earth
Sciences

HOUSTON, TEXAS

April 2013

RICE UNIVERSITY

**Transport of Surfactant and Foam in Porous Media for
Enhanced Oil Recovery Processes**

by

Kun Ma

A THESIS SUBMITTED
IN PARTIAL FULFILLMENT OF THE
REQUIREMENTS FOR THE DEGREE

Doctor of Philosophy

APPROVED, THESIS COMMITTEE

George J. Hirasaki, co-Chair
Professor, Department of Chemical and
Biomolecular Engineering

Sibani Lisa Biswal, co-Chair
Assistant Professor, Department of
Chemical and Biomolecular Engineering

Clarence A. Miller
Professor, Department of Chemical and
Biomolecular Engineering

Helge M. Gonnermann
Assistant Professor, Department of Earth
Sciences

HOUSTON, TEXAS
April 2013

Abstract

Transport of Surfactant and Foam in Porous Media for Enhanced Oil Recovery Processes

by

Kun Ma

The use of foam-forming surfactants offers promise to improve sweep efficiency and mobility control for enhanced oil recovery (EOR). This thesis provides an in depth understanding of transport of surfactant and foam through porous media using a combination of laboratory experiments and numerical simulations. In particular, there are several issues in foam EOR processes that are examined. These include screening of surfactant adsorption onto representative rock surfaces, modeling of foam flow through porous media, and studying the effects of surface wettability and porous media heterogeneity.

Surfactant adsorption onto rock surfaces is a main cause of foam chromatographic retardation as well as increased process cost. Successful foam application requires low surfactant adsorption on reservoir rock. The focus of this thesis is natural carbonate rock surfaces, such as dolomite. Surfactant adsorption was found to be highly dependent on electrostatic interactions between surfactants and rock surface. For example, the nonionic surfactant Tergitol 15-S-30 exhibits low adsorption on dolomite under alkaline conditions. In

contrast, high adsorption of cationic surfactants was observed on some natural carbonate surfaces. XPS analysis reveals silicon and aluminum impurities exist in natural carbonates, but not in synthetic calcite. The high adsorption is due to the strong electrostatic interactions between the cationic surfactants and negative binding sites in silica and/or clay.

There are a number of commercial foam simulators, but an approach to estimate foam modeling parameters from laboratory experiments is needed to simulate foam transport. A one-dimensional foam simulator is developed to simulate foam flow. Chromatographic retardation of surfactants caused by adsorption and by partition between phases is investigated. The parameters in the foam model are estimated with an approach utilizing both steady-state and transient experiments. By superimposing contour plots of the transition foam quality and the foam apparent viscosity, one can estimate the reference mobility reduction factor ($fmmob$) and the critical water saturation ($fmdry$) using the STARS foam model. The parameter $epdry$, which regulates the abruptness of the foam dry-out effect, can be estimated by a transient foam experiment in which 100% gas displaces surfactant solution at 100% water saturation.

Micromodel experiments allow for pore-level visualization of foam transport. We have developed model porous media systems using polydimethylsiloxane. We developed a simple method to tune and pattern the wettability of polydimethylsiloxane (PDMS) to generate porous media models with specific structure and wettability. The effect of wettability on flow patterns is observed in gas-liquid flow. The use of foam to divert flow from high permeable to low

permeable regions is demonstrated in a heterogeneous porous micromodel. Compared with 100% gas injection, surfactant-stabilized foam effectively improves the sweep of the aqueous fluid in both high and low permeability regions of the micromodel. The best performance of foam on fluid diversion is observed in the lamella-separated foam regime, where the presence of foam can enhance gas saturation in the low permeable region up to 45.1% at the time of gas breakthrough.

In conclusion, this thesis provides new findings in surfactant adsorption onto mineral surfaces, in the methodology of estimating foam parameters for reservoir simulation, and in micromodel observations of foam flow through porous media. These findings will be useful to design foam flooding in EOR processes.

Acknowledgments

I would like to express my sincere thankfulness to my thesis advisors, Dr. George J. Hirasaki and Dr. Sibani Lisa Biswal, for guiding me in my scientific research during my Ph.D study. Their wisdom and insightful ideas, authoritative knowledge, tremendous support, and inspirational encouragement have helped me a lot in accomplishing this thesis.

I thank Dr. Clarence A. Miller for helpful discussions in the study of surfactant adsorption and for serving as a member of my thesis committee.

I thank Dr. Helge M. Gonnermann for being as one of my thesis committee members.

I want to thank Ms. Maura C. Puerto and Mr. Leyu Cui for suggestions and assistance in various experiments. I acknowledge Dr. Robert Li for teaching me foam flooding experiments and Dr. Gautam Kini for training me microfluidic fabrication. I thank Dr. Dichuan Li who taught me the MATLAB image analysis. I am grateful to Dr. Rouhi Farajzadeh (Delft University of Technology), Dr. William R. Rossen (Delft University of Technology), and Dr. Jose Luis Lopez-Salinas for discussions in foam modeling study. I thank all my labmates from Hirasaki's and Biswal's labs for their support in my PhD research in the past four years.

I thank all the undergraduate students, Rachel Liontas, Yezi Dong, Tianlong Wang, Chang Da, Javier Rivera, and Pradnya Bhawalkar, who contributed to part of the experimental measurements in this thesis.

I thank Dr. Keith P. Johnston (University of Texas at Austin) and Dr. Quoc Nguyen (University of Texas at Austin) for collaboration in this research project and for discussions in foam study.

Financial support from the Abu Dhabi National Oil Company (ADNOC) and the US Department of Energy (under Award No. DE-FE0005902) is acknowledged.

At the end, I would like to thank my wife Le Shi for her support and encouragement in my Ph.D study.

Table of contents

Abstract.....	i
Acknowledgments.....	iv
Table of contents	vi
List of figures	x
List of tables.....	xiv
<i>Chapter 1 Introduction</i>	1
1.1 CO₂ foam in enhanced oil recovery	1
1.1.1 Overview of enhanced oil recovery	1
1.1.2 Foam mobility control for CO ₂ EOR	4
1.2 Foam transport in porous media	6
1.2.1 Darcy’s law for multi-phase flow	6
1.2.2 Foam microstructure and mobility.....	8
1.2.3 Foam generation and coalescence.....	10
1.2.4 Foam modeling techniques	15
1.3 Surfactant retention in CO₂ foam process	17
1.3.1 Overview of surfactants.....	17
1.3.2 Surfactant adsorption on formation minerals.....	19
1.3.3 Surfactant partition between phases	20
1.3.4 Surfactant precipitation	22
1.4 Thesis structure	23
1.5 References	24
<i>Chapter 2 Surfactant adsorption on carbonate materials</i>	28
2.1 Materials and methods	28
2.1.1 Materials.....	28

2.1.2 Characterization of surface chemistry with XPS and XRD.....	31
2.1.3 ζ potential measurements	32
2.1.4 Static adsorption experiments.....	32
2.1.5 Analysis of surfactant concentration.....	33
2.2 Static adsorption on natural dolomite.....	34
2.2.1 Anionic Surfactants	34
2.2.2 Cationic Surfactants	35
2.2.3. Nonionic Surfactants.....	36
2.2.4. Zwitterionic Surfactants	38
2.2.5. Comparison in a bar chart	42
2.3 Effect of non-carbonate impurities on adsorption results.....	43
2.3.1. Results of ζ potential and static adsorption on various substrates	44
2.3.2. Surface characterization by XPS and XRD	48
2.4 Conclusions	52
2.5 References.....	53

Chapter 3 Simulation of foam flow and chromatographic retardation of surfactants55

3.1 1-D foam simulator and the foam model	55
3.1.1 Algorithm for different foam injection strategies.....	55
3.1.2 The STARS foam model.....	60
3.2 Modeling surfactant transport in two-phase flow	62
3.3 Chromatographic retardation of surfactant.....	67
3.3.1 Dynamic adsorption.....	67
3.3.2 Phase partition	71
3.4 Conclusions	79
3.5 References.....	81

Chapter 4 Estimation of parameters for the simulation of foam flow in porous media82

4.1 Materials and Methods	82
4.1.1 Experimental setup	82
4.1.2 Foam model.....	86
4.2 Results and discussion	87
4.2.1 Experimental results of foam flooding	87
4.2.2 Foam modeling results with the dry-out function.....	92
4.2.3 Non-unique solutions to match the transition foam viscosity	113
4.2.4 Discussion on multi-variable multi-dimensional search.....	120
4.2.5 Numerical oscillation in transient foam simulation.....	124
4.2.6 Sensitivity of foam parameters.....	132
4.3 Conclusions	137
4.4 References	139

Chapter 5 Visualization of foam transport in microchannels and

micromodels of heterogeneous porous media141

5.1 Wettability control in microfluidic devices	141
5.1.1 Materials and methods.....	141
5.1.2 Results and discussions	145
5.2 Effect of surface wettability on bubble pinch-off in microchannels	164
5.2.1 Microfluidic design.....	164
5.2.2 Flow patterns in low capillary numbers	165
5.2.3 Gas pressure threshold	170
5.3 Visualization of foam transport in heterogeneous micromodels	174
5.3.1 Design and operation of the micromodel.....	174
5.3.2 Results and discussions	176
5.4 Conclusions	191
5.5 References	193

Chapter 6 Conclusions and future work.....197

6.1 Summary of main findings	197
---	-----

6.1.1 Screening of low-adsorbing surfactant on carbonates.....	197
6.1.2 Modeling foam flow and surfactant transport in porous media.....	198
6.1.3 Estimation of parameters for foam simulation in porous media.....	200
6.1.4 Micromodel study of foam flow in porous media.....	202
6.2 Future work.....	204

Appendix A **Nomenclature in the simulation of surfactant and foam**

transport in porous media.....	208
---------------------------------------	------------

<i>Appendix B</i> MATLAB code for 1-D foam simulation.....	212
---	------------

List of figures

Figure 1-1. EOR projects in the USA.....	3
Figure 1-2. Pore-level schematic of fluid distribution for foam flow.....	8
Figure 1-3. Schematics of (a) the snap-off mechanism, (b) the lamella-division mechanism, (c) the leave-behind mechanism for foam generation.....	11
Figure 1-4. Schematic of disjoining pressure function Π.....	14
Figure 1-5. Schematic representation of surfactant phase behavior and the effect of formulation variables on emulsions.....	21
Figure 2-1. Static adsorption of anionics on dolomite powder (Carl Pool, old) in DI water at room temperature.....	34
Figure 2-2. Static adsorption of cationics on dolomite powder (Carl Pool, old) in DI water at room temperature.....	35
Figure 2-3. HPLC profile of Tergitol 15-S-30 (0.2 wt%) in DI water.....	36
Figure 2-4. Static adsorption of Tergitol 15-S-30 on dolomite powder (Carl Pool, old) in DI water at room temperature.....	37
Figure 2-5. HPLC profiles of (a) CAHS (0.2 wt% cocamidopropyl hydroxysultaine) and (b) LAB (0.21 wt% lauryl betaine) in DI water with an ELSD detector.....	38
Figure 2-6. Static adsorption of zwitterionics on dolomite powder (Carl Pool, old) in DI water and synthetic brine at room temperature.....	41
Figure 2-7. Comparison of surfactant adsorption on dolomite (Carl Pool, old) in DI water at room temperature.....	43
Figure 2-8. Comparison of static adsorption of SDS and CPC on synthetic calcite, silica and kaolin in DI water at room temperature.....	45
Figure 2-9. Comparison of static adsorption of SDS and CPC on various natural carbonates in DI water at room temperature.....	47
Figure 2-10. Comparison of atomic composition of various materials measured by X-ray photoelectron spectroscopy (XPS).....	49
Figure 2-11. Analysis of HCl-insoluble impurities with X-ray Diffraction (XRD) from top to bottom: (a) dolomite (Carl Pool); (b) dolomite (ScienceLab.com); (c) limestone (Franklin); (d) limestone (Carthage).....	50
Figure 2-12. Correlation between surfactant adsorption plateau and XPS results of carbonate minerals.....	52
Figure 3-1. Comparison of effluent history of continuous injection of surfactants to a water-saturated dolomite formation.....	69

Figure 3-2. Comparison of effluent history of 0.5 PV finite slug injection of surfactants to a water-saturated dolomite formation	70
Figure 3-3. Simulation results of surfactant concentration profiles in aqueous phase using the parameters listed in Table 3-2	72
Figure 3-4. Simulation results of saturation profiles using the parameters listed in Table 3-2	73
Figure 3-5. Simulation results of gas pressure profiles using the parameters listed in Table 3-2	74
Figure 3-6. Simulation results of surfactant concentration profiles in aqueous phase using the parameters listed in Table 3-2 except for K_{sgw}.....	76
Figure 3-7. Simulation results of saturation profiles in aqueous phase using the parameters listed in Table 3-2 except for K_{sgw}	78
Figure 3-8. Simulation results of gas pressure profiles in aqueous phase using the parameters listed in Table 3-2 except for K_{sgw}.....	79
Figure 4-1. Schematic of the apparatus for foam experiments in System B.....	84
Figure 4-2. The effect of foam quality on foam apparent viscosity in System A	88
Figure 4-3. A typical foam apparent viscosity history of co-injection experiments in System B	89
Figure 4-4. The effect of foam quality on foam apparent viscosity in System B	90
Figure 4-5. The effect of foam quality on aqueous saturation in System B	91
Figure 4-6. Foam apparent viscosity as a function of water saturation using $f_{mob}=33000$ and $f_{dry}=0.0730$	96
Figure 4-7. Gas fractional flow as a function of water saturation using $f_{mob}=33000$ and $f_{dry}=0.0730$	98
Figure 4-8. Flow chart for matching transition foam flow in porous media at steady state using the proposed hybrid contour plot method.....	101
Figure 4-9. (a) Contour plot of transition foam quality as a function of f_{mob} and f_{dry}. (b) Contour plot of foam apparent viscosity as a function of f_{mob} and f_{dry}.....	102
Figure 4-10. Superposition of contour plots in Figure 9(a) and (b) to find the position (the purple dot, $f_{mob}=3.30 \times 10^4$ and $f_{dry}=0.073$) where f_g^t (the red curve) and $\mu_{foam,app}^t$ (the blue curve) cross over.	103
Figure 4-11. Comparison of foam apparent viscosities between model fit and experiment in System A.....	104
Figure 4-12. Comparison of foam apparent viscosities between model fit and experiment in System B.....	105

Figure 4-13. Comparison in water saturation between experimental data and modeling results in System B using the parameters in Table 4-1 (System B) and Figure 4-12.....	107
Figure 4-14. Model fit to experimental data in System B with different preset $epdry$.....	108
Figure 4-15. Residual sum of squares as a function of $epdry$ for modeling the steady-state experiments in System B.	110
Figure 4-16. Comparison between transient experimental data and simulation results in System B.....	111
Figure 4-17. Flow chart of the non-graphical approach to match experimental data at the transition foam quality with a preset $epdry$	114
Figure 4-18. Location of the roots which match transition foam data using the hybrid contour plot method on a log-log scale.....	116
Figure 4-19. Comparison of model fit with experimental data using two sets of parameters found in Figure 4-18.	118
Figure 4-20. Graphical illustration of S_w^*, S_w^t, and $fmdry$	119
Figure 4-21. Comparison of model fit with experimental data using the multi-dimensional 3-parameter estimation.	123
Figure 4-22. Comparison of foam apparent viscosity history between finite difference method and method of characteristics	126
Figure 4-23. Investigation of numerical oscillation in FD simulation in which 100% gas displaces surfactant solution at 100% water saturation.....	128
Figure 4-24. Investigations of factors which may affect numerical oscillation in the FD simulation of 100% gas displacing 100% surfactant solution	131
Figure 4-25. The influence of changing the exponent n_w in the k_{rw} function on foam modeling parameters	134
Figure 4-26. The influence of changing the connate water saturation S_{wc} on foam modeling parameters	135
Figure 4-27. The influence of changing the parameter $epdry$ on other foam modeling parameters	136
Figure 5-1. Schematic of the two-step process of wettability control for microfluidic devices.....	144
Figure 5-2. The effect of patterned wettability on displacement efficiency of aqueous dye solution by air in homogeneous porous media.....	148
Figure 5-3. The effect of curing time on surface hydrophilization process of PDMS at 80 °C.....	150
Figure 5-4. Wettability maintenance by keeping UV/ozone-treated PDMS (1-hour curing at 80 °C) surface in contact with DI water.....	152

Figure 5-5. The schematic of migration of LMW species in PDMS (a) during UV-ozone treatment; (b) upon air exposure; (c) upon water immersion	154
Figure 5-6. (a) Experimental data for hydrophobic recovery in air of PDMS (after 1-hour curing and 4-hour UV-ozone treatment). (b) Experimental data of how time for UV-ozone exposure changes PDMS wettability using a 1-hour curing time.....	159
Figure 5-7. Simulation of how changes in the initial concentration of LMW species affect the PDMS surface hydrophilization process with UV-ozone	161
Figure 5-8. Simulation of how diffusivity of non-polar groups influences the wettability of the PDMS surface	163
Figure 5-9. Microfluidic hydrodynamic flow-focusing pattern in this study	165
Figure 5-10. CO₂/aqueous phase flow patterns observed in hydrodynamic focusing microchannels.....	166
Figure 5-11. Comparison of CO₂/water flow patterns in hydrodynamic focusing microchannels with different wettability	168
Figure 5-12. Comparison of CO₂/AOS1618 solution flow patterns in hydrodynamic focusing microchannels with different wettability.....	170
Figure 5-13. Pressure threshold for CO₂ thread to enter downstream channels without surfactants in aqueous phase.	172
Figure 5-14. Pressure threshold for CO₂ thread to enter downstream channels with 0.2 wt% AOS1618 in aqueous phase.....	173
Figure 5-15. Microfluidic design of the heterogeneous porous micromodel	175
Figure 5-16. Displacement profiles in high and low permeable regions before gas breakthrough within the image captured	181
Figure 5-17. Snapshots of the porous media at gas breakthrough within the image captured.....	183
Figure 5-18. Comparison of (a) gas phase saturation and (b) dimensionless gas propagation front at gas breakthrough within the image captured.....	187

List of tables

Table 2-1. Characterization of adsorbent materials used in this study	29
Table 2-2. List of surfactants in this thesis	30
Table 3-1. Parameters for simulation of surfactant transport in Section 3.3.1	68
Table 3-2. Parameters for CO₂ foam simulation in this work (4000 psi, 120 °C).....	71
Table 4-1. Parameters for foam modeling in this work.....	95
Table 4-2. Parameters for the simulation of transient foam in Figure 4-24	129
Table 5-1. Wettability of the microfluidic devices shown in Figure 5-2	146
Table 5-2. List of the parameters in the model for LMW PDMS transport	156
Table 5-3. Wettability of microchannels in this study.....	166
Table 5-4. Summary of foam experiments in the heterogeneous micromodel	177

Chapter 1

Introduction

1.1 CO₂ foam in enhanced oil recovery

1.1.1 Overview of enhanced oil recovery

Typical crude oil recovery involves primary, secondary, and tertiary, or enhanced oil recovery (EOR) processes. In the primary recovery process, crude oil is produced by means of the pressure differential between the high pressure reservoir and atmospheric pressure above ground. Generally, primary production is followed by secondary recovery techniques, which include waterflooding and pressure maintenance. It is estimated that a recovery of 35% to 50% original oil in place (OOIP) can be achieved by waterflooding (Green and Willhite 1998).

EOR utilizes miscible gases, chemicals, and/or thermal energy to displace additional crude oil from an oil field (Lake 1989; Green and Willhite 1998). EOR processes are usually conducted after waterflooding. If successful EOR techniques can be implemented, an oil bank will be created as the injected fluids advance from the injection wells to the production wells, due to the mobilization of residual oil droplets.

Three major categories of EOR approaches will be briefly discussed below: thermal recovery, chemical injection and gas injection. Other EOR methods, such as microbial injection, are not addressed here.

Thermal recovery utilizes heat to recover the oil, which can be subdivided into hot-water floods, steam processes, and in-situ combustion. For example, steam injection can decrease the viscosity of the heavy viscous oil, such that the flow resistance of oil through the reservoir is reduced. Thermal methods are promising processes to enhance heavy oil production (Osterloh and Jones 2003), however, they do not contribute much to light crude oil recovery due to low viscosity reduction.

Chemical EOR methods mainly include polymer flooding, alkaline flooding, surfactant flooding, and their various combinations, such as Alkaline-Surfactant-Polymer (ASP) flooding (Liu, Zhang et al. 2008). Different chemicals account for different mechanisms of oil recovery enhancement. High-molecular weight water-soluble polymers can increase the viscosity of the aqueous phase significantly at low concentrations, leading to improved waterflooding performance with higher volumetric displacement efficiency. In some cases, such as polyacrylamide, the rock permeability is also reduced due to polymer retention (Green and Willhite 1998). However, the major concerns for polymer flooding are their effectiveness at high salinity and/or high temperature conditions and the chemical costs (Buchgraber, Clemens et al. 2009). Surfactant flooding can reduce oil-water interfacial tension (IFT) and/or alter wettability (Hirasaki and Zhang 2004) and thereby increase oil recovery. However, the most serious limitation for surfactant flooding is its high cost and losses as a result of adsorption to formation surfaces, phase partitioning and trapping, and precipitation in some hard brine cases. A promising cost-effective EOR process is to combine surfactant flooding with gas

injection to generate foam. This offers better mobility control and utilizes less chemicals.

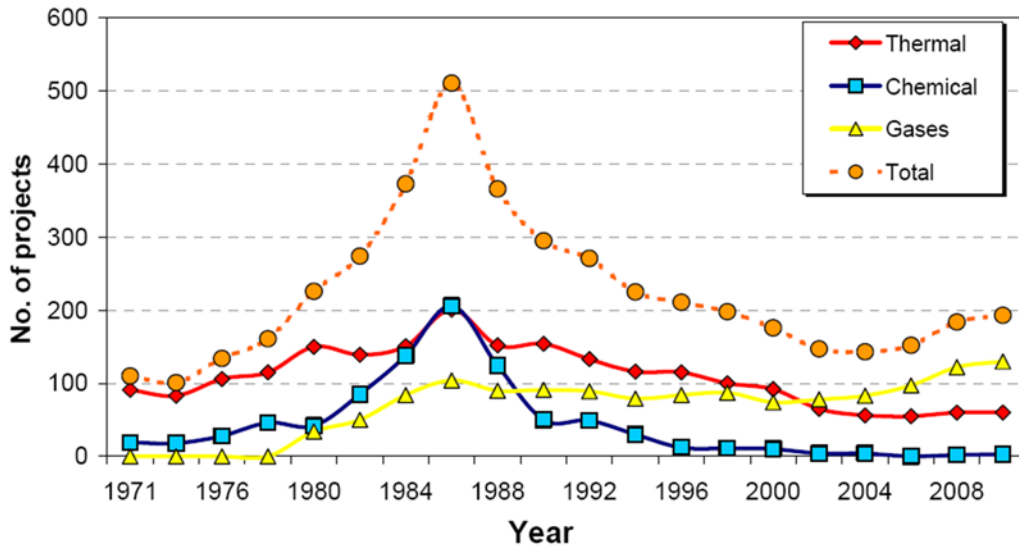


Figure 1-1. EOR projects in the USA (Alvarado and Manrique 2010)

Gas injection uses gases such as natural gas, nitrogen, or carbon dioxide as displacing fluids to recover additional oil. This method is also known as miscible flooding, because the displacing fluids should be miscible with the reservoir oil either at first contact (FCM) or after multiple contacts (MCM) (Green and Willhite 1998). Figure 1-1 shows the evolution of EOR projects during the last 40 years in the United States (Alvarado and Manrique 2010). In particular, EOR production from gas injection has been increasing, which is mainly due to an increase in CO₂ floods (Thomas 2008). Among various kinds of gas drives, the CO₂ miscible method (Holm 1959) has exhibited strong growth in the past 30 years, due to its relatively low minimum miscibility pressures (MMP) with a wide range of crude oils, as well as the benefit of the sequestration of CO₂ in oil reservoir. An

obstacle of CO₂ EOR process is the unfavorable mobility ratio of CO₂ versus oil, which will be discussed below. These obstacles can be overcome by making CO₂ foam to conduct this EOR process with good mobility control and improved recovery efficiency.

1.1.2 Foam mobility control for CO₂ EOR

As mentioned previously, CO₂ has good miscibility with a wide range of crude oils. Depending on the system pressure, it can be fully miscible with the lighter hydrocarbon components (up to 14 carbons) and partially miscible with heavier hydrocarbon components (Heller 1994). However, due to the low viscosity of CO₂ compared with oil and water, unfavorable mobility ratio will result. Additionally, reservoir formation is usually extremely heterogeneous, which will lead to channeling, gravity override and early breakthrough of injected CO₂. These effects will finally account for only a small portion of the oil swept by CO₂ in the heterogeneous oil reservoirs (Heller 1994).

In order to overcome the low sweep efficiency of CO₂ injection and increase the ultimate oil recovery, it is necessary to reduce the mobility of the injected CO₂. Two basic strategies have been developed to achieve this goal:

(1) The Water-Alternating-Gas (WAG) process operates via the injection of alternating slugs of brine and CO₂. Water slugs can reduce the mobility of these CO₂ slugs, and sequential banks of fluids (oil, water and CO₂) are expected to

propagate from injection wells to production wells. The weakness of this technique is that the extraction of hydrocarbon by CO₂ is low, due to increased water flow and trapped oil (Bernard, Holm et al. 1980) and the contact between CO₂ and oil may be shielded by injected brine.

(2) The CO₂ foam process. CO₂ foams are concentrated CO₂-in-water emulsions, which can increase the effective viscosity of the gas by several orders of magnitude and thus decrease the mobility of CO₂ (Heller 1994). To successfully achieve CO₂ foam mobility control in an oil reservoir, however, there are still several challenges that need to be addressed: screening of an applicable surfactant at reservoir conditions, concentration of the surfactant, slug sizes and frequency to be injected, etc. Optimization of the entire process will rely on the trade-off between the cost of materials and the amount of oil recovered.

Most CO₂ foam studies have focused on the evaluation of the foam performance in core samples with commercially available surfactants. Chaser CD-1045, for example, has been suggested as a suitable surfactant for CO₂ foam application at temperatures up to 50 °C and pressures up to 10000 kPa (Khalil and Asghari 2006). However, a good foaming agent is still far from its successful application in oil reservoirs, and one should consider the issues such as overall cost, decrease in injectivity and surfactant losses, which can hamper CO₂ foam application. Meanwhile, the application for high temperature and high salinity reservoir EOR requires further evaluation for suitable surfactants that are stable under these harsher conditions. In order to attain good mobility control for CO₂ foam, different reservoirs should adopt different surfactants. Experimentally

measuring and theoretically modeling chromatographic surfactant retardation will be useful to optimize injection strategy for CO₂ foam EOR application.

1.2 Foam transport in porous media

1.2.1 Darcy's law for multi-phase flow

To describe the flow of a fluid through porous media, Darcy's law can be employed, which was originally determined experimentally by Henry Darcy. Eqn (1.1) shows Darcy's law for phase j in porous media in multi-phase flow processes:

$$\vec{u}_j = -\lambda_{rj} k \cdot (\vec{\nabla} p_j - \rho_j g \vec{\nabla} D) \quad (1.1)$$

where

$$\lambda_{rj} = \frac{k_{rj}}{\mu_j} \quad (1.2)$$

In Eqn (1.1), \vec{u}_j is the superficial velocity of phase j , which is defined as the volumetric flow rate of phase j divided by the cross-sectional area of the porous medium: $\vec{u}_j = \frac{\vec{q}_j}{A}$. $\vec{\nabla} p_j$ is the pressure gradient, and $\rho_j g \vec{\nabla} D$ accounts for the gravity effect. In the case of one-dimensional horizontal flow, $\rho_j g \vec{\nabla} D$ can be

neglected. k is the permeability of the porous media. λ_{rj} is called the relative mobility of phase j , which can be further represented by Eqn (1.2).

In Eqn (1.2), k_{rj} is the relative permeability of phase j , which is usually a function of fluid saturation S_j . μ_j is the viscosity of phase j . The mobility λ_j of phase j is defined as the product of medium permeability and phase j relative mobility: $\lambda_j = \lambda_{rj} \cdot k$. In calculations involving a displacement process, a useful term is the mobility ratio M , of the invading and displaced phases:

$$M = \lambda_i / \lambda_d \quad (1.3)$$

where λ_i is the mobility of the invading phase and λ_d is the mobility of the displaced phase. A value of M larger than 1.0 is referred as an unfavorable mobility ratio, while a value of M smaller than 1.0 is referred as a favorable mobility ratio.

In the case of single-phase flow, we have $k_{rj} = 1$ and Eqn (1.1) reduces to Eqn (1.4):

$$\vec{u}_j = -\frac{k}{\mu_j} \cdot (\vec{\nabla} p_j - \rho_j g \vec{\nabla} D) \quad (1.4)$$

1.2.2 Foam microstructure and mobility

In reservoir applications, foam in porous media is defined as a dispersion of gas in liquid such that the liquid phase is continuous and at least some part of the gas phase is made discontinuous by thin liquid films called lamellae (Hirasaki 1989). Unlike the bulk foam, the behavior of foam in porous media is highly dependent on the geometry of the porous media, including the pore size, shape and connectivity. Figure 1-2 shows the schematic morphology of foam generated in porous media.

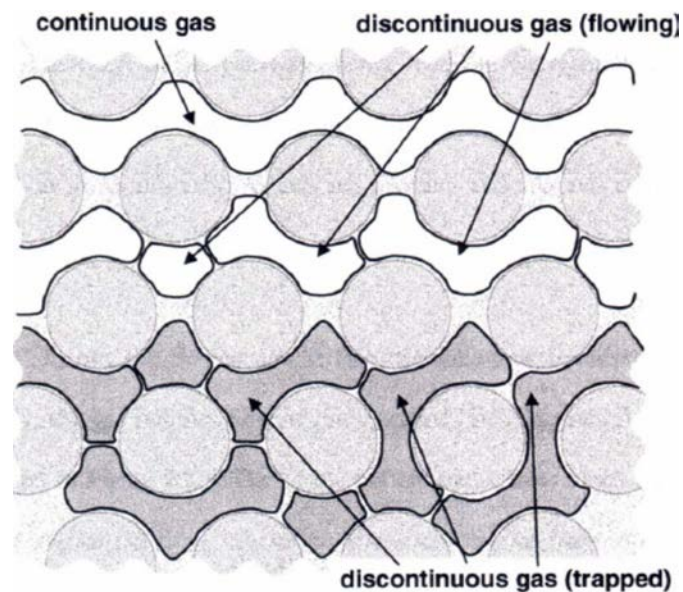


Figure 1-2. Pore-level schematic of fluid distribution for foam flow (Radke and Gillis 1990)

Typical pressure gradient contours of steady-state foam flooding indicate that two regimes exist in which foam flows through porous media: low-quality

regime and high-quality regime (Osterloh and Jante Jr 1992). In the low-quality foam regime, the gas bubbles are widely spaced in porous media and are separated by thick liquid lenses. In the high-quality foam regime, which is also known as the individual-lamellae regime (Hirasaki and Lawson 1985), the pore-spanning bubbles are closely packed and separated by individual lamellae.

Reasonably high gas fractional flows are expected to be used in most foam EOR applications, where the individual-lamellae foam is dominant. In this regime, it is important to distinguish continuous-gas foams from discontinuous-gas foams. In a discontinuous-gas foam, the entire gas phase is made discontinuous by lamellae (Falls, Hirasaki et al. 1988). Discontinuous foams can be either trapped or flowing (Figure 1-2), depending on the pressure gradient of the system. In a continuous-gas foam the medium usually contains several interconnected gas channels over macroscopic distances, as shown in Figure 1-2.

Foam is not a phase in reservoir rocks because most of the liquid separates from the gas upon entering the rock (Bernard, Holm et al. 1965). To describe foam mobility in porous media, one needs to separately discuss the mobility of its constituent phases. In a water-wet system, neither the relative permeability nor the viscosity of the aqueous phase is dependent on whether the gas exists as foam; however, the presence of foam can reduce gas-phase mobility by decreasing relative permeability of gas and increasing apparent gas viscosity (Bernard and Holm 1964). For continuous-gas foams, the reduction of gas relative permeability is the only effect of foam. However, for discontinuous-gas foams, the flow resistance of lamellae contributes to the increase of the apparent

viscosity of the gaseous phase (Hirasaki and Lawson 1985). Thus, discontinuous-gas foams typically have better mobility control than continuous-gas foams.

The number of lamellae per unit volume present in porous media governs foam mobility control, and it is defined as “foam texture”. According to this definition, the bubble size is inversely proportional to the foam texture at relative low water saturation. Finely textured foam with small bubbles can reduce gaseous phase mobility significantly, making it a strong foam, compared with a coarsely textured, or weak foam. However, foam texture depends on many factors, such as pore structure, surfactant formulation, flow rate, etc. A foam model is necessary to correlate foam mobility with various experimental factors, so as to explain and predict experimental data. Additionally, in order to create strong foams, there is a minimum pressure gradient ∇p_{\min} above which the discontinuous trapped foams can be mobilized and much higher apparent viscosity can be obtained (Rossen 1990).

1.2.3 Foam generation and coalescence

1.2.3.1 Foam generation

It is generally accepted that there are three fundamental pore-level foam generation mechanisms in porous media: snap-off, lamellae division and leave-behind.

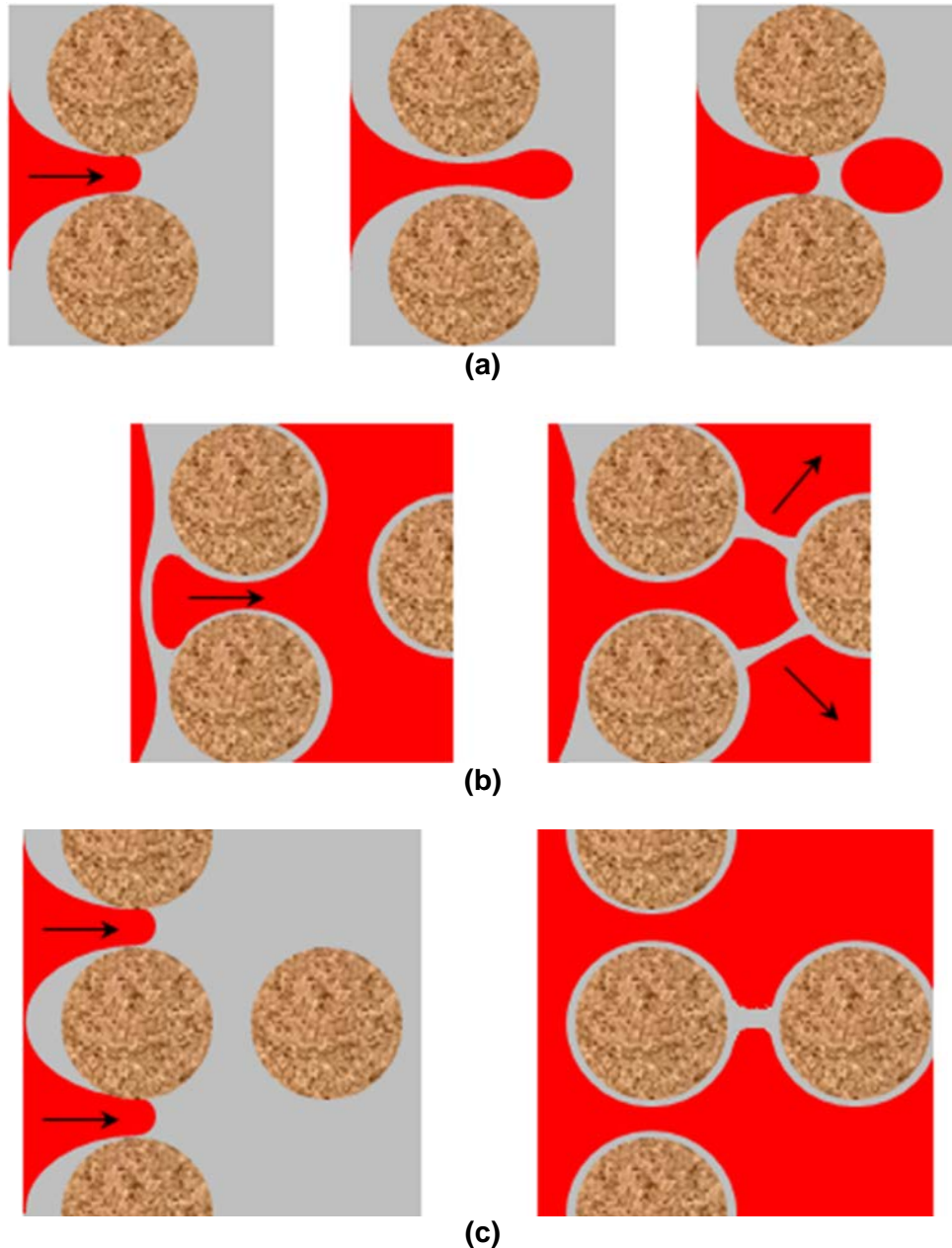


Figure 1-3. Schematics of (a) the snap-off mechanism, (b) the lamella-division mechanism, (c) the leave-behind mechanism for foam generation. The circles filled with brownish cork texture represent rocks, the phase with grey color represents aqueous phase, and the phase with red color represents gas phase. The black arrows indicate flow direction. Adapted from Kovscek and Radke 1994 (Kovscek and Radke 1994).

Figure 1-3(a) shows how bubble snap-off occurs through a pore throat. The pore throat is previously filled with aqueous phase (surfactant solution). After the

gas front enters the pore, a gas finger and two aqueous phase collars will form in the pore throat. Due to the reduced curvature and the corresponding decrease of local capillary pressure when the gas finger passes through the pore throat, a liquid pressure gradient will be created to make the wetting collars grow and finally cause bubble snap-off.

Capillary snap-off is one important mechanism for foam generation in porous media. It is found that the mobility of gaseous phase can be reduced by several-hundred fold if the discontinuous-gas foams are solely generated by snap-off mechanism (Ettinger and Radke 1992). The occurrence of snap-off depends on local dynamic capillary pressure (Falls, Hirasaki et al. 1988), as well as pore geometry and wettability (Li and Wardlaw 1986). The effect of pore wettability on bubble break-up will also be investigated in this thesis.

The second foam generation mechanism, lamella division, is illustrated in Figure 1-3(b). One of the prerequisites for lamella division is that a lamella must pre-exist and have been generated by another foam generation mechanism, such as capillary snap-off. When the lamella comes across a branch point, it will split into two individual lamellae provided that the capillary number is above a critical value. The trapped bubbles in the surrounding pores can create different resistance in the downstream channels, which can also affect whether lamella division happens.

The third foam generation mechanism “leave-behind” is shown in Figure 1-3(c). One can find that the process is similar to that in capillary snap-off, while the

difference is that there are two gas fingers in adjacent pore throats in order to create the “leave-behind” lamella. A lens parallel to the flow direction is left behind as two gas fingers converge downstream. This mechanism can result in continuous-gas foams if no other mechanisms are present, which does not lead to strong foam generation.

1.2.3.2 Foam coalescence

Foams are not thermodynamically stable, and foam generation in porous media is always accompanied with foam coalescence process. There are two major mechanisms accounting for foam coalescence: capillary suction and gas diffusion.

Capillary suction causes direct breakage of the lamella, which is the primary mechanism for foam coalescence. Although both mechanisms are dominated by capillary pressure, capillary suction is strongly dependent on surfactant formulation compared with capillary snap-off. To describe the influence of this dependence on liquid film stability, a disjoining pressure function Π is introduced to represent the interactions between two surfaces which form a lamella. Higher capillary pressure is required to balance Π , when lamella thickness decreases until it reaches a critical thickness h^{cr} (corresponding to the maximum disjoining pressure, Figure 1-4), and the lamella is no longer stable and finally breaks. When mechanical disturbances exist in the system, the lamella can collapse with a thickness larger than h^{cr} (Bikerman 1973).

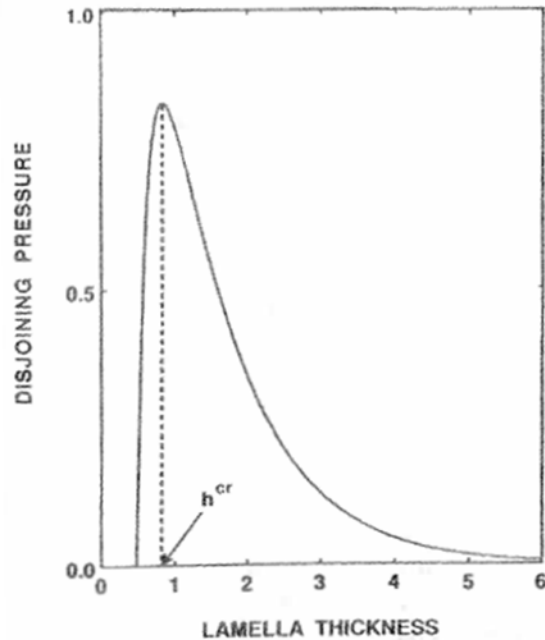


Figure 1-4. Schematic of disjoining pressure function Π (Rossen 1996).

An important finding in foam coalescence is the understanding of the limiting capillary pressure (P_c^*) for foam stability (Khatib, Hirasaki et al. 1988). When conditions are favorable for generation of finer textured foam, the resulting reduced gas mobility reduces the water saturation, which increases the capillary pressure until the rate of foam coalescence equals foam generation. In the high-quality foam regime, gas bubbles are separated by thin liquid lamellae resulting in a relatively dry foam and its behavior is determined by the limiting capillary pressure and bubble coalescence (Khatib, Hirasaki et al. 1988; Alvarez, Rivas et al. 2001).

Another foam decay mechanism is gas diffusion coalescence. This mechanism is caused by the pressure difference of contiguous bubbles with different curvatures. According to Young-Laplace equation, smaller bubbles will

have larger pressure, and mass transfer of the gas will be initiated from smaller bubbles to larger bubbles by this driving force. Finally the smaller bubbles will shrink and disappear, and the larger bubbles will expand. This process is also known as “bubble Ostwald ripening” in some literature (Tcholakova, Mitrinova et al. 2011). It is noticeable that this mechanism is limited in porous media compared with bulk foams, because the bubbles are pore-spanning and lamella curvature is not so directly related to bubble size (Rossen 1996).

1.2.4 Foam modeling techniques

Various foam models have been proposed to simulate foam flow through porous media, among which the most promising ones are the mechanistic methods based on bubble population balance and the semi-empirical methods based on fractional flow theory. The population-balance foam model is a mechanistic method to describe foam flow through porous media (Falls, Hirasaki et al. 1988; Patzek 1988). It has received wide attention because it physically describes the generation and decay of foam lamellae and dynamically tracks the mobility of foam. In this model, foam texture is modeled explicitly with a bubble population-balance equation and gas mobility is expressed as a function of foam texture, water saturation and other factors (Kam, Nguyen et al. 2007). This foam model has successfully matched several laboratory experiments (Friedmann, Chen et al. 1991; Kavscek, Patzek et al. 1995; Bertin, Quintard et al. 1998), and is capable of simulating foam behavior in both the high-quality and low-quality

regimes upon the modification of net foam generation (Dholkawala, Sarma et al. 2007; Afsharpoor, Lee et al. 2010; Chen, Gerritsen et al. 2010). However, there are some limitations in this foam model, such as the difficulty in obtaining the modeling parameters, especially at the field scale, and determining the minimum pressure gradient for foam generation (Kam, Nguyen et al. 2007). Additionally, the foam generation term in this model does not distinguish between snap-off and lamella division at various conditions (Tanzil, Hirasaki et al. 2002; Rossen 2003).

In the early studies of the semi-empirical methods, the effect of foam on gas mobility reduction is expressed with a mobility reduction factor (MRF), which reduces the relative permeability of the gas phase depending on surfactant concentration, oil saturation and capillary number (Mohammadi, Coombe et al. 1993). Advances to these semi-empirical methods incorporate the mechanistic physics of foam transport to the MRF using the fractional flow theory. According to the fixed- P_c^* model (Zhou and Rossen 1995), the effect of limiting capillary pressure above which foam collapses is included in the foam model in terms of a critical water saturation. This concept was later adopted in a commercial reservoir simulator STARSTM with a modified expression (Cheng, Reme et al. 2000). Vassenden and Holt proposed a similar model by modifying the gas relative permeability with experimental validation (Vassenden and Holt 2000). On the other hand, lamella creation and coalescence are balanced by assuming local steady state, and a model modifying gas phase viscosity through foam texture is constructed (Dholkawala, Sarma et al. 2007; Afsharpoor, Lee et al.

2010). In this model, foam texture is a function of water saturation and pressure gradient if the water saturation is above the critical water saturation. According to Darcy's law, decreasing relative permeability or increasing viscosity of the gas phase by the same factor results in the same mathematical expression.

Therefore, it doesn't make a difference if a viscosity-based model versus a relative-permeability-based model (STARS™) is utilized. The semi-empirical foam model using the fractional flow theory (Cheng, Reme et al. 2000), or the STARS™ foam model (Computer Modeling Group 2007), has been widely used to describe foam flow through porous media in the oil and gas industry. These applications include simulation of surfactant-alternating-gas (SAG) processes (Renkema and Rossen 2007) and simultaneous injection of surfactant solution and gas (Masalmeh, Wei et al. 2011), simulation of oil displacement by foam (Ashoori, van der Heijden et al. 2010; Liu, Andrianov et al. 2011; Zanganeh, Kam et al. 2011), interpretation of experimental data of co-injection of gas and surfactant solution on the 10 m scale (Vassenden, Holt et al. 1999) and in Berea cores (Chalbaud, Moreno et al. 2002), and simulation of foam process at reservoir scale from the Snorre field in Norway (Skauge, Aarra et al. 2002).

1.3 Surfactant retention in CO₂ foam process

1.3.1 Overview of surfactants

A surfactant (a contraction of "surface active agent") is a substance that is energetically favorable to adsorb onto the surfaces or interfaces between phases

(Miller and Neogi 2008). Surfactants can reduce interfacial tension between two phases, and also allow easier spreading of the wetting phase on solid. Surfactants are amphiphilic, which means that they contain both hydrophilic groups (their heads) and hydrophobic groups (their tails).

With respect to the hydrophilic moiety of the molecule, a surfactant can be categorized into one of the four groups: anionics, cationics, nonionics, and zwitterionics (amphoteric). An anionic surfactant carries a net negative charge on its headgroup, while a cationic surfactant carries a positive charge. If a surfactant contains a headgroup with both positive and negative charged groups, it is termed zwitterionic. A nonionic surfactant does not have charged group in its hydrophilic moiety.

An important characteristic of a surfactant is its critical micelle concentration (CMC). A micelle is a colloidal-sized cluster of surfactant molecules in a liquid, which is formed when bulk surfactant concentration is above the CMC. Above the CMC, addition of surfactants to the bulk solution will increase the number of micelles, but not change much the number of non-aggregating surfactant molecules. Due to this mechanism, many physical properties change significantly in the vicinity of the CMC. For example, the interfacial tension decreases rapidly when increasing surfactant concentration below the CMC, but is nearly unchanged above the CMC (Miller and Neogi 2008).

Some surfactants can be good foaming agents for EOR applications (Heller 1994). Evaluation of a foaming agent is of great importance in CO₂ foam EOR

process. A suitable foaming agent should have a high apparent viscosity and insignificant chromatographic retardation in porous media. Additionally, the factors causing surfactant retention will also be investigated both experimentally and theoretically. Surfactant retention in EOR processes can be caused by at least three mechanisms: adsorption onto mineral surface, phase partitioning into a static or slow-moving phase, and precipitation (Green and Willhite 1998).

1.3.2 Surfactant adsorption on formation minerals

A number of factors can cause surfactant adsorption at the solid-liquid interface, including ion exchange or pairing, acid-base interaction, polarization of π electrons, dispersion forces, and hydrophobic bonding (Rosen 2004). Although the relative importance of these forces can be different for each surfactant, there are some general trends of adsorption for the same type of surfactants. For example, nonionic surfactants generally have less adsorption on carbonate formations than anionic surfactants. This is because carbonate, such as calcite or dolomite, is normally positively charged at neutral pH, and the ionic interactions between surfactants and mineral surface mainly account for the high adsorption of anionic surfactants.

Various studies have been done for both static and dynamic adsorption experiments. In batch equilibrium tests, it is found that static adsorption of surfactants can be described with a Langmuir-type isotherm (Lake 1989; Adamson and Gast 1997) for some surfactant systems. According to the

Langmuir adsorption isotherm, the amount of adsorption typically increases with surfactant concentration until a plateau is reached at a sufficiently high concentration of surfactant. When the adsorption is measured dynamically, e.g. in coreflooding tests, it is important to be cognizant of its rate-dependency. Higher flow rates will lead to less adsorption with the same throughput of surfactant solution. However, low reservoir flow rates, especially those away from a wellbore, makes the adsorption quasi-steady state and the rate-dependency is not a major concern (Green and Willhite 1998).

Surfactant adsorption can be detrimental to CO₂ foam process. If the surfactant front propagates slower than the foam front, CO₂ will lose mobility control in the region where surfactant has not reached. During field operation, pH and salinity are important controllable variables for the injection fluids, which can affect the amount of adsorption by altering mineral surface electric potential. Potential determining ions CO_3^{2-} and HCO_3^- have been identified to reduce anionic surfactant adsorption by changing the surface charge of calcite (Hirasaki and Zhang 2004).

1.3.3 Surfactant partition between phases

Although the CO₂-soluble surfactants can be designed to be injected with CO₂, they will partition into aqueous and oleic phases depending on the corresponding partition coefficients. Surfactant trapped in residual oil phase, which can result in significant chromatographic retention in porous media, should

be reduced. This can be achieved by optimizing the salinity in aqueous phase to minimize surfactant partition into oleic phase (Glover, Puerto et al. 1979; Hirasaki 1981; Hirasaki, Van Domselaar et al. 1983).

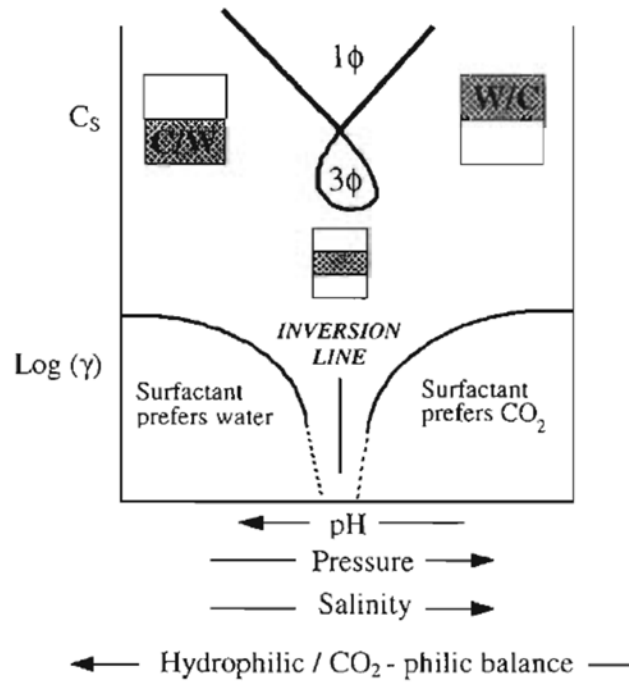


Figure 1-5. Schematic representation of surfactant phase behavior and the effect of formulation variables on emulsions (Psathas, Sander et al. 2002). ϕ represents the phases, and γ represents the interfacial tension.

The partition of surfactant between CO₂ and water is important for designing the injection strategy. A hydrophilic-CO₂philic balance (HCB) value has been defined to characterize the phase behavior of the emulsions in compressed CO₂-water system (da Rocha, Harrison et al. 1999). For large HCB values, the surfactant prefers the aqueous phase and CO₂-in-water micro or macroemulsion will result (da Rocha, Harrison et al. 1999). Figure 1-5 shows how formulation

variables, including pH, salinity, pressure, temperature, and HCB, can manipulate the phase behavior of an emulsion in the CO₂-water system.

For stable CO₂-in-water foams, it is currently thought the HCB of the surfactant should prefer the water of the balanced state in Figure 1-5. However, high partition of surfactant in aqueous phase may lead to significant chromatographic retardation of the surfactant if it is injected with CO₂. The trade-off between phase partitioning and foam strength can be optimized through the foam simulator.

1.3.4 Surfactant precipitation

The precipitation of ionic surfactants can limit the application of surfactant formulations in CO₂ foam EOR. Precipitation is caused by high salinity and/or multivalent ions in the surfactant solutions. This phenomenon has been observed when anionic surfactants are used, due to its association with metal ions in brine (Somasundaran, Celik et al. 1984). The types of cations, surfactant concentration, salt concentration, and temperature are all determining factors for surfactant precipitation.

It has also been recognized that the tolerance of salinity and hardness can be increased by adding nonionic surfactant to ionic surfactant solutions (Stellner and Scamehorn 1986). Generally, nonionic surfactants can be designed to be resistant to hard water, multivalent metallic cations, electrolyte at high

concentration (Rosen 2004). In this thesis, we will focus on cationic, zwitterionic, and nonionic foaming agents to avoid precipitation problems. The surfactant should also be selected in a way that the reservoir temperature is above the Krafft point (the minimum temperature at which surfactants form micelles) and below the cloud point (the temperature at which dissolved surfactants are no longer completely soluble, precipitating as a second phase giving a cloudy appearance) of the surfactant.

1.4 Thesis structure

This thesis is organized as follows:

Chapter 2 presents the experimental results of surfactant adsorption on carbonate materials.

Chapter 3 presents the simulator development and the simulation of chromatographic retardation for understanding surfactant and foam transport in oil reservoirs.

Chapter 4 discusses the estimation of foam modeling parameters for simulation of foam flow in porous media.

Chapter 5 demonstrates micromodel visualization of foam transport in microchannels and heterogeneous porous media.

Chapter 6 concludes the thesis and provides suggestions for future work.

1.5 References

- Adamson, A. W. and A. P. Gast (1997). Physical chemistry of surfaces. New York, Wiley.
- Afsharpoor, A., G. S. Lee, et al. (2010). "Mechanistic simulation of continuous gas injection period during surfactant-alternating-gas (SAG) processes using foam catastrophe theory." Chemical Engineering Science **65**(11): 3615-3631.
- Alvarado, V. and E. Manrique (2010). "Enhanced Oil Recovery: An Update Review." Energies **3**(9): 1529-1575.
- Alvarez, J. M., H. J. Rivas, et al. (2001). "Unified model for steady-state foam behavior at high and low foam qualities." SPE Journal **6**(3): 325-333.
- Ashoori, E., T. L. M. van der Heijden, et al. (2010). "Fractional-flow theory of foam displacements with oil." SPE Journal **15**(2): 260-273.
- Bernard, G. G. and L. W. Holm (1964). "Effect of foam on permeability of porous media to gas." Society of Petroleum Engineers Journal **4**(3): 267-274.
- Bernard, G. G., L. W. Holm, et al. (1980). "Use of Surfactant to Reduce Co₂ Mobility in Oil Displacement." Society of Petroleum Engineers Journal **20**(4): 281-292.
- Bernard, G. G., L. W. Holm, et al. (1965). "Effect of Foam on Trapped Gas Saturation and on Permeability of Porous Media to Water." Journal of Petroleum Technology **17**(9): 1062-&.
- Bertin, H. J., M. Y. Quintard, et al. (1998). "Development of a bubble-population correlation for foam-flow modeling in porous media." SPE Journal **3**(4): 356-362.
- Bikerman, J. J. (1973). Foams. New York, Springer-Verlag.
- Buchgraber, M., T. Clemens, et al. (2009). The Displacement of Viscous Oil by Associative Polymer Solutions. SPE Annual Technical Conference and Exhibition. New Orleans, Louisiana, Society of Petroleum Engineers.
- Chalbaud, C. A., R. A. Moreno, et al. (2002). Simulating foam process for a Venezuelan pilot test. SPE Annual Technical Conference and Exhibition. San Antonio, Texas, Copyright 2002, Society of Petroleum Engineers Inc.
- Chen, Q., M. G. Gerritsen, et al. (2010). "Modeling foam displacement with the local-equilibrium approximation: theory and experimental verification." SPE Journal **15**(1): 171-183.
- Cheng, L., A. B. Reme, et al. (2000). Simulating foam processes at high and low foam qualities. SPE/DOE Improved Oil Recovery Symposium. Tulsa, Oklahoma.
- Computer Modeling Group (2007). "STARSTM user's guide." Calgary, Alberta, Canada.
- da Rocha, S. R. P., K. L. Harrison, et al. (1999). "Effect of surfactants on the interfacial tension and emulsion formation between water and carbon dioxide." Langmuir **15**(2): 419-428.
- Dholkawala, Z. F., H. K. Sarma, et al. (2007). "Application of fractional flow theory to foams in porous media." Journal of Petroleum Science and Engineering **57**(1-2): 152-165.
- Ettinger, R. A. and C. J. Radke (1992). "Influence of Texture on Steady Foam Flow in Berea Sandstone." SPE Reservoir Engineering **7**(1): 83-90.

- Falls, A. H., G. J. Hirasaki, et al. (1988). "Development of a mechanistic foam simulator: the population balance and generation by snap-Off." SPE Reservoir Engineering **3**(3): 884-892.
- Friedmann, F., W. H. Chen, et al. (1991). "Experimental and simulation study of high-temperature foam displacement in porous media." SPE Reservoir Engineering **6**(1): 37-45.
- Glover, C. J., M. C. Puerto, et al. (1979). "Surfactant Phase-Behavior and Retention in Porous-Media." Society of Petroleum Engineers Journal **19**(3): 183-193.
- Green, D. W. and G. P. Willhite (1998). Enhanced oil recovery. Richardson, TX, Henry L. Doherty Memorial Fund of AIME, Society of Petroleum Engineers.
- Heller, J. P. (1994). "CO₂ foams in enhanced oil-recovery." Foams: Fundamentals and Applications in the Petroleum Industry **242**: 201-234.
- Hirasaki, G. and D. L. Zhang (2004). "Surface chemistry of oil recovery from fractured, oil-wet, carbonate formations." Spe Journal **9**(2): 151-162.
- Hirasaki, G. J. (1981). "Application of the Theory of Multicomponent, Multiphase Displacement to Three-Component, Two-Phase Surfactant Flooding." **21**(2): 191-204.
- Hirasaki, G. J. (1989). "The steam-foam process." Journal of Petroleum Technology **41**(5): 449-456.
- Hirasaki, G. J. and J. B. Lawson (1985). "Mechanisms of foam flow in porous media - apparent viscosity in smooth capillaries." Society of Petroleum Engineers Journal **25**(2): 176-190.
- Hirasaki, G. J., H. R. Van Domselaar, et al. (1983). "Evaluation of the Salinity Gradient Concept in Surfactant Flooding." Society of Petroleum Engineers Journal **23**(3): 486-500.
- Holm, L. W. (1959). "Carbon Dioxide Solvent Flooding for Increased Oil Recovery." Transactions of the American Institute of Mining and Metallurgical Engineers **216**: 225-231.
- Kam, S. I., Q. P. Nguyen, et al. (2007). "Dynamic simulations with an improved model for foam generation." SPE Journal **12**(1): 35-48.
- Khalil, F. and K. Asghari (2006). "Application of CO₂-foam as a means of reducing carbon dioxide mobility." Journal of Canadian Petroleum Technology **45**(5): 37-42.
- Khatib, Z. I., G. J. Hirasaki, et al. (1988). "Effects of capillary pressure on coalescence and phase mobilities in foams flowing through porous media." SPE Reservoir Engineering **3**(3): 919-926.
- Kovscek, A. R., T. W. Patzek, et al. (1995). "A mechanistic population balance model for transient and steady-state foam flow in Boise sandstone." Chemical Engineering Science **50**(23): 3783-3799.
- Kovscek, A. R. and C. J. Radke (1994). "Fundamentals of foam transport in porous-media." Foams: Fundamentals and Applications in the Petroleum Industry **242**: 115-163.
- Lake, L. W. (1989). Enhanced oil recovery. Englewood Cliffs, N.J., Prentice Hall.
- Li, Y. and N. C. Wardlaw (1986). "The Influence of Wettability and Critical Pore Throat Size Ratio on Snap-Off." Journal of Colloid and Interface Science **109**(2): 461-472.

- Liu, M., A. Andrianov, et al. (2011). Sweep efficiency in CO₂ foam simulations with oil. SPE EUROPEC/EAGE Annual Conference and Exhibition. Vienna, Austria, Society of Petroleum Engineers.
- Liu, S., D. Zhang, et al. (2008). "Favorable Attributes of Alkaline-Surfactant-Polymer Flooding." SPE Journal **13**(1): pp. 5-16.
- Masalmeh, S. K., L. Wei, et al. (2011). Mobility Control for Gas Injection in Heterogeneous Carbonate reservoirs: Comparison of Foams versus Polymers. SPE Middle East Oil and Gas Show and Conference. Manama, Bahrain.
- Miller, C. A. and P. Neogi (2008). Interfacial phenomena : equilibrium and dynamic effects. Boca Raton, FL, CRC Press/Taylor & Francis.
- Mohammadi, S. S., D. A. Coombe, et al. (1993). "Test of steam-foam process for mobility control in South-Casper Creek reservoir." Journal of Canadian Petroleum Technology **32**(10): 49-54.
- Osterloh, W. T. and M. J. Jante Jr (1992). Effects of gas and liquid velocity on steady-state foam flow at high temperature. SPE/DOE Enhanced Oil Recovery Symposium. Tulsa, Oklahoma, 1992 Copyright 1992, Society of Petroleum Engineers Inc.
- Osterloh, W. T. and J. Jones (2003). "Novel thermal process for recovery of extremely shallow heavy oil." Spe Reservoir Evaluation & Engineering **6**(2): 127-134.
- Patzek, T. W. (1988). "Description of foam flow in porous media by the population balance method." Acs Symposium Series **373**: 326-341.
- Psathas, P. A., E. A. Sander, et al. (2002). "Mapping the stability and curvature of emulsions of H₂O and supercritical CO₂ with interfacial tension measurements." Journal of Dispersion Science and Technology **23**(1-3): 65-80.
- Radke, C. J. and J. V. Gillis (1990). "A Dual Gas Tracer Technique for Determining Trapped Gas Saturation During Steady Foam Flow in Porous Media." SPE Annual Technical Conference and Exhibition, 23-26 September 1990, New Orleans, Louisiana.
- Renkema, W. J. and W. R. Rossen (2007). Success of foam SAG processes in heterogeneous reservoirs. SPE Annual Technical Conference and Exhibition. Anaheim, California, U.S.A., Society of Petroleum Engineers.
- Rosen, M. J. (2004). Surfactants and interfacial phenomena. Hoboken, N.J., Wiley-Interscience.
- Rossen, W. R. (1990). "Theory of mobilization pressure-gradient of flowing foams in porous media.1. Incompressible foam." Journal of Colloid and Interface Science **136**(1): 1-16.
- Rossen, W. R. (1996). "Foams in Enhanced Oil Recovery." Foams: theory, measurements, and applications **57**: 413-464.
- Rossen, W. R. (2003). "A critical review of Roof snap-off as a mechanism of steady-state foam generation in homogeneous porous media." Colloids and Surfaces a-Physicochemical and Engineering Aspects **225**(1-3): 1-24.
- Skauge, A., M. G. Arra, et al. (2002). Foam-assisted WAG: experience from the Snorre field. SPE/DOE Improved Oil Recovery Symposium. Tulsa, Oklahoma, Copyright 2002, Society of Petroleum Engineers Inc.
- Somasundaran, P., M. Celik, et al. (1984). "The Role of Surfactant Precipitation and Redissolution in the Adsorption of Sulfonate on Minerals." **24**(2): 233-239.

- Stellner, K. L. and J. F. Scamehorn (1986). "Surfactant Precipitation in Aqueous-Solutions Containing Mixtures of Anionic and Nonionic Surfactants." Journal of the American Oil Chemists Society **63**(4): 566-574.
- Tanzil, D., G. Hirasaki, J. , et al. (2002). Conditions for foam generation in homogeneous porous media. SPE/DOE Improved Oil Recovery Symposium. Tulsa, Oklahoma, Copyright 2002, Society of Petroleum Engineers Inc.
- Tcholakova, S., Z. Mitrinova, et al. (2011). "Control of Ostwald Ripening by Using Surfactants with High Surface Modulus." Langmuir **27**(24): 14807-14819.
- Thomas, S. (2008). "Enhanced oil recovery - An overview." Oil & Gas Science and Technology-Revue D Ifp Energies Nouvelles **63**(1): 9-19.
- Vassenden, F. and T. Holt (2000). "Experimental foundation for relative permeability modeling of foam." SPE Reservoir Evaluation & Engineering **3**(2): 179-185.
- Vassenden, F., T. Holt, et al. (1999). "Foam propagation on semi-reservoir scale." SPE Reservoir Evaluation & Engineering **2**(5): 436-441.
- Zanganeh, M. N., S. I. Kam, et al. (2011). "The method of characteristics applied to oil displacement by foam." SPE Journal **16**(1): 8-23.
- Zhou, Z. and W. R. Rossen (1995). "Applying fractional-flow theory to foam processes at the "limiting capillary pressure"." SPE Advanced Technology Series **3**(1): 154-162.

Chapter 2

Surfactant adsorption on carbonate materials

This chapter presents experimental results of static surfactant adsorption on carbonate materials. Various foaming surfactants are evaluated using adsorption measurements. High performance liquid chromatography (HPLC) methods are utilized for measuring nonionic and zwitterionic surfactants. The influence of non-carbonate impurities on surfactant adsorption behavior on carbonates is explained.

2.1 Materials and methods

2.1.1 Materials

Four natural carbonate materials, including dolomite and limestone, are used in this work. The particle size, surface area, ζ -potential at unadjusted pH, and source of these materials are listed in Table 2-1. To distinguish different sources of the carbonate samples, the dolomite samples supplied by Vital Earth / Carl Pool and Sciencelab.com, Inc are referred as dolomite (Carl Pool) and dolomite (Sciencelab.com), respectively. The limestone samples supplied by Franklin Minerals and Carthage Crushed Limestone are referred as limestone (Franklin) and limestone (Carthage), respectively. Note that we find significantly different adsorption results with two different batches of dolomite supplied by Vital Earth /

Carl Pool. Thus the dolomite materials from this supplier are divided into dolomite (Carl Pool, old) and dolomite (Carl Pool, new).

Table 2-1. Characterization of adsorbent materials used in this study

Material	Size	BET surface area (m ² /g)	ζ-potential (mV)	Source
dolomite	≤74 μm (200+ mesh)	0.97	8.0±3.5 (pH=10.0)	Vital Earth / Carl Pool (new), Gladewater, TX, USA
dolomite	≤74 μm (200+ mesh)	0.89	19.5±6.6 (pH=10.1)	Sciencelab.com, Inc. (Catalog# SLD4477), USA
limestone	420 to 840 μm (20/40 mesh)	0.29	NA*	Franklin Minerals, Nolanville, TX, USA
limestone	≤420 μm (40+ mesh)	1.23	29.6±2.7 (pH=10.0)	Carthage Crushed Limestone, Carthage, MO, USA
calcite	5 μm	1.65	4.2±7.2 (pH=9.8)	Alfa Aesar (Catalog# 11403), USA
silica	≤10 μm	1.16	-47.3±2.5 (pH=6.0)	U.S. Silica Company, Pacific, MO, USA
kaolin	0.1 to 4 μm	26.61	-38.0±7.6 (pH=4.8)	Sigma-Aldrich (Catalog# K7375), USA

*: Not measured.

Chemical-grade synthetic calcium carbonate (99.5% metals basis) powder supplied by Alfa Aesar is used as a standard calcite sample. According to the manufacturer, this calcite sample has a uniform size of 5 μm. Fine round silica flour (MIN-U-SIL10, U.S. Silica Company) is used as a representative silica [SiO₂] material. In order to remove Fe₂O₃ and other metal oxides in the original sample, the silica flour is washed with 1 mol/L HCl, 0.01 mol/L NaHCO₃ solution and

deionized water sequentially and is dried in a convection oven at 80 °C overnight prior to use. Kaolin [Al₂Si₂O₅(OH)₄] powder (Sigma-Aldrich) is used as a typical clay material in this study.

The BET (Brunauer-Emmett-Teller) surface areas of the samples are measured using a Quantachrome Autosorb-3b BET Surface Analyzer. The results are shown in Table 2-1.

Table 2-2. List of surfactants in this thesis

Trade name (Manufacturer)	Chemical name	Acronym	Surfactant type
-- (Sigma-Aldrich)	sodium dodecyl sulfate	SDS	anionic
AGENT X-3153-026 (Stepan)	sodium (C1618) alpha olefin sulfonate	AOS 1618	anionic
Petrostep S-2A (Stepan)	sodium (C1518) internal olefin sulfonate	IOS 1518	anionic
Steol CS-330 (Stepan)	sodium laureth sulfate, 3 moles EO	CS 330	anionic
-- (Sigma-Aldrich)	dodecyltrimethylammonium bromide	DTAB	cationic
-- (Sigma-Aldrich)	hexadecylpyridinium chloride	CPC	cationic
Ethomeen C/25A (AkzoNobel)	polyoxyethylene (15) cocoalkylamines	C25A	cationic
Tergitol 15-S-30 (Dow)	secondary alcohol ethoxylate, 31 EO	15-S-30	nonionic
AMPHOSOL CS-50 (Stepan)	cocamidopropyl hydroxysultaine	CAHS	zwitterionic
MACKAM LAB (Rhodia)	lauryl and myristyl betaines	LAB	zwitterionic

Various surfactants are evaluated in the adsorption tests. These surfactants are listed in Table 2-2. Unless otherwise specified, acronyms for the surfactants shown in Table 2-2 will be used in the rest of this thesis.

Some adsorption experiments are performed in synthetic brine in addition to DI water. The synthetic brine contains 182.31g/L NaCl, 58.33g/L CaCl₂, and 25.62 g/L MgCl₂.

2.1.2 Characterization of surface chemistry with XPS and XRD

X-ray Photoelectron Spectroscopy (XPS) is performed on the adsorbent materials using a scanning XPS microprobe (PHI Quantera XPS, Physical Electronics, Inc). At depths of 3-5 nm from the surface of the sample, the chemical composition is revealed using XPS. Three parallel experiments are conducted with different sampling spots for each adsorbent to identify the surface heterogeneity of the material. The atomic composition is attained by analyzing the characteristic peaks of binding energy through high resolution scan of the elements. Powder X-ray Diffraction (XRD) is conducted to examine the physico-chemical make-up of HCl-insoluble solids in natural carbonate samples using Rigaku D/Max Ultima II Powder XRD instrument. The results are analyzed with JADE 9.4 data processing software (MDI, Inc.) using the ICDD (International Center for Diffraction Data) PDF4+ database to identify the mineralogy.

2.1.3 ζ potential measurements

The ζ potential measurements follow the procedure of Jiang, et al (Jiang, Hirasaki et al. 2010) with a slight modification. The samples are prepared in 0.01 mol/L NaCl solution with a suspension of 1.0 wt% absorbent material. Unless otherwise specified, the pH or ionic strength of the suspension is not adjusted. The mixture is subsequently shaken overnight at 180 rpm to reach equilibrium. Before each measurement, the mixture is taken out from the shaker and settled for 30 min to obtain a stable suspension after sedimentation of larger particles.

The ζ potential of the suspension is measured by a zeta potential analyzer (ZetaPALS, Brookhaven Instruments Corporation). Each sample is analyzed by ZetaPALS through 10 repetitive measurements. The average ζ potential of 10 measurements is chosen as the ζ potential value of the sample.

2.1.4 Static adsorption experiments

Surfactants are dissolved in deionized water or synthetic brine at various concentrations to serve as initial surfactant solutions, respectively. The adsorbent material is mixed with surfactant solution in 50-ml centrifuge tubes at various weight/volume ratios to obtain different data points on the adsorption isotherm. The centrifuge tubes with adsorbent-dispersed surfactant solution are subsequently placed on a reciprocal shaker (Model E6010, Eberbach Corporation) and shaken at 180 rpm for at least 24 hours at room temperature.

After that, the samples are centrifuged at 8000 rpm for 30 min and the supernatant is titrated to determine residual (equilibrium) surfactant concentration.

2.1.5 Analysis of surfactant concentration

The concentration of anionic surfactants (SDS, AOS 1618, IOS 1518 and CS 330) are analyzed by potentiometric titration using an automatic titrator (716 DMS Titrino, Metrohm USA) and an ion selective electrode (Part No. XT12-0001, Analytical Sensors & Instrument, Ltd). The titrant is 0.001 mol/L 1,3-didecyl-2-methyl imidazolinium chloride (TEGO ® trant A100) supplied by Metrohm USA. The pH values of the supernatant after centrifugation are determined by a pH meter (Corning 320).

The concentrations of cationics DTAB and CPC are also analyzed by potentiometric titration with the same titrator (716 DMS Titrino, Metrohm USA) and electrode (Part No. XT12-0001, Analytical Sensors & Instrument, Ltd) described previously for the anionic surfactants. The titrant is 0.001 mol/L SDS in deionized water.

The concentration of C25A is measured with colorimetric two-phase titration using 0.001 mol/L CS 330 as a titrator and methylene blue as an indicator.

The concentrations of 15-S-30, CAHS and LAB are analyzed with high performance liquid chromatography (HPLC). The HPLC system is equipped with a surfactant column (Dionex Acclaim Surfactant, 4.6 x250mm) and an evaporative light scattering detector (ELSD). Mobile phases contain HPLC grade acetonitrile as organic phase and deionized water as aqueous phase.

2.2 Static adsorption on natural dolomite

All static adsorption measurements in sections 2.2.1 to 2.2.4 are performed on dolomite (Carl Pool, old) without adjusting pH, i.e., under alkaline conditions.

2.2.1 Anionic Surfactants

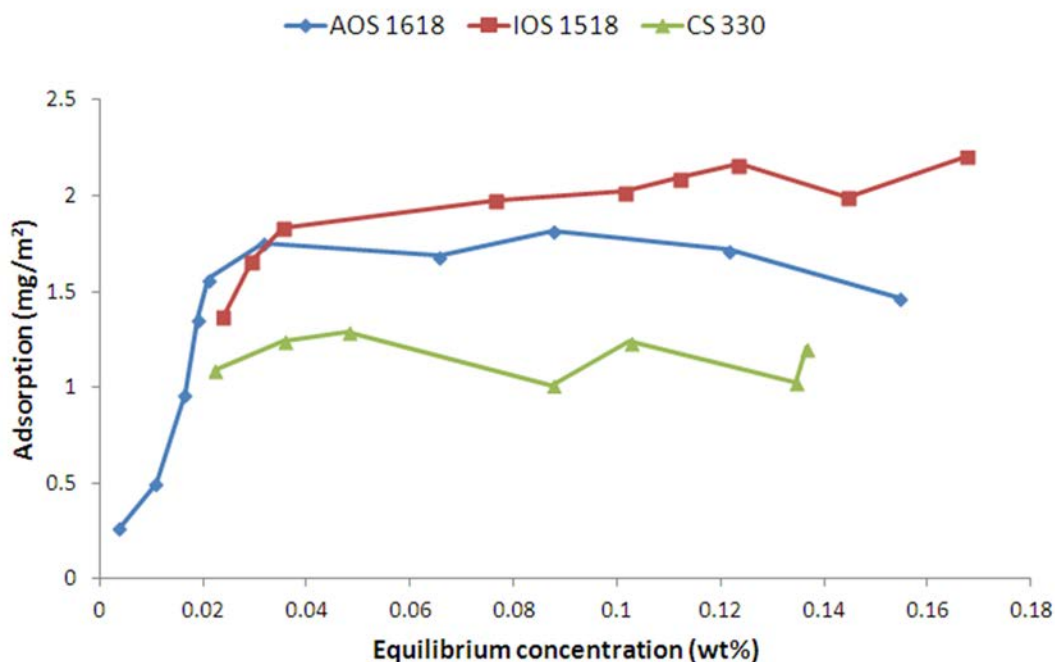


Figure 2-1. Static adsorption of anionics on dolomite powder (Carl Pool, old) in DI water at room temperature.

The comparison of adsorption of different anionic surfactants on dolomite powder (Carl Pool, old) in DI water is shown in Figure 2-1. Compared with AOS 1618, IOS 1518 shows a higher adsorption plateau (2.1 mg/m²). However, the ethoxylated sulfate CS 330 shows much lower adsorption, with a plateau of only 1.1 mg/m². With ethoxylated groups on the hydrophobe of the surfactant, CS 330

is more water soluble and has a reduced adsorption at the water/dolomite interface.

2.2.2 Cationic Surfactants

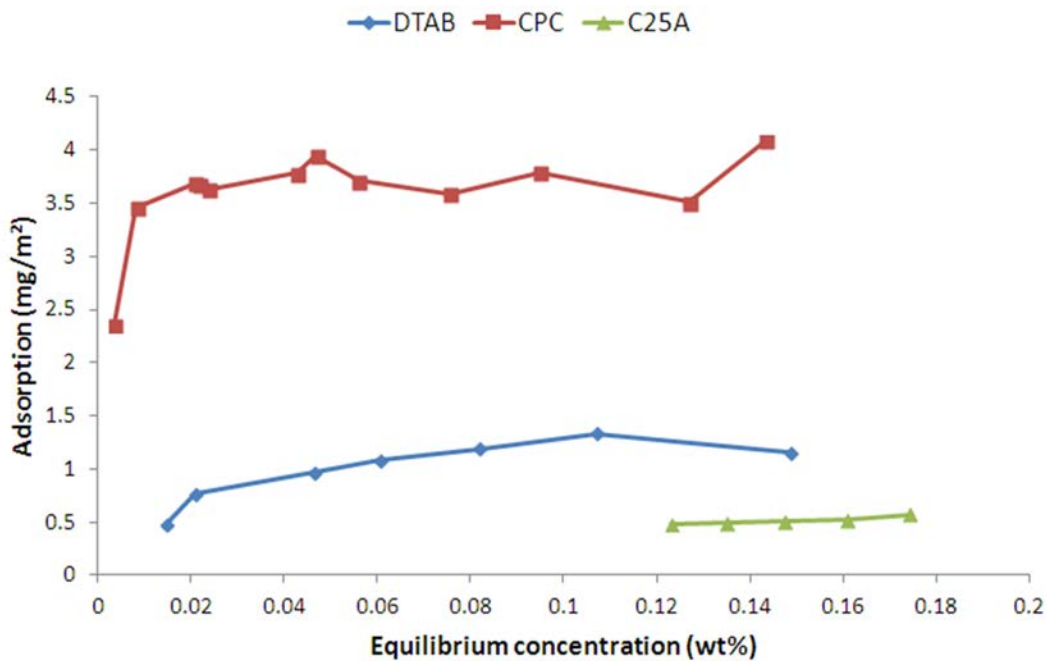


Figure 2-2. Static adsorption of cationics on dolomite powder (Carl Pool, old) in DI water at room temperature.

The adsorption of three cationic surfactants on dolomite (Carl Pool, old) in DI water at room temperature is shown in Figure 2-2. The adsorption plateau of CPC is as high as 3.2 mg/m^2 , which is not originally expected on the positive-charged dolomite surface. Later in this chapter I will show that this result is caused by impurities in this dolomite sample. The adsorption plateau of DTAB is 1.2 mg/m^2 , which is much lower than CPC. The ethoxylated amine C25A exhibits

a promising low adsorption with a plateau of only 0.54 mg/m². This observation indicates weak interaction of the 15-EO ethoxylated amine C25A with dolomite surface even in the presence of impurities, making this surfactant a good candidate for EOR applications with low cost due to adsorption. The weak interaction between C25A and dolomite is likely caused by the unprotonated state of this surfactant under alkaline conditions.

2.2.3. Nonionic Surfactants

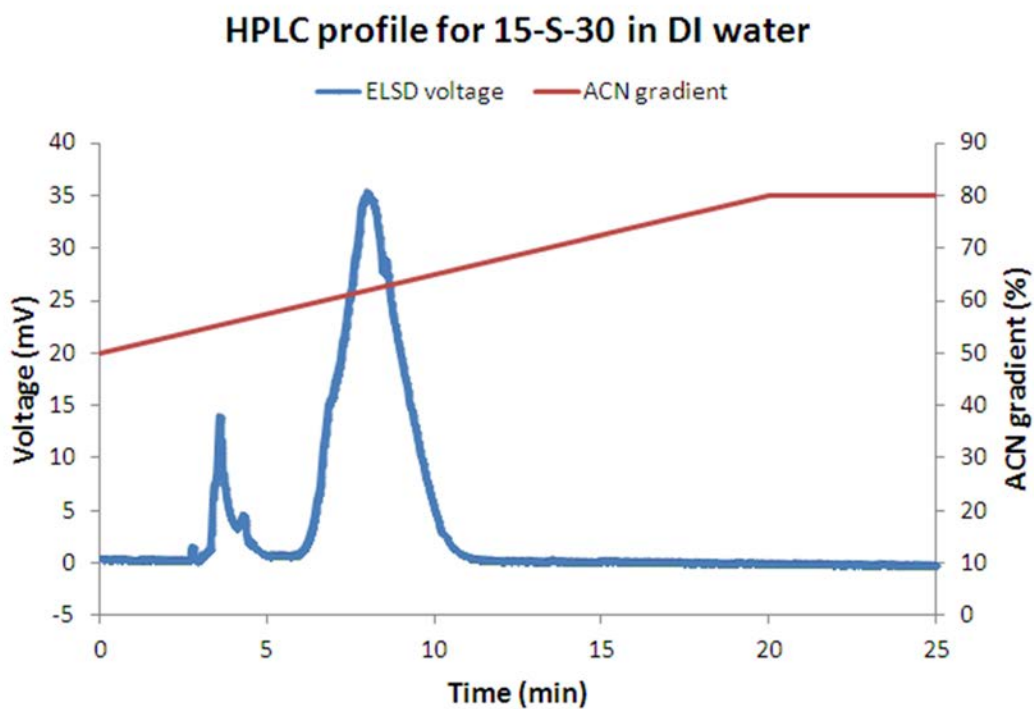


Figure 2-3. HPLC profile of Tergitol 15-S-30 (0.2 wt%) in DI water. Injection: 50 μ L; Column Temperature: 25 $^{\circ}$ C; Mobile Phase: 100mM Ammonium Acetate(pH5.5)/ACN; Flow rate: 1 ml/min; ELSD setting: 60 $^{\circ}$ C, 3.5 Bar.

We analyze the nonionic surfactant Tergitol 15-S-30 using HPLC. Several gradient elution approaches are tried and Figure 2-3 shows an optimized profile we obtain. The first peak at 3.6 min indicates the presence of salt in the surfactant sample, and the second large peak at 8.0 min is the surfactant peak. The surfactant concentration is calibrated using the surfactant peak in the range of 0 to 0.2 wt%.

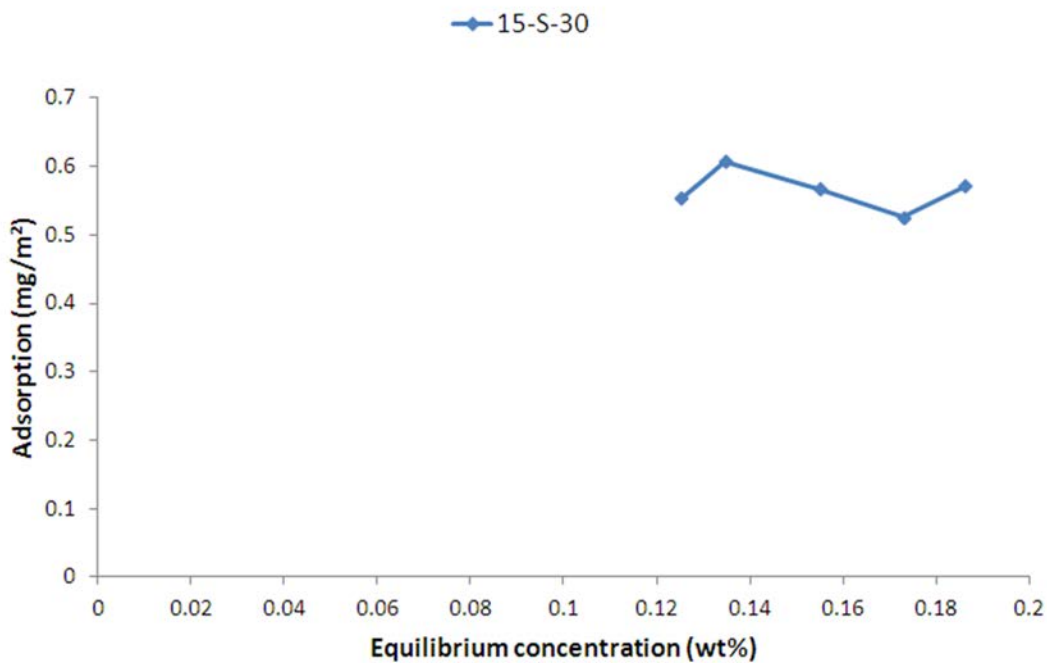
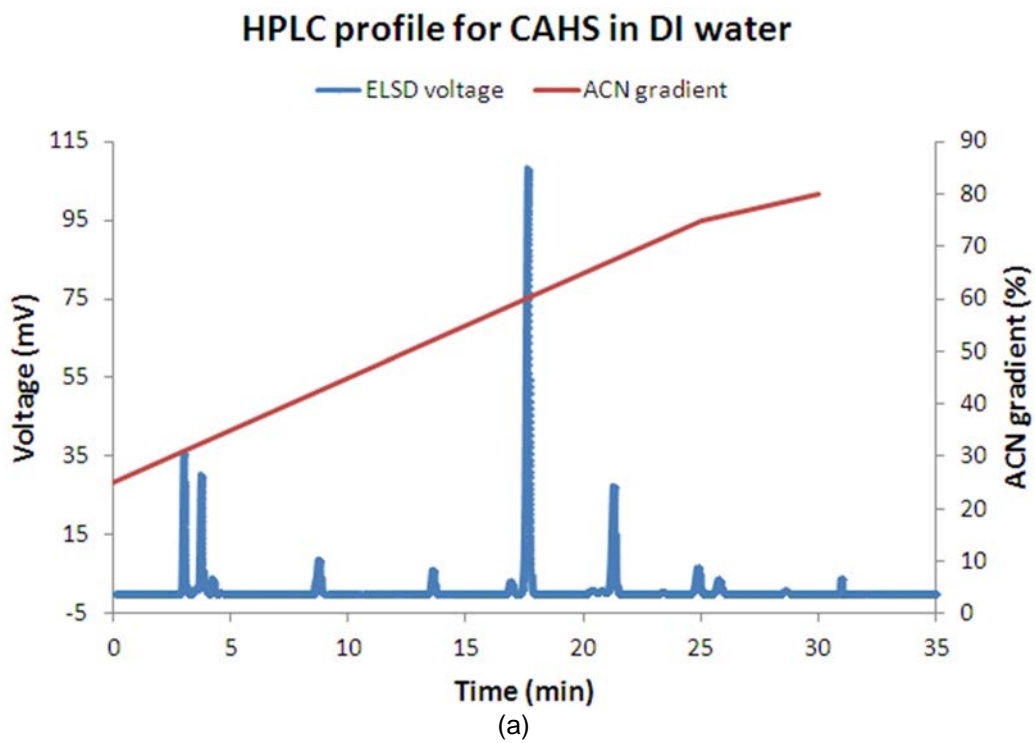


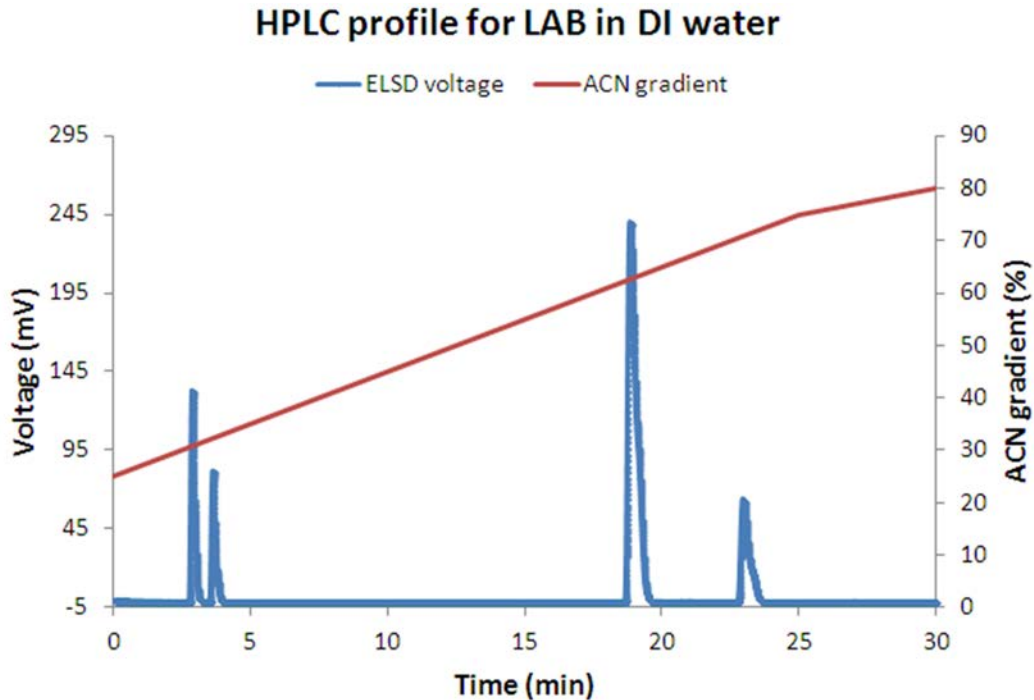
Figure 2-4. Static adsorption of Tergitol 15-S-30 on dolomite powder (Carl Pool, old) in DI water at room temperature.

The adsorption experiments are performed with a fixed initial concentration 0.2 wt%. Due to the low CMC, only the points from the adsorption plateau are obtained (Figure 2-4). The adsorption plateau is around 0.6 mg/m², similar to the adsorption value found for a cationic surfactant, C25A. The absence of charged

hydrophilic head in this nonionic surfactant causes weak electrostatic interaction between the surfactant and dolomite surface, leading to low adsorption.

2.2.4. Zwitterionic Surfactants



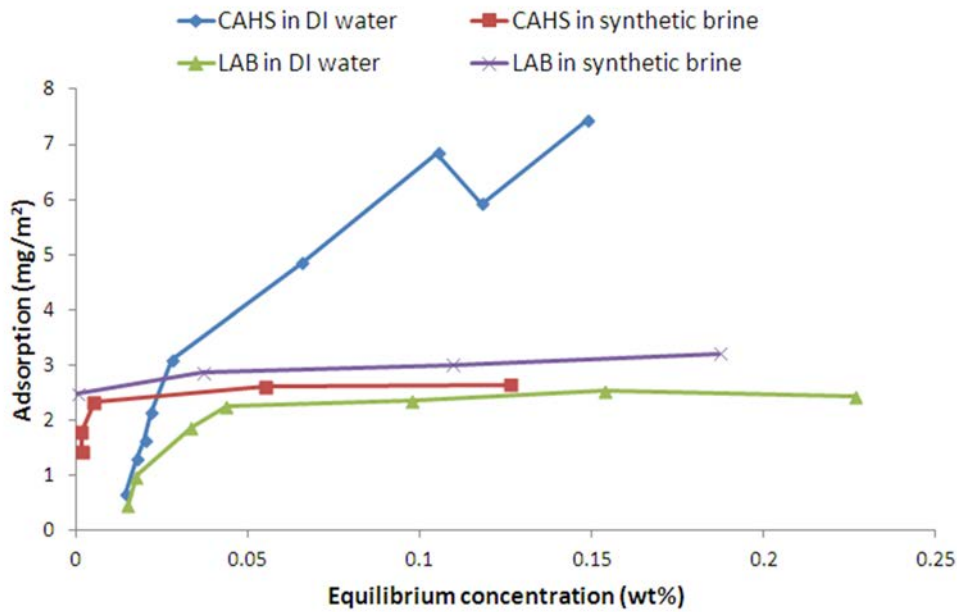


(b)

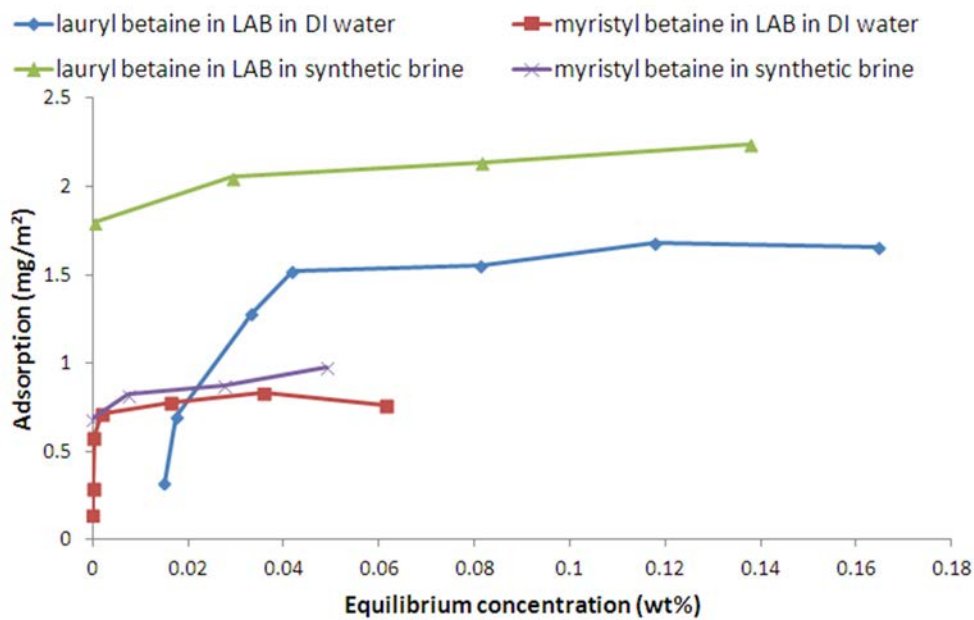
Figure 2-5. HPLC profiles of (a) CAHS (0.2 wt% cocamidopropyl hydroxysultaine) and (b) LAB (0.21 wt% lauryl betaine) in DI water with an ELSD detector.

The concentrations of the zwitterionic surfactant CAHS and LAB are also determined by the HPLC method. The HPLC results of CAHS and LAB are shown in Figure 2-5 (a) and (b), respectively. In Figure 2-5 (a), the highest peak at 17.6 min is the one for the main component cocamidopropyl hydroxysultaine in the analyzed CAHS sample. In Figure 2-5(b), two main components, lauryl betaine (the peak at 18.8 min) and myristyl betaine (the peak at 22.9 min), are identified in the analyzed LAB sample using the HPLC analysis. Due to shorter length of the hydrophobe, lauryl betaine has less retention time than myristyl betaine. We use these identified peaks to calibrate surfactant concentration for adsorption measurements.

Figure 2-6 (a) shows the adsorption results of CAHS and LAB on dolomite powder (Carl Pool, old) in both DI water and synthetic brine. One of the advantages of these two surfactants is that they are soluble in high salinity brine. As indicated in Section 2.1.1, the synthetic brine has a high salinity with approximately 22% TDS. The adsorption of CAHS in DI water is much higher than that in synthetic brine. The adsorbed surfactant is zwitterionic, which contains a head with two oppositely charged groups. At higher concentrations, lateral interactions between hydrocarbon chains and ion–dipole interaction between the charged groups at the surface and the zwitterionic head are important in the adsorption process (Zajac, Chorro et al. 1997; Zhang and Somasundaran 2006). It is probable that additional electrolyte strength weakens the ion–dipole interaction in the adsorption process of CAHS on dolomite, leading to reduced adsorption. However, the adsorption behavior of LAB is not similar to that of CAHS. The adsorption plateau of LAB in DI water is 2.4 mg/m^2 , which is much lower than that of CAHS under the same condition. As shown in Figure 2-6(a), the existence of additional electrolyte strength in synthetic brine increases the adsorption of total betaines to an adsorption plateau of around 3.1 mg/m^2 . The reason why high salinity increases the adsorption of LAB is not clear yet. Figure 2-6(a) also shows that high salinity significantly reduces the critical micelle concentration (CMC) of both CAHS and LAB.



(a)



(b)

Figure 2-6. Static adsorption of zwitterionics on dolomite powder (Carl Pool, old) in DI water and synthetic brine at room temperature. (a) Comparison of adsorption between CAHS and LAB; (b) Comparison of adsorption between different components in LAB.

Lauryl betaine and myristyl betaine in LAB are analyzed separately. Figure 2-6 (b) compares the adsorption of these components in both DI water and synthetic brine. Note that the results shown in Figure 2-6(b) should be distinguished from the experiments in which only lauryl betaine or only myristyl betaine is existent in the system. The synergistic effect between these two components may cause the apparent low CMC for myristyl betaine in DI water shown in Figure 2-6(b). High salinity causes a substantial increase in the adsorption of lauryl betaine and a slight increase in the adsorption of myristyl betaine.

2.2.5. Comparison in a bar chart

We compare all the plateau values of surfactant adsorption on dolomite (Carl Pool, old) in DI water in Figure 2-7. In Figure 2-7, the surfactants are listed in the order of anionics (AOS 1618, IOS 1518 and CS 330), cationics (DTAB, CPC and C25A), nonionics (15-S-30), and zwitterionics (CAHS and LAB). Among these different types of surfactants, the ethoxylated amine C25A and the nonionic surfactant 15-S-30 exhibit promising low adsorption on dolomite powder. These surfactants can be potentially considered for EOR applications. However, for high temperature, high salinity reservoirs, one should be concerned about the relatively low cloud points of nonionic surfactants, above which surfactants precipitate out of aqueous solution. However, some ethoxylated amines may show high cloud points in high salinity brine. For example, it was reported that

C25A (ethoxylated 15 EO cocoamine) exhibited a cloud point of 118 °C in 182 g/L NaCl solution after protonation (pH=4) (Chen, Elhag et al. 2012). The ethoxylated amines are switchable nonionic-cationic surfactants, which may be further screened and optimized for CO₂ foam application with potential low adsorption on carbonates.

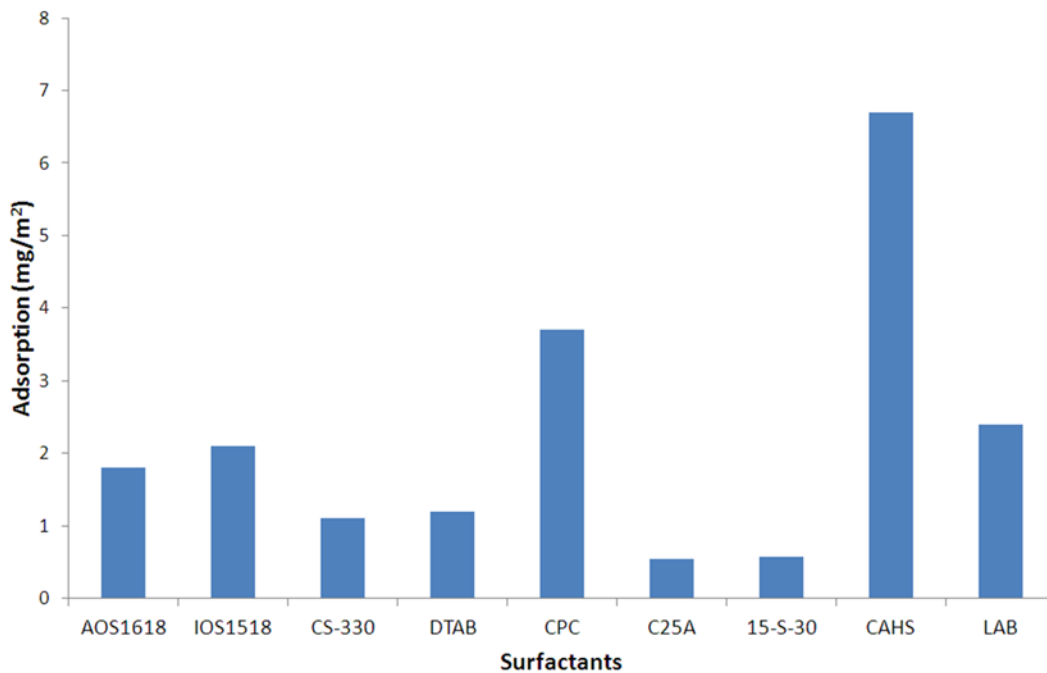


Figure 2-7. Comparison of surfactant adsorption on dolomite (Carl Pool, old) in DI water at room temperature.

2.3 Effect of non-carbonate impurities on adsorption results

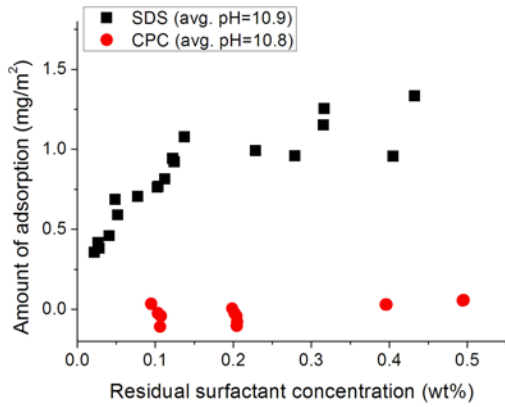
High adsorption of cationic surfactants (such as CPC) on dolomite is surprising and contrary to the observations of low adsorption of CPC on

carbonates in the literature (Tabatabai, Gonzalez et al. 1993). In this part we explore the reason behind this observation. As mentioned previously, different batches of dolomite materials exhibit different adsorption behavior. Because the dolomite (Carl Pool, old) was irreplaceable after finishing the experiments in Section 2.2, a new batch of dolomite supplied by Vital Earth / Carl Pool was utilized (Carl Pool, new).

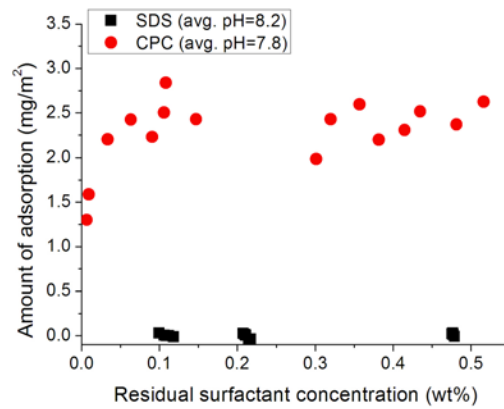
2.3.1. Results of ζ potential and static adsorption on various substrates

Figure 2-8 shows a comparison of static adsorption between CPC and SDS on synthetic calcite powder, silica flour and kaolin powder. The average pH indicated in Figure 2-8 is not adjusted with either acid or alkali, which reflects the natural interactions between surfactant solution and mineral surface. The adsorption of CPC on synthetic calcite is negligible compared with that of SDS as indicated in Figure 2-8(a), which is consistent with the literature (Tabatabai, Gonzalez et al. 1993). Some of the data points show negative adsorption of CPC on calcite surface in Figure 2-8(a). This means that the concentration of CPC in the vicinity of calcite surface is lower than that in the bulk, which is presumably caused by the strong electrostatic repulsion between the cationic CPC and the positively-charged calcium ions on calcite. The ζ -potential of calcite is close to zero (4.2 ± 7.2 mV) at a pH of 9.8 (Table 2-1), which is consistent with the finding in the literature for synthetic calcite suspended in 0.01 mol/L NaCl solution with an isoelectric pH of 9.6 (Pierre, Lamarche et al. 1990). Since the surface of calcite is not strongly charged near a pH around 10, it is likely that the

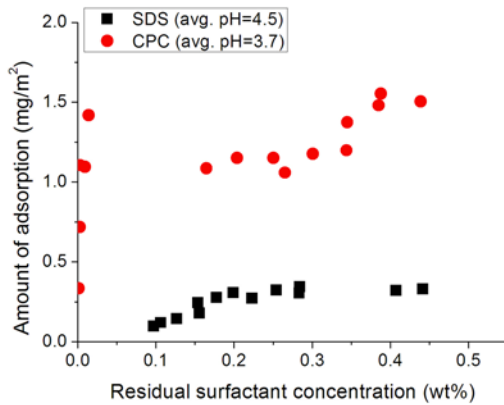
electrostatic attraction between CPC and negatively-charged carbonate ions at the calcite surface is weak compared with the repulsion between CPC and calcium ions.



(a) calcite (Alfa Aesar)



(b) silica (Min-U-Sil 10)



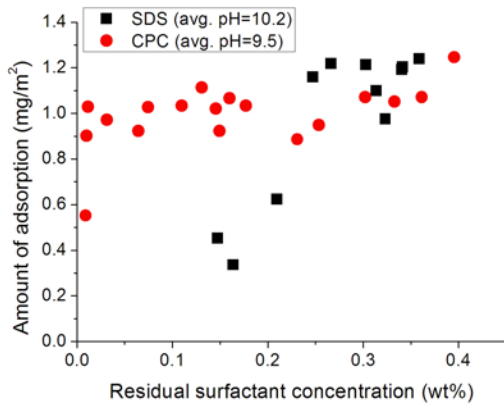
(c) kaolin (Sigma Aldrich)

Figure 2-8. Comparison of static adsorption of SDS and CPC on synthetic calcite, silica and kaolin in DI water at room temperature. The pH is not adjusted with either acid or alkaline.

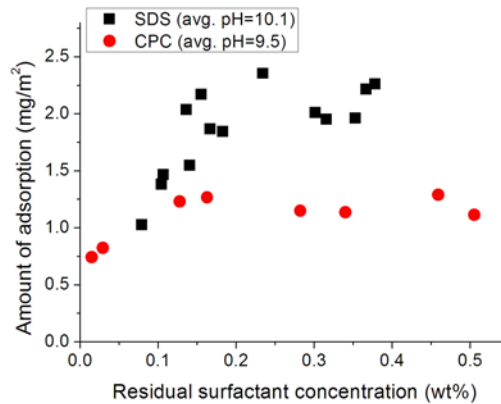
Table 2-1 shows a negative zeta potential (-47.3 ± 2.5 mV) when silica flour is suspended in 0.01 mol/L NaCl solution. At a pH of 8, the silica surface is strongly negatively charged. High adsorption of positively-charged CPC and negligible

adsorption of negatively-charged SDS on silica flour are observed in Figure 2-8(b). The behavior is completely opposite to the case with synthetic calcite in Figure 2-8(a). Therefore, if natural carbonates contain a substantial amount of silica, significant adsorption of CPC may occur.

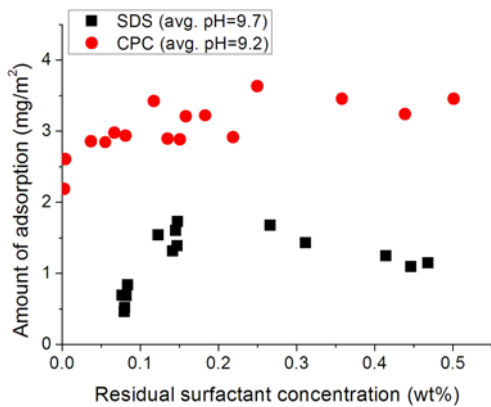
We use kaolin as a typical clay material to compare the adsorption of CPC and SDS. An acidic condition ($\text{pH} = 4.8$) is observed when kaolin is suspended in 0.01 mol/L NaCl solution as shown in Table 2-1. The zeta potential of kaolin under this condition is -38.0 ± 7.6 mV, which indicates an overall negative surface charge. It was reported that an increase in pH led to a more negatively-charged kaolin surface (Yukselen and Kaya 2003; Jiang, Hirasaki et al. 2010). As shown in Figure 2-8(c), both the cationic CPC and the anionic SDS adsorb onto kaolin, because both positive and negative binding sites exist on this mineral surface depending on pH (Qun, Vasudevan et al. 1991; Zhou and Gunter 1992; Jiang, Hirasaki et al. 2010). An increase in pH alters the charge on the edges of kaolin, which can further reduce the adsorption of SDS (Qun, Vasudevan et al. 1991). The basal planes of kaolin are unconditionally negatively charged, which causes a substantial adsorption of CPC as shown in Figure 2-8(c). If kaolin is found to be an impurity in natural carbonate sample, the negative binding sites in kaolin may cause significant adsorption of CPC especially in alkaline conditions.



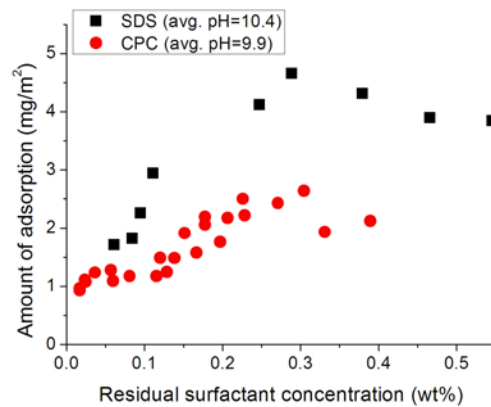
(a) dolomite (Carl Pool)



(b) dolomite (ScienceLab.com)



(c) limestone (Franklin)



(d) limestone (Carthage)

Figure 2-9. Comparison of static adsorption of SDS and CPC on various natural carbonates in DI water at room temperature. The pH is not adjusted with either acid or alkaline.

As shown in Table 2-1, these carbonate materials are collected from different places in the US and used without further purification. It has been noted that a very small amount of impurities in natural carbonates can possibly provide significant variations in zeta potential measurements (Moulin and Roques 2003). In Table 2-1 we observe that the zeta potential of various natural carbonate samples suspended in 0.01 mol/L NaCl solution ranges from 8.0 to 29.6 mV,

while the pH is somehow close to each other. Therefore, the effect of impurities on surfactant adsorption should not be ignored.

Figure 2-9 shows the comparison of adsorption of SDS and CPC on four natural carbonates in terms of mass adsorbed per unit surface area. In Figure 2-9(a), SDS and CPC show almost the same adsorption plateaus slightly above 1 mg/m² on dolomite (Carl Pool). However, the adsorption of SDS is substantially higher than that of CPC on dolomite (ScienceLab.com) (Figure 2-9(b)) and limestone (Carthage) (Figure 2-9(d)), and much low than that of CPC on limestone (Franklin) (Figure 2-9(c)). The absolute amount of adsorption in term of mass per unit surface area also varies a lot with different minerals. Compare with the base case on synthetic calcite in Figure 2-8(a), the most probable key factor which plays an important role in SDS/CPC adsorption is the amount and distribution of impurities in natural carbonate materials.

2.3.2. Surface characterization by XPS and XRD

We characterize the atomic surface composition of various minerals using X-ray photoelectron spectroscopy (XPS). Figure 2-10 shows the comparison of the XPS results for the elements calcium (Ca), magnesium (Mg), aluminum (Al) and silicon (Si). The elements carbon (C) and oxygen (O) are also observed in all carbonate samples, however, they are not shown in Figure 3 since they have no apparent contribution to the cationic CPC adsorption on calcite (Figure 2-8(a)) and the anionic SDS mainly interacts with Ca and Mg other than C and O.

Ca is observed in all carbonate minerals (samples 1-5) but not in kaolin (sample 6) or silica (sample 7). Significant amount of Mg is observed in dolomite (samples 1-2) but not in calcite (sample 5). Small amount of Mg exists in limestone (samples 3-4). These observations are all consistent with the typical chemical compositions of these minerals.

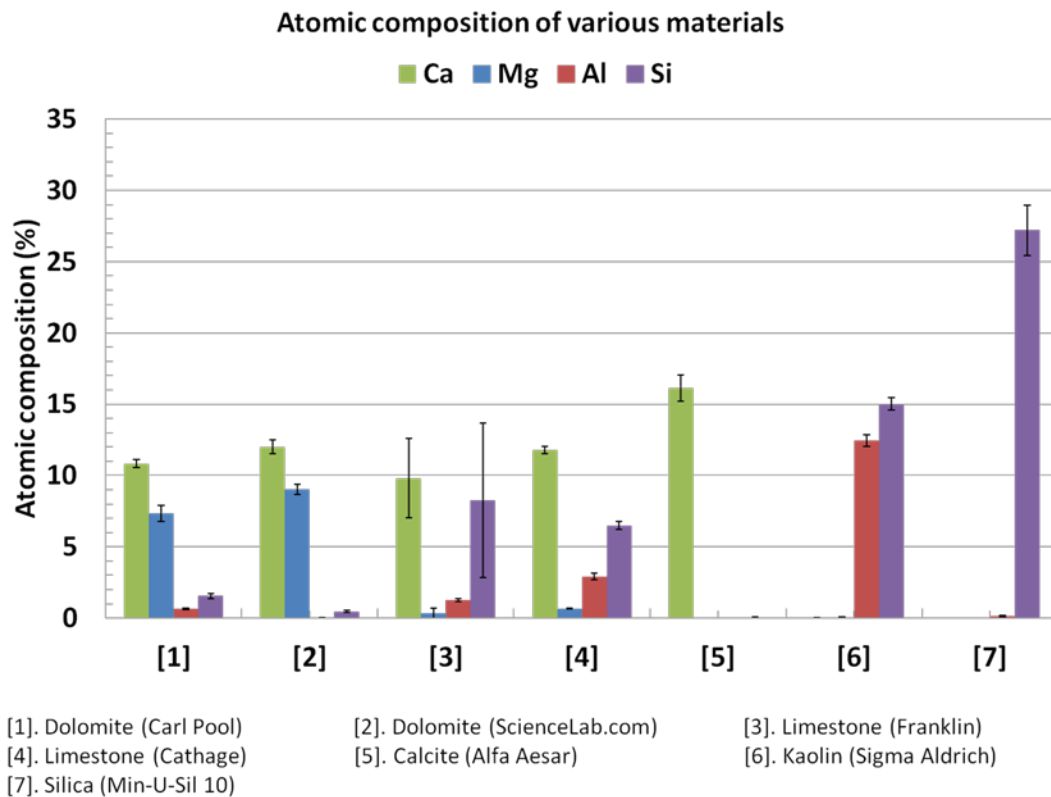


Figure 2-10. Comparison of atomic composition of various materials measured by X-ray photoelectron spectroscopy (XPS).

What is of interest is the amount of Si and Al in natural carbonates. As shown in Figure 2-10, Si is found in all four natural carbonates (samples 1-4), while Al is found in all carbonate samples except the dolomite from ScienceLab.com. Neither Si nor Al is found in the synthetic calcite powder (sample 5). These findings may explain why there is such a large difference in

SDS/CPC adsorption on different carbonates. The existence of Si and Al on natural carbonates can provide strong negative binding sites to adsorb cationic surfactants such as CPC, mainly through electrostatic interactions.

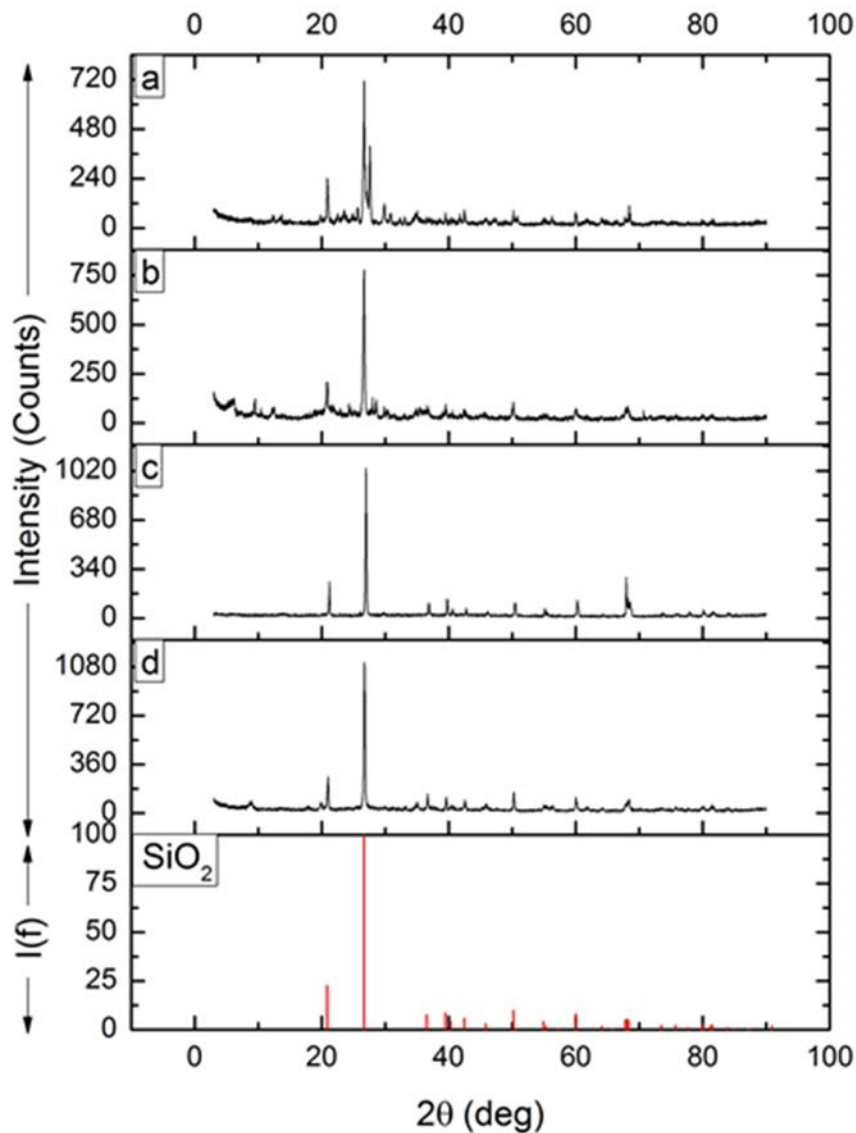


Figure 2-11. Analysis of HCl-insoluble impurities with X-ray Diffraction (XRD) from top to bottom: (a) dolomite (Carl Pool); (b) dolomite (ScienceLab.com); (c) limestone (Franklin); (d) limestone (Carthage). The bottom of the stackplot shows the reference pattern of SiO_2 normalized by the highest peak.

We use XRD to investigate what minerals exist in the HCl-insoluble impurities of natural carbonates which contribute to the significant differences in adsorption behavior of ionic surfactants. The results shown in Figure 2-11 indicate that the majority of the HCl-insoluble impurities in all four natural carbonate samples is silica (SiO_2). As aluminum is also found in natural carbonate samples using XPS, it may exist as the minority component in the HCl-insoluble impurities in various forms. For example, qualitative minor component analysis in Figure 2-11(d) indicates the existence of muscovite or fuchsite in this sample (Carthage limestone) according to the ICDD database.

We collect the adsorption plateaus of SDS and CPC from Figures 2-8 and 2-9 for five carbonate samples. Figure 2-12(a) shows the change in adsorption plateaus of SDS and CPC with the atomic ratio of $(\text{Si}+\text{Al})/(\text{Ca}+\text{Mg})$ of the carbonate minerals. The trend indicates that the adsorption plateau of CPC increases with the atomic ratio of $(\text{Si}+\text{Al})/(\text{Ca}+\text{Mg})$, while the adsorption plateau of SDS appears not to be a monotonic function of the atomic ratio of $(\text{Si}+\text{Al})/(\text{Ca}+\text{Mg})$. This observation clearly indicates that low adsorption of CPC occurs on natural carbonates with low Si and Al content.

Figure 2-12(b) compares the adsorption plateaus of CPC and SDS in Figure 2-12(a) by plotting the plateau ratio CPC/SDS with the atomic ratio of $(\text{Si}+\text{Al})/(\text{Ca}+\text{Mg})$. Based on the five data points shown in Figure 2-12(b), it is observed that the adsorption plateau ratio of CPC/SDS increases with the atomic ratio of $(\text{Si}+\text{Al})/(\text{Ca}+\text{Mg})$ of the minerals at low Si and Al regions (less than 20%). Thus, the cationic CPC can be advantageous over the anionic SDS in terms of

low adsorption if the carbonate minerals have low Si and Al. The adsorption plateau ratio of CPC/SDS varies a lot when the atomic ratio of (Si+Al)/(Ca+Mg) becomes high (more than 70%). In addition to the adsorption on kaolin shown in Figure 2-8(c), the interactions of SDS with other types of clay minerals with positively-charged binding sites which possibly exist in natural carbonates need to be explored.

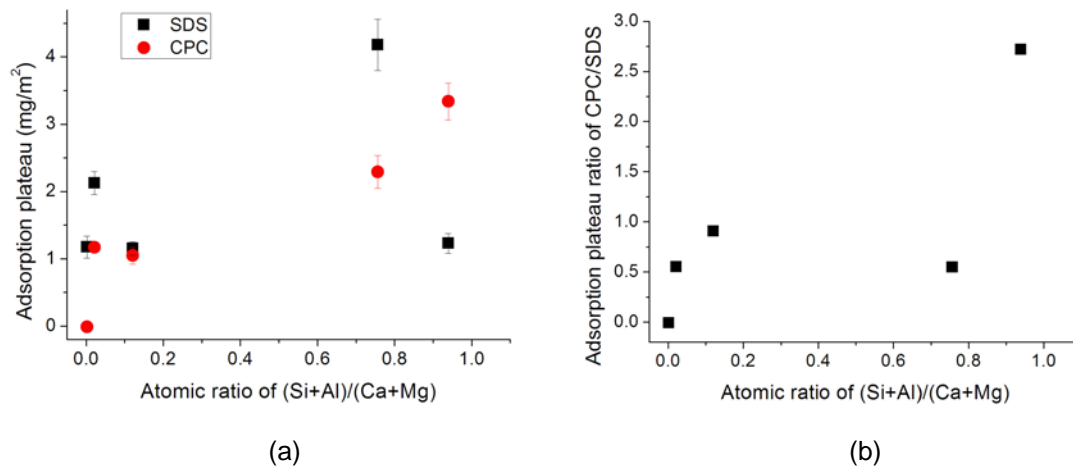


Figure 2-12. Correlation between surfactant adsorption plateau and XPS results of carbonate minerals. (a) Comparison of SDS and CPC adsorption plateaus on carbonate minerals in terms of the atomic ratio of (Si+Al)/(Ca+Mg); (b) Adsorption plateau ratios of CPC/SDS on carbonate minerals in terms of the atomic ratio of (Si+Al)/(Ca+Mg). The pH is not adjusted with either acid or alkaline as shown in Figure 2-8(a) and Figure 2-9.

2.4 Conclusions

Comparisons between anionic, cationic, nonionic and zwitterionic surfactant adsorption on natural dolomite shows that the nonionic surfactant Tergitol 15-S-30 and the ethoxylated cationic surfactant Ethomeen C/25A exhibit the lowest

adsorption in alkaline conditions. Low electrostatic interaction between the surfactant and the dolomite surface is the main reason for the low adsorption behavior.

The unexpected high adsorption of some cationic surfactants on natural dolomite is explored. Four natural carbonates, including two limestone samples and two dolomite samples, are used to evaluate the adsorption behavior of the anionic surfactant SDS and the cationic surfactant CPC. The XPS analysis reveals that a substantial amount of silicon and aluminum exists in natural dolomite and limestone but not in synthetic calcite. It is found that the adsorption plateau of CPC on carbonates highly depends on the silicon and aluminum composition in the carbonate samples due to the strong electrostatic interaction between CPC and negative binding sites in silica and/or clay. Our result indicates that low adsorption of CPC on carbonates is only valid when the silicon and aluminum content is low. Cationics do not have the advantage of low adsorption compared with anionics on some of the carbonate samples in which the silicon and aluminum content is relatively high.

2.5 References

- Chen, Y., A. S. Elhag, et al. (2012). Ethoxylated Cationic Surfactants For CO₂ EOR In High Temperature, High Salinity Reservoirs. SPE Improved Oil Recovery Symposium. Tulsa, Oklahoma, USA, Society of Petroleum Engineers.
- Jiang, T. M., G. J. Hirasaki, et al. (2010). "Characterization of Kaolinite zeta Potential for Interpretation of Wettability Alteration in Diluted Bitumen Emulsion Separation." Energy & Fuels **24**: 2350-2360.
- Moulin, P. and H. Roques (2003). "Zeta potential measurement of calcium carbonate." Journal of Colloid and Interface Science **261**(1): 115-126.

- Pierre, A., J. M. Lamarche, et al. (1990). "Calcium as Potential Determining Ion in Aqueous Calcite Suspensions." Journal of Dispersion Science and Technology **11**(6): 611-635.
- Qun, X., T. V. Vasudevan, et al. (1991). "Adsorption of Anionic Nonionic and Cationic Nonionic Surfactant Mixtures on Kaolinite." Journal of Colloid and Interface Science **142**(2): 528-534.
- Tabatabai, A., M. V. Gonzalez, et al. (1993). "Reducing Surfactant Adsorption in Carbonate Reservoirs." Spe Reservoir Engineering **8**(2): 117-122.
- Yukselen, Y. and A. Kaya (2003). "Zeta potential of kaolinite in the presence of alkali, alkaline earth and hydrolyzable metal ions." Water Air and Soil Pollution **145**(1): 155-168.
- Zajac, J., C. Chorro, et al. (1997). "Thermodynamics of micellization and adsorption of zwitterionic surfactants in aqueous media." Langmuir **13**(6): 1486-1495.
- Zhang, R. and P. Somasundaran (2006). "Advances in adsorption of surfactants and their mixtures at solid/solution interfaces." Advances in Colloid and Interface Science **123**: 213-229.
- Zhou, Z. H. and W. D. Gunter (1992). "The Nature of the Surface-Charge of Kaolinite." Clays and Clay Minerals **40**(3): 365-368.

Simulation of foam flow and chromatographic retardation of surfactants

The previous chapter describes the importance in the consideration of surfactant adsorption. The experimental results of static adsorption can be utilized in simulation of equilibrium transport of surfactants. This chapter presents the algorithm for modeling surfactant and foam transport in 1-D homogeneous porous media. Chromatographic retardation of surfactants due to adsorption onto the formation and phase partition is simulated using a foam simulator.

3.1 1-D foam simulator and the foam model

3.1.1 Algorithm for different foam injection strategies

This simulator utilized uses a finite difference method IMPES (implicit in pressure, explicit in saturation) for pressure and phase saturation calculation, and forward difference, one-point upstream weighting method for surfactant concentration calculation. It can solve one-dimensional incompressible isothermal two-phase flow problems.

Saturation and pressure profile for each phase, concentration profile for surfactant and non-adsorbing tracer, effluent and pressure drop history can be

determined by the simulator. According to the pressure drop history, foam apparent viscosity can be obtained.

Either two-phase co-injection or Surfactant-Alternating-Gas (SAG) injection can be simulated in this simulator. For co-injection process, we have the boundary condition of f_g^{BC} (v/v) gas injection and $(1 - f_g^{BC})$ (v/v) surfactant solution injection at $x=0$, and the differential equations, initial conditions and boundary conditions are described below. For SAG process, we have alternate boundary conditions of $f_g^{BC} = 1$ and $f_g^{BC} = 0$ at a certain frequency.

Momentum balance (Darcy's law):

$$u_w = -\frac{kk_{rw}(S)}{\mu_w} \frac{\partial p_w}{\partial x} \quad (3.1)$$

$$u_g = -\frac{kk_{rg}(S)}{\mu_g} \frac{\partial p_g}{\partial x} \quad (3.2)$$

Mass balance:

$$\phi \frac{\partial S_w}{\partial t} + \frac{\partial u_w}{\partial x} = 0 \quad (3.3)$$

$$\phi \frac{\partial S_g}{\partial t} + \frac{\partial u_g}{\partial x} = 0 \quad (3.4)$$

$$S_w + S_g = 1.0$$

Capillary pressure between phases:

$$p_g - p_w = P_c(S)$$

Initial saturation:

$$S_g(x,0) = S_{g,IC}$$

Boundary condition:

$$x = 0: u_w = (1 - f_g^{BC}) \cdot u^{BC}, u_g = f_g^{BC} \cdot u^{BC}$$

$$x = L: P_c = 0, p_g = p_g^{BC} \text{ after gas breakthrough}$$

We use the following dimensionless variables: $t_D = \frac{u^{BC} t}{\phi L}$, $x_D = \frac{x}{L}$,

$$k_{rwD} = \frac{k_{rw}(S_w)}{k_{rw}^0}, k_{rgD} = \frac{k_{rg}(S_g, C_{wD})}{k_{rg}^0}, M = \frac{k_{rg}^0 \mu_w}{k_{rw}^0 \mu_g}, u_{wD} = \frac{u_w}{u^{BC}}, u_{gD} = \frac{u_g}{u^{BC}}. \text{ Note that}$$

u^{BC} is the total superficial velocity for both phases, so the dimensionless velocity

for each phase is the same as its corresponding fractional flow: $u_{wD} = \frac{u_w}{u^{BC}} = f_w$,

$u_{gD} = \frac{u_g}{u^{BC}} = f_g$ and we will use f_w and f_g instead of u_{wD} and u_{gD} henceforth.

By specifying a characteristic pressure $p^* = \frac{u^{BC} \mu_g L}{k k_{rg}^0}$ we have dimensionless

pressure: $\Phi_D = p_{gD} = \frac{p_g - p_g^{BC}}{p^*}$, $p_{wD} = \frac{p_w - p_g^{BC}}{p^*}$. Meanwhile, the dimensionless

capillary pressure is $P_{cD}(S) = \frac{\sigma / \sqrt{k/\phi}}{p^*} J(S) = N_{P_c} J(S) = \Phi_D - p_{wD}$.

Then we develop Eqns (3.5) and (3.6):

$$f_w = \frac{u_w}{u^{BC}} = -\frac{kk_{rw}(S)}{\mu_w u^{BC}} \frac{\partial p_w}{\partial x} = -\frac{kk_{rw}(S)}{\mu_w u^{BC} L} \cdot \frac{u^{BC} \mu_g L}{kk_{rg}^0} \cdot \frac{\partial p_{wD}}{\partial x_D} = -\frac{k_{rwD}(S)}{M} \cdot \frac{\partial(\Phi_D - P_{cD}(S))}{\partial x_D} \quad (3.5)$$

$$f_g = \frac{u_g}{u^{BC}} = -\frac{kk_{rg}(S)}{\mu_g u^{BC}} \frac{\partial p_g}{\partial x} = -\frac{kk_{rg}(S)}{\mu_g u^{BC} L} \cdot \frac{u^{BC} \mu_g L}{kk_{rg}^0} \cdot \frac{\partial \Phi_D}{\partial x_D} = -k_{rgD}(S) \cdot \frac{\partial \Phi_D}{\partial x_D} \quad (3.6)$$

Now, substitute all dimensionless terms into Eqns (3.1) to (3.4), reformulate the equations and use the IMPES finite difference formulation, we will get the algebraic equations as below:

$$\begin{aligned} & \lambda_{i+1/2}^n (\Phi_{D_{i+1}}^{n+1} - \Phi_{D_i}^{n+1}) - \lambda_{i-1/2}^n (\Phi_{D_i}^{n+1} - \Phi_{D_{i-1}}^{n+1}) \\ &= \frac{1}{M} [k_{rwD,i+1/2}^n (P_{cD,i+1}^n - P_{cD,i}^n) - k_{rwD,i-1/2}^n (P_{cD,i}^n - P_{cD,i-1}^n)] \end{aligned} \quad (3.7)$$

$$S_{g_i}^{n+1} - S_{g_i}^n = \frac{\Delta t_D}{(\Delta x_D)^2} [k_{rgD,i+1/2}^n (\Phi_{D_{i+1}}^{n+1} - \Phi_{D_i}^{n+1}) - k_{rgD,i-1/2}^n (\Phi_{D_i}^{n+1} - \Phi_{D_{i-1}}^{n+1})] \quad (3.8)$$

where $\lambda = k_{rgD} + \frac{k_{rwD}}{M}$

However, if $i=1$ we need $\Phi_{D_0}^{n+1}$ and $P_{cD,0}^n$. Inlet boundary conditions at $x_D = 0$ should be applied for f_g^{BC} gas injection and $(1 - f_g^{BC})$ for surfactant solution injection. According to Eqns (3.5) and (3.6), we have

$$f_w|_{x=0} = -\frac{k_{rwD}|_{S_w=1-f_g^{BC}}}{M} \cdot \frac{\partial(\Phi_D - P_{cD}(S))}{\partial x_D} = 1 - f_g^{BC} \quad (3.9)$$

$$f_g \Big|_{x=0} = -k_{rgD} \Big|_{S_w=1-f_g^{BC}} \cdot \frac{\partial \Phi_D}{\partial x_D} = f_g^{BC} \quad (3.10)$$

Relative permeability curves need be used to calculate $k_{rwD} \Big|_{S_w=1-f_g^{BC}}$ and $k_{rgD} \Big|_{S_w=1-f_g^{BC}}$ in Eqns (3.9) and (3.10). By writing Eqns (3.9) and (3.10) with finite difference approximation, we get

$$-\frac{k_{rwD,1/2}^n \cdot (\Phi_{D1}^{n+1} - P_{cD,1}^n) - (\Phi_{D0}^{n+1} - P_{cD,0}^n)}{M \Delta x_D} = 1 - f_g^{BC} \quad (3.11)$$

$$-k_{rgD,1/2}^n \cdot \frac{(\Phi_{D1}^{n+1} - \Phi_{D0}^{n+1})}{\Delta x_D} = f_g^{BC} \quad (3.12)$$

where $k_{rwD,1/2} = k_{rwD} \Big|_{S_w=1-f_g^{BC}}$ and $k_{rgD,1/2} = k_{rgD} \Big|_{S_w=1-f_g^{BC}}$.

By adding Eqns (3.11) and (3.12), one can have the equations as follows,

$$-\lambda_{1/2}^n \cdot (\Phi_{D1}^{n+1} - \Phi_{D0}^{n+1}) + \frac{k_{rwD,1/2}^n}{M} \cdot (P_{cD,1}^n - P_{cD,0}^n) = \Delta x_D \quad (3.13)$$

$$k_{rgD,1/2}^n \cdot (\Phi_{D1}^{n+1} - \Phi_{D0}^{n+1}) = (-\Delta x_D) \cdot f_g^{BC} \quad (3.14)$$

where $\lambda_{1/2}^n = k_{rgD,1/2}^n + \frac{k_{rwD,1/2}^n}{M}$

then substitute Eqns (3.13) and (3.14) into Eqns (3.7) and (3.8) to derive boundary conditions at $x_D = 0$.

At $x_D = 1$, the boundary conditions are $P_{cD}|_{x_D=1} = P_{cD,NX+1/2} = 0$ (before gas breakthrough) and $\Phi_D|_{x_D=1} = \Phi_{D,NX+1/2} = 0$. Then Eqn (3.7) can be solved by tridiagonal matrix inversion from $i=1$ to $i=NX$ (LU decomposition is used) to get the flow potential at the new time level. After that, the saturation can be calculated through Eqn (3.8) at the new time level.

3.1.2 The STARS foam model

We use the Corey model, one of most commonly used relative permeability models, in this simulator for both aqueous and gas phases. As discussed in Chapter 1, aqueous phase mobility is independent of whether the gas exists as foam, and the presence of foam can reduce gas-phase mobility. Due to this feature and combined with the fact that gas phase relative permeability and viscosity always come together, we only modify the gas phase relative permeability as a result of the presence of foam, and keep the same gas phase viscosity, which is the same principle as previous studies (Vassenden and Holt 2000; Computer Modeling Group 2007; Ashoori, van der Heijden et al. 2010; Zanganeh, Kam et al. 2011).

$$k_{rw} = k_{rw}^0 \times S_{wD}^{n_w} \quad (\text{water / surfactant solution relative permeability with or without foam}) \quad (3.15)$$

$$k_{rg}^{nf} = k_{rg}^0 \times (1 - S_{wD})^{n_s} \quad (\text{gas relative permeability without foam}) \quad (3.16)$$

where $S_{wD} = \frac{S_w - S_{wc}}{1 - S_{gr} - S_{wc}}$ (normalized water saturation)

We use dimensionless relative permeability $k_{rD} = k_r / k_r^0$ in the IMPES formulation for finite difference method:

$$k_{rwD} = k_{rw} / k_{rw}^0 = \left(\frac{S_w - S_{wc}}{1 - S_{gr} - S_{wc}} \right)^{n_w} \quad (3.17)$$

$$k_{rgD}^{nf} = k_{rg}^{nf} / k_{rg}^0 = \left(\frac{1 - S_{gr} - S_w}{1 - S_{gr} - S_{wc}} \right)^{n_g} \quad (3.18)$$

The STARSTM foam model is employed in this work. This foam model assumes local steady state, which means that foam creation and decay mechanisms occur relatively fast compared with flow through porous media (Renkema and Rossen 2007). Based on the reported literature, the STARSTM foam model is shown in Eqns (3.19) and (3.20) (Ashoori, van der Heijden et al. 2010; Zanganeh, Kam et al. 2011):

$$k_{rg}^f = k_{rg}^{nf} \times FM \quad (3.19)$$

$$FM = \frac{1}{1 + fmmob \times F_1 \times F_2 \times F_3 \times F_4 \times F_5 \times F_6} \quad (3.20)$$

Eqns (3.19) and (3.20) indicate that this foam model uses a mobility reduction factor called FM to change the relative permeability of the gas phase in the presence of foam. The mobility reduction factor FM includes 6 functions (F_1 to F_6 , subscripts corresponding to different functions may vary in different

versions) to describe different factors on gas mobility reduction. In this work we mainly focus on estimating the parameters in the functions F_1 (surfactant-concentration-dependent function) and F_2 (water-saturation-dependent function) shown in Eqns (3.21) and (3.22).

$$F_1 = \begin{cases} \left(\frac{C_s}{fmsurf}\right)^{epsurf} & \text{for } C_s < fmsurf \\ 1 & \text{for } C_s \geq fmsurf \end{cases} \quad (3.21)$$

$$F_2 = 0.5 + \frac{\arctan[epdry(S_w - fmdry)]}{\pi} \quad (3.22)$$

The details of the functions, F_3 (oil-saturation-dependent function), F_4 (gas-velocity-dependent function), F_5 (critical-capillary-number-dependent function) and F_6 (salinity-dependent function) can be found elsewhere (Computer Modeling Group 2007) and are not discussed here.

3.2 Modeling surfactant transport in two-phase flow

Surfactants are not originally in porous media during CO₂ foam EOR process, and the transport of surfactants through porous media should be modeled such that foam mobility control can be described. We start deriving the equation for surfactant transport from material balance.

Based on mass balance over a representative elementary volume, species i (can be surfactant, water or gas) conservation equation is (Lake 1989):

$$\frac{\partial W_i}{\partial t} + \vec{\nabla} \cdot \vec{N}_i - R_i = 0 \quad (3.23)$$

where W_i is the overall concentration of i in units of mass of i per unit bulk

$$\text{volume, } W_i = \phi \sum_{j=1}^{N_p} \rho_j S_j \omega_{ij} + (1 - \phi) \rho_s \omega_{is};$$

$$\vec{N}_i \text{ is species } i \text{ flux, } \vec{N}_i = \sum_{j=1}^{N_p} (\rho_j \omega_{ij} \vec{u}_j - \phi \rho_j S_j K_{ij}^* \cdot \vec{\nabla} \omega_{ij});$$

We will make the following assumptions: immiscible ($\omega_{ij} = \delta_{ij}$), incompressible and isothermal ($\rho_j = \rho_j^0$), homogeneous (ϕ is constant), one dimensional, no reaction ($R_i = 0$).

In this case, we have 3 species (surfactant, gas and water) and 2 phases (gas and aqueous phases). Now let species i be surfactant and we will use the subscript “s” instead of “i”. The surfactant is considered to be present in both aqueous phase and CO₂-rich phase. We also need to consider the mass adsorbed on the mineral surface, i.e. ω_{ss} .

Then Eqn (3.23) becomes

$$\frac{\partial[\phi(\rho_w S_w \omega_{sw} + \rho_g S_g \omega_{sg})]}{\partial t} + \frac{\partial[(1 - \phi) \rho_s \omega_{ss}]}{\partial t} + \vec{\nabla} \cdot (\rho_w \omega_{sw} \vec{u}_w - \phi \rho_w S_w K_{sw}^* \cdot \vec{\nabla} \omega_{sw} + \rho_g \omega_{sg} \vec{u}_g - \phi \rho_g S_g K_{sg}^* \cdot \vec{\nabla} \omega_{sg}) = 0$$

Let $C_{sw} = \rho_w \omega_{sw}$, $C_{sg} = \rho_g \omega_{sg}$ and $C_{ss} = \rho_s \omega_{ss}$ be the mass concentration of the component “s” (surfactant) in aqueous phase, CO₂-rich phase and adsorbed on mineral surface, respectively. Then in one dimensional case we have:

$$\begin{aligned} & \phi \frac{\partial(C_{sw}S_w + C_{sg}S_g)}{\partial t} + (1-\phi) \frac{\partial C_{ss}}{\partial t} + \frac{\partial(C_{sw}u_w + C_{sg}u_g)}{\partial x} \\ & = \phi [K_{sw}^* \frac{\partial}{\partial x} (S_w \frac{\partial C_{sw}}{\partial x}) + K_{sg}^* \frac{\partial}{\partial x} (S_g \frac{\partial C_{sg}}{\partial x})] \end{aligned} \quad (3.24)$$

We define $f_w = \frac{u_w}{u^{BC}}$, $f_g = \frac{u_g}{u^{BC}}$, $t_D = \frac{u^{BC}t}{\phi L}$, $x_D = \frac{x}{L}$, $Pe_w = \frac{Lu^{BC}}{\phi K_{sw}^*}$, $Pe_g = \frac{Lu^{BC}}{\phi K_{sg}^*}$,

then Eqn (3.24) becomes:

$$\begin{aligned} & \frac{\partial(C_{sw}S_w + C_{sg}S_g)}{\partial t_D} + \frac{1-\phi}{\phi} \cdot \frac{\partial C_{ss}}{\partial t_D} + \frac{\partial(C_{sw}f_w + C_{sg}f_g)}{\partial x_D} \\ & = \frac{1}{Pe_w} \cdot \frac{\partial}{\partial x_D} (S_w \frac{\partial C_{sw}}{\partial x_D}) + \frac{1}{Pe_g} \frac{\partial}{\partial x_D} (S_g \frac{\partial C_{sg}}{\partial x_D}) \end{aligned}$$

or

$$\begin{aligned} & \frac{\partial(C_{sw}S_w + C_{sg}S_g + \frac{1-\phi}{\phi}C_{ss})}{\partial t_D} + \frac{\partial(C_{sw}f_w + C_{sg}f_g)}{\partial x_D} \\ & = \frac{1}{Pe_w} \cdot \frac{\partial}{\partial x_D} (S_w \frac{\partial C_{sw}}{\partial x_D}) + \frac{1}{Pe_g} \frac{\partial}{\partial x_D} (S_g \frac{\partial C_{sg}}{\partial x_D}) \end{aligned} \quad (3.25)$$

Now we define the partition coefficient of the surfactant between CO₂-rich phase and aqueous phase: $K_{sgw} = \frac{C_{sg}}{C_{sw}}$. Meanwhile, we know the Langmuir-type

correlation between C_{ss} and C_{sw} :

$$C_{ss} = \rho_s a_s \Gamma_{s,\max} \cdot \frac{\alpha C_{sw}}{1 + \alpha C_{sw}} \quad (3.26)$$

Therefore, both C_{ss} and C_{sg} can be correlated with C_{sw} . Eqn (3.26) is solved by forward difference, one-point upstream weighting method, and the algebraic equation for finite difference approximation is:

$$\begin{aligned} & \frac{(C_{sw,i}^{n+1} S_{w,i}^{n+1} + C_{sg,i}^{n+1} S_{g,i}^{n+1} + \frac{1-\phi}{\phi} C_{ss,i}^{n+1}) - (C_{sw,i}^n S_{w,i}^n + C_{sg,i}^n S_{g,i}^n + \frac{1-\phi}{\phi} C_{ss,i}^n)}{\Delta t_D} \\ & + \frac{(C_{sw,i+1/2}^n f_{w,i+1/2}^n + C_{sg,i+1/2}^n f_{g,i+1/2}^n) - (C_{sw,i-1/2}^n f_{w,i-1/2}^n + C_{sg,i-1/2}^n f_{g,i-1/2}^n)}{\Delta x_D} \\ & = \frac{1}{Pe_w} \cdot \frac{S_{w,i+1/2}^n (C_{sw,i+1}^n - C_{sw,i}^n) - S_{w,i-1/2}^n (C_{sw,i}^n - C_{sw,i-1}^n)}{(\Delta x_D)^2} \\ & + \frac{1}{Pe_g} \cdot \frac{S_{g,i+1/2}^n (C_{sg,i+1}^n - C_{sg,i}^n) - S_{g,i-1/2}^n (C_{sg,i}^n - C_{sg,i-1}^n)}{(\Delta x_D)^2} \end{aligned} \quad (3.27)$$

To solve Eqn (3.27), we should be aware that the variables with a superscript “n” are known, and Eqn (3.27) can be simplified as follows:

$$C_{sw,i}^{n+1} S_{w,i}^{n+1} + C_{sg,i}^{n+1} S_{g,i}^{n+1} + \frac{1-\phi}{\phi} C_{ss,i}^{n+1} = N_{temp} \quad (3.28)$$

where N_{temp} is a temporary variable and can be calculated through Eqn (3.29):

$$\begin{aligned}
N_{temp} &= (C_{sw,i}^n S_{w,i}^n + C_{sg,i}^n S_{g,i}^n + \frac{1-\phi}{\phi} C_{ss,i}^n) \\
&+ \Delta t_D \cdot \left[\frac{1}{Pe_w} \cdot \frac{S_{w,i+1/2}^n (C_{sw,i+1}^n - C_{sw,i}^n) - S_{w,i-1/2}^n (C_{sw,i}^n - C_{sw,i-1}^n)}{(\Delta x_D)^2} \right. \\
&+ \frac{1}{Pe_g} \cdot \frac{S_{g,i+1/2}^n (C_{sg,i+1}^n - C_{sg,i}^n) - S_{g,i-1/2}^n (C_{sg,i}^n - C_{sg,i-1}^n)}{(\Delta x_D)^2} \\
&\left. - \frac{(C_{sw,i+1/2}^n f_{w,i+1/2}^n + C_{sg,i+1/2}^n f_{g,i+1/2}^n) - (C_{sw,i-1/2}^n f_{w,i-1/2}^n + C_{sg,i-1/2}^n f_{g,i-1/2}^n)}{\Delta x_D} \right]
\end{aligned}$$

(3.29)

Now we can substitute Eqn (3.26) and $K_{sgw} = \frac{C_{sg}}{C_{sw}}$ into Eqn (3.28), and get

the following equation:

$$C_{sw,i}^{n+1} S_{w,i}^{n+1} + K_{sgw} C_{sw,i}^{n+1} S_{g,i}^{n+1} + \frac{1-\phi}{\phi} \rho_s a_s \Gamma_{s,max} \cdot \frac{\alpha C_{sw,i}^{n+1}}{1 + \alpha C_{sw,i}^{n+1}} = N_{temp} \quad (3.30)$$

Eqn (3.30) is essentially a quadratic equation for the unknown variable

$C_{sw,i}^{n+1}$ and can be solved directly:

$$A \cdot (C_{sw,i}^{n+1})^2 + B \cdot C_{sw,i}^{n+1} + C = 0 \quad (3.31)$$

where

$$A = \alpha (S_{w,i}^{n+1} + K_{sgw} S_{g,i}^{n+1})$$

$$B = S_{w,i}^{n+1} + K_{sgw} S_{g,i}^{n+1} + \frac{1-\phi}{\phi} \rho_s a_s \Gamma_{s,max} \alpha - \alpha N_{temp}$$

$$C = -N_{temp}$$

One can find that “A” is always positive unless both $S_{w,i}^{n+1}$ and $S_{g,i}^{n+1}$ are zero. In this case, we can find the positive root of the quadratic equation by Eqn (3.32):

$$C_{sw,i}^{n+1} = \frac{-B + \sqrt{B^2 - 4AC}}{2A} \quad (3.32)$$

Note that in equilibrium transport processes we have $K_{sgw} = \frac{C_{sg}}{C_{sw}}$ in porous media. However, this relationship is not necessarily true for the injection boundary condition, which means that $C_{sg,inj}$ does not have to be equal to

$K_{sgw} \cdot C_{sw,inj}$. To implement the concentration boundary conditions, in Eqn (3.29)

when $i = 1$ (the first grid block) we use $C_{sw,i-1}^n = C_{sw,i-1/2}^n = C_{sw,inj}$ and

$$C_{sg,i-1}^n = C_{sg,i-1/2}^n = C_{sg,inj}.$$

3.3 Chromatographic retardation of surfactant

Adsorption and phase partitioning of surfactant cause chromatographic retardation in porous media. In this section we perform dynamic simulations of these processes.

3.3.1 Dynamic adsorption

We perform dynamic simulation to evaluate the chromatographic retardation of various surfactants on dolomite formation. The parameters for simulation of surfactant transport are listed in Table 3-1.

Table 3-1. Parameters for simulation of surfactant transport in Section 3.3.1

Parameter	Value	Comment
NX	100	total grid blocks in x direction
Δt_D	0.001	dimensionless time step
ρ_s (g/cm^3)	2.93	density of dolomite (Carl Pool)
a_s (m^2/g)	0.1	specific surface area of the formation
$\Gamma_{s,max}$ (mg/m^2)	2.4	adsorption plateau of LAB
	1.8	adsorption plateau of AOS 1618
	0.5	adsorption plateau of C25A
α (L/g)	10	a parameter in the Langmuir isotherm
$C_{sw,inj}$ (g/L)	2.0	injected surfactant concentration
ϕ	0.25	porosity of the formation
Pe	500	Peclet number

Three surfactants (LAB, AOS1618, C25A) are simulated using the plateau values on dolomite powder (Carl Pool, old) shown in Figure 2-7. The transport of surfactant through a dolomite formation with a surface area of 0.1 m²/g is simulated. The porosity of the formation is assumed to be 0.25. In order to include the effect of dispersion on surfactant propagation, a Peclet number of 500 is used for all cases.

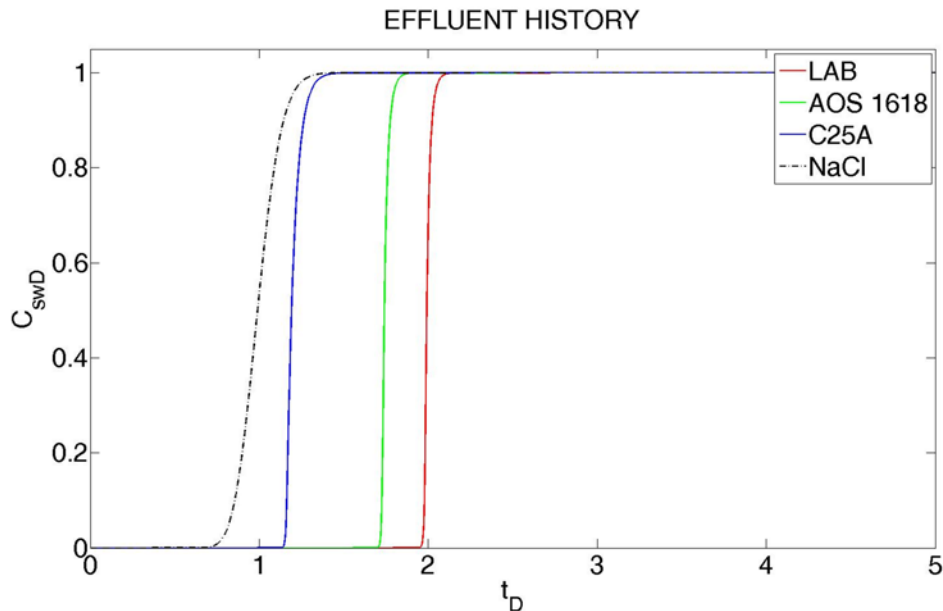


Figure 3-1. Comparison of effluent history of continuous injection of surfactants to a water-saturated dolomite formation. The parameters used in finite difference simulation are listed in Table 3-1.

The simulated results in Figure 3-1 shows the surfactant retention on dolomite formation. The dashed line is the effluent history of a non-adsorbing tracer (for example, NaCl) which serves as a control case. Little chromatographic retardation is indicated with the low-adsorbing surfactant C25A, while significant retention is shown with LAB and AOS 1618. In the case of LAB, it takes about 2 pore volumes (PV) for the surfactant to break through.

High adsorption of surfactants causes significant issues in finite slug injection, which means that a surfactant slug is injected to a water-saturated porous medium followed by water injection. In the case of no adsorption (NaCl in Figure 3-2), the effluent history is close to a Gaussian distribution which is caused by dispersion. The effluent history of the low-adsorbing surfactant C25A

shows a slight chromatographic retardation and tailing after the peak. This tailing phenomenon is more significant in the cases of LAB and AOS 1618 due to high adsorption onto the formation. In finite slug injection in the absence of dispersion, the adsorption front is a shock wave and the desorption tail is a spreading wave. If the finite slug is small and the adsorption is high, the spreading wave catches up with the shocking wave before it breaks through, causing a significant decrease in peak effluent concentration. In Figure 3-2 the peak effluent concentration of LAB is only about 10% of the injected concentration. The effluent is smeared out due to high adsorption on dolomite formation. Therefore, it is crucial to select low adsorbing surfactant formulations for EOR applications.

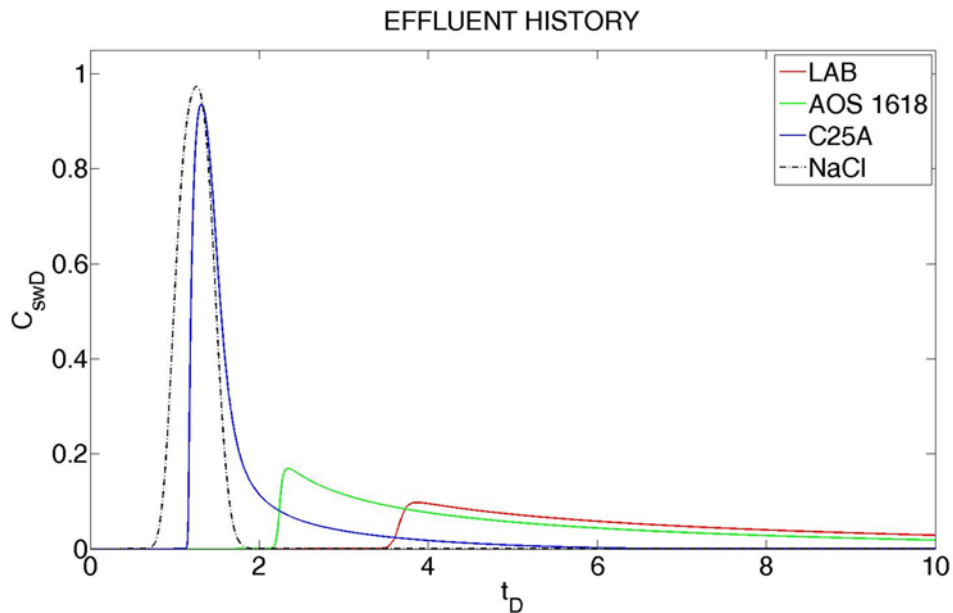


Figure 3-2. Comparison of effluent history of 0.5 PV finite slug injection of surfactants to a water-saturated dolomite formation. The parameters used in finite difference simulation are listed in Table 3-1.

3.3.2 Phase partition

3.3.2.1. Effect of injection phase

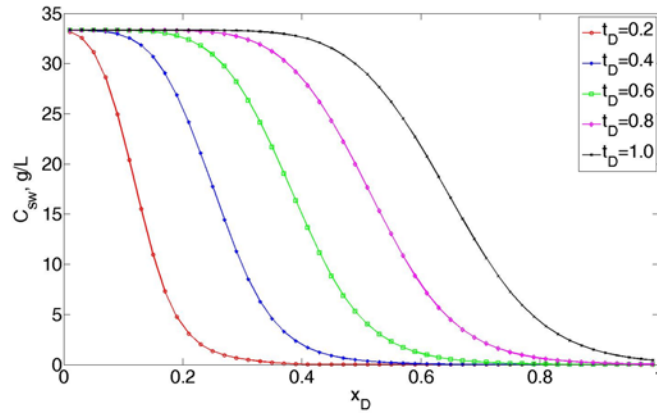
Table 3-2. Parameters for CO₂ foam simulation in this work (4000 psi, 120 °C)

Parameter	Value	Comment or reference
NX	50	
$\Delta t_D / \Delta x_D$	0.005	
$epdry$	1000	
$fmmob$	500	
$fmdry$	0.25	
$fmsurf$	10	in g/L
S_{wc}	0.05	connate water saturation
S_{gr}	0.05	residual gas saturation
μ_w	0.00024	in Pa·s, http://www.peacesoftware.de/einigewerte
μ_g	0.000045	in Pa·s, http://www.peacesoftware.de/einigewerte
k_{rw}^0	0.2	(Ashoori, van der Heijden et al. 2010)
k_{rg}^0	0.94	(Ashoori, van der Heijden et al. 2010)
n_w	4.2	(Ashoori, van der Heijden et al. 2010)
n_g	1.3	(Ashoori, van der Heijden et al. 2010)
K_{sgw}	0.05	$K_{sgw} = C_{sg} / C_{sw}$
k	1.0	in darcy, permeability of the formation
L	1.0	in ft, length of the formation
ϕ	0.25	porosity of the formation
u^{BC}	20	in ft/day, total injected superficial velocity
Pe_w	500	Peclet number of the aqueous phase
Pe_g	500	Peclet number of the CO ₂ -rich phase

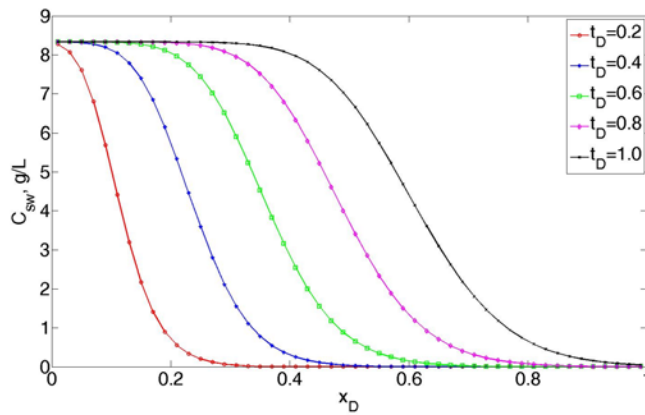
If the surfactant is CO₂-soluble, it can be injected with either CO₂ or water.

We compare two cases with 10 g/L injection surfactant concentration in CO₂-rich phase and in aqueous phase, respectively. The rest of the parameters are shown

in Table 3-2. The targeting reservoir has a pressure of 4000 psi and a temperature of 120 °C.

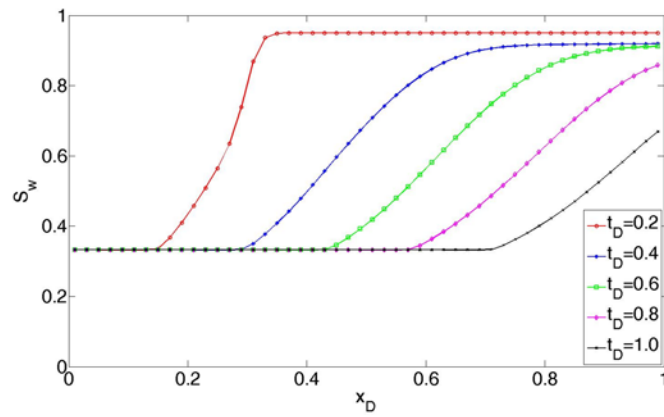


(a) 10 g/L surfactant is injected with CO₂

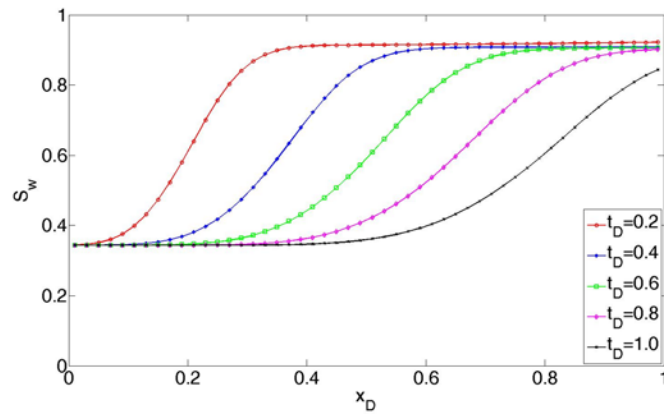


(b) 10 g/L surfactant is injected with water

Figure 3-3. Simulation results of surfactant concentration profiles in aqueous phase using the parameters listed in Table 3-2. Injected gas fraction is $f_g=80\%$.

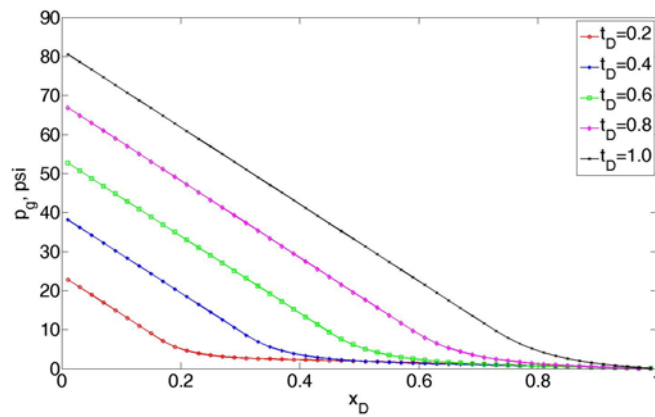


(a) 10 g/L surfactant is injected with CO₂

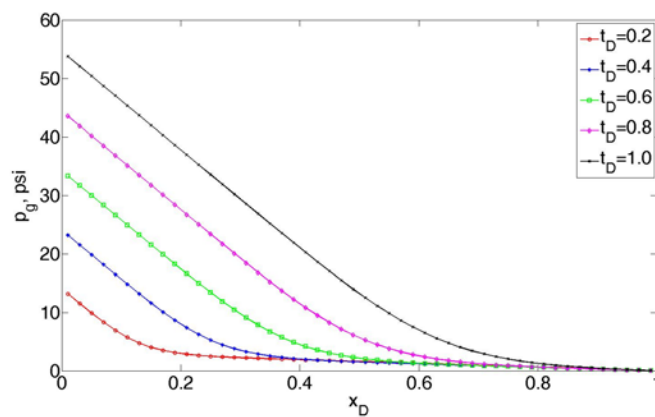


(b) 10 g/L surfactant is injected with water

Figure 3-4. Simulation results of saturation profiles using the parameters listed in Table 3-2. Injected gas fraction is $f_g=80\%$.



(a) 10 g/L surfactant is injected with CO₂



(b) 10 g/L surfactant is injected with water

Figure 3-5. Simulation results of gas pressure profiles using the parameters listed in Table 3-2. Injected gas fraction is $f_g=80\%$.

The injected gas fraction is 80% in both cases shown in Figures 3-3 to 3-5. We observe that foam propagates faster if the surfactant is injected with CO₂ at 10 g/L than the case that surfactant is dissolved in water at 10g/L. However, this result is due to the fact that relatively high foam quality ($f_g=80\%$) is injected. If the comparison of foam propagation rate is on the basis of pore volumes of surfactants injected, the case in which the surfactant is injected with water

exhibits better efficiency. The reason behind this phenomenon is that we set the critical surfactant concentration ($fmsurf$) to be 10g/L in aqueous phase. If the surfactant with a small partition coefficient ($K_{sgw} = C_{sg} / C_{sw}$) is injected with CO₂ at 10g/L, the aqueous surfactant concentration is much higher than $fmsurf$ while it doesn't contribute to improved foam strength according to the foam model.

3.3.2.2. Effect of partition coefficient

Now we investigate the effect of surfactant partition coefficient on foam transport. In Figure 3-6, the partition coefficient of surfactant between CO₂-rich phase and aqueous phase ranges from 0.05 to 10. The surfactant is injected with CO₂ at a foam quality of 80%. According to material balance, an increase in partition coefficient causes a decrease in surfactant concentration in aqueous phase as shown in Figure 3-6. This also leads to faster surfactant propagation in porous media if the partition coefficient is large (surfactant favors CO₂).

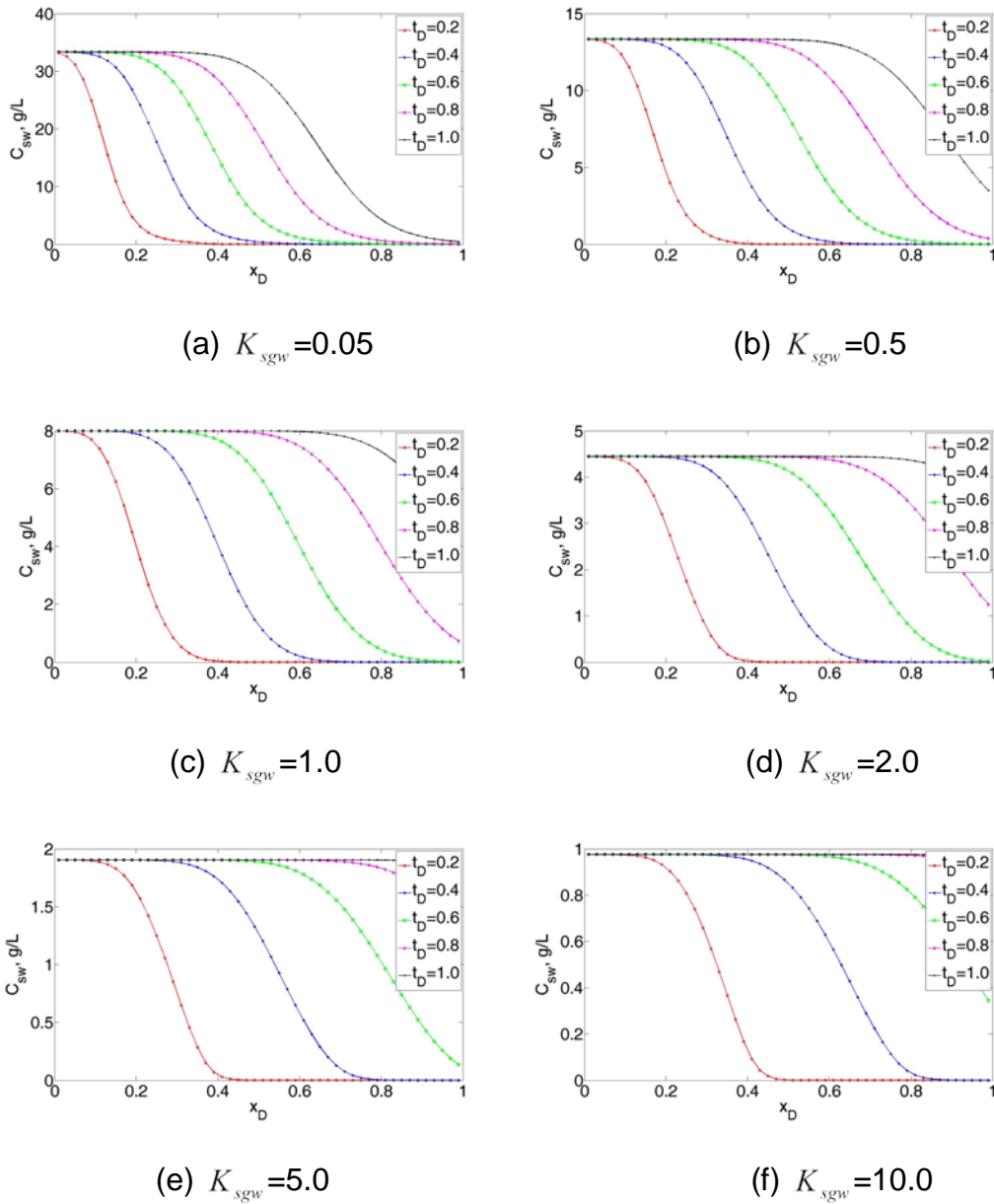
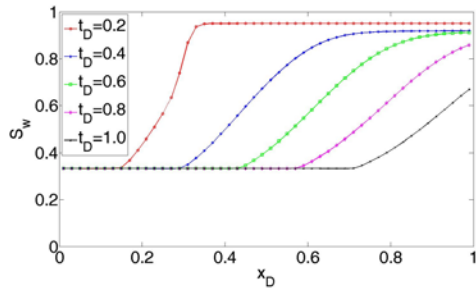


Figure 3-6. Simulation results of surfactant concentration profiles in aqueous phase using the parameters listed in Table 3-2 except for K_{sgw} . 10 g/L surfactant is injected with CO_2 . Injected gas fraction is $f_g=80\%$.

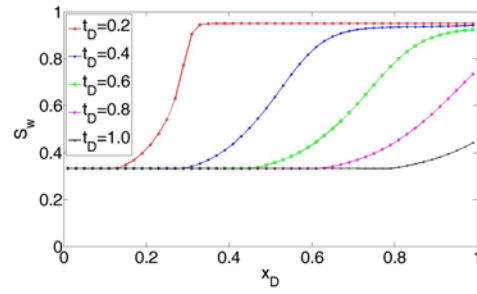
Figure 3-7 shows the effect of partition coefficient on water saturation profiles. We can see that the foam front propagates faster when K_{sgw} increases. When K_{sgw} increases from 0.05 to 0.5 the sweep efficiency increases at 1.0 TPV,

resulting in less water left in the porous media. However, a further increase in K_{sgw} leads to an increase in water saturation in the swept region, resulting in poorer sweep efficiency at 1.0 TPV. This is because that full-strength foam is not achieved when the surfactant concentration in aqueous phase drops below 10 g/L ($fmsurf$). Therefore, the process should be controlled in such a way that the surfactant concentration in aqueous phase is right at the concentration above which foam strength is independent of surfactant concentration ($fmsurf$).

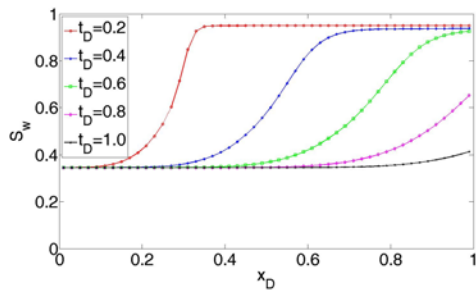
Figure 3-8 shows the pressure profiles with different partition coefficients. The result indicates that the pressure gradient is surfactant-concentration-dependent. For a partition coefficient at 0.05 or 0.5, the pressure gradient is essentially the same when foam sweeps through the system. However, surfactant concentration in aqueous phase becomes a limiting factor for foam strength when the partition coefficient becomes larger than 1.0. This leads to a decrease in pressure gradient in porous media as shown in Figure 3-8.



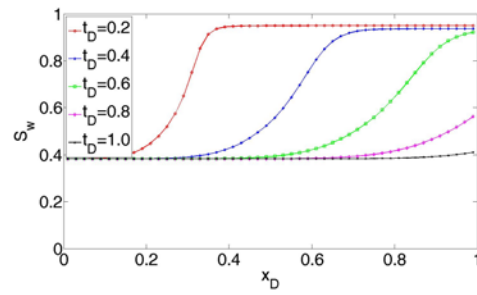
(a) $K_{sgw} = 0.05$



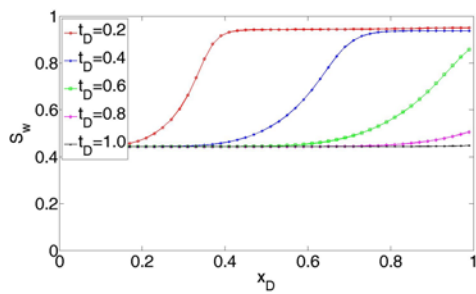
(b) $K_{sgw} = 0.5$



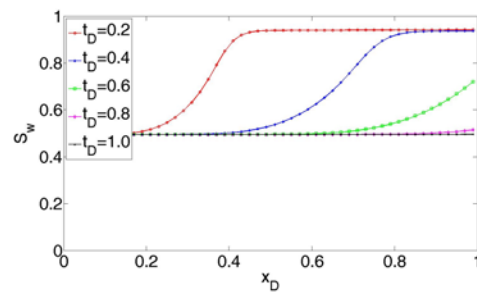
(c) $K_{sgw} = 1.0$



(d) $K_{sgw} = 2.0$



(e) $K_{sgw} = 5.0$



(f) $K_{sgw} = 10.0$

Figure 3-7. Simulation results of saturation profiles in aqueous phase using the parameters listed in Table 3-2 except for K_{sgw} . 10 g/L surfactant is injected with CO_2 . Injected gas fraction is $f_g=80\%$.

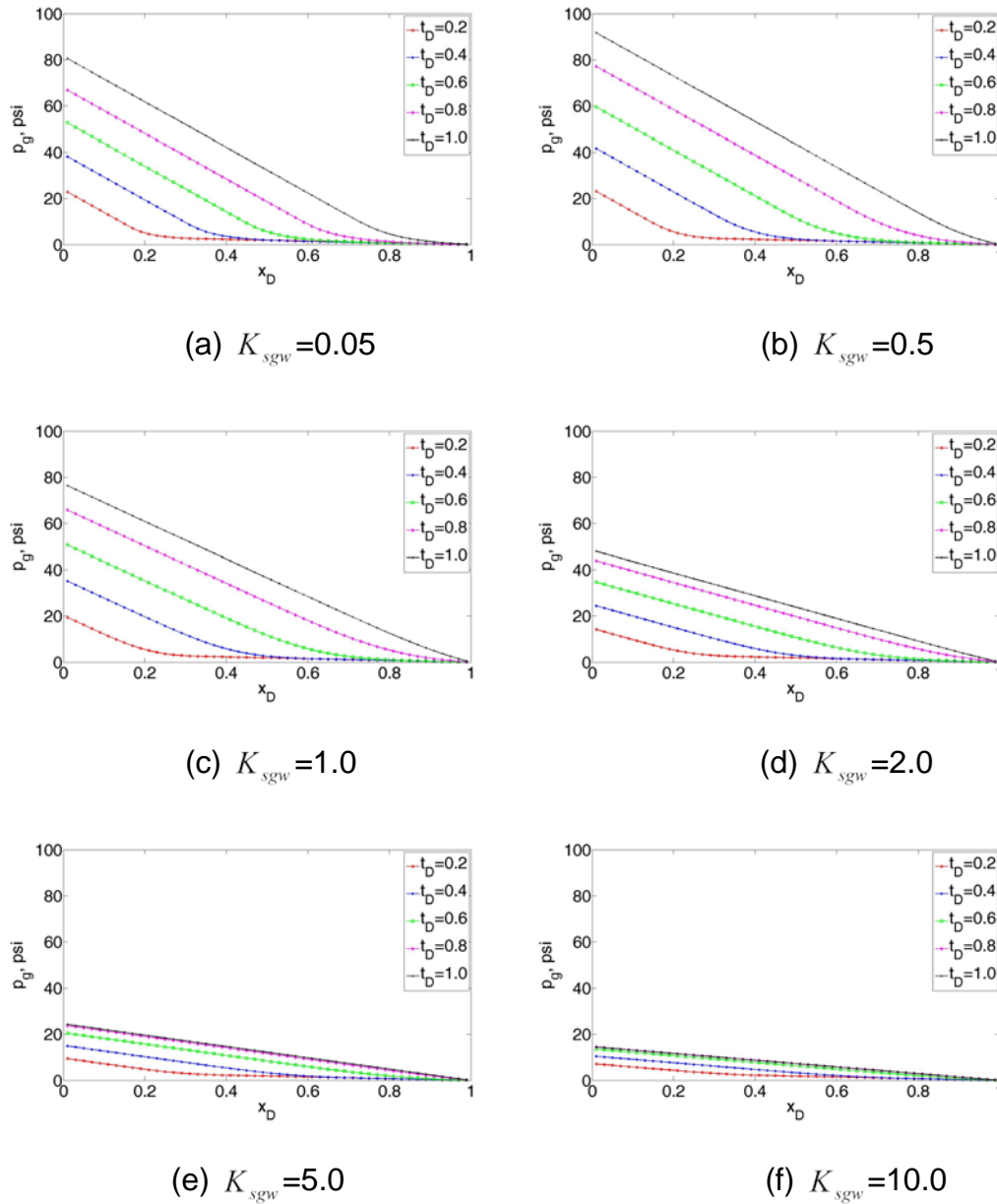


Figure 3-8. Simulation results of gas pressure profiles in aqueous phase using the parameters listed in Table 3-2 except for K_{sgw} . 10 g/L surfactant is injected with CO_2 . Injected gas fraction is $f_g=80\%$.

3.4 Conclusions

A finite difference foam simulator embedded with a semi-empirical foam model is developed. The simulator is able to simulate one-dimensional two-

phase foam flow through porous media. IMPES (implicit in pressure and explicit in saturation) formulation is used to calculate pressure and saturation in the system, and a convective diffusion equation is derived to compute surfactant transport in foam flow. This convective diffusion equation is solved using forward difference, one-point upstream weighting method. The effects of adsorption on formation rock and partition between CO₂-rich phase and aqueous phase on surfactant transport are included in the simulation.

By comparing the dynamic adsorption of three different surfactants (LAB, AOS 1618, C25A) using the simulator and experimental results of static adsorption, one can evaluate the effect of adsorption on chromatographic retardation of the surfactants. In finite slug injection of the surfactants, high adsorption causes severe interactions of the leading shock wave and the tailing spreading wave, which significantly smears out the effluent. Low adsorbing surfactant such as C25A is highly desirable for a successful foam process.

A simulation study was made on the effect of surfactant-partition coefficient (CO₂/Water) on foam propagation during co-injection in one dimension with no adsorption. The surfactant could be injected in either water or CO₂. The simulator was modeled so that surfactant can be injected either with CO₂ or water. The foam strength with co-injection will be the same if the equilibrium concentrations in aqueous phase are the same. If the surfactant is injected with CO₂ at a fixed concentration, increasing partition coefficient between CO₂ and water (surfactant favors CO₂) leads to faster foam propagation. However, the foam strength will decline if the surfactant concentration in the aqueous phase is below f_{msurf} . For

co-injection, the injection concentration should be chosen such that the aqueous surfactant concentration is equal to $fmsurf$ if it is desired to have maximum foam strength but yet not waste surfactant.

3.5 References

- Ashoori, E., T. L. M. van der Heijden, et al. (2010). "Fractional-flow theory of foam displacements with oil." SPE Journal **15**(2): 260-273.
- Computer Modeling Group (2007). "STARSTM user's guide." Calgary, Alberta, Canada.
- Lake, L. W. (1989). Enhanced oil recovery. Englewood Cliffs, N.J., Prentice Hall.
- Renkema, W. J. and W. R. Rossen (2007). Success of foam SAG processes in heterogeneous reservoirs. SPE Annual Technical Conference and Exhibition. Anaheim, California, U.S.A., Society of Petroleum Engineers.
- Vassenden, F. and T. Holt (2000). "Experimental foundation for relative permeability modeling of foam." SPE Reservoir Evaluation & Engineering **3**(2): 179-185.
- Zanganeh, M. N., S. I. Kam, et al. (2011). "The method of characteristics applied to oil displacement by foam." SPE Journal **16**(1): 8-23.

Chapter 4

Estimation of parameters for the simulation of foam flow in porous media

This chapter presents a method for estimating foam simulation parameters from laboratory experiments. One can use the proposed method to fit both steady-state and transient experiments. The non-uniqueness in parameter estimation, parameter sensitivity, and numerical artifacts are also discussed in this chapter.

4.1 Materials and Methods

4.1.1 Experimental setup

Two experimental systems, Systems A and B, are used to collect data in 1-D foam flooding processes. The experimental data in these two systems will be fit with the STARSTM foam model with an approach developed in this chapter.

The details of experimental operation in System A are referred to the literature (Lopez-Salinas 2012). We briefly reiterate the experimental procedure here. A proprietary surfactant blend ZAC (code name Z-R₁₁-ZFG₁₂ + A-R₁-AFG + C-R₃-CFG₃) is used as the foaming agent in System A. The ZAC blend with 0.1

wt% total surfactant concentration in synthetic brine is used in the experiments. The synthetic brine contains 27.0 g/L NaCl, 1.3 g/L CaCl₂, 11.2 g/L MgCl₂ • 6H₂O and 4.8 g/L Na₂SO₄. All aqueous solutions are prepared with DI water (resistivity 18.2 M Ω -cm), and 30 ppm of Na₂SO₃ as oxygen scavenger. The foam experiments are done at 94°C by co-injecting pre-purified gas nitrogen and surfactant solution into a vertical packed 20-40 mesh silica sand column (ID=2.29 cm, L=38.1 cm, k=100 darcy, 20/40 Ottawa Silica Sand US-Silica) from the bottom at a total injected superficial velocity ($u_w + u_g$) of 33 ft/day (2.7 cm³/min).

An internal olefin sulfonate, IOS1518, is used as the foaming surfactant in the foam flooding experiments in System B. This product was manufactured by Stepan (19.42 wt% activity, Lot.# 18239-032708) with a trade name of Petrostep S-2A. Silica sand 20/40 (U.S. Silica Company) is used to pack the porous media in the 1-D glass column (30010 Glass Pipe Conical, Scientific Glass and Instruments Inc.). The sand pack has a diameter of 2.58 cm and a length of 27.5 cm. A permeability of 158.0 darcy and a porosity of 36.0% are determined for this system.

In System B, the water saturation in porous media is measured by weighing the sand pack using a weighing balance (Sartorius Balance BP 3100S, USA) after all valves are closed and the sand pack is separated from other equipment. Zero water saturation corresponds to the weight of fresh sand pack before water injection; 100% water saturation corresponds to the weight of water-saturated sand pack after water injection to the system which was previously filled with CO₂.

By excluding the dead volume (1.5 ml), a linear relationship between the water saturation and the weight of the sand pack is employed to determine the water saturation at a specific weight. After this calibration, surfactant solutions are used as the aqueous phase in foam experiments other than water. The density difference between the surfactant solution (1.016 g/ml) and water (0.997 g/ml) is used to calculate the aqueous phase saturation based on the method described above.

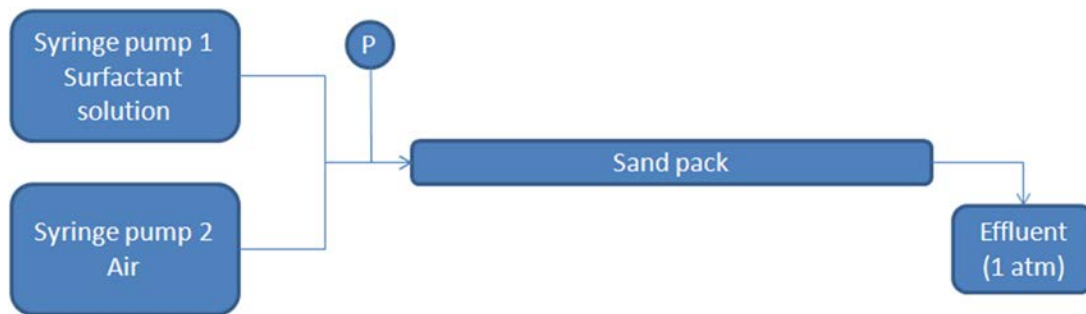


Figure 4-1. Schematic of the apparatus for foam experiments in System B.

The sand pack is filled with DI water before the foam generation experiment. IOS1518 with a final concentration of 0.2 wt% is dissolved in 1.0 wt% NaCl brine. 2.0 PV of surfactant solution is injected to the porous media to satisfy surfactant adsorption. A series of steady-state co-injection experiments start from 99% air injection displacing surfactant solution and end up with 10% air injection. The experimental setup of System B is shown in Figure 4-1. Surfactant solution is co-injected with air to the sand pack using syringe pumps (Harvard Apparatus MODEL 22) at a total superficial velocity ($u_w + u_g$) of 20 ft/day. Because of the

lack of internal taps in the glass sand-pack holder, a pressure transducer (Validyne Engineering MODEL DP7) is located at the inflow end, and it is assumed to be measuring pressure drop across the porous media. The outflow end is open to atmosphere. When a steady state is achieved and the pressure drop reaches a plateau value, the pressure drop is averaged over the period of the steady state.

A transient (continuous gas injection) experiment is performed using the same sand pack and a mass flow meter (Matheson Model 8200) to control the flow rate of the injected gas phase. After saturated with DI water, the sand pack is placed vertically and 4.0 PV of 0.2 wt% IOS1518 in 1.0 wt% NaCl is injected from bottom to top to displace DI water. Then the sand pack is placed horizontally to allow N₂ injection to the system. The flow rate of N₂ is 20 ft/day in standard condition (or 2.212 sccm).

The foam apparent viscosity, which is the pressure gradient normalized with respect to the permeability and the total flux of surfactant solution and gas, is calculated through Eqn (4.1):

$$\mu_{foam,app} = \frac{-k\nabla p}{u_w + u_g} \quad (4.1)$$

There are other forms of foam apparent viscosity in the literature such as the one using gas superficial velocity in the denominator (Falls, Musters et al. 1989). It shouldn't matter in the parameter estimation process which form of foam apparent viscosity is used. The reason this form is chosen is because the

proposed approach is consistent with the method using the contour plot of pressure gradient (Cheng, Reme et al. 2000) since a fixed total flow rate is used in our experiments.

4.1.2 Foam model

The STARS™ foam model (2007 version (Computer Modeling Group 2007; Farajzadeh, Wassing et al. 2012)) is employed in this work. This foam model assumes local steady state, which means that foam creation and decay mechanisms occur relatively fast compared with flow through porous media (Renkema and Rossen 2007). Based on the reported literature, the STARS™ foam model is shown in Eqns (4.2) and (4.3) (Ashoori, van der Heijden et al. 2010; Zanganeh, Kam et al. 2011):

$$k_{rg}^f = k_{rg}^{nf} \times FM \quad (4.2)$$

$$FM = \frac{1}{1 + fmmob \times F_1 \times F_2 \times F_3 \times F_4 \times F_5 \times F_6} \quad (4.3)$$

Eqns (4.2) and (4.3) indicate that this foam model uses a mobility reduction factor called FM to change the relative permeability of the gas phase in the presence of foam. The mobility reduction factor FM includes 6 functions (F_1 to F_6 , subscripts corresponding to different functions may vary in different versions) to describe different factors on gas mobility reduction. In this work we mainly

focus on estimating the parameters in the function F_2 (water-saturation-dependent function) shown in Eqn (4.4).

$$F_2 = 0.5 + \frac{\arctan[epdry(S_w - fmdry)]}{\pi} \quad (4.4)$$

The details of the functions, F_1 (surfactant-concentration-dependent function), F_3 (oil-saturation-dependent function), F_4 (shear-thinning function), F_5 (critical-capillary-number-dependent function) and F_6 (salinity-dependent function) can be found elsewhere (Computer Modeling Group 2007; Farajzadeh, Wassing et al. 2012) and are not discussed here. The experiments disclosed in this chapter are performed at a fixed total superficial velocity, and we assume no shear-thinning effect in the foam model. However, the shear-thinning effect should be considered if the function F_4 is gas-velocity-dependent rather than total-velocity-dependent.

4.2 Results and discussion

4.2.1 Experimental results of foam flooding

4.2.1.1 Foam experiments in System A

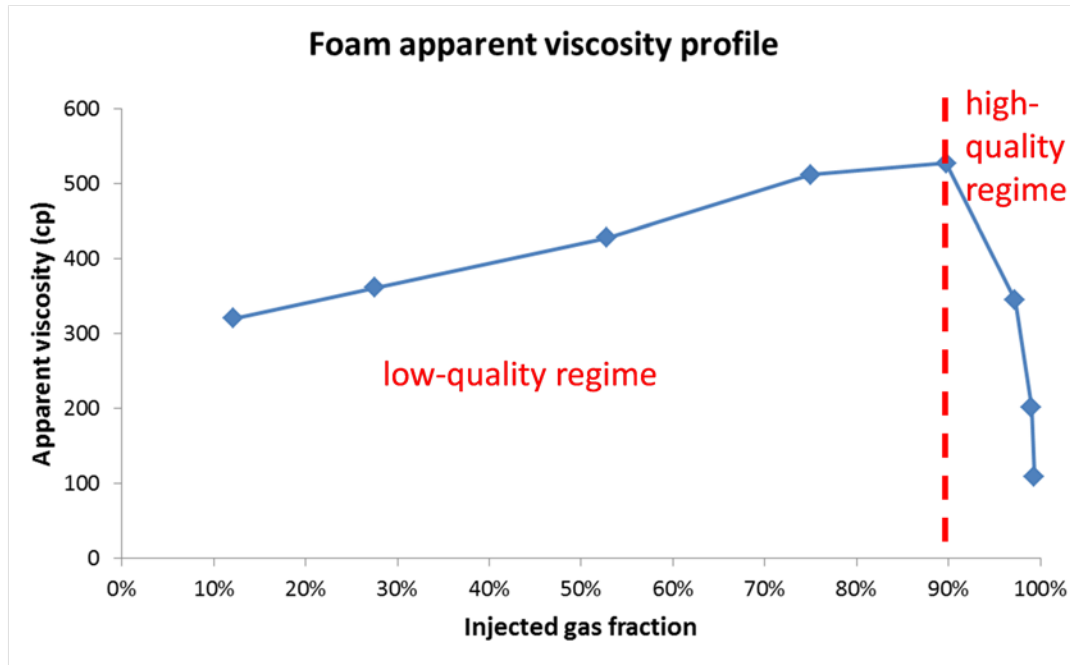


Figure 4-2. The effect of foam quality on foam apparent viscosity in System A. Experimental data is obtained from literature (Lopez-Salinas 2012). The total superficial velocity is 33 ft/day.

A set of steady-state foam experiments at a total superficial velocity of 33 ft/day in System A is obtained from literature (Ma, Lopez-Salinas et al.). The effect of foam quality (gas fractional flow) on foam apparent viscosity is shown in Figure 4-2. We observe two distinctive foam regimes in Figure 4-2: the high-quality (high-gas-fractional-flow) regime and the low-quality (low-gas-fractional-flow) regime (Osterloh and Jante Jr 1992; Alvarez, Rivas et al. 2001). The foam apparent viscosity increases when injected gas fraction increases in the low-quality regime, and decreases when injected gas fraction increases in the high-quality regime. At the boundary of the two regimes, foam obtains its maximum apparent viscosity at a given surfactant concentration and total superficial velocity. The gas fractional flow at the boundary of these two regimes is known

as the transition foam quality (Alvarez, Rivas et al. 2001). The data points in Figure 4-2 show a transition foam quality at 90% gas injection with a maximum foam apparent viscosity of 527 cp.

4.2.1.2 Foam experiments in System B

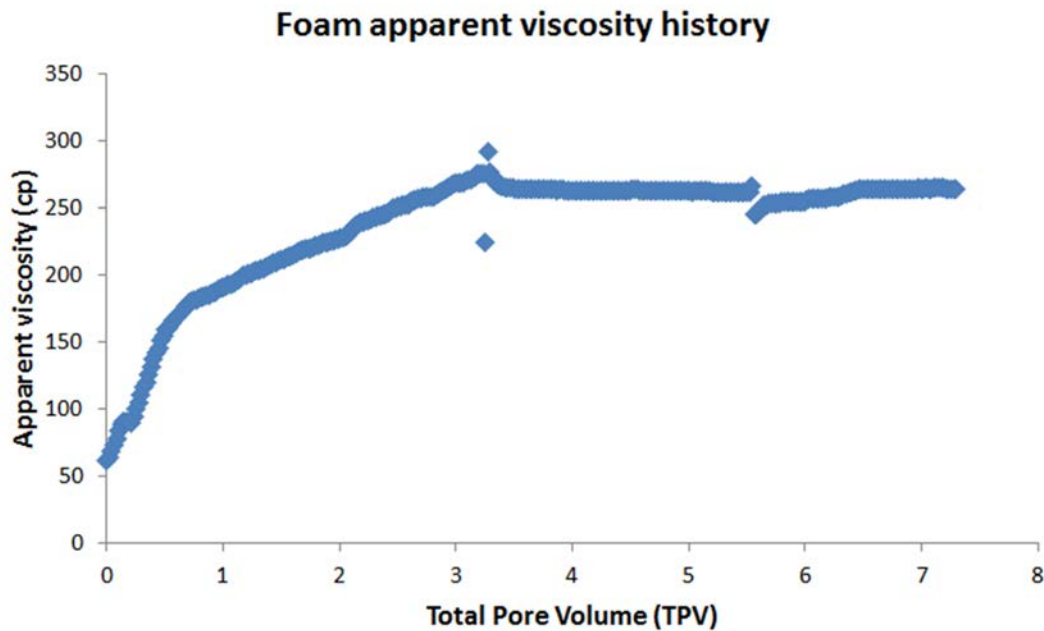


Figure 4-3. A typical foam apparent viscosity history of co-injection experiments in System B. The total superficial velocity is 20 ft/day with an injected gas fraction of 70%.

Figure 4-3 is for depicting a typical foam apparent viscosity history of our co-injection experiments in System B. The total superficial velocity is 20 ft/day with an injected gas fraction of 70%. The pressure drop in the system is recorded every 30 sec. The foam apparent viscosity reaches steady state after about 3.5 TPV. The sudden pressure changes at 3.3 and 5.6 TPV are due to the operation

of refilling injectants. The steady-state foam apparent viscosity (263 cp) for 70% gas injection is obtained by averaging the plateau viscosities.

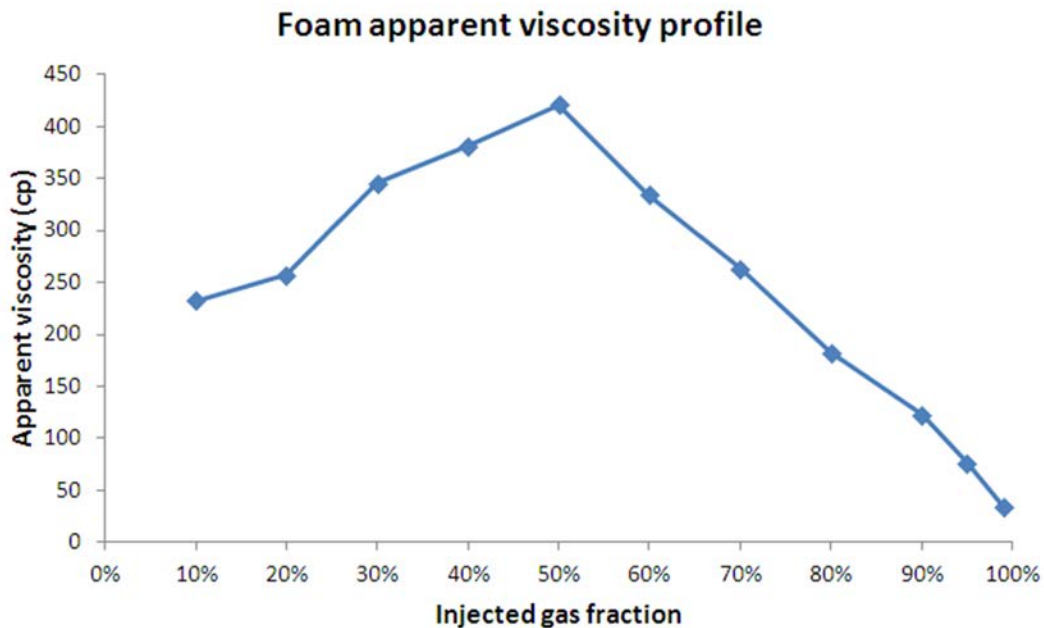


Figure 4-4. The effect of foam quality on foam apparent viscosity in System B. The total superficial velocity is 20 ft/day.

The effect of foam quality on foam apparent viscosity in System B is shown in Figure 4-4. In this system, the transition foam apparent viscosity is 421 cp with a pressure difference of 7.59 psi across the sand pack. The transition foam quality in System A (90%) is much higher than the one in System B (50%). It was shown that the transition foam quality is a function of core permeability, surfactant concentration, and overall flow rates (Alvarez, Rivas et al. 2001). The results presented here indicate that the transition foam quality also strongly depends on the surfactant formulation in geometrically similar porous media.

The effect of foam quality (f_g) on the saturation of aqueous phase (S_w) is shown in Figure 4-5. Typical fractional flow curves show that higher f_g (or lower f_w) results in lower S_w in the absence of foam. The effect of f_g on S_w in the presence of foam is investigated in System B within the range of f_g from 10% to 99%, and it is found that S_w is relatively constant over a wide range of foam qualities.

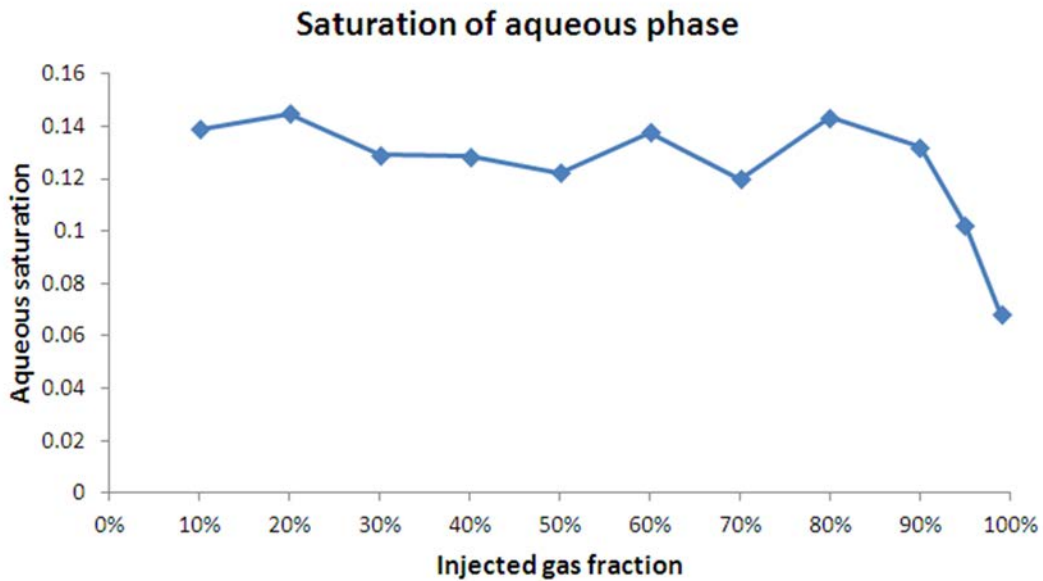


Figure 4-5. The effect of foam quality on aqueous saturation in System B. The total superficial velocity is 20 ft/day.

4.2.2 Foam modeling results with the dry-out function

4.2.2.1 Distinction between S_w^t and $fmdry$

By assuming incompressible, isothermal flow and the absence of capillary pressure and using 1-D Darcy's law we have

$$u_w = \frac{-kk_{rw} \nabla p}{\mu_w} \quad (4.5)$$

$$u_g = \frac{-kk_{rg}^f \nabla p}{\mu_g} \quad (4.6)$$

Combined with Eqn (4.1) we obtain

$$\mu_{foam.app} = \frac{k \nabla p}{\frac{kk_{rw} \nabla p}{\mu_w} + \frac{kk_{rg}^f \nabla p}{\mu_g}} = \frac{1}{\frac{k_{rw}(S_w)}{\mu_w} + \frac{k_{rg}^f(S_g)}{\mu_g}} \quad (4.7)$$

Note that the compressibility of the gas phase affects flow rates of gas, which leads to the fact that the upstream foam quality is less than that downstream in 1-D steady-state experiments. The superficial velocity is not constant even though the mass flux is constant at steady state. If the average foam quality is used instead of the injected foam quality, the transition foam quality will become larger. Meanwhile, the relative permeability is a function of saturation, and in two-phase flow we have

$$S_w + S_g = 1 \quad (4.8)$$

$$k_{rw} = k_{rw}^0 \left(\frac{S_w - S_{wc}}{1 - S_{gr} - S_{wc}} \right)^{n_w} \quad (4.9)$$

$$k_{rg}^f = k_{rg}^0 \left(1 - \frac{S_w - S_{wc}}{1 - S_{gr} - S_{wc}} \right)^{n_g} \cdot \frac{1}{1 + f_{mob} \times F_2} \quad (4.10)$$

Here the function F_2 is described in Eqn (4.4). According to Eqns (4.7)-(4.10),

$\mu_{foam,app}$ is a function of S_w when other parameters are fixed.

In order to calculate gas fractional flow from Eqns (4.5) and (4.6), we have

$$f_g = \frac{u_g}{u_w + u_g} = \frac{1}{1 + \frac{k_{rw}(S_w)}{\mu_w} \cdot \frac{\mu_g}{k_{rg}^f(S_g)}} \quad (4.11)$$

Therefore, in a two-phase system f_g is also a function of S_w only if other parameters stay unchanged. Through Eqns (4.7) and (4.11), one can calculate

$\mu_{foam,app}$ and f_g as functions of S_w .

We define $\mu_{foam,app}^t$ as the transition foam apparent viscosity between the high-quality and low-quality foam regimes. $\mu_{foam,app}^t$ is also the maximum foam apparent viscosity if the foam quality varies and the total flow rate is fixed. The water saturation at which $\mu_{foam,app}^t$ is obtained through Eqn (4.7) is defined as the transition water saturation (S_w^t). The gas fractional flow calculated at the transition water saturation with Eqn (4.11) is defined as the transition foam

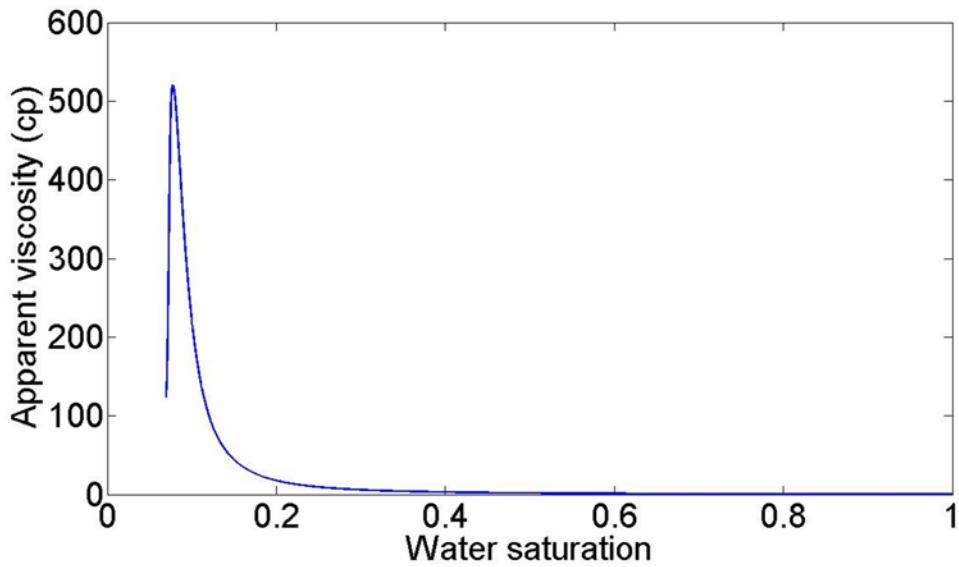
quality (f_g^t). The transition foam quality was also used in the literature with a symbol of f_g^* , and the corresponding water saturation was S_w^* (Cheng, Reme et al. 2000). If $epdry$ is sufficiently large, S_w^* , S_w^t , and the foam modeling parameter $fmdry$ approach each other (Cheng, Reme et al. 2000). In this section, we show the distinction between S_w^t and $fmdry$ if a relatively small value of $epdry$ is used. A small value of $epdry$ indicates a gradual transition between the high-quality and low-quality foam regimes.

An example case is discussed below for matching the experimental data in System A. With a set of foam modeling parameters ($epdry = 500$, $fmmob = 33000$ and $fmdry = 0.0730$), $\mu_{foam,app}$ vs. S_w is shown in Figure 4-6 using the rest of the parameters for System A in Table 1. Unless otherwise specified, a preset value (500) of $epdry$ is used to perform the steady-state model fit in this work. The choice of $epdry$ and the effect of $epdry$ on foam modeling are discussed in Section 4.2.2.4. A connate water saturation (S_{wc}) of 0.07 is used as shown in Table 4-1. S_{wc} can be estimated by matching experimentally measured water saturation for System B, which is discussed in Section 4.2.2.3.

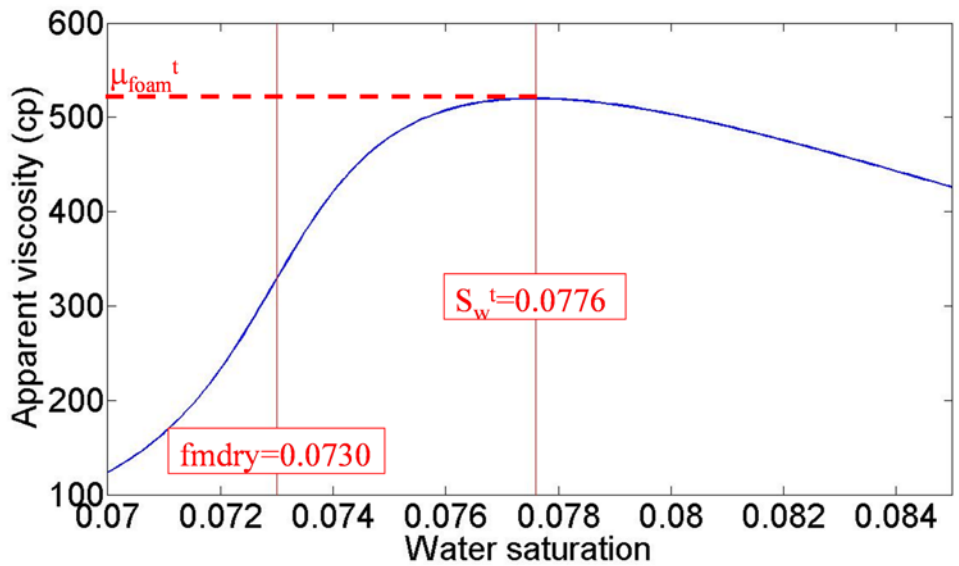
Table 4-1. Parameters for foam modeling in this work

Parameter	Value	Reference
$epdry$	500	
S_{wc}	0.07	
S_{gr}	0	(Kam, Nguyen et al. 2007)
$\mu_w(cp)$ (System A)	0.3	(Bruges, Latto et al. 1966)
$\mu_w(cp)$ (System B)	1.0	(Bruges, Latto et al. 1966)
$\mu_g(cp)$ (System A&B)	0.02	(Lemmon and Jacobsen 2004)
k_{rw}^0	0.79	(Kam, Nguyen et al. 2007)
k_{rg}^0	1.0	(Kam, Nguyen et al. 2007)
n_w	1.96	(Kam, Nguyen et al. 2007)
n_g	2.29	(Kam, Nguyen et al. 2007)

The parameters in relative permeability curves in Table 4-1 are obtained from the literature for unconsolidated sandpacks (Kam, Nguyen et al. 2007). These parameters are selected to demonstrate how to estimate foam parameters in the dry-out function. Foam parameters are sensitive to the parameters in relative permeability curves, especially the exponent in the k_{rw} curve. The sensitivity of foam modeling parameters to the parameters in relative permeability curves will be discussed in Section 4.2.6.



(a)

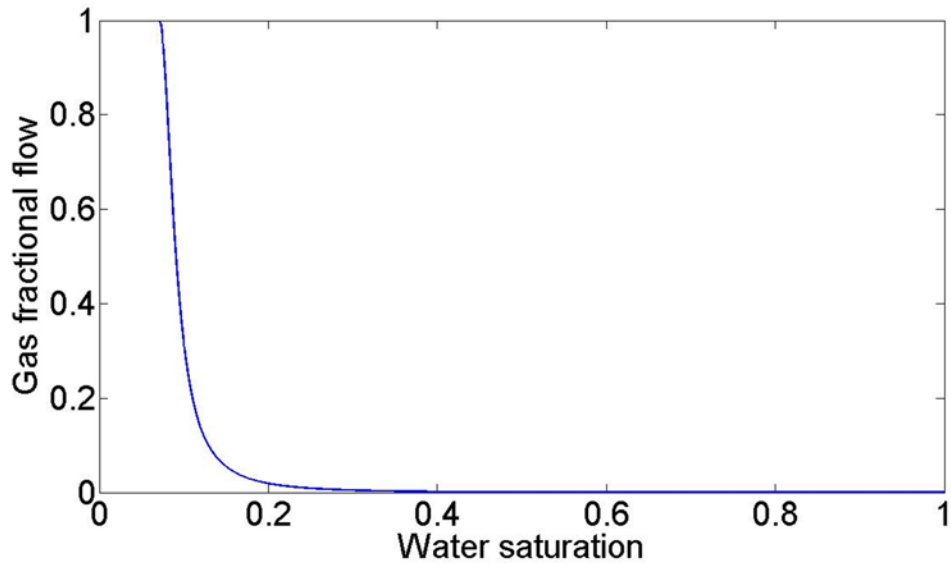


(b)

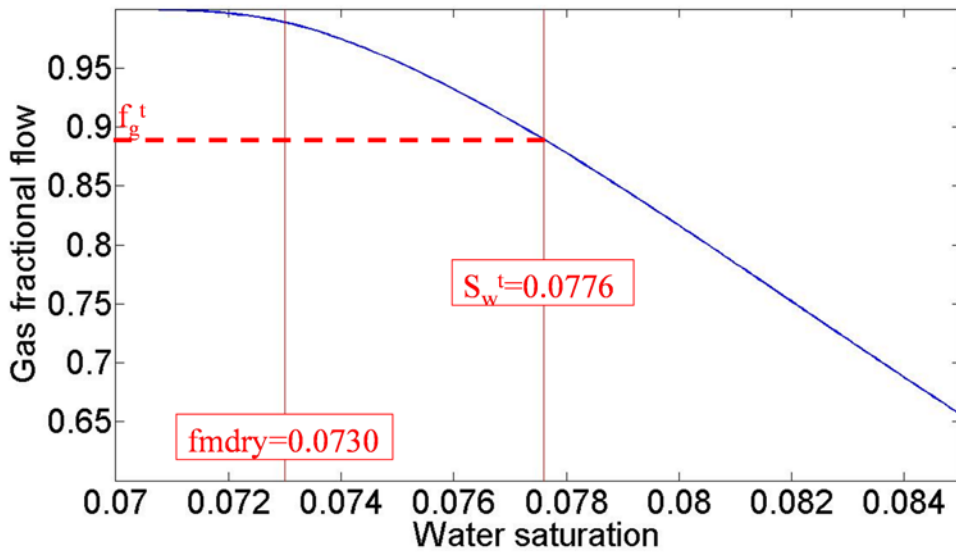
Figure 4-6. Foam apparent viscosity as a function of water saturation using $f_{mob} = 33000$ and $f_{mdry} = 0.0730$: (a) full profile; (b) close-up profile near f_{mdry} . The rest of the parameters used are shown in Table 4-1 (System A) with a preset $epdry$ of 500.

There exists a maximum foam apparent viscosity ($\mu_{foam,app}^t$) with changing foam qualities in Figure 4-6, which corresponds to the transition water saturation (S_w^t) and the transition foam quality (f_g^t). However, S_w^t is not equivalent to the parameter $fmdry$, which is designed to be the critical water saturation (the dry-out function F_2 in Eqn (4.4) is equal to 0.5 when $S_w = fmdry$) in the STARS™ foam model (Cheng, Reme et al. 2000) as indicated in Figure 4-6(b). In the case of $fmmob = 33000$ and $fmdry = 0.0730$, we obtain $S_w^t = 0.0776$ through a 1-D golden section search function “fminbnd” in MATLAB (The MathWorks Inc 2012).

Despite the small difference between $fmdry$ and S_w^t in this example, assuming S_w^t to be equal to $fmdry$ can cause significant error in calculating the transition foam quality f_g^t as shown in Figure 4-7(b). This is due to the fact that the $f_g - S_w$ curve is steep near $S_w = fmdry$ for describing the effect of the limiting capillary pressure (Figure 4-7). Therefore, S_w^t needs to be calculated using the algorithm instead of being assumed to be the parameter $fmdry$ especially when a relatively small value of $epdry$ is used.



(a)



(b)

Figure 4-7. Gas fractional flow as a function of water saturation using $f_{mob} = 33000$ and $f_{mdry} = 0.0730$: (a) full profile; (b) close-up profile near f_{mdry} . The rest of the parameters are used as shown in Table 4-1 (System A) with a preset $epdry$ of 500.

4.2.2.2 Hybrid contour plot method

Cheng and coworkers (Cheng, Reme et al. 2000) showed how to fit the parameters to steady-state laboratory coreflood data using the STARS™ foam model. This method is based on the hypothesis that the experimental ∇p data is vertical in the high-quality regime and horizontal in the low-quality regime in order to draw the contours of ∇p to fit the model parameters. The shape of the discontinuous slope between vertical and horizontal lines can cause numerical oscillation in finite difference simulation. We will discuss it in Section 4.2.5.

We propose an alternative approach for fitting experimental data by fixing total velocity of both gas and liquid and changing gas fractional flow. This approach estimates the parameters f_{mob} and f_{dry} by matching the transition foam apparent viscosity ($\mu_{foam,app}^t$) at the transition foam quality (f_g^t) in this set of experimental data. The parameter ep_{dry} is estimated by examining the fit to the rest of the steady-state data and the transient experiment with continuous gas injection.

In this section we introduce a hybrid contour plot method to estimate the parameters f_{mob} and f_{dry} in steady-state experiments. The procedure tackles three equations with three unknown variables: S_w^t , f_{mob} and f_{dry} :

$$\mu_{foam,app}(S_w^t, f_{mob}, f_{dry}) = \max_{S_w} \mu_{foam,app}(S_w, f_{mob}, f_{dry}) \quad (4.12)$$

$$\mu_{foam,app}^t = \frac{1}{\frac{k_{rw}(S_w^t)}{\mu_w} + \frac{k_{rg}^f(S_w^t, fmmob, fmdry)}{\mu_g}} \quad (4.13)$$

$$f_g^t = \frac{1}{1 + \frac{k_{rw}(S_w^t)}{\mu_w} \cdot \frac{\mu_g}{k_{rg}^f(S_w^t, fmmob, fmdry)}} \quad (4.14)$$

Note that the explicit expression of Eqn (4.12) can be written with the substitution of Eqns (4.7)-(4.10). The flow chart of the proposed hybrid contour plot method is shown in Figure 4-8. In the contour plot 1, S_w^t is solved using the golden section search method (the command “fminbnd” in MATLAB (The MathWorks Inc 2012)), then f_g^t is calculated based on the value of S_w^t as well as $fmmob$ and $fmdry$. In the contour plot 2, S_w is solved with a zero-finding function (the command “fzero” in MATLAB (The MathWorks Inc 2012)), then $\mu_{foam,app}$ is calculated based on the value of S_w as well as $fmmob$ and $fmdry$.

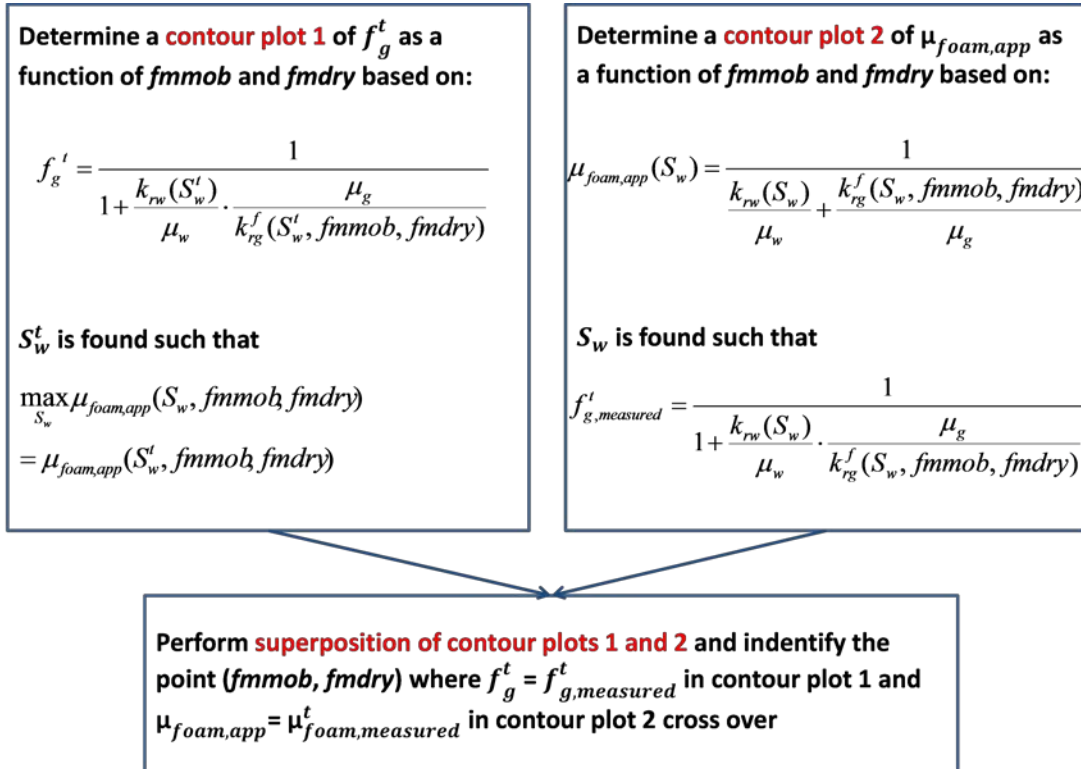


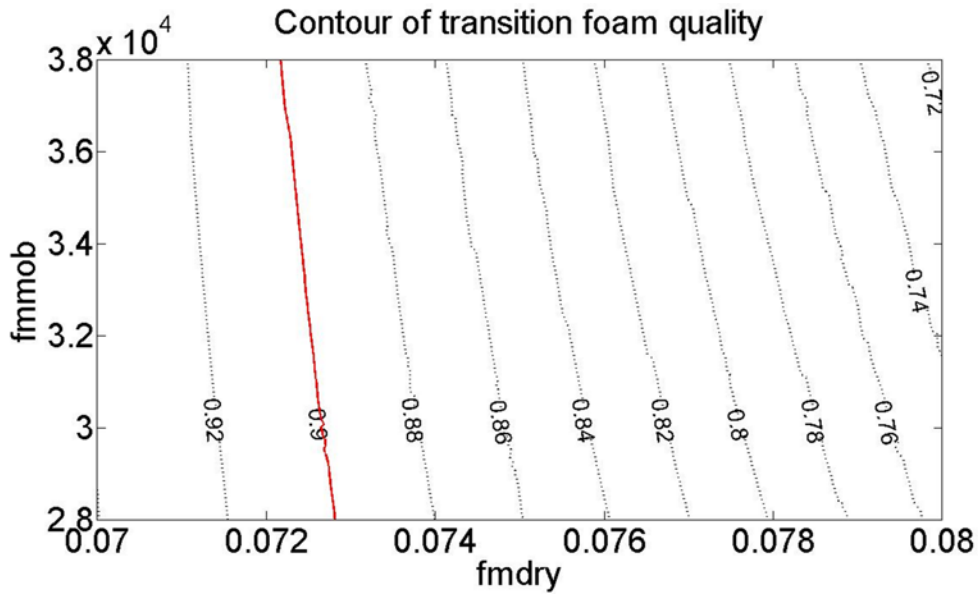
Figure 4-8. Flow chart for matching transition foam flow in porous media at steady state using the proposed hybrid contour plot method.

Fit for System A.

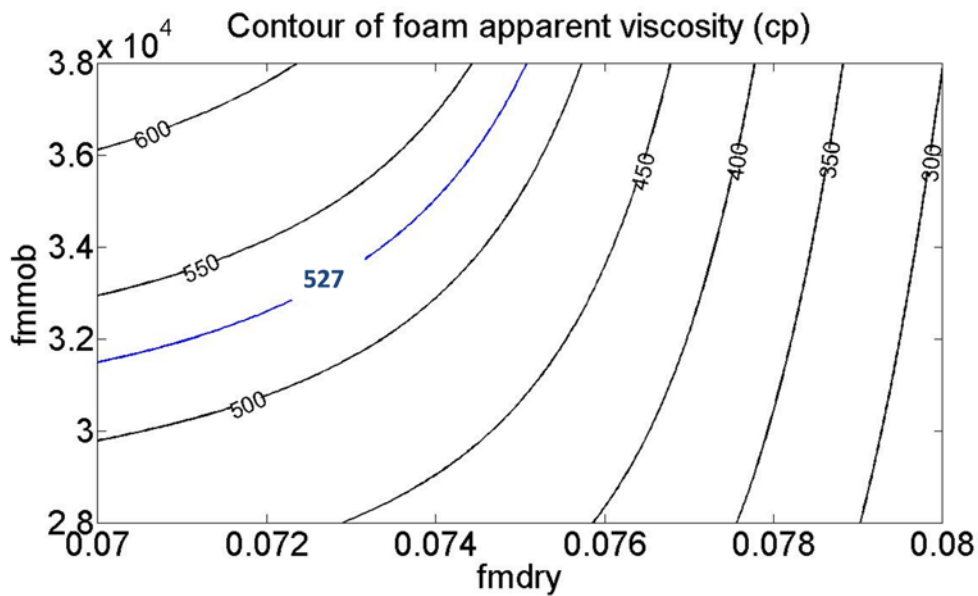
We show the matching process of System A in Figure 4-2 as an example to explain the procedure in Figure 4-8 in detail. In this case, $f_g^t = 0.9$ and

$\mu_{foam,app}^t = 527$ cp are obtained from the experimental data in Figure 4-2.

According to the procedure in Figure 4-8, contour plots of f_g^t and $\mu_{foam,app}$ (at $f_g = f_{g,measured}^t$) with respect to $fmmob$ and $fmdry$ using MATLAB are drawn in color in Figure 4-9(a) and (b), respectively.



(a)



(b)

Figure 4-9. (a) Contour plot of transition foam quality as a function of f_{mmob} and f_{mdry} . The experimental transition foam quality is shown as the red curve. (b) Contour plot of foam apparent viscosity as a function of f_{mmob} and f_{mdry} . Injected gas fraction is set to be 0.9. The experimental transition foam apparent viscosity is shown as the blue curve. The rest of the parameters are used as shown in Table 4-1 (System A) with a preset ep_{dry} of 500.

Superposition of Figure 4-9(a) and (b) leads to a hybrid contour plot shown in Figure 4-10. In Figure 4-10, the red curve represents the contour line of $f_g^t = 0.9$ in Figure 4-9(a), and the blue curve represents the contour line of $\mu_{foam,app}^t = 527 \text{ cp}$ in Figure 4-9(b). The point (purple dot) where the red curve and the blue curve intersect indicates the parameters we search for matching the experimental data ($f_g^t = 0.9$ and $\mu_{foam,app}^t = 527 \text{ cp}$). In this case, we obtain $fmmob = 3.30 \times 10^4$ and $fmdry = 0.073$ from Figure 4-10 after enlarging the plot in MATLAB.

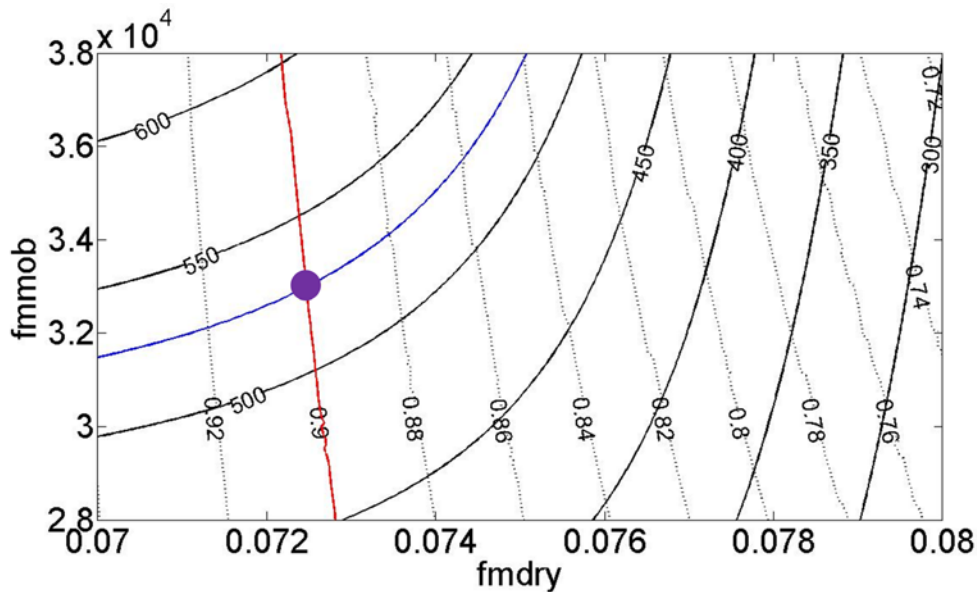


Figure 4-10. Superposition of contour plots in Figure 9(a) and (b) to find the position (the purple dot, $fmmob = 3.30 \times 10^4$ and $fmdry = 0.073$) where $f_g^t = 0.9$ (the red curve) and $\mu_{foam,app}^t = 527 \text{ cp}$ (the blue curve) cross over.

Using $f_{mob} = 3.30 \times 10^4$ and $f_{dry} = 0.073$, the parameters in Table 4-1 (System A) and Eqns (4.7) and (4.11), we compare the modeling profile of foam apparent viscosity with the experimental data in Figure 4-11. The simulation results match the experimental data at the transition foam quality, indicating that our calculation is accurate and the proposed procedure in Figure 4-8 is valid. The modeling result matches the trend of the experimental data with some underestimation of the data points at low gas fractions. This underestimation could possibly be due to trapped gas effect which we don't include here.

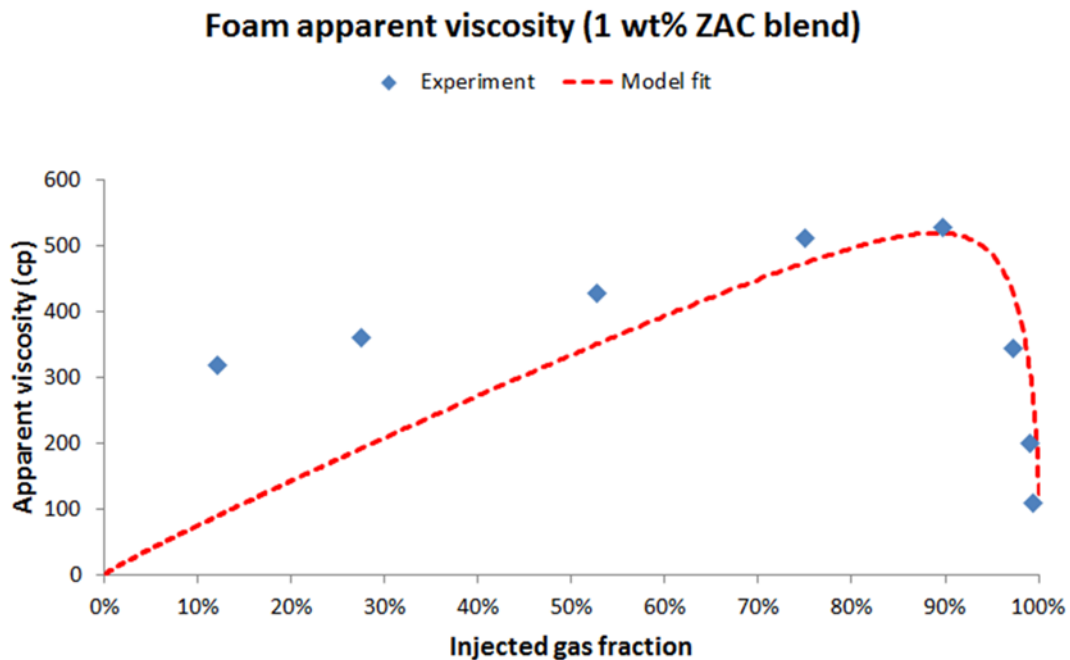


Figure 4-11. Comparison of foam apparent viscosities between model fit and experiment in System A. $f_{mob} = 3.30 \times 10^4$ and $f_{dry} = 0.073$ are used in the foam model. The rest of the parameters are used as shown in Table 4-1 (System A) with a preset ep_{dry} of 500.

There is more than one way to solve Eqns (4.12) to (4.14). We will elaborate a direct numerical method and compare it with the findings using the hybrid contour plot method in Section 4.2.3.1.

Fit for System B.

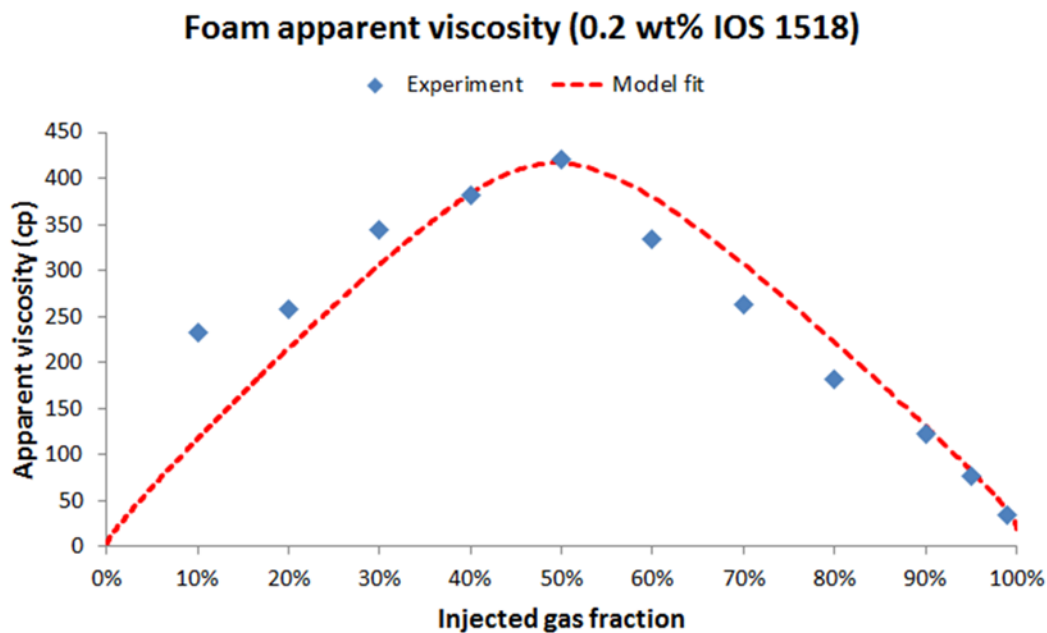


Figure 4-12. Comparison of foam apparent viscosities between model fit and experiment in System B. $fmmob = 4.72 \times 10^4$ and $fmdry = 0.101$ are used in the foam model. The rest of the parameters are used as shown in Table 4-1 (System B) with a preset $epdry$ of 500.

Using the same approach, we model the experimental data at a total superficial velocity of 20 ft/day (Figure 4-4) in System B with the F_2 function in the STARS™ foam model. The rest of the parameters are listed in Table 4-1

(System B). According to the experimental transition foam data shown in Figure 4-4 ($f_g^t = 0.5$ and $\mu_{foam,app}^t = 421 \text{ cp}$), one can obtain the parameters $f_{mmob} = 4.72 \times 10^4$ and $f_{mdry} = 0.101$ as shown in Figure 4-12. Both high-quality and low-quality foam regimes are well modeled using this approach with the STARS™ foam model.

4.2.2.3 Comparison in water saturation

We compare the water saturation profile for System B in Figure 4-13 using the parameters in Table 4-1 and Figure 4-12. The modeling results are relatively close to the measured water saturation. The experimental data in Figure 4-13 is not strictly monotonically decreasing, possibly due to measurement uncertainty in low water saturation and the entrance and end effect in the system (Du, Beni et al. 2008; Farajzadeh, Andrianov et al. 2009). The measurement uncertainty could possibly be that the water saturation has some fluctuations when the pressure drop appears stable at the steady state, and that the water saturation in flow lines including dead volume may not be equal to the one in the sand pack. Note that we use $S_{wc} = 0.07$ in Table 4-1, which enables us to match the experimental data of measured water saturation. If one wants to get a closer match to a particular part in the water saturation profile, S_{wc} can be adjusted slightly. As initially S_{wc} is unknown, a good practice may be to use a value of S_{wc} for a similar system in the literature (0.04, for example (Kam, Nguyen et al. 2007)). Then a search for foam modeling parameters can be conducted. After that, one can compare the

water saturation between modeling results and experimental data. If the water saturation is overestimated or underestimated, some fine tunings of S_{wc} are needed to obtain good match to experimental data. In this case a slight increase in S_{wc} from 0.04 to 0.07 results in an increase in estimated $fmdry$, but no significant change is found in $epdry$ value (around 500) for both transient and steady-state experiments.

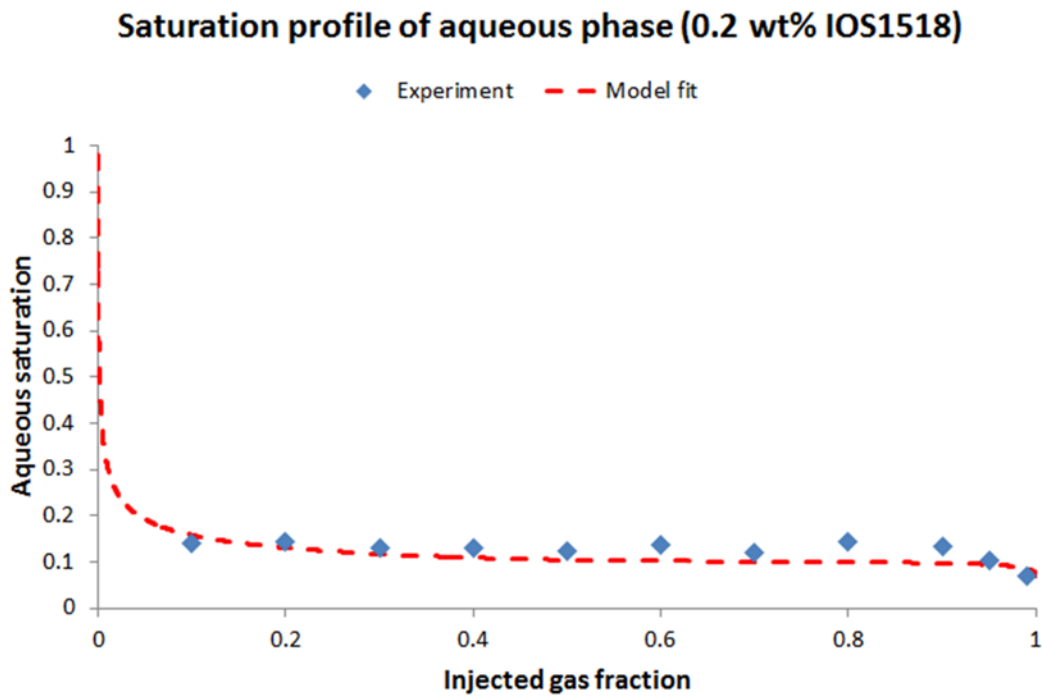


Figure 4-13. Comparison in water saturation between experimental data and modeling results in System B using the parameters in Table 4-1 (System B) and Figure 4-12.

4.2.2.4 Estimation of $epdry$

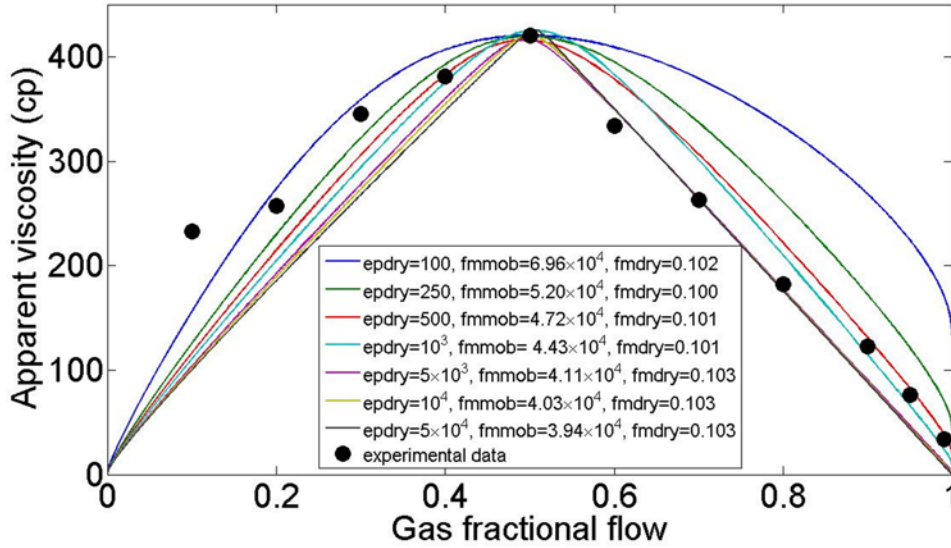


Figure 4-14. Model fit to experimental data in System B with different preset $epdry$. $fmmob$ and $fmdry$ are calculated using the method shown in Figure 8 for each value of $epdry$. Except for $epdry$, the rest of the parameters are used as shown in Table 4-1 (System B).

The parameter $epdry$ regulates the slope of the F_2 curve when S_w is near $fmdry$. It was found that reducing $epdry$ causes a deviation of ∇p contours from exactly vertical lines in the high-quality regime and exactly horizontal lines in the low quality regime (Cheng, Reme et al. 2000). To identify which value of $epdry$ provides best fit to all of the steady-state experiments, we define the residual sum of squares deviation (RSS) by comparing the relative difference between modeling results and experimental data:

$$RSS = \sum_{i=1}^n \left(\frac{\mu_{i,calculated} - \mu_{i,measured}}{\mu_{i,measured}} \right)^2 \quad (4.15)$$

The calculated foam apparent viscosities are based on the hybrid contour plot method shown in Figures 4-8 to 4-10 in which the transition foam data is fit with a precision of three significant digits. We use the 11 steady-state experimental data points in System B as an example to show how RSS varies with $epdry$. The model fit with different preset $epdry$ is shown in Figure 4-14 using the method described in Figure 4-8. As indicated in Figure 4-15, there exists a minimal RSS in a range between 100 and 50,000 for $epdry$. For this set of experimental data, the minimum of RSS is obtained with an $epdry$ value of around 500.

Nevertheless, for other values of $epdry$ which are larger than 500, the fit to steady-state data also seems reasonable (Figure 4-14) with relatively small RSS values shown in Figure 4-15. This is implying that a wide range of $epdry$ can be used to model this set of steady-state data.

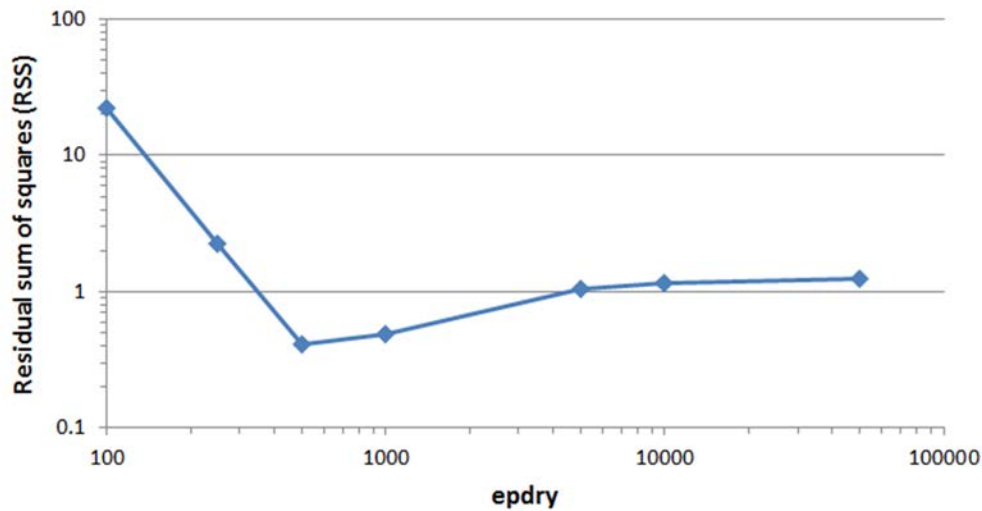


Figure 4-15. Residual sum of squares as a function of $epdry$ for modeling the steady-state experiments in System B. $fmdry$ and $fmdry$ are calculated using the method shown in Figure 8 for each preset value of $epdry$. Except for $epdry$, the rest of the parameters are used as shown in Table 4-1 (System B).

An additional transient (continuous gas injection) experiment may further narrow down the range of $epdry$ which we should consider. The experimental procedure is described in Section 4.1.1, which is continuous gas injection to a surfactant-solution-saturated sand pack at a constant flow rate. We program an in-house foam simulator using the IMPES (implicit in pressure and explicit in saturation) finite difference algorithm to conduct transient simulation and to match experimental data. 200 grid blocks ($NX=200$) are used for the transient simulation and the rest of the parameters are consistent with those in Table 4-1 except for $epdry$. The capillary pressure function is set to zero and the algorithm assumes 1-D, incompressible, isothermal flow.

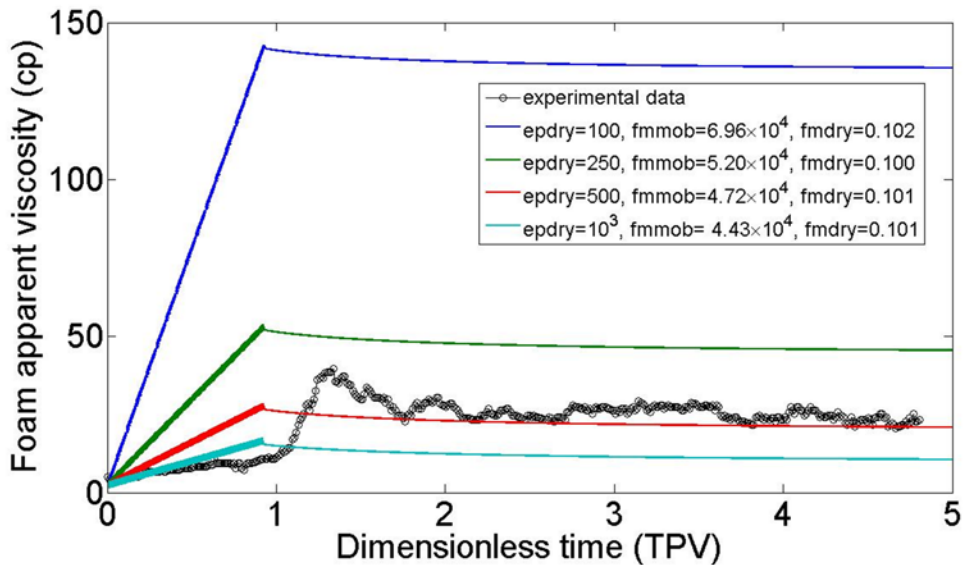


Figure 4-16. Comparison between transient experimental data and simulation results in System B. $fmmob$ and $fmdry$ are calculated using the method shown in Figure 8 for each value of $epdry$. Except for $epdry$, the rest of the parameters are used as shown in Table 4-1 (System B).

As shown in Figure 4-16, foam apparent viscosity gradually goes up when gas is injected into the porous medium. The maximum apparent viscosity (39.6 cp) is achieved at 1.34 TPV in the experiment. After 1.34 TPV, a typical dry-out effect is observed and foam gradually loses the strength as an effect of the limiting capillary pressure (Khatib, Hirasaki et al. 1988). Note that we define the total pore volume (TPV) of injected gas using the gas volume with an ambient absolute pressure (14.7 psia). If we define 1 TPV gas using the average pressure at the peak apparent viscosity, then the time for peak apparent viscosity should be 1.31 TPV which does not make much difference compared with 1.34 TPV. So the compressibility of gas cannot explain the late peak in foam apparent viscosity.

Meanwhile, the time of gas breakthrough observed in this experiment is 0.70 TPV, which is much earlier than the time when the maximum foam strength is observed. This observation indicates that after gas breakthrough foam is still being created and refined in porous media. It is possible that weak foam (coarse bubbles) travels ahead of strong foam (fine bubbles) in this experiment.

The foam modeling parameters used in Figure 4-16 are a subset of those in Figure 4-14. Among different sets of model fit using the estimation method proposed in Figure 4-8, it appears that the parameter set with an *epdry* slightly smaller than 500 is close to experimental observation especially after gas breakthrough. Figure 4-16 also reveals an issue with the STARS™ foam model: foam generation is faster in the simulation than the experiment. The population balance model (Falls, Hirasaki et al. 1988; Patzek 1988; Kovscek, Patzek et al. 1995; Bertin, Quintard et al. 1998; Myers and Radke 2000; Kam and Rossen 2003) may describe in-situ foam generation and coalescence more accurately than the local steady-state STARS™ foam model.

Nevertheless, if one accepts the local-steady-state model fit to these data, then the suitable value of *epdry* is around 500 for matching both steady-state and transient experiments in System B. However, how the value of *epdry* depends on other properties in the system, such as surfactant type and concentration, still needs further investigation.

4.2.3 Non-unique solutions to match the transition foam viscosity

4.2.3.1 Non-graphical solution

In Section 4.2.2.2 we introduced a hybrid contour plot method to match the transition foam viscosity between the high-quality regime and the low-quality regime. Here we discuss how to solve this problem non-graphically and how to deal with the issue of non-uniqueness.

We show how to match the experimental data of 0.2 wt% IOS1518 at the transition foam quality ($f_g^t(\text{measured}) = 0.5$ and $\mu_{\text{foam,app}}^t(\text{measured}) = 421 \text{ cp}$) using the parameters listed in Table A1 as an example. If the solution exists, one can use the derivative method and the root-finding algorithm to solve Eqns (4.12) to (4.14). However, a modern strategy is to use search algorithms for finding minimum without deriving the derivative. Figure 4-17 shows the flow chart of our proposed non-graphical search method to fit experimentally measured f_g^t and

$$\mu_{\text{foam,app}}^t$$

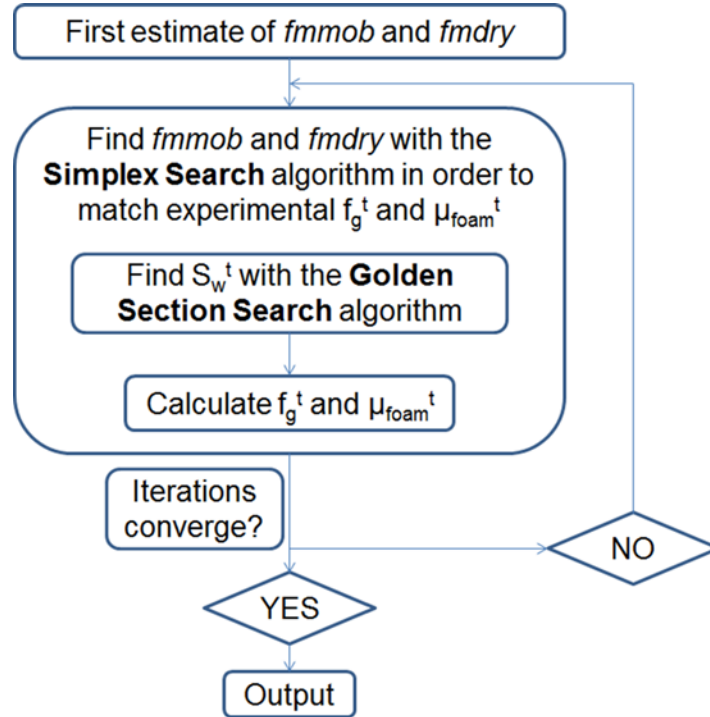


Figure 4-17. Flow chart of the non-graphical approach to match experimental data at the transition foam quality with a preset $epdry$.

As shown in Figure 4-17, this approach uses the simplex search method (the built-in function “fminsearch” in MATLAB (The MathWorks Inc 2012)) to find $fmmob$ and $fmdry$ and the golden section search method (the built-in function “fminbnd” in MATLAB (The MathWorks Inc 2012)) inside the simplex search loop to find S_w^t . The objective functions (Fun_1 and Fun_2) for minimization using the simplex search in the outer loop and the golden section search in the inner loop are shown in Eqns (4.16) and (4.17), respectively:

$$\begin{aligned} & \min Fun_1(fmmob, fmdry) \\ & = \left(\frac{\mu_{foam,app}^t - \mu_{foam,app}^t(measured)}{\mu_{foam,app}^t(measured)} \right)^2 + \left(\frac{f_g^t - f_g^t(measured)}{f_g^t(measured)} \right)^2 \end{aligned} \quad (4.16)$$

$$\min Fun_2(S_w) = -\mu_{foam,app}(S_w) \quad (4.17)$$

Using an initial guess of $fmmob = 10000$ and $fmdry = 0.1$, we obtain

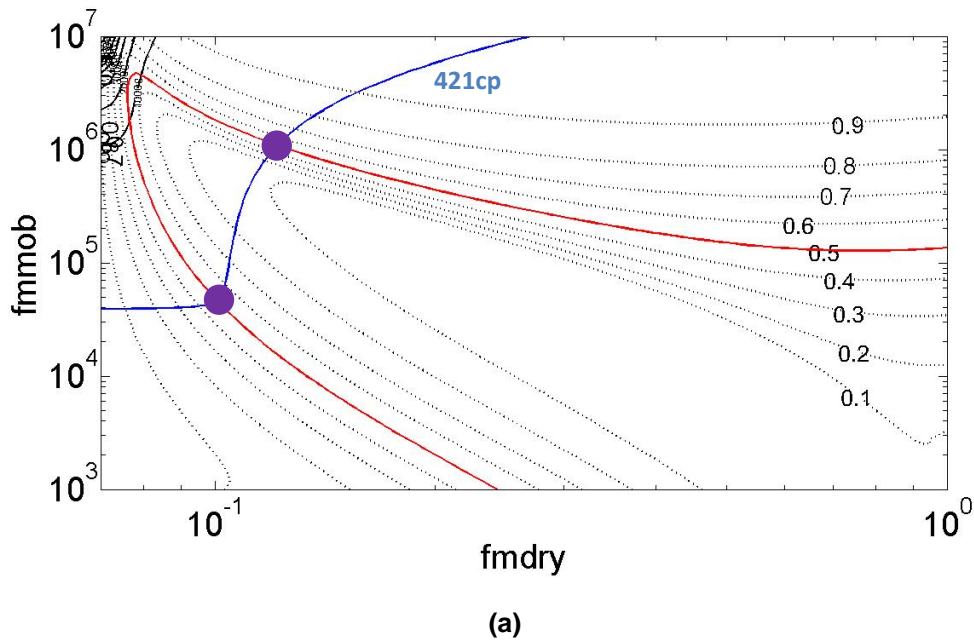
$fmmob = 47196$ and $fmdry = 0.1006$ with a preset $epdry$ of 500. This result is consistent with the solution obtained through the hybrid contour plot method in Section 4.2.2.2 if the difference in significant digits is considered.

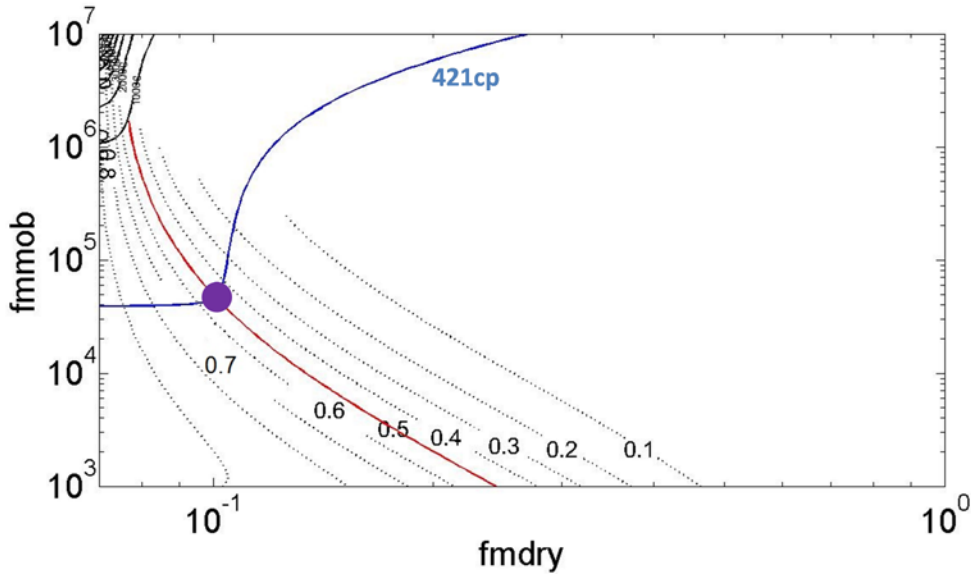
4.2.3.2 Strategy to handle the non-uniqueness problem

The success using the approach proposed in Section 4.2.3.1 highly depends on the initial guess of $fmmob$ and $fmdry$. For example, if we use an initial guess of $fmmob = 10^6$ and $fmdry = 0.1$, the algorithm ends up with a solution of $fmmob = 1.0897 \times 10^6$ and $fmdry = 0.1216$. This set of solution can also match the experimental data at the transition foam quality.

It is necessary to use the graphical method to investigate the existence and uniqueness of the solutions. As stated in Section 4.2.2.2, the solution can be found by superimposing the contour plots of the transition foam quality and the foam apparent viscosity (Ma, Lopez-Salinas et al.). However, only the value of 0.1006 for $fmdry$ was observed in our previous work due to the limited parameter domain which has been scanned. In Figure 4-18(a), we scan the

parameter domains for $fmmob$ over 4 orders of magnitude (10^3 to 10^7). Interestingly, the second solution is found as the contour of the transition foam quality (the red curve in Figure 4-18) forms a circuitous curve instead of a monotonic decreasing curve. These two pairs of solutions for $fmmob$ and $fmdry$, as indicated by the intersections between the blue curve and the red curve in Figure 4-18(a), are consistent with the finding in Figure 4-17 using the non-graphical method and appropriate starting values of the parameters.





(b)

Figure 4-18. Location of the roots which match transition foam data using the hybrid contour plot method on a log-log scale. (a) shows the parameter scan in the range of $10^3 < fmmob < 10^7$ and $0 < fmdry < 1$; (b) shows part of Figure 2(a) where $fmdry$ is smaller than S_w^t . The rest of the parameters are used as shown in Table 4-1 with a preset $epdry$ of 500. The purple dots in both figures indicate where $f_g^t = 0.5$ (the red curve) and $\mu_{foam,app}^t = 421 \text{ cp}$ (the blue curve) cross over.

In order to evaluate how well these two sets of solutions fit experiments, we compare them with experimental data in Figure 4-19. The red curve (model fit 1) using the solution which satisfies $fmdry < S_w^t$ well fits the experimental data, while the green curve (model fit 2) does not appear to fit the experiments. Moreover, the green curve indicates a foam apparent viscosity of over 250 cp even at 100% gas injection, which is physically unreasonable. Thus, this set of non-physical solution needs to be eliminated in the algorithm. In Figure 4-18(b) we only displays part of the hybrid contour plot which satisfies $fmdry < S_w^t$. The non-

physical solution shown in the green curve in Figure 4-19 is ruled out by limiting the solution to the one for which $fmdry < S_w^t$.

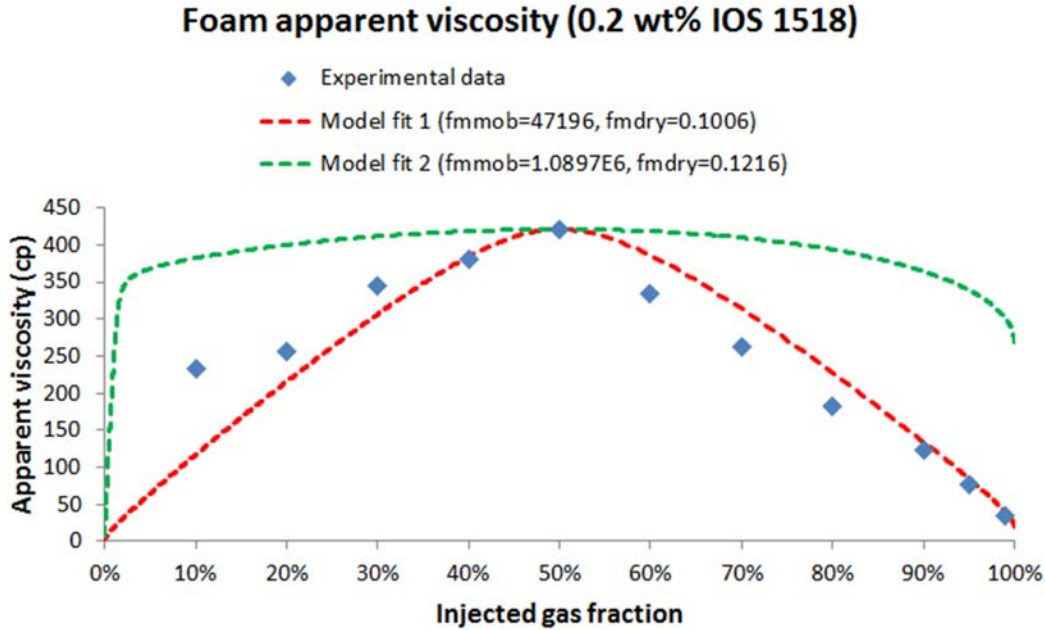
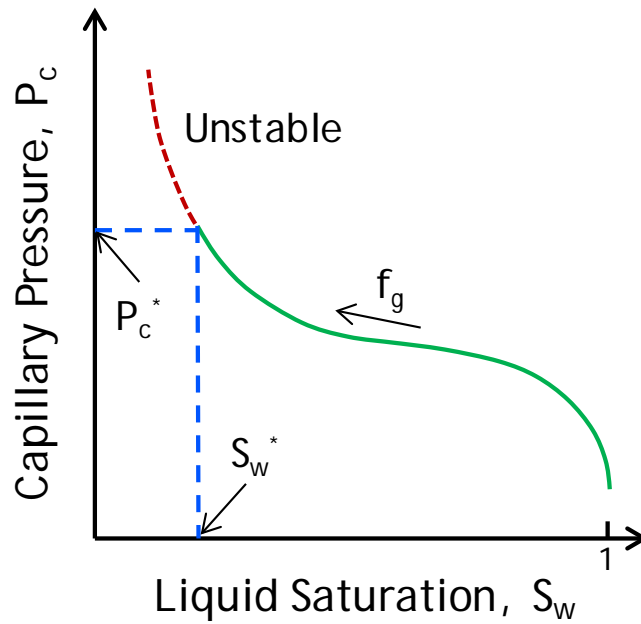


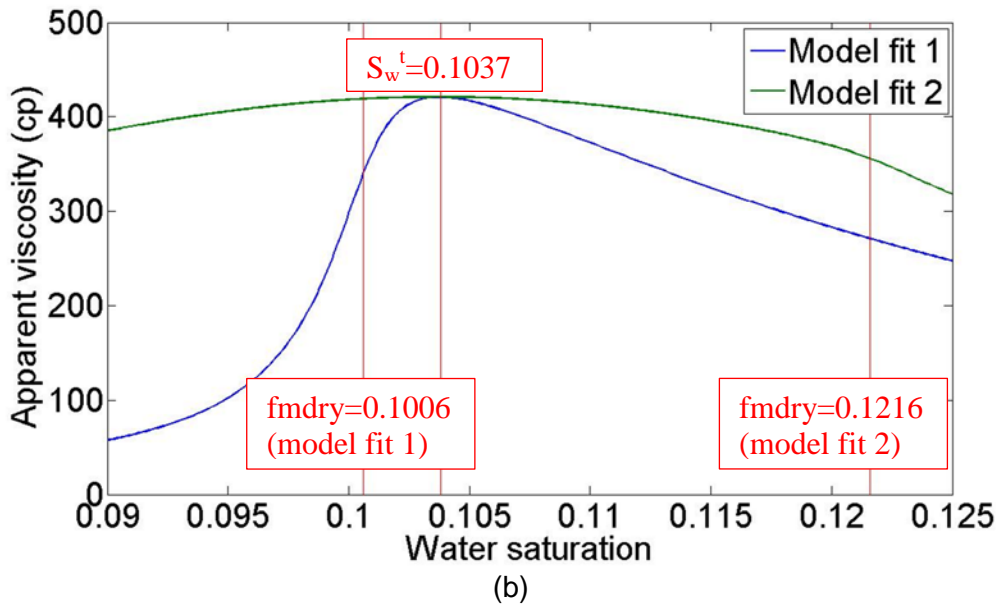
Figure 4-19. Comparison of model fit with experimental data using two sets of parameters found in Figure 4-18. The rest of the parameters are used as shown in Table 4-1 with a preset $epdry$ of 500. In “model fit 1”, $fmdry$ is smaller than S_w^t ; in “model fit 2”, $fmdry$ is larger than S_w^t .

The dry-out function in the STARSTM foam model is designed to describe the effect of the limiting capillary pressure (P_c^*) on foam stability (Cheng, Reme et al. 2000). As shown in Figure 4-20(a), P_c^* corresponds to a limiting water saturation (S_w^*) for a given system. S_w^* approaches both the transition water saturation (S_w^t) and the parameter $fmdry$ in the STARSTM foam model if a sufficiently large $epdry$ is used (Cheng, Reme et al. 2000). However, a smaller $epdry$ may be needed for matching transient (continuous gas injection) experiments as

indicated in Section 4.2.2.4. In this case, there is a substantial difference between f_{mdry} and S_w^t . Foam should not dry out in the low-quality regime (right-hand side of S_w^t in Figure 4-20(b)) as bubble trapping and mobilization rather than coalescence dominates foam stability. Therefore, one should pick the value of f_{mdry} in the high-quality regime (left-hand side of S_w^t in Figure 4-20(b)) and exclude the root in the low quality regime from this point of view.



(a)



(b)
Figure 4-20. Graphical illustration of S_w^* , S_w^t , and $fmdry$. (a) The concept of the limiting capillary pressure (P_c^*) and the limiting water saturation (S_w^*), adapted from literature (Khatib, Hirasaki et al. 1988; Farajzadeh, Andrianov et al. 2012); (b) Comparison of $\mu_{foam,app} - S_w$ curves in the vicinity of S_w^t between model fit 1 and 2.

4.2.4 Discussion on multi-variable multi-dimensional search

Multi-variable multi-dimensional search methods are considered as useful approaches to find an optimal set of multiple parameters. These techniques in general fall into two categories: unconstrained methods and constrained methods. The details of various optimization methods are available in the literature (Fletcher 1987; Aster, Thurber et al. 2005). If the goal of fitting foam parameters is to minimize the residual sum of squares for all available experimental data, the problem can be stated as:

$$\min f(fmmob, fmdry, epdry) = \sum_{i=1}^n \omega_i \left(\frac{\mu_{foam,i,calculated} - \mu_{foam,i,measured}}{\mu_{foam,i,measured}} \right)^2 \quad (4.18)$$

s.t. $fmmob > 0$, $S_{wc} \leq fmdry \leq 1 - S_{gr}$, and $epdry > 0$

where $\mu_{foam,i,calculated}$ is the calculated foam apparent viscosity at the corresponding gas fractional flow $f_{g,i,measured}$. The value of $\mu_{foam,i,calculated}$ is computed through Eqn (4.13) and the value of $\mu_{foam,i,measured}$ is taken from all experimental data, not just the transition value. A set of weighting parameters, , denoted as ω_i in Eqn (4.18), is usually employed to indicate expected standard deviation of each experimental point. In the following analysis we hypothesize that the weighting parameters are all equal to unity except for a value of 5 for the transition value ($\omega_i = 5$ when $\mu_{foam,i,measured} = \mu_{foam}^t$).

This problem is essentially a search for a constrained 3-variable optimization. If appropriate initial values are chosen, unconstrained optimization can be implemented to perform the search. The built-in simplex search function “fminsearch” in MATLAB begins with an initial estimate and attempt to finds a local minimum of a scalar function of several variables (The MathWorks Inc 2012). For a specific set of experimental data, we can estimate $fmmob$, $fmdry$, and $epdry$ simultaneously using this function. However, inappropriate initial values may lead to failure using the simplex search. For example, if we use an initial guess of ($fmmob = 1$, $fmdry = S_{wc}$ and $epdry = 1$) for matching all experimental data points in Figure 3, the unconstrained search provides a set of

non-physical results ($fmmob = 3018.9$, $fmdry = -81.67$ and $epdry = 316.5$) with a negative $fmdry$. In order to have a wider range of initial guesses applicable to search the global minimum, a feasible way to add the constraints to unconstrained optimization is to use the penalty function (Avriel 1976; Bazaraa, Sherali et al. 2006). We use the constraint $fmdry \geq S_{wc}$ as a penalty function and construct a new objective function in Eqn (4.19):

$$\min f(fmmob, fmdry, epdry) = \sum_{i=1}^n \omega_i \left(\frac{\mu_{foam,i,calculated} - \mu_{foam,i,measured}}{\mu_{foam,i,measured}} \right)^2 + (fmdry - S_{wc})^2 \cdot \Theta$$

$$\Theta = \begin{cases} 0, & \text{when } fmdry \geq S_{wc} \\ \sigma_k, & \text{when } fmdry < S_{wc} \end{cases} \quad (4.19)$$

In Eqn (4.19), Θ is the penalty function and σ_k is the penalty coefficient. Several iterations may be needed to implement the penalty function method if the solution does not converge quickly. The solution from the previous iteration is used as the initial guess and the penalty coefficient is increased in each iteration to solve the unconstrained problem (Avriel 1976; Bazaraa, Sherali et al. 2006). Specifically for the experimental data in Figure 4-19, we start with an initial guess of ($fmmob = 1$, $fmdry = S_{wc}$ and $epdry = 1$) and a penalty coefficient of $\sigma_k = 0.1$. The solution quickly converges to ($fmmob = 60873$, $fmdry = 0.1039$ and $epdry = 629.2$) using the “fminsearch” function in MATLAB without the need of increasing σ_k . The result is shown in Figure 4-21.

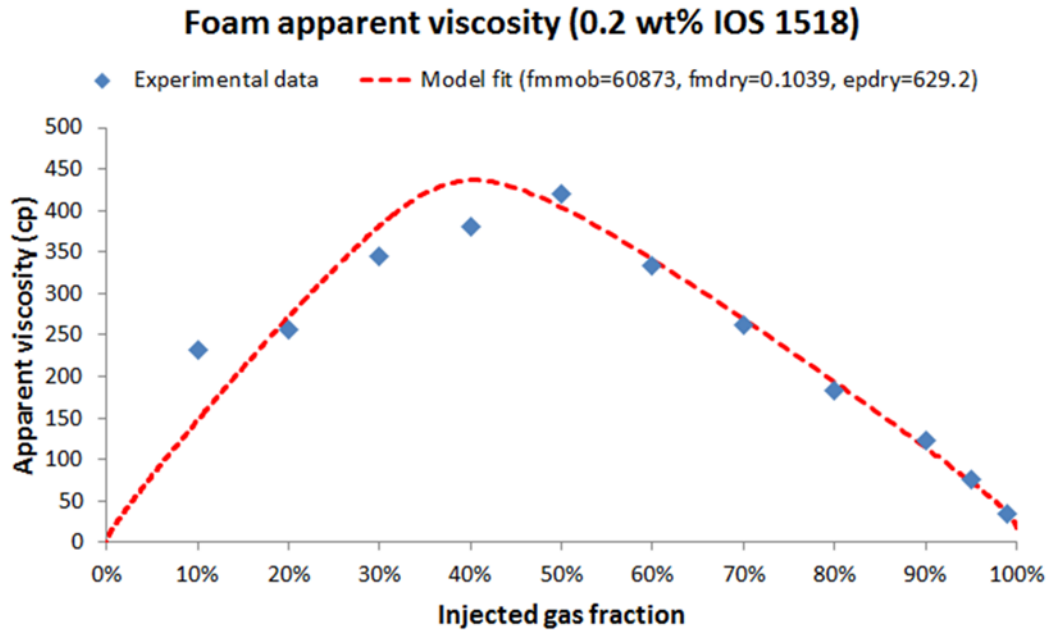


Figure 4-21. Comparison of model fit with experimental data using the multi-dimensional 3-parameter estimation. The rest of the parameters are used as shown in Table 4-1.

Compared with the 2-parameter model fit in Figure 4-19 which exactly fit the transition fractional flow and viscosity, this unconstrained optimization method provides a good fit to all the data points. However, this approach misses the fit to the transition foam quality (around 10% absolute error) as shown in Figure 4-21, which may be caused by assuming zero trapped gas saturation, i.e., $S_{gr} = 0$. A closer fit to the transition data is possible by giving more weight to the transition data during the fitting ($\omega_i > 5$ when $\mu_{foam,i,measured} = \mu_{foam}^t$). The finding of $epdry = 629.2$ indicates that a small value of $epdry$ (less than 1000) shows a good fit to this set of steady-state experimental data, which represents a gradual transition between the high-quality and the low-quality foam regime. The fitting

method focusing on the transition foam data in Section 4.2.3.1 is still valuable for a preliminary estimation of the parameters, as the strongest foam at the transient foam quality is possibly least affected by trapped gas, minimum pressure gradient and gravity segregation in 1-D experiments. These effects will be evaluated in the future and added to the model fit if they significantly affect the model fit. In general, the main challenge of using multi-variable multi-dimensional search is the possibility of reaching local minimum. This issue is especially significant when available experimental data points are not abundant and too many modeling parameters are used. To avoid this problem, one can choose an initial guess using the 2-parameter search method shown in Section 4.2.3.1 and add constraints to the searching algorithm as needed.

4.2.5 Numerical oscillation in transient foam simulation

It has been noted that $epdry$ should not be too large in order to have acceptable stability and run time in simulators using the finite difference algorithm (Cheng, Reme et al. 2000; Zanganeh, Kraaijevanger et al. 2012). In Figure 4-16, we simulated the transient foam process of continuous gas injection to 100% surfactant-solution-saturated porous media. Now we compare the result of finite difference simulation (FD) with the method of characteristics (MOC) and investigate how significant the numerical artifact is in the finite difference simulation. We discuss the case with the dry-out function in the foam model only. In order to compare the MOC solution with the FD simulation, we use the same

set of foam parameters ($fmmob = 47196$, $fmdry = 0.1006$ and $epdry = 500$) in the following computation. The rest of the parameters are listed in Table A1. The details of the MOC calculation are shown in the appendix. The FD algorithm with a standard IMPES (implicit in pressure and explicit in saturation) formulation is used to simulate the transient foam process in which 100% gas displaces 100% surfactant solution.

The local foam apparent viscosity ($\mu_{foam,app}$) and the average foam apparent viscosity ($\bar{\mu}_{foam,app}$) are defined in Eqns (4.20) and (4.21), respectively. $\mu_{foam,app}$ is a function of time and distance, which reflects the local normalized pressure gradient as foam advances in porous media. $\bar{\mu}_{foam,app}$ is a function of time, which reflects the averaged, overall normalized pressure gradient in the system. The methods for computing $\bar{\mu}_{foam,app}$ in MOC and FD simulation are shown in the appendix.

$$\mu_{foam,app} = \frac{1}{\frac{k_{rw}}{\mu_w} + \frac{k_{rg}^f}{\mu_g}} \quad (4.20)$$

$$\bar{\mu}_{foam,app} = -\frac{k(p_{out} - p_{in})}{(u_w + u_g)L} \quad (4.21)$$

Figure 4-22 shows the apparent viscosity history of the transient foam process in which 100% gas displaces 100% surfactant solution. According to Figure 4-22, these two methods are consistent with each other after gas

breakthrough where the foam starts drying out and the apparent viscosity decreases when time increases. However, the result using the FD simulation exhibits some oscillations before gas breakthrough. A zoom-in investigation reveals that this oscillation is periodic and the apparent viscosity is consistently overshoot compared with the result obtained with the MOC approach.

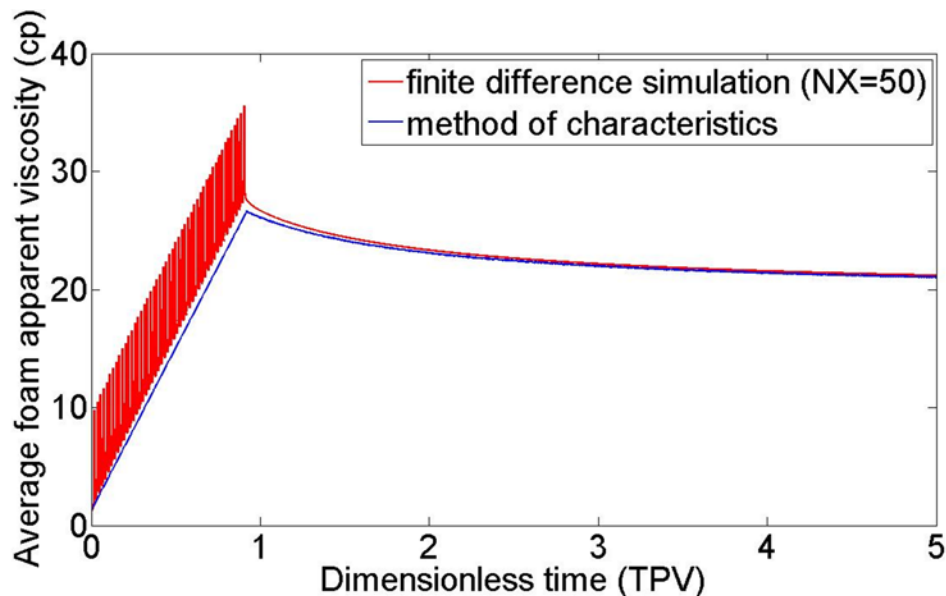


Figure 4-22. Comparison of foam apparent viscosity history between finite difference method and method of characteristics. $NX = 50$ and $\Delta t_D = 0.005 \Delta x_D$ (in finite difference simulation), $f_{mob} = 47094$, $f_{mdry} = 0.1006$ and $ep_{dry} = 500$. The rest of the parameters are used as shown in Table 4-1.

Figure 4-23(a) shows the zoom-in details in the periodic oscillation in the case shown in Figure 4-22 with a period of about 0.02 TPV. The saturation profiles at 0.5100 TPV and 0.5162 TPV are plotted in Figure 4-23(b) and (c), which represent small and large deviations of foam apparent viscosity history using the FD simulation from using MOC, respectively. The local foam apparent viscosity profiles at 0.5100 TPV and 0.5162 TPV are shown in Figure 4-23(d) and

(e), respectively. One can find that significant deviations of the FD solution from the MOC solution occur near the foam displacement front. The MOC solution assumes a discontinuous change in saturation across the front while the FD solution has intermediate values of saturation change. The gas saturation in the 28th grid block at 0.5162 TPV (Figure 4-23 (c)) is 0.8975 using the finite difference method, which is very close to the transition gas saturation ($S_g^t = 1 - S_w^t = 0.8963$) shown as a spike in Figure 4-23 (g). Therefore, a substantially higher local foam apparent viscosity results in the 28th grid block at 0.5162 TPV in Figure 4-23 (e). This fact leads to a pressure discontinuity at the foam displacement front in FD simulation. Figure 4-23 (f) shows the flow potential (dimensionless gas pressure, $\Phi_D = (p_g - p_g^{BC}) k k_{rg}^0 / u^{BC} \mu_g L$) at 0.5100 TPV and 0.5162 TPV, respectively. The flow potential at 0.5162 TPV shows a large discontinuity between the 28th and the 29th grid blocks, indicating an overshoot in pressure in the 28th grid block; while the flow potential at 0.5100 TPV does not indicate a significant overshooting issue.

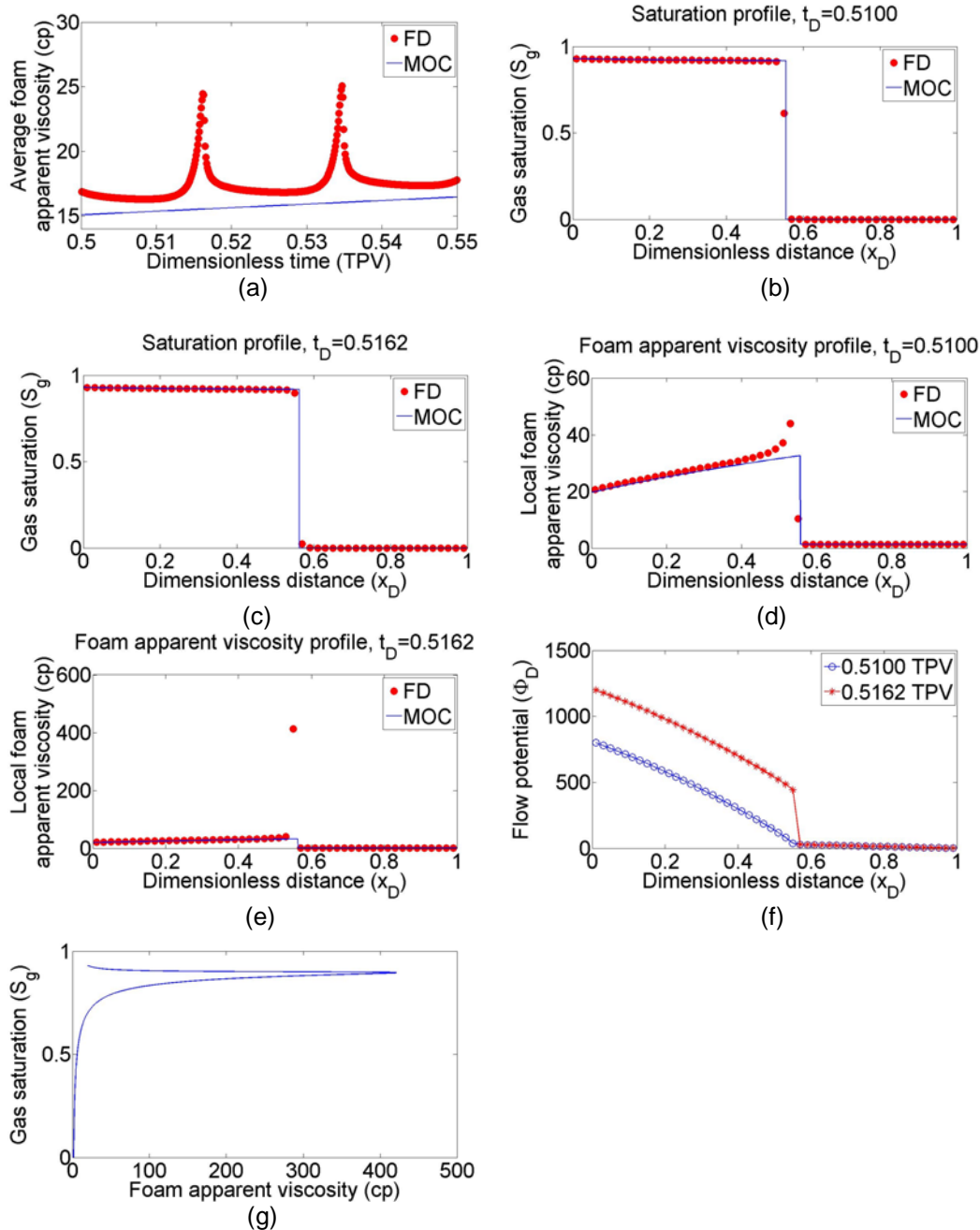


Figure 4-23. Investigation of numerical oscillation in FD simulation in which 100% gas displaces surfactant solution at 100% water saturation: (a) average foam apparent viscosity history from 0.50 to 0.55 TPV; (b) saturation profile at 0.5100 TPV; (c) saturation profile at 0.5162 TPV; (d) local foam apparent viscosity profile at 0.5100 TPV; (e) local foam apparent viscosity profile at 0.5162 TPV; (f) flow potential profiles at 0.5100 TPV and 0.5162 TPV; (g) the relationship between gas saturation and foam apparent viscosity. $NX = 50$, $\Delta t_D = 0.005 \Delta x_D$, $fmmob = 47196$, $fmdry = 0.1006$ and $epdry = 500$. The rest of the parameters are used as shown in Table 4-1.

In order to understand the main factors in finite difference simulation which contribute to this numerical artifact observed in Figure 4-22 and 4-23, we simulate five cases of the transient foam simulation in which 100% gas displaces 100% surfactant solution. The parameters that are altered among different cases are shown in Table 4-2 in bold.

Table 4-2. Parameters for the simulation of transient foam in Figure 4-24.

Parameter	Case 1	Case 2	Case 3	Case 4	Case 5
$\Delta t_D / \Delta x_D$	0.005	0.0005	0.005	0.005	0.005
NX	50	50	200	50	50
$epdry$	500	500	500	500	100
$fmmob$	47196	47196	47196	28479	69618
$fmdry$	0.1006	0.1006	0.1006	0.2473	0.1020
n_w	1.96	1.96	1.96	4.0	1.96

The foam modeling parameters in Table 1 are intended to fit the experimental data of $f_g^t = 0.5$ and $\mu_{foam,app}^t = 421 \text{ cp}$ as shown in Figure 8(a). The rest of the parameters are used as shown in Table A1.

Cases 1, 2 and 3 share the same set of foam modeling parameters. The parameter sets in all five cases in Table 4-2 exhibit good fit to steady-state data at the transition foam quality ($f_g^t = 0.5$ and $\mu_{foam,app}^t = 421 \text{ cp}$) as shown in Figure 4-24(a). Figure 4-24(b) shows the base case (Case 1) using a total grid block numbers of $NX = 50$ and a time step size of $\Delta t_D = 0.005\Delta x_D$, which is essentially the same as that in Figure 4-22. In Case 2 (Figure 4-24(c)) we decrease the time step size to 1/10 of the one in the base case, however, no significant change is

observed in the numerical oscillations. This result reveals that the IMPES simulator is numerically stable in terms of selection of time step size in the base case. The total grid blocks are increased to $NX = 200$ in Case 3 (Figure 4-24(d)) and significant reduction in the amplitude of numerical oscillation is observed compared with the base case. Also, it is observed that the frequency of the oscillation is proportional to the number of gridblocks. This observation indicates that an increase in total grid block numbers in the FD simulation leads to a better approximation to the solution using the MOC approach, at the cost of increasing computational time during the simulation. The reason behind this is that the contribution of the pressure drop in the grid block exactly at foam displacement front is smaller when the size of the grid block is smaller.

The parameters used in relative permeability curves and the foam modeling parameters also affects the numerical oscillation. They can change the shape of foam apparent viscosity as a function of saturation (Figure 4-23(g)), and a less sharp peak in Figure 4-23(g) will result a less significant oscillation. The increase in the exponent of the water relative permeability curve (Case 4, Figure 4-24(e)) from 1.96 to 4.0 does not help reduce numerical oscillation because the steady-state $\mu_{foam,app} - f_g$ curve in Case 4 does not differ much from that in Case 1 as shown in Figure 4-24(a). As indicated in Case 5 (Figure 4-24(f)), a decrease in $epdry$ causes a decrease in the amplitude of numerical oscillation in foam apparent viscosity history before gas breakthrough. This result indicates that a more gradual transition between the high-quality and low-quality regimes reduces numerical oscillation. Additionally, a weaker foam, which requires a smaller

$fmmob$, can also lead to a smaller amplitude in numerical oscillation. This is consistent with the practice of most foam simulation studies using a small $fmmob$ and a small $epdry$ in order to avoid numerical issues (Farajzadeh, Andrianov et al. 2012).

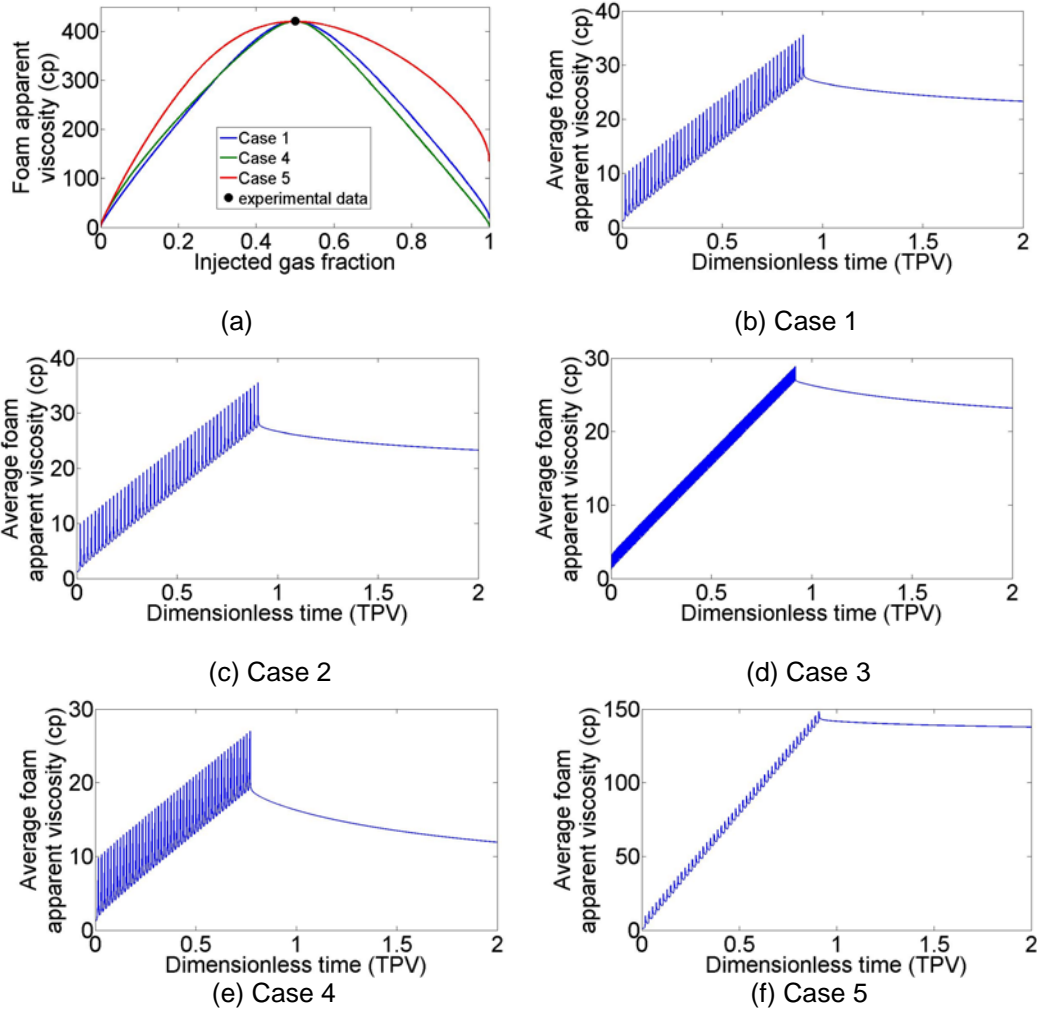


Figure 4-24. Investigations of factors which may affect numerical oscillation in the FD simulation of 100% gas displacing 100% surfactant solution. (a). Model fit to transition steady-state experimental data. (b) to (f). Transient simulation of Cases 1 to 5. The parameters in Cases 1 to 5 are listed in Table 4-2. The rest of the parameters are used as shown in Table 4-1.

Therefore, only strong foams with an abrupt transition between the high-quality and low-quality regimes may exhibit significant numerical oscillation. Since foam modeling parameters can be estimated by a combination of matching both steady-state and transient experiments, a practical way to minimize this numerical oscillation issue is to select an acceptable number of total grid blocks and a large time step which does not affect the numerical stability in the FD simulation. The crux to reduce the numerical oscillation in foam apparent viscosity history is to smear out the foam displacement front and to avoid the sharp change in local apparent viscosity at the foam front in the FD simulation.

4.2.6 Sensitivity of foam parameters

Parameters in the STARSTM foam model are sensitive to the estimation of the parameters which are used to model gas-water flow in porous media in the absence of foam. It was found that in general k_{rw} functions were more nonlinear for consolidated sandstones than for sandpacks and that an increase in the nonlinearity of k_{rw} could benefit the Surfactant-Alternating-Gas (SAG) process (Ashoori and Rossen 2012). It is important to recognize that one cannot apply the same set of foam parameters to different porous media without experimental verification. For example, the transition foam quality (f_g^t) was shown to decrease significantly when permeability decreased from a sandpack to a Berea core using the same surfactant formulation (Bio-Terge AS-40 surfactant supplied by Stepan,

a C14-16 sodium α -olefin sulfonate) (Alvarez, Rivas et al. 2001). In order to demonstrate the sensitivity of foam modeling parameters with respect to two-phase flow parameters, we match the experimental data ($f_g^t(measured) = 0.5$ and $\mu_{foam,app}^t(measured) = 421 \text{ cp}$) using the dry-out function in the STARSTM foam model with changes in the parameters of the exponent in the k_{rw} function (n_w) and connate water saturation (S_{wc}^t) shown in Figure 4-25 and 4-26.

The nonlinearity of the k_{rw} function is controlled by the exponent n_w as shown in Figure 4-25(a). An increase in n_w leads to a more curved k_{rw} curve. It is found that the experimental data ($f_g^t(measured) = 0.5$ and $\mu_{foam,app}^t(measured) = 421 \text{ cp}$) in Figure 4-25(b) cannot be fit with the STARSTM foam model if n_w is equal to 1. We fit the experimental data at the transition foam quality using values of n_w from 1.5 to 4.0. The model fit appears similar in the low-quality regime and distinguishable differences in the high-quality-regime with higher predicted apparent viscosity using lower value of n_w . Moreover, Figure 4-25(c) and (d) show strong dependence of the foam modeling parameters $fmmob$ and $fmdry$ on the exponent n_w of the k_{rw} curve with a preset $epdry$ of 500. $fmmob$ decreases by about one-half when n_w increases from 1.5 to 4.0, while $fmdry$ increases significantly with n_w . As the transition water saturation S_w^t is

designed to be slightly larger than $fmdry$, it also increases with n_w (Figure not shown).

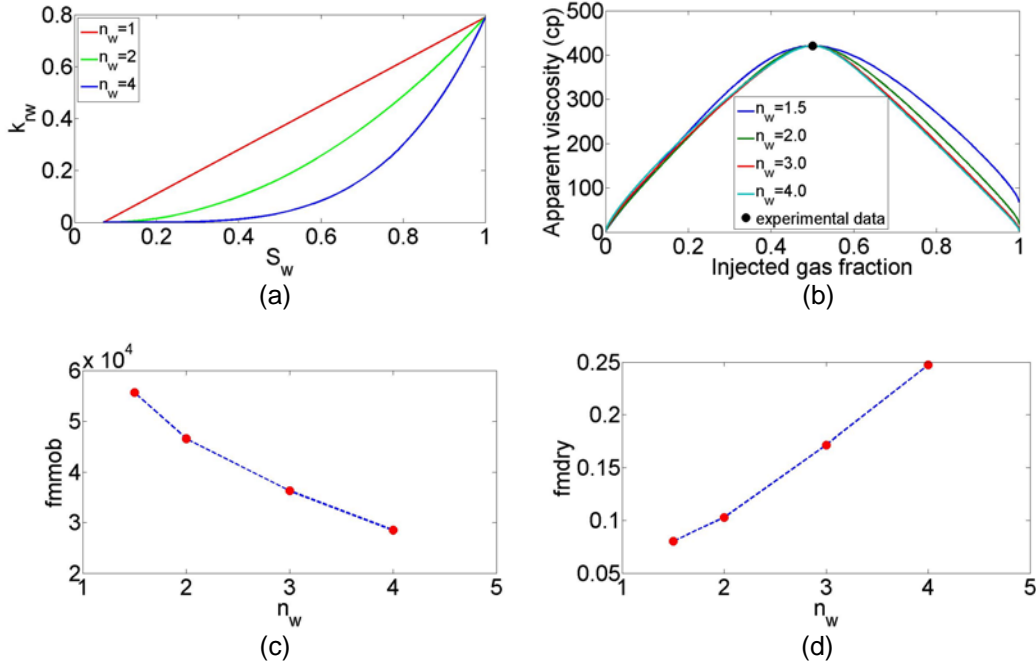


Figure 4-25. The influence of changing the exponent n_w in the k_{rw} function on foam modeling parameters. The rest of the parameters are used as shown in Table 4-1 with a preset $epdry$ of 500. (a) The k_{rw} curve with different exponent n_w ; (b) model fit to the steady-state transition foam data with different exponent n_w ; (c) change of $fmmob$ with the exponent n_w in the model fit of Figure 4-25(b); (d) change of $fmdry$ with the exponent n_w in the model fit of Figure 4-25(b).

The connate water saturation S_{wc} is another important parameter that can affect the estimation of foam modeling parameters. Figure 4-26(a) shows indistinguishable model fit to experimental data using different values of S_{wc} (0.05, 0.10, and 0.15). The influence of S_{wc} on $fmmob$ is weak as shown in Figure 4-26(c), however, S_{wc} significantly affects the estimation of $fmdry$ and a quasilinear

monotonic increasing relationship with a slope close to 1 in observed Figure 4-26(d). The way to estimate S_{wc} in the presence of foam is to match experimental measured fractional flow curve (Figure 4-26(b)) as discussed in Section 4.2.2.3.

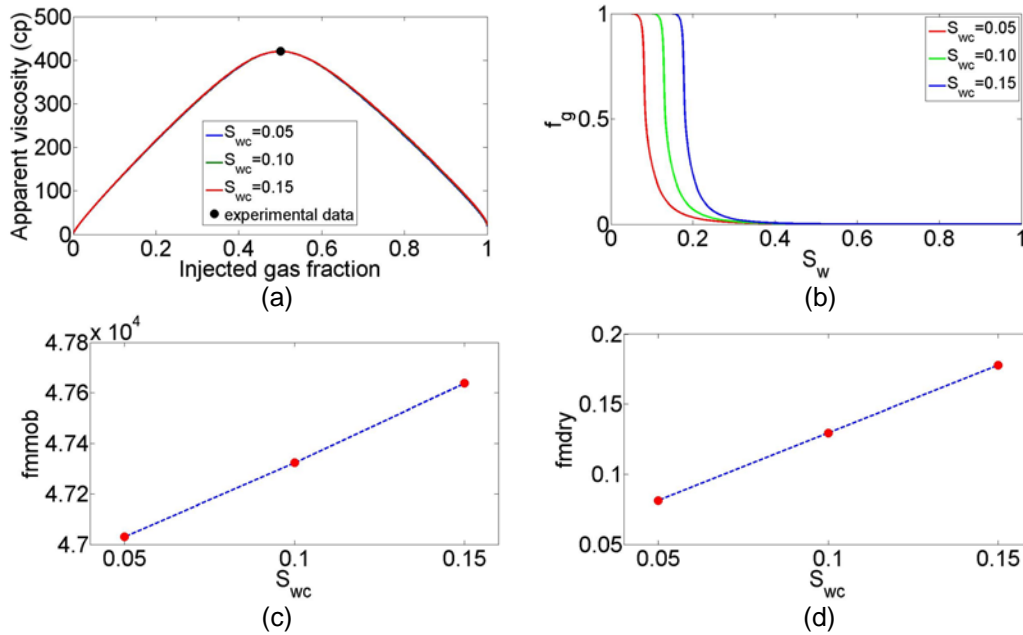


Figure 4-26. The influence of changing the connate water saturation S_{wc} on foam modeling parameters. The rest of the parameters are used as shown in Table 4-1 with a preset $epdry$ of 500. (a) Model fit to the steady-state transition foam data with different S_{wc} ; (b) fractional flow curve with different S_{wc} ; (c) change of f_{mmob} with S_{wc} in the model fit of Figure 4-26(a); (d) change of f_{mdry} with S_{wc} in the model fit of Figure 4-26(a).

In Section 4.2.2.4 we showed a wide range of $epdry$ could be used to estimate f_{mmob} and f_{mdry} at the transition foam quality in steady-state experiments. We verify the results here in Figure 4-27 with the numerical method proposed in Figure 4-17 and show the parameter sensitivity to $epdry$. Figure 4-

27(a) showed that different preset $epdry$ ranging from 500 to 500,000 can fit the transition experimental data using the non-graphical approach proposed in Figure 4-17. $fmmob$ decreases when $epdry$ increases (Figure 11(b)) till $fmmob$ approaches a plateau value, while $fmdry$ only exhibits a subtle change in the third significant digit in response to $epdry$ (Figure 4-27(b)). This is because $fmdry$ asymptotically approaches S_w^t when $epdry$ is sufficiently large, while S_w^t is independent of $epdry$. In the case of $f_g^t = 0.5$ and $\mu_{foam,app}^t = 421 \text{ cp}$.

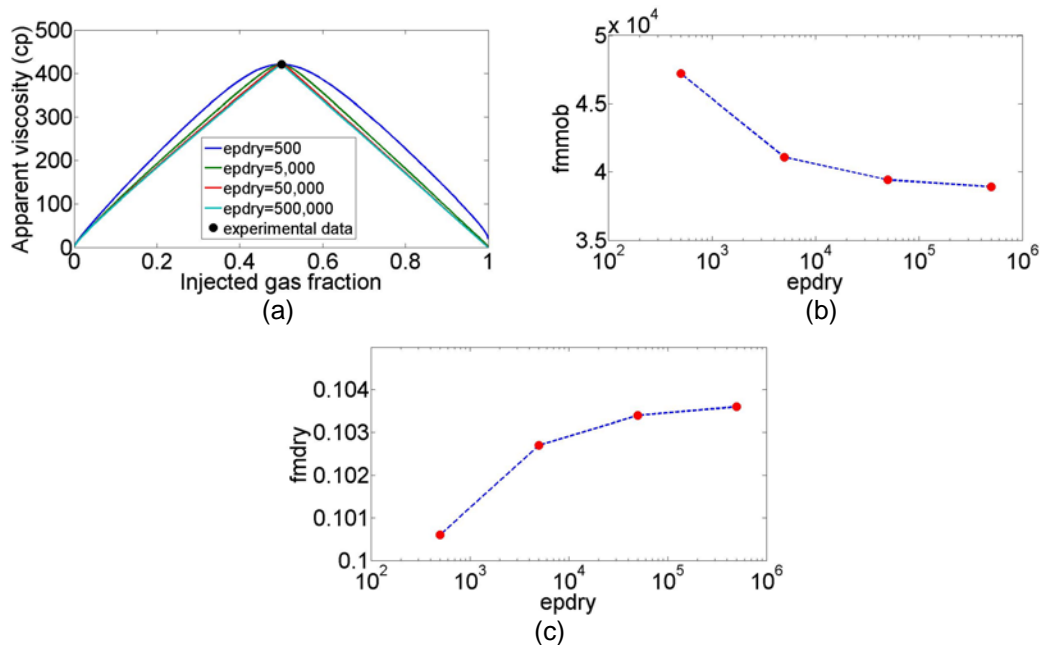


Figure 4-27. The influence of changing the parameter $epdry$ on other foam modeling parameters. The rest of the parameters are used as shown in Table 4-1. (a) Model fit to the steady-state transition foam data with different $epdry$; (b) change of $fmmob$ with $epdry$ in the model fit of Figure 4-27(a); (c) change of $fmdry$ with $epdry$ in the model fit of Figure 4-27(a).

4.3 Conclusions

In summary, we propose a facile approach to obtain the parameters in the STARS™ foam model for foam simulation. Two systems with different experimental conditions are successfully modeled using the proposed technique. This approach estimates the parameters $fmmob$ and $fmdry$ by matching the transition foam apparent viscosity ($\mu_{foam,app}^t$) at the transition foam quality (f_g^t). The parameter $epdry$ is estimated by examining the fit to the rest of the steady-state data and the transient experiment with continuous gas injection. To achieve a better accuracy of model fit at the transition foam quality, the difference between the foam model parameter $fmdry$ and the transition water saturation S_w^t is identified and a method to precisely calculate S_w^t is developed. The difference between $fmdry$ and S_w^t becomes large when $epdry$ becomes small, which corresponds to a more gradual transition between the high-quality foam regime and the low-quality foam regime. We show how a different preset $epdry$ leads to different $fmmob$ and $fmdry$ for fitting a set of steady-state experimental data using the proposed approach. For the 0.2 wt% IOS1518 system, we demonstrate that an additional transient experiment with continuous gas injection is necessary to narrow down the range for $epdry$. The combination of steady-state and transient experiments may lead to an estimation of a unique set of parameters in the dry-out foam model.

For a preset $epdry$, it is found that two pairs of values of $fmmob$ and $fmdry$ can sometimes match steady-state f_g^t and $\mu_{foam,app}^t$. By applying the constraint $fmdry < S_w^t$ one can rule out the solution which does not match the rest of experimental data points.

To match all available data points using multi-dimensional multi-variable search, one can use the unconstrained optimization approach with an appropriate initial guess which is close to the global optimum. The penalty function method for constrained optimization can be applied for a wider range of initial guesses.

Finite difference simulation for the transient foam process is generally consistent with the method of characteristics. A less abrupt change in foam mobility in the foam displacement front is needed to minimize the numerical oscillation in the average foam apparent viscosity history. Small $epdry$ leads to lower amplitude in numerical oscillation and larger apparent viscosity when foam breaks through.

Foam parameters are sensitive to the parameters in relative permeability curves. For foam parameter estimation by matching steady-state f_g^t and $\mu_{foam,app}^t$, the water relative permeability exponent n_w affects the estimation of both $fmmob$ and $fmdry$, and the connate water saturation S_{wc} is particularly influential in estimating $fmdry$. An increase in $epdry$ causes a decrease in $fmmob$, but no substantial change is found in $fmdry$.

4.4 References

- Alvarez, J. M., H. J. Rivas, et al. (2001). "Unified model for steady-state foam behavior at high and low foam qualities." SPE Journal **6**(3): 325-333.
- Ashoori, E. and W. R. Rossen (2012). "Can Formation Relative Permeabilities Rule Out a Foam EOR Process?" SPE Journal **17**(2): 340-351.
- Ashoori, E., T. L. M. van der Heijden, et al. (2010). "Fractional-flow theory of foam displacements with oil." SPE Journal **15**(2): 260-273.
- Aster, R. C., C. H. Thurber, et al. (2005). Parameter estimation and inverse problems. Amsterdam ; Boston, Elsevier Academic Press.
- Avriel, M. (1976). Nonlinear programming : analysis and methods. Englewood Cliffs, Prentice-Hall.
- Bazaraa, M. S., H. D. Sherali, et al. (2006). Nonlinear programming : theory and algorithms. New York, NY ; Chichester, Wiley.
- Bertin, H. J., M. Y. Quintard, et al. (1998). "Development of a bubble-population correlation for foam-flow modeling in porous media." SPE Journal **3**(4): 356-362.
- Bruges, E. A., B. Latto, et al. (1966). "New correlations and tables of coefficient of viscosity of water and steam up to 1000 bar and 1000 degrees C." International Journal of Heat and Mass Transfer **9**(5): 465-480.
- Cheng, L., A. B. Reme, et al. (2000). Simulating foam processes at high and low foam qualities. SPE/DOE Improved Oil Recovery Symposium (SPE 59287). Tulsa, Oklahoma.
- Computer Modeling Group (2007). "STARSTM user's guide." Calgary, Alberta, Canada.
- Du, D. X., A. N. Beni, et al. (2008). "Effect of water solubility on carbon dioxide foam flow in porous media: An X-ray computed tomography study." Industrial & Engineering Chemistry Research **47**(16): 6298-6306.
- Falls, A. H., G. J. Hirasaki, et al. (1988). "Development of a mechanistic foam simulator: the population balance and generation by snap-Off." SPE Reservoir Engineering **3**(3): 884-892.
- Falls, A. H., J. J. Musters, et al. (1989). "The Apparent Viscosity of Foams in Homogeneous Bead Packs." SPE Reservoir Engineering **4**(2): 155-164.
- Farajzadeh, R., A. Andrianov, et al. (2009). "Comparative Study of CO₂ and N₂ Foams in Porous Media at Low and High Pressure-Temperatures." Industrial & Engineering Chemistry Research **48**(9): 4542-4552.
- Farajzadeh, R., A. Andrianov, et al. (2012). "Foam-oil interaction in porous media: Implications for foam assisted enhanced oil recovery." Advances in Colloid and Interface Science **183**: 1-13.
- Farajzadeh, R., B. M. Wassing, et al. (2012). "Foam assisted gas-oil gravity drainage in naturally-fractured reservoirs." Journal of Petroleum Science and Engineering **94-95**: 112-122.
- Fletcher, R. (1987). Practical methods of optimization. Chichester ; New York, Wiley.
- Kam, S. I., Q. P. Nguyen, et al. (2007). "Dynamic simulations with an improved model for foam generation." SPE Journal **12**(1): 35-48.

- Kam, S. I. and W. R. Rossen (2003). "A model for foam generation in homogeneous media." SPE Journal **8**(4): 417-425.
- Khatib, Z. I., G. J. Hirasaki, et al. (1988). "Effects of capillary pressure on coalescence and phase mobilities in foams flowing through porous media." SPE Reservoir Engineering **3**(3): 919-926.
- Kovscek, A. R., T. W. Patzek, et al. (1995). "A Mechanistic Population Balance Model for Transient and Steady-State Foam Flow in Boise Sandstone." Chemical Engineering Science **50**(23): 3783-3799.
- Lemmon, E. W. and R. T. Jacobsen (2004). "Viscosity and thermal conductivity equations for nitrogen, oxygen, argon, and air." International Journal of Thermophysics **25**(1): 21-69.
- Lopez-Salinas, J. L. (2012). Transport of Components and Phases in Surfactant/Foam EOR Process for a Giant Carbonate Reservoir. PhD Thesis, Rice University.
- Ma, K., J. L. Lopez-Salinas, et al. "Estimation of parameters for the simulation of foam flow through porous media: Part 1; the dry-out effect." Energy & Fuels: Submitted.
- Myers, T. J. and C. J. Radke (2000). "Transient foam displacement in the presence of residual oil: Experiment and simulation using a population-balance model." Industrial & Engineering Chemistry Research **39**(8): 2725-2741.
- Osterloh, W. T. and M. J. Jante Jr (1992). Effects of gas and liquid velocity on steady-state foam flow at high temperature. SPE/DOE Enhanced Oil Recovery Symposium (SPE 24179). Tulsa, Oklahoma.
- Patzek, T. W. (1988). "Description of foam flow in porous media by the population balance method." Acs Symposium Series **373**: 326-341.
- Renkema, W. J. and W. R. Rossen (2007). Success of foam SAG processes in heterogeneous reservoirs. SPE Annual Technical Conference and Exhibition (SPE 110408). Anaheim, California, U.S.A.
- The MathWorks Inc (2012). "MATLAB User's Guide." Natick, MA, USA.
- Zanganeh, M. N., S. I. Kam, et al. (2011). "The method of characteristics applied to oil displacement by foam." SPE Journal **16**(1): 8-23.
- Zanganeh, M. N., J. F. B. M. Kraaijevanger, et al. (2012). Adjoint-Based Optimization of a Foam EOR Process. 13th European Conference on the Mathematics of Oil Recovery. Biarritz, France.

Visualization of foam transport in microchannels and micromodels of heterogeneous porous media

This chapter presents the understanding of foam transport at the pore-level using micromodels. The use of micromodels to visualize foam transport is a good approach to understand the mechanism of in situ foam generation and fluid diversion (Jeong and Corapcioglu 2003; Kavscek, Tang et al. 2007; Rossen 2008; Li, Hirasaki et al. 2012). In this study, a novel method to precisely control the wettability of micromodel surface was developed. We utilize this method to investigate the effect of wettability on gas bubble break-up in microfluidic flow-focusing geometry. We also demonstrate the improved sweep efficiency by foam in heterogeneous 2-D porous media containing varying permeability while maintaining the same porosity.

5.1 Wettability control in microfluidic devices

5.1.1 Materials and methods

5.1.1.1 Fabrication of microfluidic devices

The channel pattern for the micromodel is designed using AutoCAD. The porous medium typically consists of a 4000 μm (length) \times 3520 μm (width)

rectangular reservoir with a quadrilateral network of cylindrical pillars with a radius of 150 μm aligned at a distance of 60 μm . For wettability patterning purpose, this porous medium is divided into the upper half and the bottom half, and the fluid inlet is designed in the middle of the two halves with a channel width of 200 μm . Two 200 μm wide fluid outlets are designed at the upper and lower right corners of the porous medium. Based on the designed geometry, the overall porosity of this porous medium is 45.0%.

The microfluidic devices are fabricated with standard soft lithography techniques (Xia and Whitesides 1998; Kini, Lai et al. 2010) as described below. A 4-inch silicon wafer (University Wafer) is used as a substrate and cleaned with IPA (Sigma Aldrich), followed by a DI water rinse. To dehydrate the surface, the substrate is baked at 200 $^{\circ}\text{C}$ for 5 min on a hotplate. The SU-8 50 photoresist (Microchem Corporation) is spin coated onto a 4" silicon wafer (University Wafer) with a spin coater (Headway Research Inc.) at 2000 rpm for 30 sec. The substrate is pre-baked on a hot plate at 95 $^{\circ}\text{C}$ for 20 min before exposure. An SF-100 maskless lithography tool (Intelligent Micro Patterning, LLC) is used to expose the photoresist with the desired pattern. After exposure, a post-exposure bake is performed at 95 $^{\circ}\text{C}$ for 5 min. The substrate is subsequently developed in SU-8 developer (Microchem Corporation) for 6 min at room temperature, which results in a positive microfluidic pattern relief on the substrate. A pattern thickness of 75 μm is determined by a Dektak 6M profilometer (Veeco Instruments), which is the resulting height of the PDMS porous medium.

To fabricate the microfluidic device, a poly(dimethylsiloxane) (PDMS) elastomer kit (Sylgard 184; Dow Corning Corp) is used. The kit consists of a liquid silicon elastomer base (vinyl-terminated PDMS) and a curing agent (mixture of a platinum complex and copolymers of methylhydrosiloxane and dimethylsiloxane) that are combined in a 10:1 ratio and poured onto the silicon master in a Petri dish. The wafer and PDMS are degassed under vacuum for 20 min and cured at 80 °C in a convective oven. The curing time varies from 0.5 hour to 24 hours. After curing, the patterned PDMS is removed from the silicon master and inlet and outlet holes are punched into the PDMS using a cork borer. To pattern the wettability of the surface, the patterned PDMS is treated with UV-ozone (Novascan Technologies, Inc.) prior to bonding. As reported by the manufacturer, a low-pressure mercury vapor lamp with an output of 20 mW/cm² at a distance of 25 mm is used in the UV-ozone instrument. A photomask is used to shield part of the microfluidic pattern from UV light (Figure 5-1). Our alignment tool (ATS115 motion controller, Aerotech, Inc.) is able to achieve a resolution of 5 μm in the patterning process. The area masked by the black regions is shielded from the UV-ozone and remains hydrophobic after UV-ozone exposure, while the unmasked region alters its wettability depending on the time of UV-ozone exposure. Finally, the patterned PDMS piece is placed in an UV-ozone chamber for an additional 5 minutes and then immediately brought into contact with a blank (featureless) PDMS that has been processed with the same conditions. Note that the 5 minute UV-ozone treatment used for bonding is not long enough

to significantly alter the wettability of the PDMS. After sealing, the microfluidic device is immediately saturated with DI water prior to experiments.

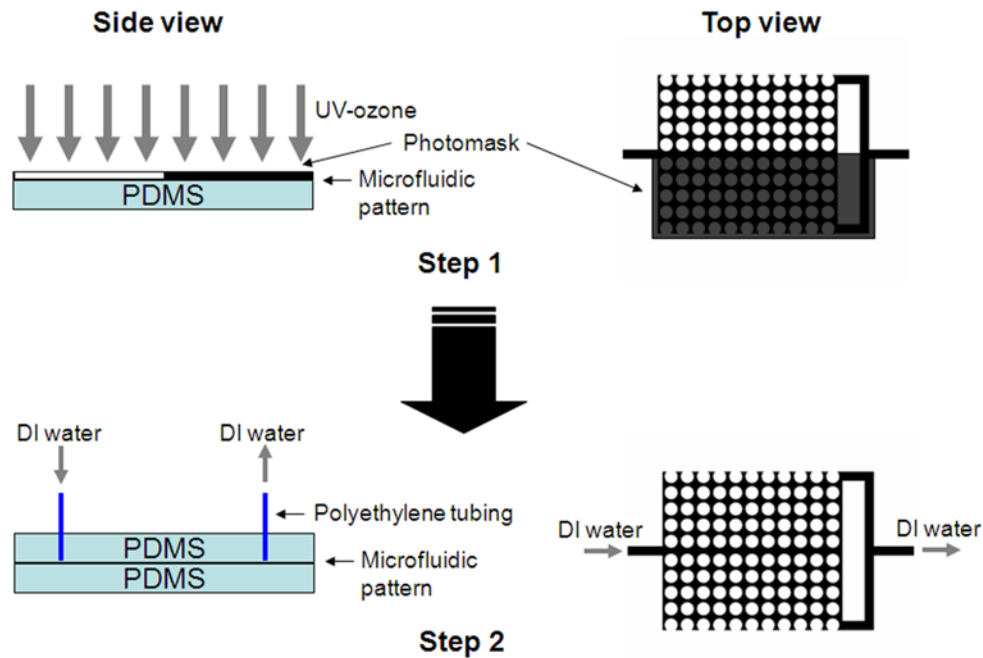


Figure 5-1. Schematic of the two-step process of wettability control for microfluidic devices. Step 1: UV-ozone treatment with a photomask to selectively expose the surface of PDMS; Step 2: bond the microfluidic device and fill it with DI water to maintain the wettability.

5.1.1.2 Apparatus for evaluating wettability patterning

The effect of surface wettability is tested by observing how well gas displaces a dye solution from the porous media. The microfluidic device is placed on the stage of an inverted microscope (Olympus IX 71). To saturate the porous media with water, a syringe pump (Harvard Apparatus PHD 2000) is used at the outflow end to pull out the fluid. After a 48-hour water immersion, a 3.0 wt%

aqueous dye solution (ESCO Foods Inc.) is injected into the microfluidic device until the color of aqueous phase in the porous medium is homogeneous. Then air is injected at a volumetric flow rate of 1.0 ml/hr into the system. A CCD camera (Phantom V4.3, Vision Research, Inc.) is used to record the flow patterns that emerge once the gas thread enters the porous medium.

5.1.1.3 Monitoring Surface Wettability

To determine the surface wettability inside the microfluidic device, an unpatterned PDMS is treated with the same conditions, including UV-ozone oxidation (with or without the photomask) and water immersion, as the patterned PDMS. The thickness of all PDMS pieces in this study is controlled uniformly at 2.8 ± 0.2 mm. The water static contact angle of the unpatterned piece of PDMS is measured by the sessile drop method with a KSV CAM 200 contact angle and surface tension meter (KSV Instruments Ltd.). All the experimental data of contact angles are acquired by three repeated measurements. There is no significant difference of static contact angle on PDMS between DI water and the diluted dye solution used in our experiments.

5.1.2 Results and discussions

5.1.2.1 Wettability patterning

Table 5-1. Wettability of the microfluidic devices shown in Figure 5-2

Microfluidic device	Water static contact angle (°)		Graph	Remarks
	Upper half	Bottom half		
A	7.5	96.7	Figure 2(a)	wettability-patterned device
B	7.5	7.5	Figure 2(b)	hydrophilic device

Table 5-1 shows the wettability of two microfluidic devices used in this study. In both devices, the PDMS is subject to 1-hour curing and 4-hour UV-ozone treatment. In Device A, the upper half is exposed to UV-ozone and made hydrophilic with a water contact angle of 7.5° while and the bottom half is masked and kept hydrophobic with a water contact angle of 96.7°. As a control, Device B, is exposed completely and has a uniform hydrophilic surface with a static water contact angle of 7.5°.

Both devices are primed with DI water for 48 hours, and saturated with dye solution before air injection, as shown in Figure 5-2. After air injection, in Device A, the dye solution is displaced only in part of the hydrophobic half, while the hydrophilic half remains saturated with dye solution. Figure 5-2(a) shows the saturation snapshot after a 2-min air injection. In comparison, air displaces the dye solution without discrimination in Device B, due to the homogeneous wettability condition. In both devices, after air breaks through the outflow end and forms a continuous gas channel, the saturation snapshot remains unchanged.

In the control sample (Device B), the wettability is homogeneous and the air penetrates through the porous media in both halves initially. As the gas thread

continues displacing the liquid, the gas will choose the path with the least resistance until it reaches one of the outlets. After gas breakthrough, the newly injected air will preferentially follow the path of the continuous gas channel, making it difficult to breakthrough another outlet as shown in Figure 5-2(b). Repeated experiments show that, in a random manner, the air will always choose one outlet to breakthrough while the other outlet remains filled with dye solution, leading to an asymmetric flow path.

In porous media, the capillary pressure across the interface of air and dye solution can be described with the Young–Laplace equation:

$$P_{capillary} = \frac{2\sigma \cos \theta}{r} \quad (5.1)$$

where r is the characteristic radius of the pore throat, σ is the interfacial tension between the two phases, and θ is the static contact angle of the aqueous phase. In our case, since there is no significant difference of static contact angles on PDMS between DI water and the dye solution, we describe the wettability in terms of water static contact angle. According to Eqn (5.1), a smaller water contact angle leads to larger value of capillary pressure, which creates larger barrier for air to displace dye solution in the hydrophilic region given the same size of pore throats. Therefore, in Figure 5-2(a) the dye solution is preferentially displaced the hydrophobic half in the porous medium. In contrast, in Figure 2(b) the capillary pressure is uniform for both halves, and the injected air permeates through both halves of the device.

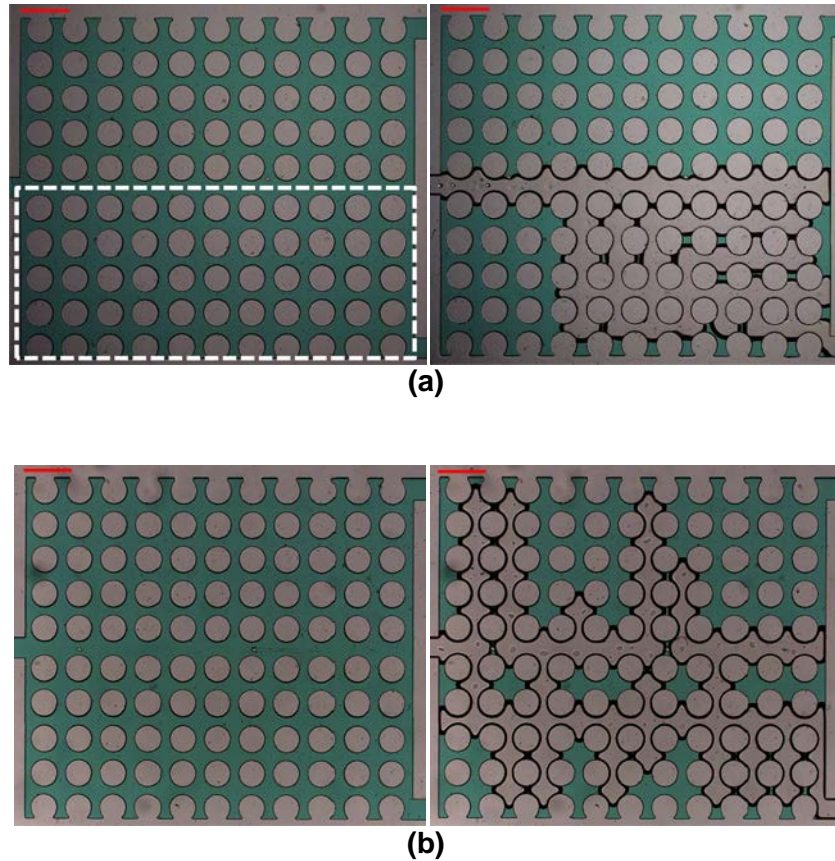


Figure 5-2. The effect of patterned wettability on displacement efficiency of aqueous dye solution by air in homogeneous porous media. Left: initially saturated with dye solution; Right: after 2 min air injection at a volumetric flow rate of 1.0 ml/hr. The red scale bar at the upper left corner represents 500 μm . The wettability conditions for both devices are shown in Table 5-1. (a) Top view of the porous medium in Device A. The masked area is indicated in a white dashed box. (b) Top view of the porous medium in Device B.

The experimental results shown in Figure 5-2 demonstrate that the wettability of PDMS can be successfully patterned in microfluidic devices with the proposed approach.

5.1.2.2 Effect of curing time on surface modification by UV-ozone

In order to precisely tune the wettability of PDMS surface, an understanding of how curing time influences the PDMS surface is necessary. After exposure to

UV-ozone or oxygen plasma, oxidized PDMS surfaces gradually recover their hydrophobicity with time, mainly because low molecular weight (LMW) species in the PDMS move from bulk to the surface causing the generated hydrophilic groups to migrate into the bulk PDMS to achieve a new equilibrium. Thermal curing can eliminate low molecular weight (LMW) species in PDMS thereby reducing the rate of hydrophobic recovery of plasma-treated hydrophilic PDMS surface (Eddington, Puccinelli et al. 2006). Moreover, we demonstrate that additional curing time can also accelerate the surface hydrophilization process of PDMS. As shown in Figure 5-3 for a fixed curing temperature of 80 °C, the static water contact angle at varying UV-ozone exposure times varies with curing time. In the first hour after UV-ozone treatment, there is little difference in the water contact angle for the PDMS cured for various times except for the one with 0.5-hour curing. The differences emerge after the one hour UV-ozone exposure, where PDMS pieces with longer curing times exhibit a faster surface hydrophilization process. The UV-ozone oxidation process, which makes the PDMS surface hydrophilic, competes with the migration of LMW species towards the surface, which makes it hydrophobic. Thus, the existence of large amount of LMW species weakens the efficiency of UV-ozone oxidation. Meanwhile, when the curing time is extended from 3 days to 7 days, the surface hydrophilization results show no significant difference from that with 24-hour curing time (data not shown). A possible explanation is that the amount of LMW species reaches its lower limit after 24-hour thermal aging at 80 °C, with the given mixing ratio of the

silicon elastomer base and the curing agent. These results suggest that one can shorten the UV-ozone treatment time by extending the curing time of PDMS.

In addition to the curing time, varying the ratio of elastomer base and curing agent will also affect the rate of surface hydrophilization process. It is thought that the low molecular weight (LMW) species, which dominates the hydrophobic recovery process of PDMS, is a result of either uncrosslinked linear PDMS chains or residual crosslinking agent (Eddington, Puccinelli et al. 2006). Based on the absorbed mass concentration of LMW species in PDMS, a similar effect on surface hydrophilization is expected if the ratio of elastomer base and curing agent is varied.

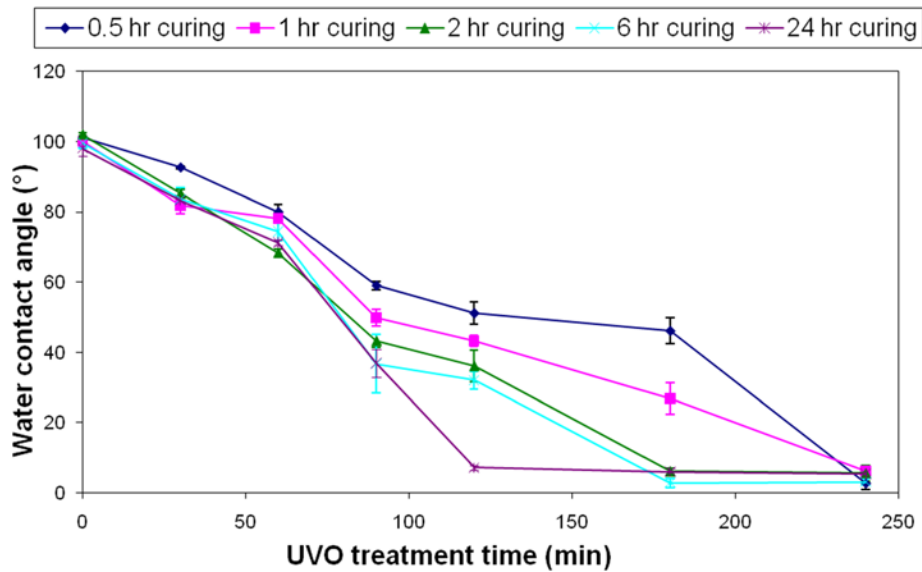


Figure 5-3. The effect of curing time on surface hydrophilization process of PDMS at 80 °C.

5.1.2.3 Wettability maintenance by water immersion

Previous studies have shown that water immersion is an effective way to achieve relatively stable wettability of a plasma-treated hydrophilic PDMS surface with a static water contact angle of less than 10° (Chen and Lindner 2007). In this study, we extend the previous conclusions to a partially water-wet system after UV-ozone oxidation.

As shown in Figure 5-4, after different periods (1 to 4 hours) of UV-ozone treatment, the PDMS surfaces obtain different water contact angles (78° to 6°). The curing conditions chosen are 80°C for 1 hour as typical operations for fabricating PDMS microfluidic devices, and the oxidized PDMS surfaces are kept in contact with water up to 7 days. The static water contact angles are recorded to monitor the wettability change during this process. Initially, a decrease of water contact angle is observed for all of PDMS pieces, presumably due to water absorption of the PDMS matrix (Andrade 1985; Chen and Lindner 2007). Interestingly, for the 4-hour UV-ozone treated piece, there is a slight increase in the water contact angle after 24-hour water immersion indicating that hydrophobic recovery occurs and competes with the effect of water absorption, and the rate of hydrophobic recovery is influenced by degree of surface hydrophilization. After 48 hours of water contact, the wettability of oxidized PDMS surface becomes relatively stable up to 7 days, which enables one to precisely control the wettability of an air/water system in the microfluidic devices.

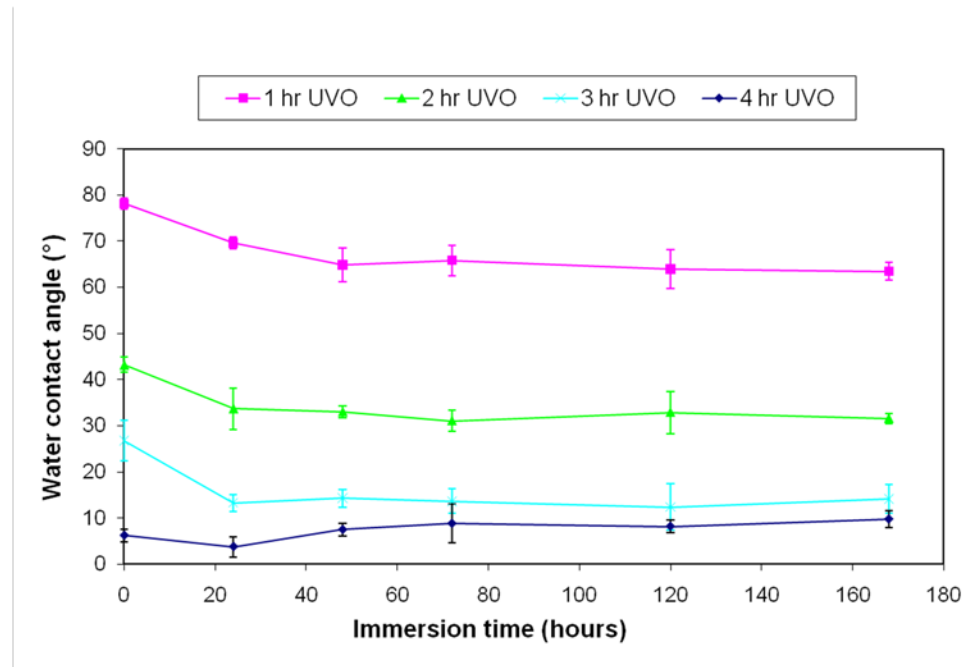


Figure 5-4. Wettability maintenance by keeping UV/ozone-treated PDMS (1-hour curing at 80 °C) surface in contact with DI water.

Hydrophobic recovery in PDMS is influenced by ambient conditions, such as humidity, temperature and the water that is retained inside the polymer matrix. At room temperature, the presence of water provides a much more polar environment than air at the oxidized PDMS surface, and the Si-OH functional groups in the treated PDMS can hydrogen bond with water. It is thought that the large difference in dielectric constants between PDMS and water slows down the migration of LMW species toward the surface and hampers the reorientation of the hydrophilic groups inward toward bulk PDMS in the presence of aqueous solution (Chen and Lindner 2007). Thus, we observe stable wettability when the PDMS is immersed in water compared to exposure in air.

Meanwhile, for non-aqueous applications, it is important to realize that many organic solvents can swell PDMS (Lee, Park et al. 2003) and are not suitable for

PDMS microfluidic devices. Nevertheless, several types of oil which exhibit good compatibility with PDMS can be used in microfluidic experiments, such as vegetable oils and heavy mineral oil (Spiendiani, Nicoletta et al. 2003). Although not discussed in this thesis, it would be interesting to investigate how these oils may affect the migration of LMW species in PDMS and the wettability at the oxidized surface, which is helpful to evaluate the reliability of our proposed technique in the presence of oil.

5.1.2.4 Model analysis of surface hydrophilization and hydrophobic recovery process

5.1.2.4.1 Description of the diffusive reaction model

In order to understand the surface hydrophilization process of PDMS with UV-ozone and the subsequent hydrophobic recovery process, we extend the model developed by Kim and coworkers (Kim, Chaudhury et al. 2006) to describe hydrophobic recovery to include the effect of UV-ozone surface hydrophilization. It is observed that an oxidized surface layer (Figure 5-5) with SiO_x structures is formed at the surface of PDMS during the UV-ozone process (Berdichevsky, Khandurina et al. 2004), and the composition of bulk PDMS stays unchanged (Efimenko, Wallace et al. 2002). In a similar way, an oxidized surface layer is formed at the PDMS surface during active electrical discharges, such as oxygen plasma.

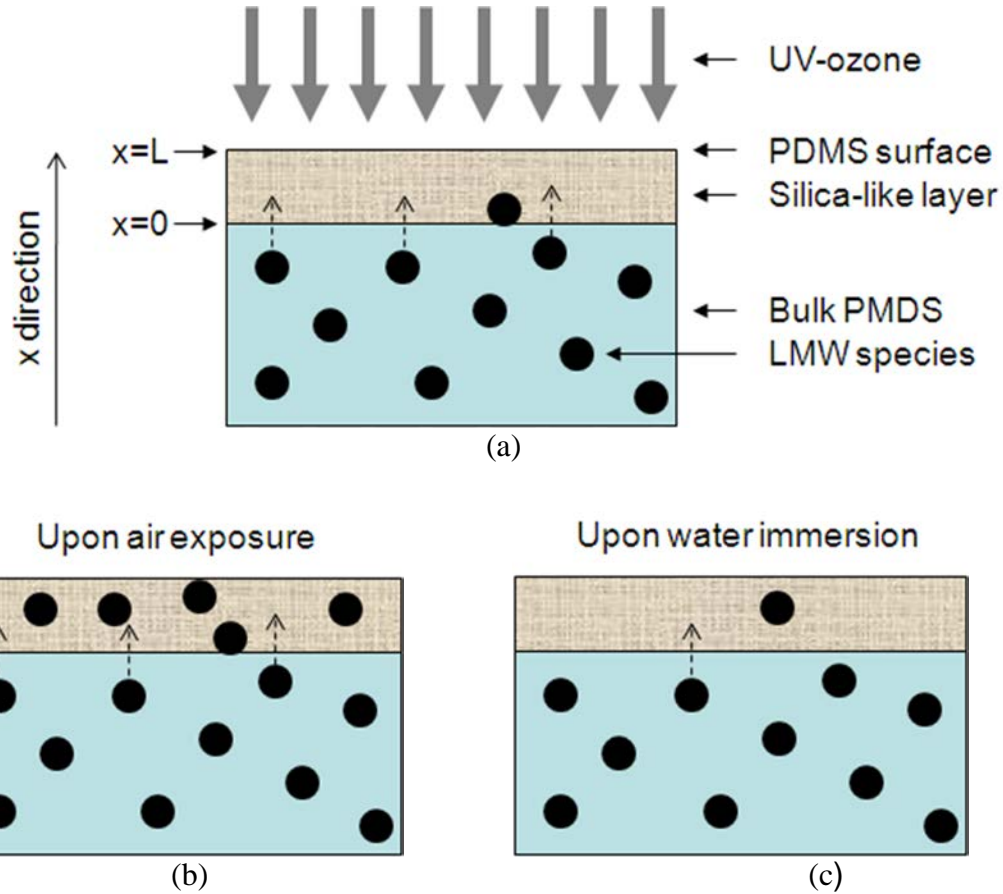


Figure 5-5. The schematic of migration of LMW species in PDMS (a) during UV-ozone treatment; (b) upon air exposure; (c) upon water immersion. The dimensions are not to scale. Modified from Kim and coworkers (Kim, Chaudhury et al. 2006).

In one of the models developed by Kim and coworkers, the hydrophobic recovery of electrically discharged PDMS surface is described using a one-dimensional homogeneous diffusion equation:

$$\frac{\partial C_{np}}{\partial t} = D_{np} \frac{\partial^2 C_{np}}{\partial x^2} \quad (5.2)$$

where C_{np} is the adsorbed mass concentration of LMW species, D_{np} is the diffusivity of LMW species in the oxidized surface layer, and x is the direction toward the surface of PDMS. They also used the Cassie equation (Cassie and

Baxter 1944) to correlate the adsorbed mass of LMW species with the water static contact angle:

$$\cos \theta = f_{po} \cos \theta_{po} + f_{np} \cos \theta_{np} \quad (5.3)$$

where the subscripts po and np represent polar and non-polar (LMW species) groups in the oxidized surface layer, and f denotes the areal fraction of the component. An assumption made is that the areal fractions can be estimated with the fraction of the adsorbed mass concentration of the LMW species (Holmesfarley, Reamey et al. 1987; Kim, Chaudhury et al. 2006), and the non-polar groups are essentially the same as LMW species based on this assumption. Thus, Kim and coworkers derived the water contact angle θ_t at time t as shown in Eqn (5.4):

$$\begin{aligned} \cos \theta_t &\approx \frac{C_0 - C_{np}}{C_0} \cos \theta_{po} + \frac{C_{np}}{C_0} \cos \theta_{np} \\ &= \cos \theta_{np} + (\cos \theta_{po} - \cos \theta_{np}) \left(1 - \frac{C_{np}}{C_0}\right) \end{aligned} \quad (5.4)$$

where C_0 is the maximum adsorbed mass concentration of LMW species in the oxidized surface layer.

Extending the above model to a UV-ozone process requires an understanding of the kinetics involved in this process. Unlike the oxygen plasma, the UV-ozone surface hydrophilization takes place over several hours so that there is a competition between the surface hydrophilization and the hydrophobic recovery. It is generally accepted that the dominating reaction during PDMS surface modification process is the conversion of methyl groups into hydroxyl and bridging oxygen species (Mirley and Koberstein 1995; Efimenko, Wallace et al.

2002; Fu, Qui et al. 2010). However, the oxidation rate of PDMS surface decreases significantly as the reaction progresses with UV-ozone exposure (Mirley and Koberstein 1995). The results of sum frequency vibrational spectroscopy showed that the concentration of methyl groups on PDMS surface decreased exponentially with time, which was described with first-order reaction kinetics of removal and in-situ regeneration of methyl groups (Ye, Gu et al. 2006). However, slowing-down of the oxidation rate may also be caused by the rate-limiting diffusion of oxidative groups into PDMS network, according to the depth profile with Auger electron spectroscopy (Chan, Thomas et al. 1998).

Table 5-2. List of the parameters in the model for LMW PDMS transport

Parameter	Value	Unit	Remark
D_{np}	3.67×10^{-12}	cm^2 / s	diffusivity of LMW species
k	6.0×10^{-5}	$(g / cm^3)^{1-n} / s$	reaction rate constant
n	0.6	--	reaction order
C_{np0}	0.1	g / cm^3	initial LMW species concentration after curing
θ_{po}	0	degree	contact angle of polar groups
θ_{np}	100	degree	contact angle of LMW species
L	1.0×10^{-3}	cm	thickness of the oxidized surface layer

The complex nature of this oxidation reaction and limiting data of kinetic characterization make it challenging to quantitatively describe this process. We tentatively employ a power-law kinetic model to represent the reaction of PDMS surface oxidation with UV-ozone, and the transport of LMW species can be described with:

$$\frac{\partial C_{np}}{\partial t} = D_{np} \frac{\partial^2 C_{np}}{\partial x^2} - k C_{np}^n \quad (5.5)$$

where k is the reaction rate constant and n is the reaction order.

We program a finite difference algorithm with a grid point formulation in MATLAB to calculate Eqn (5.5), which contains 50 grid points equally spaced in the oxidized surface layer along the direction perpendicular to the PDMS surface. The parameters of the simulation are listed in Table 5-2. The thickness of the PDMS layer oxidized by UV-ozone treatment ($10 \mu m$) is based on the experimental observation of a cross-section of a microchannel (Berdichevsky, Khandurina et al. 2004), which is independent of the time of UV-ozone exposure. The initial adsorbed mass concentration of LMW species C_{np0} before UV-ozone oxidation is based on a Freundlich adsorption isotherm which has been used to model a hydrophobic recovery process of PDMS in the previous work (Kim, Chaudhury et al. 2006). The contact angles of polar and non-polar groups are 0° and 100° , which correspond to complete water-wet condition and unoxidized condition of PDMS surface, respectively. In Table 5-2, the diffusivity D_{np} , the reaction rate constant k and the reaction order n are obtained through a process of parameter estimation of the experimental data described below.

5.1.2.4.2 Parameter estimation

As C_{np0} is dependent on the curing time of PDMS at elevated temperature, we estimate the parameters with a fixed curing time (1-hour), and will discuss the effect of curing time on surface hydrophilization in the following section. Based

on our experimental data of hydrophobic recovery of PDMS after 1-hour curing and 4-hour UV-ozone treatment, we estimate the diffusivity of LMW species in the oxidized surface layer via the golden section search method (Kiefer 1953). In a hydrophobic recovery process, Eqn (5.5) reduces to Eqn (5.2) due to the absence of the reaction term, and it is solved with the following initial and boundary conditions:

$$\text{IC: } C_{np}(t=0, x) = \frac{C_{is} - C_{np0}}{L}x + C_{np0}$$

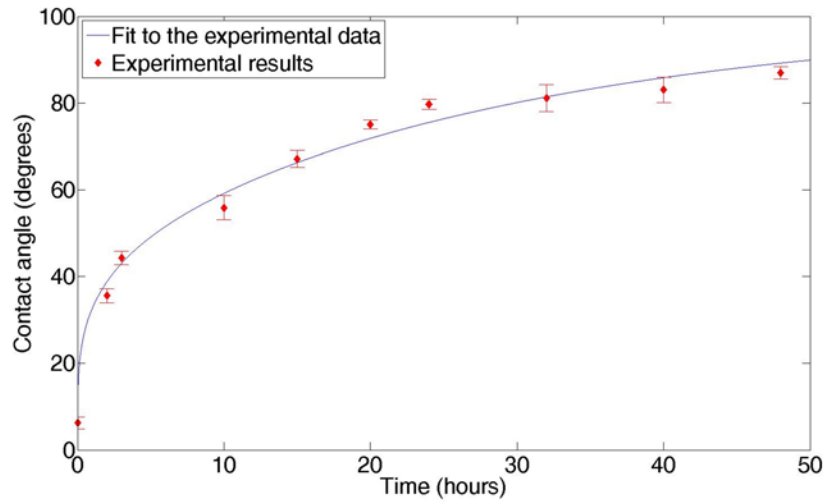
$$\text{BCs: } C_{np}(t, x=0) = C_{np0} \text{ (inner boundary as shown in Figure 5-5(a))}$$

$$\frac{\partial C_{np}(t, x=L)}{\partial x} = 0 \text{ (outer boundary as shown in Figure 5-5(a))}$$

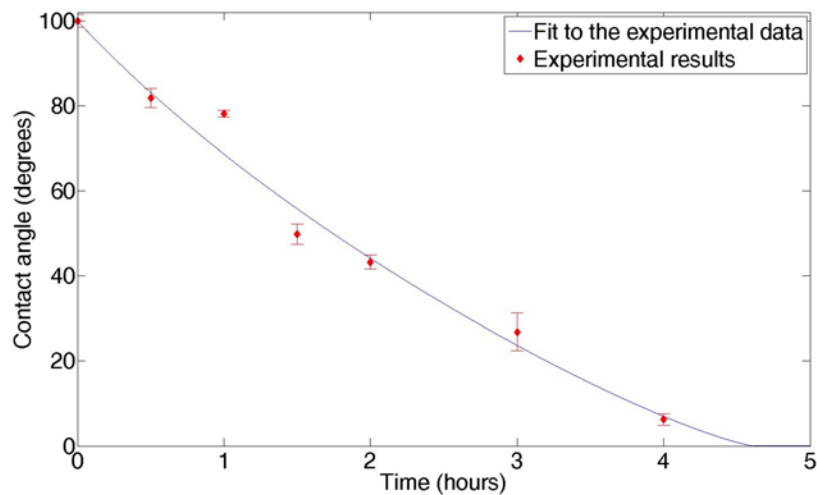
where C_{is} is the initial adsorbed mass concentration of LMW species at the outer surface of the oxidized surface layer, which is calculated through Eqn (5.4) with an initial contact angle of the hydrophobic recovery right after UV-ozone treatment.

The initial condition is a linear LMW concentration profile through the oxidized surface. At the interface of the oxidized surface ($x=L$), the concentration of LMW species is determined from the UV-ozone treatment. This initial condition can vary as a function of UV exposure time, oxygen content, and initial LMW concentration in the PDMS. The linear profile accounts for in-situ chain scission of PDMS at high doses of energy (Olah, Hillborg et al. 2005), which increases the LMW species in the sub-surface region (Kim, Chaudhury et al. 2006), leading to a faster hydrophobic recovery in air. At the inner boundary, C_{np} is assumed to be

a constant C_{np0} due to the large amount of LMW species residing in PDMS matrix, while at the outer boundary it is assumed to be no flux for C_{np} such that the LMW species accumulate at the surface of PDMS.



(a)



(b)

Figure 5-6. (a) Experimental data for hydrophobic recovery in air of PDMS (after 1-hour curing and 4-hour UV-ozone treatment). The diffusion coefficient D_{np} is estimated by fitting Eqn (5.2) to the experimental data. (b) Experimental data of how time for UV-ozone exposure changes PDMS wettability using a 1-hour curing time. The derived reaction rate constant k and the reaction order n are derived by fitting Eqn (5.5) to the experimental data.

The results in Figure 5-6(a) yield an optimized diffusivity D_{np} of 3.67×10^{-12} cm^2/s for the LMW species, which is several orders of magnitude lower than the measured diffusivity ($\sim 10^{-8}$ to 10^{-7} cm^2/s) of silicone fluid in a silicone elastomer at room temperature (Gent and Tobias 1982; Rice, Diaz et al. 1988; Mathison, Yates et al. 1991). This indicates that LMW species diffuses slower in the oxidized surface layer near the surface than in the bulk PDMS matrix. The existence of hydroxyl groups, generated during UV-ozone treatment, increases the dielectric constant of the oxidized layer compared with bulk PDMS.

The next step is to determine the kinetic parameters for the UV-ozone process. Before the UV-ozone treatment, the initial condition of $C_{np}(t=0, x) = C_{np0}$ applies for Eqn (5.5) in the oxidized surface layer, due to the homogeneous nature of cured PDMS. The boundary conditions are identical to those in the hydrophobic recovery process. Thus, for any reaction rate constant, k , and reaction order, n , Eqn (5.5) can be solved numerically with our finite difference algorithm.

A series of two-parameter contour plots are performed to obtain the optimal k and n using the experimental data from 1-hour curing PDMS shown in Figure 5-3. According to the results of this approach, the parameters that best fit the experimental data are $k = 6.0 \times 10^{-5} (\text{g}/\text{cm}^3)^{1-n} / \text{s}$ and $n = 0.6$, respectively.

Although the kinetics associated with the UV-ozone oxidation process still to be understood and developed, our power-law reaction model fits well to the experimental data through the one-dimensional diffusive reaction equation, as shown in Figure 5-6(b).

5.1.2.4.3 Effect of the concentration of LMW species

We have already shown in Figure 5-3 that additional curing time accelerates the surface hydrophilization process of PDMS with UV-ozone. As the initial adsorbed mass concentration of LMW species C_{np0} is dependent on the curing time of PDMS, we vary the value of C_{np0} to investigate this effect on surface hydrophilization in our model.

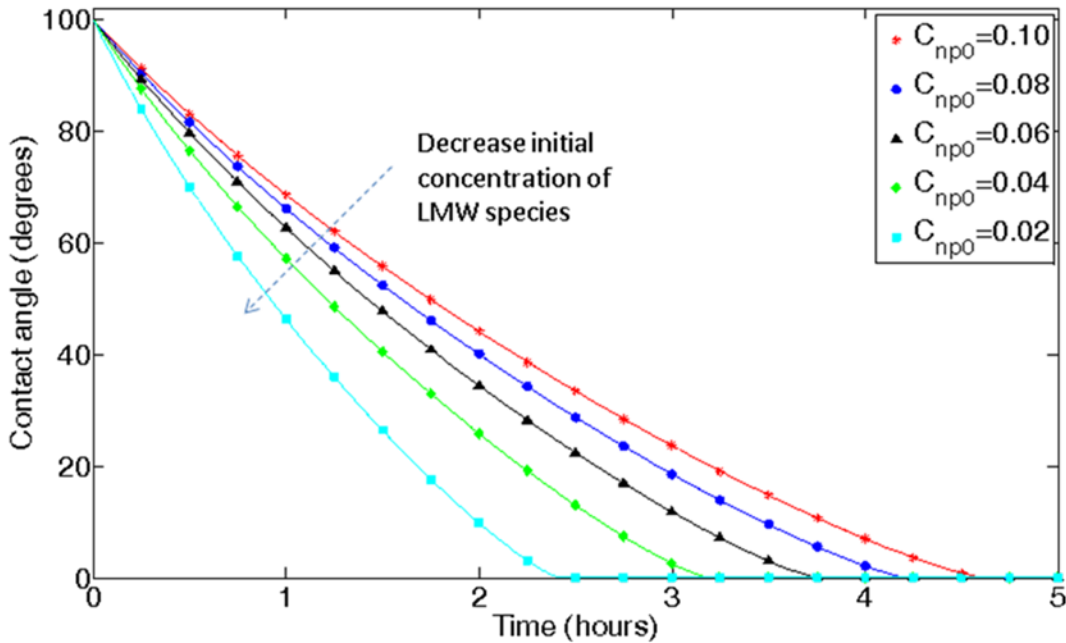


Figure 5-7. Simulation of how changes in the initial concentration of LMW species affect the PDMS surface hydrophilization process with UV-ozone. The unit of C_{np0} shown in the legend is g/cm^3 . All other parameters are consistent with those in Table 5-2.

In Figure 5-7, C_{np0} ranges from 0.02 to 0.10 g/cm^3 , with other parameters staying unchanged. The results in Figure 5-6 show that less initial adsorbed

mass concentration of LMW species leads to fast surface hydrophilization of PDMS, which is consistent with the trend observed in Figure 5-3. We also find that with the parameters in Table 5-2, the process of UV-ozone treatment of PDMS in Figure 5-7 is in a reaction-dominated regime. Decreasing the diffusivity does not improve the rate of surface hydrophilization. However, increasing the diffusivity by an order of magnitude would significantly slow down the surface hydrophilization process at all C_{np0} levels (data not shown). Thus, the effect of C_{np0} on PDMS hydrophilization mainly contributes to the kinetics of the oxidation process of LMW species in the oxidized surface layer.

The small differences in the water contact angle for various curing time in the first hour observed in Figure 5-3 is not predicted by our simulation results in Figure 5-6, indicating that there are other factors that influence surface hydrophilization, such as the concentration-dependent diffusion of LMW species. Other kinetic models need to be investigated in the future in order to improve the model.

5.1.2.4.4 Effect of the diffusivity of LMW species

We vary the diffusivity of LMW species in the hydrophobic recovery process. Figure 5-8 shows the effect of the diffusivity on the rate of hydrophobic recovery of PDMS, and the lower diffusivity results in better wettability maintenance of the oxidized PDMS surface. If the diffusivity is five orders of magnitude lower than that was calculated in Figure 5-5(a), the wettability is expected to be very stable over a week, according to the simulation results in Figure 5-8.

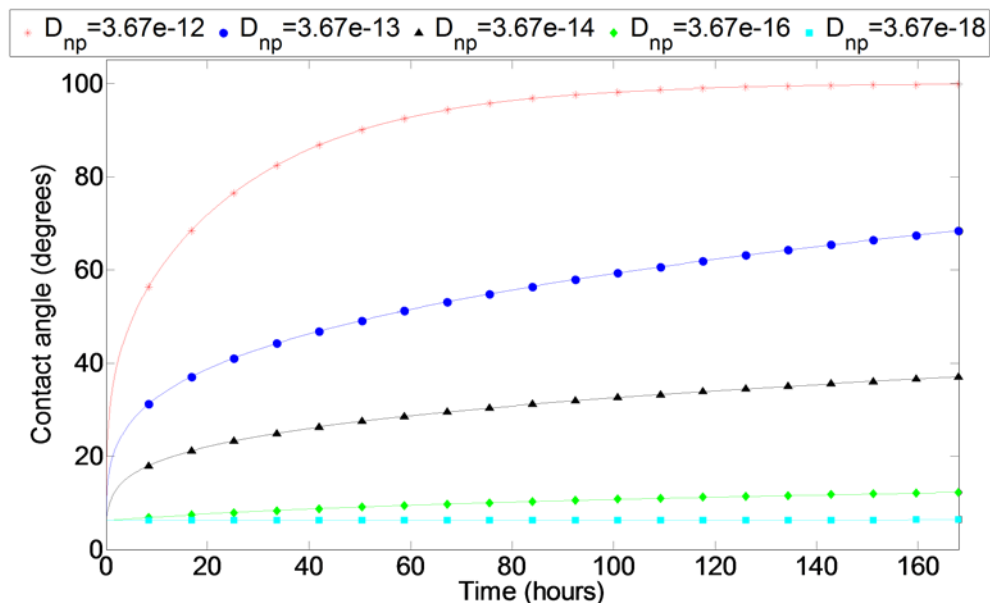


Figure 5-8. Simulation of how diffusivity of non-polar groups influences the wettability of the PDMS surface. The unit of D_{np} shown in the legend is cm^2/s . All other parameters are consistent with those given in Table 5-2 without the reaction term.

One way to control the diffusivity of LMW species is to decrease the temperature. The absorption of silicone fluid in a silicone elastomer was experimentally measured from 0 °C to 150 °C, and the variation of calculated diffusivity with temperature was found to be well represented by the Arrhenius relationship (Mathison, Yates et al. 1991). It was also shown that the hydrophobic recovery in air of plasma-treated PDMS surfaces was much slower in 4 °C or 20 °C than that in 70 °C (Chen and Lindner 2007), as a result of low diffusivity of LMW species at low temperatures. Therefore, low-temperature operations are able to slow down the rate of hydrophobic recovery of oxidized PDMS surfaces.

As indicated in Figure 5-4, exposing an oxidized PDMS surface to an aqueous environment is an effective method to control the wettability of PDMS. Other than decreasing the diffusivity of LMW species via temperature, water molecules residing in the PMDS provides additional hydrogen bonding between the hydrophilic groups, which resists the migration of LMW species toward the surface. For this reason, immersing the PDMS in water prevents the water from evaporating from the oxidized surface and retards the hydrophobic recovery. This effect is beneficial to wettability control of PDMS and may be used in combination with diffusivity control (for example, decreasing the temperature) to slow the migration of LMW species. Other fluids that strengthen the dipole interactions between the hydrophilic groups, as well as possible additives used in the uncured PDMS to inhibit hydrophobic recovery, will be studied in the future to extend the proposed technique for wettability control and patterning of PDMS.

5.2 Effect of surface wettability on bubble pinch-off in microchannels

5.2.1 Microfluidic design

The geometry of microfluidic channels in this study is sketched in Figure 5-9. CO₂ is injected from the central channel, and aqueous phase is injected from the side channels. All the channels have the same dimensions (width × height= 100 μm × 75 μm). The downstream channel after merging of all inlet channels is designed to be 10.2 cm long, as Figure 5-9 shows.

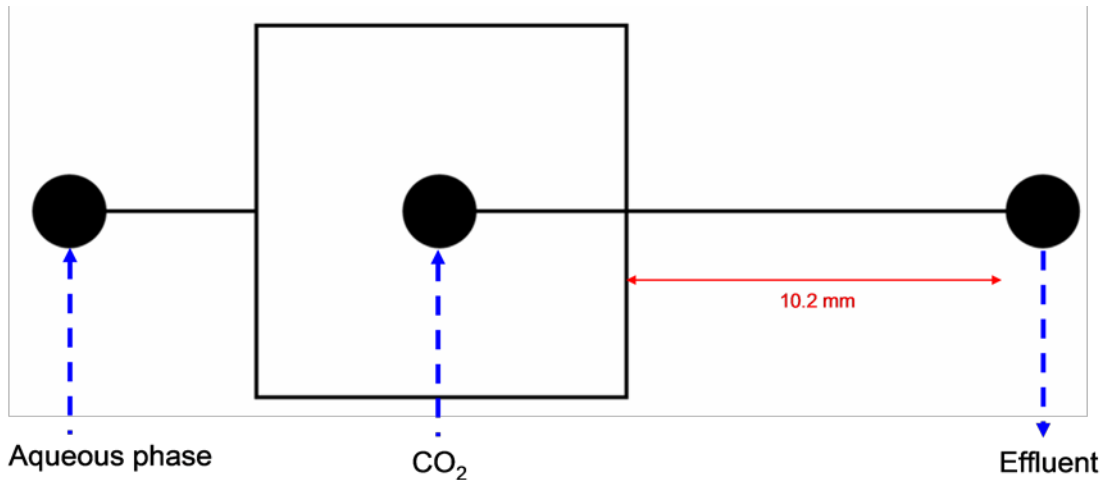


Figure 5-9. Microfluidic hydrodynamic flow-focusing pattern in this study.

The flow rate of aqueous phase (either DI water or surfactant solution) is controlled with a syringe pump (Harvard Apparatus), from 100 $\mu\text{L/hr}$ to 5000 $\mu\text{L/hr}$. In the case of surfactant solution, 0.2 wt% (active ingredient) AOS1618 (Stepan Company) is used. The inlet pressure of gas phase (CO_2) is adjusted with a pressure-control device Fluigent MFCS 8C (Fluigent Corp.), from 5 kPa to 20 kPa. Pressures larger than 20 kPa are not recommended because the bonding between the PDMS pieces is released, causing the microfluidic channel to disassemble.

5.2.2 Flow patterns in low capillary numbers

With the technique of precise wettability control, we have created surfaces with different wettability in the microchannels as described in Table 5-3. Specifically, surfaces with water static contact angles range from 8° to 98° are

developed for this study. For convenience, they are labeled as Hydrophobicity I, II, III, and IV. Within the given experimental condition of CO₂ and aqueous phase, various flow patterns were observed and listed in Figure 5-10.

Table 5-3. Wettability of microchannels in this study

Hydrophobicity	PDMS curing time	Water static contact angle (72 h water immersion)
I	7 days at 100°C	8±1°
II	1 hour at 80°C	33±1°
III	1 hour at 80°C	65±3°
IV	1 hour at 80°C	98±1°

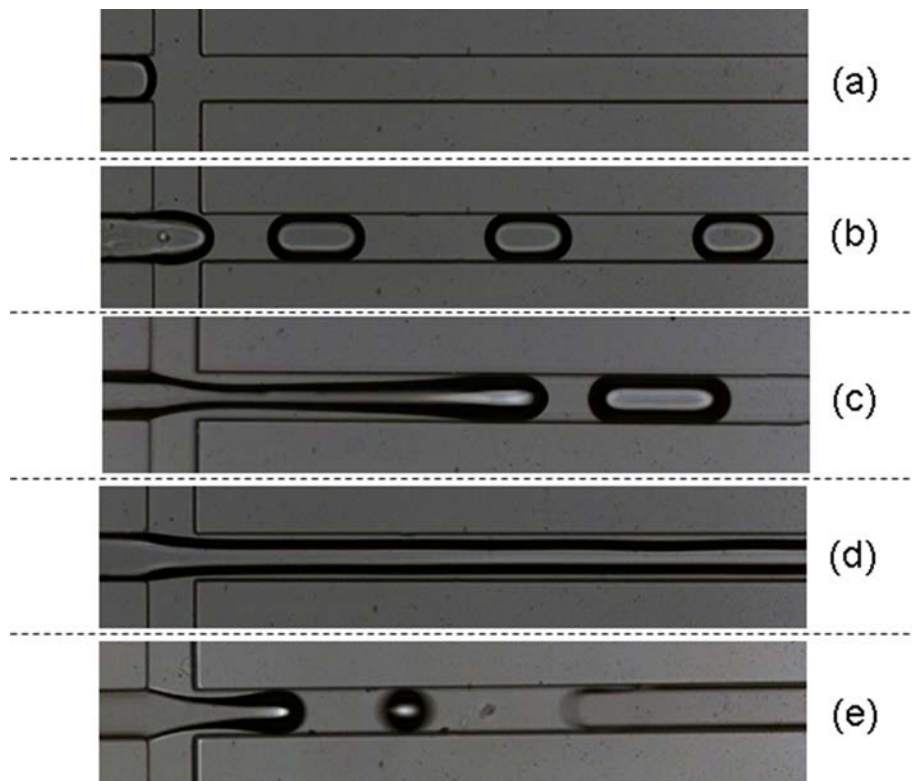


Figure 5-10. CO₂/aqueous phase flow patterns observed in hydrodynamic focusing microchannels. (a) aqueous phase flow; (b) dripping flow; (c) jetting flow; (d) stratified flow; (e) unstable slug flow., only observed in Hydrophobicity IV. Gas inlet pressure ranges from 5.0 kPa to 20.0 kPa, and aqueous phase flow rate ranges from 200 to 800 µl/hr.

In Figure 5-10, CO₂ flows from left to right, and aqueous phase squeezes the gas phase from side channels. The outflow end is located at the right-hand side. We will describe the general trend flow trends seen in Figure 5-10 when the aqueous flow rate is fixed. There exists a gas pressure threshold for the gas thread to enter the downstream channel, which is determined by wettability and downstream pressure drop, as Figure 5-10(a) shows. This pressure threshold will be analyzed in Part 5.2.3 in this chapter. When gas pressure is larger than the threshold, either dripping flow (Figure 5-10(b)) or jetting flow (Figure 5-10(c)) can be formed, depending on the flow rate of each phase and surface wettability. The bubble formation process is determined by the force balance across the moving interface, which is dominated by surface-tension and viscous forces at low capillary numbers (Bretherton 1961). When gas pressure is sufficiently large and the shear force becomes insufficient, the aqueous phase fails to pinch off the gas thread and stratified flow will be resulted in (Figure 5-10(d)). This flow regime is somehow dependent on the geometry of downstream channels, which may introduce transient phenomena due to the stability of gas cylinders (Gordillo, Ganan-Calvo et al. 2001). For example, in a zigzag downstream channel the annular flow with waves of liquid rings was observed instead of stable stratified flow (Cubaud and Ho 2004). Typically, an increasing gas inlet pressure is required for flow patterns from Figure 5-10(a) to Figure 5-10(d) in the same system, if aqueous phase flow rate stays unchanged. Additionally, in poorly water-wet system (Hydrophobicity IV), unstable slug flow is observed (Figure 5-10(e)) and the droplet size is not predictable. Flow patterns in Figure 5-10(b), (c),

and (e) are defined as bubble break-up regime, because foam is created in downstream channel essentially.

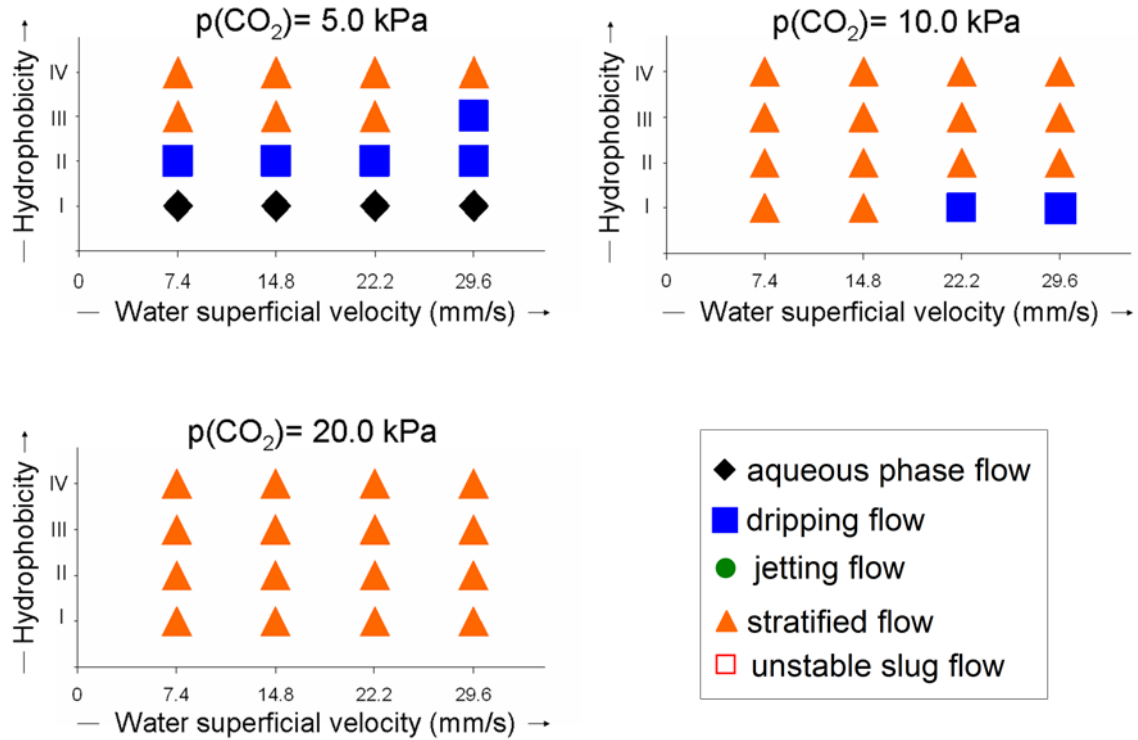


Figure 5-11. Comparison of CO₂/water flow patterns in hydrodynamic focusing microchannels with different wettability. Ca_i ranges from 1.0×10^{-4} to 4.0×10^{-4} .

Capillary number ($Ca = \frac{\mu u}{\sigma}$, where μ is the viscosity of one fluid phase, u is a characteristic velocity and σ is the interfacial tension between the two fluid phases), describes the relative importance of viscous forces versus interfacial tension forces. Fluid flow in oil reservoir, especially far from an injection well, usually has a low capillary number. For example, waterfloods typically operate at conditions where $Ca < 10^{-6}$ (Green and Willhite 1998), where capillary forces

dominate the flow in porous media. We will investigate how wettability affects flow patterns for CO₂/aqueous phase flow when aqueous capillary number Ca_l is on the order of 10^{-4} (Figure 5-11 and Figure 5-12).

The effect of wettability on CO₂/water flow patterns without surfactants is shown in Figure 5-11, where the water superficial velocity is defined as the water volumetric flow rate divided by the cross-sectional area of the downstream channel. In the three plots of Figure 5-11, CO₂ inlet pressure was chosen to be 5.0 kPa, 10.0 kPa and 20.0 kPa, respectively. It can be seen that wettability has a significant influence on two-phase flow patterns, especially at low gas inlet pressure. Lower water contact angle of PDMS surface (more hydrophilic) tends to create higher resistance for CO₂ thread to enter the cross junction. When CO₂ inlet pressure increases, the effect of wettability becomes weaker and stratified flow is created in most cases.

In the presence of a foaming surfactant (0.2 wt% AOS 1618), a much larger range of bubble break-up regime is observed, as Figure 5-12 shows. The range of aqueous flow rate is controlled the same as that without surfactant. However, due to interfacial tension reduction by surfactant, Ca_l is higher in Figure 5-12, but still on the order of 10^{-4} . More hydrophilic conditions can also result in larger resistance for gas phase flow, reflected in the difference between dripping and jetting flow patterns. A noteworthy phenomenon is observed in Hydrophobicity IV, where unstable slug flow is created instead of dripping or jetting flow. This is presumably because the aqueous phase fails to wet the channel walls and

asymmetric instability increases. Meanwhile, Figure 5-12 shows that aqueous flow was not observed in the given conditions, because the gas inlet pressure did not go low enough to lead to aqueous phase flow. We will perform calculations in Part 5.2.3 to analyze this capillary entry pressure.

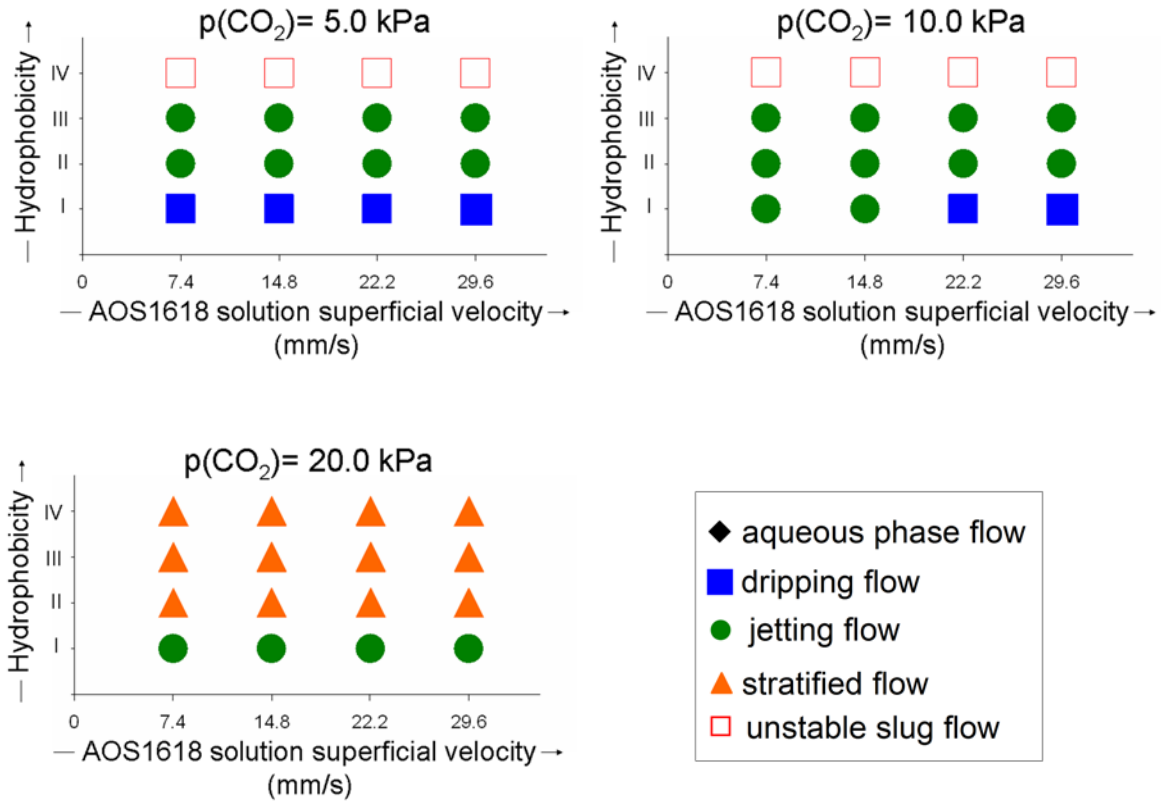


Figure 5-12. Comparison of CO₂/AOS1618 solution flow patterns in hydrodynamic focusing microchannels with different wettability. Ca_l ranges from 2.2×10^{-4} to 8.8×10^{-4} .

5.2.3 Gas pressure threshold

To explain how wettability affects CO₂/aqueous phase flow patterns, we can derive the pressure threshold in the system, above which the CO₂ thread can enter the cross junction of the focusing channels.

$$P_{threshold} = P_{capillary} + P_{dynamic} \quad (5.6)$$

$$P_{capillary} = \sigma(1/R_1 + 1/R_2) = 2(h+w)\sigma \cos \theta / hw \quad (5.7)$$

$$P_{dynamic,1} = -\frac{\mu QL_1}{\int_0^{h/2} \int_0^{w/2} \frac{[x^2 - (w/2)^2][y^2 - (h/2)^2]}{2\{[x^2 - (w/2)^2] + [y^2 - (h/2)^2]\}} dx dy} \quad (5.8)$$

$$P_{dynamic,2} = \frac{8\mu QL_2}{\pi R_2^4} \quad (5.9)$$

Eqn (5.6) shows that the pressure threshold includes two parts, $P_{capillary}$ and $P_{dynamic}$. $P_{capillary}$ is caused by the Laplace pressure across the curved interface, which can be calculated through the Young-Laplace equation (Eqn (5.7)) with the principal radii of curvature (Thompson, Brinckerhoff et al. 1993). $P_{dynamic}$ is the pressure drop along the downstream channels, including the downstream microchannel (10.2 cm long) and the effluent tubing (580 μ m ID, 21.6 cm long). With a no-slip boundary condition, we can calculate the pressure drop in the channel through the Hagen–Poiseuille equation (Eqn (5.9)) for the effluent tubing and Eqn (5.8) for rectangular downstream microchannels (Landau and Lifshietis 1959).

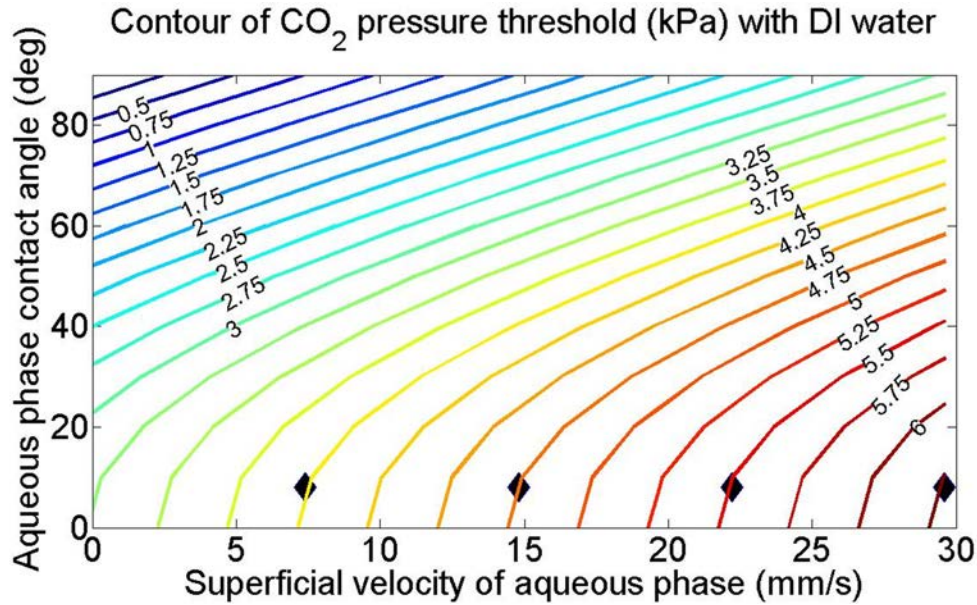


Figure 5-13. Pressure threshold for CO₂ thread to enter downstream channels without surfactants in aqueous phase. The solid diamonds represent aqueous phase flow observed in the experiments at a CO₂ inlet pressure of 5.0 kPa.

Figure 5-13 shows the contour map of pressure threshold without surfactants in aqueous phase, in terms of wettability and superficial velocity of the aqueous phase. By comparing the solid diamonds with the calculated pressure contour, one may find that two experimental points (water superficial velocity at 7.4 and 14.8 mm/s) are not in the expected region for aqueous phase flow, i.e., the calculated $P_{threshold}$ is smaller than 5.0 kPa. This is presumably because the pressure loss was not taken in account at the outlet connection between the PDMS and the effluent tubing, and the pressure threshold was underestimated. Nevertheless, Figure 5-13 clearly shows the trend that both water-wet condition and high aqueous phase velocity can result in large pressure threshold.

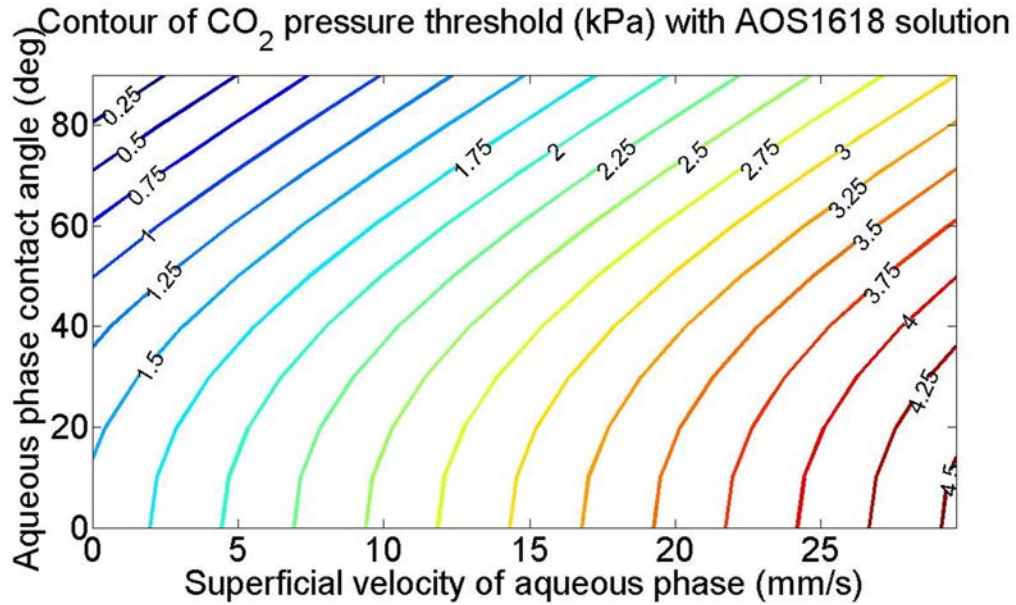


Figure 5-14. Pressure threshold for CO₂ thread to enter downstream channels with 0.2 wt% AOS1618 in aqueous phase.

In Figure 5-14, the effect of surfactant on the contour plot of pressure threshold is shown. Because the presence of surfactant can significantly lower the interfacial tension, $P_{capillary}$ decreases correspondingly. As a result, the gas pressure threshold is lower than the case without surfactant, given the same aqueous phase contact angle and flow rate. This phenomenon is confirmed by comparing Figure 5-11 with 5-12, at 5.0 kPa and Hydrophobicity I.

5.3 Visualization of foam transport in heterogeneous micromodels

5.3.1 Design and operation of the micromodel

Five inlet and outlet ports are designed in the microsystem as shown in Figure 5-15. On the left side of the pattern, a flow-focusing geometry (Garstecki, Gitlin et al. 2004) is used to generate foam by simultaneously injecting surfactant solution and gas. A long winding channel is employed downstream of the flow-focusing geometry to create a foam reservoir and to provide an additional pressure gradient to minimize back-pressure changes when diverting bubbles into the porous media. On the right side of the pattern, the porous medium (8540 μm length \times 3600 μm width) is connected to five equally distributed microchannels (200 μm width each). These channels serve to direct foam uniformly into the porous media. The high permeable region of the porous medium is composed of cylindrical pillars with a radius of 150 μm aligned at a distance of 60 μm , while the cylindrical pillars in the low permeable half have a radius of 50 μm aligned at a distance of 20 μm . Both regions have the same porosity of 45.0%. Port 4 is designed as a waste outlet.

Oxygen plasma (Plasma Cleaner PDC-32G, Harris Plasma) is used to hydrophilize the PDMS surface and bond the PDMS porous media to a blank PDMS, which is bonded to a glass slide for support, forming the microfluidic device. The wettability of the PDMS surface is carefully controlled at a static water contact angle of $22.6^\circ \pm 2.7^\circ$ with oxygen plasma and subsequent water

immersion in all experiments (Ma, Rivera et al. 2011). The height of the porous media is 60 μm .

Since the pore radius of a homogeneous porous medium scales with the square root of the permeability (Carman 1937), we estimate the permeability contrast as 4 in our porous medium, with the hydraulic radii of the pore throats in each half:

$$\frac{k_{high}}{k_{low}} = \left(\frac{R_{high}}{R_{low}} \right)^2 = \left(\frac{60^2 / 240}{60 \times 20 / 160} \right)^2 = 4$$

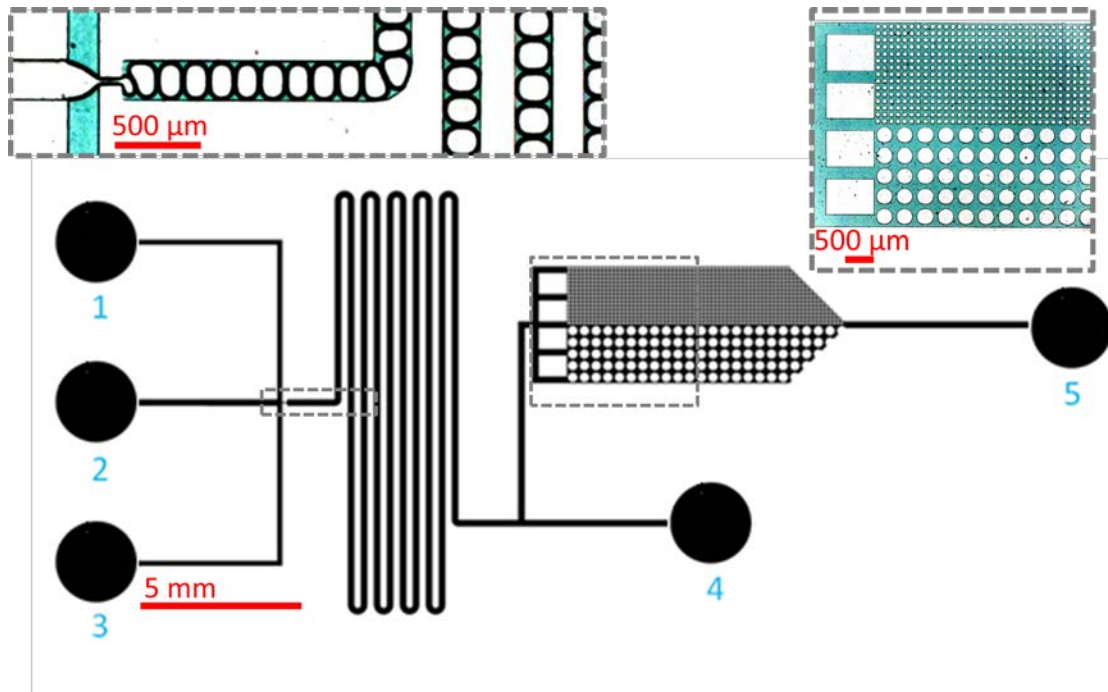


Figure 5-15. Microfluidic design of the heterogeneous porous micromodel.

A 0.2 wt% coco-betaine (Mackam CB 35, Rhodia Inc., Lot # UP0E13X01) in water is used as the surfactant solution, distilled water (18.2 M Ω ·cm) is used as

the aqueous phase, and air is used as the gas phase in all experiments. A concentration of 3.0 wt% aqueous dye (ESCO Foods, Inc.) is added to both the surfactant solution and DI water to better distinguish liquid from gas and PDMS posts.

To operate the micromodel, a syringe pump (Harvard Apparatus PHD 2000) is used for liquid injection and a microfluidic pressure pump (Fluigent MFCS-8C) is used for gas injection. The flow rates of surfactant solution range from 0 to 0.80 ml/hr, as indicated in Table 5-4. After the microfluidic device is fabricated, a surfactant-free 3.0 wt% aqueous dye solution is injected into port 5 until the porous medium is completely saturated, while port 4 is opened and ports 1-3 are closed. After port 5 is closed, surfactant solution is injected into ports 1 and 3 while air is injected into port 2 to generate bubbles in the flow-focusing geometry. The bubbles travel through the long winding channel and exit through port 4. Once uniform bubble size is observed in the long winding channel, port 4 is closed and port 5 is reopened to redirect the bubbles into the porous medium.

5.3.2 Results and discussions

The injected gas pressure is fixed at 400 mbar (4×10^4 Pa, gauge pressure) in all the foam experiments. The surfactant flow rate is varied to change the quality of the foam. To reduce the influence of the capillary end effect (Hadley and Handy 1956) in our micromodel, the length of the porous medium is designed to be more than twice its width and we choose to monitor the fluid

dynamics away from the outflow-end boundary, as used in previous micromodel studies (Romero-Zeron and Kantzas 2005). A 100% gas injection case is also studied using a gas pressure of 50 mbar in order to investigate the effect of gas inlet pressure on the sweep efficiency of aqueous solution with 100% gas. The time of gas breakthrough is defined as the time when gas first exits the right side of the captured image (the 32nd column in the low permeable region in Figure 5-17). The 11 sets of experiments are performed and listed in Table 5-4.

Table 5-4. Summary of foam experiments in the heterogeneous micromodel

Run ID	Gas inlet pressure (mbar)	Surfactant flow rate (ml/hr)	Time of gas breakthrough (sec)
1	400	0.80	2.00
2	400	0.40	1.90
3	400	0.20	2.70
4	400	0.16	4.40
5	400	0.13	5.30
6	400	0.10	7.85
7	400	0.06	9.75
8	400	0.05	11.20
9	400	0.04	8.65
10	400	0	0.03
11	50	0	0.33

As the surfactant flow rate decreases, the time of gas breakthrough increases until reaching a maximum value (11.20 sec in Run ID 8), which corresponds to a critical surfactant flow rate (0.05 ml/hr). Beyond this critical value, further decrease in the surfactant flow rate results in a decrease in the time of gas breakthrough. The time of gas breakthrough (t_{bt}) is affected by the volumetric gas flow rate (F_g) and the volume swept (V_{swept}) by gas:

$$t_{bt} = \frac{V_{swept}}{F_g} = \frac{V_{swept}}{u_g A} \quad (5.10)$$

where u_g is defined as the superficial velocity of gas phase, and A is the average cross-sectional area of the porous medium.

In the absence of foam, u_g can be correlated with the pressure drop through the porous medium using the Darcy's law in Eqn (5.11), where k is the permeability of the porous medium.

$$u_g = -\frac{kk_{rg} \nabla P_g}{\mu_g} \quad (5.11)$$

However, we measure the pressure drop of the entire system, therefore Darcy's law can only be applied to our system by a scaling analysis. It is also known that the correlation of fluid velocity and pressure gradient can be described with the Poiseuille law (Bird, Stewart et al. 2002) for one-phase flow in a single channel:

$$u_g = -\frac{R^2 \nabla P_g}{8\mu_g} \quad (5.12)$$

where R is the hydraulic radius of the channel or tubing. In the case of two-phase foam flow in a capillary tube, an apparent gas viscosity $\mu_{g,app}$ replaces μ_g , where $\mu_{g,app}$ is a function of lamellae density, liquid viscosity, bubble velocity, radius of curvature of the gas-liquid interface and capillary radius (Hirasaki and Lawson 1985). Generally, the presence of foam can greatly increase the effective viscosity of the gas phase in the capillary tube by as much as several orders of magnitude (Hirasaki and Lawson 1985; Llave, Chung et al. 1990).

By using a scaling analysis to combine the pressure drop terms in Eqns (5.11) and (5.12), the flow rate in the heterogeneous microfluidic system can be described by Eqn (5.13), where C_0 and C_1 are two positive constants ($C_0 + C_1 = 1$) scaling the contributions in pressure gradient (∇P_g) in the entire system by the porous medium and the capillary channel / tubing at the in-flow and out-flow ends, respectively, which depend on the geometry of our device:

$$u_g = -\frac{\nabla P_g}{\left(\frac{C_0}{kk_{rg}} + \frac{C_1}{R^2}\right)\mu_g} \quad (5.13)$$

Substituting Eqn (5.13) into Eqn (5.10) results in Eqn (5.14).

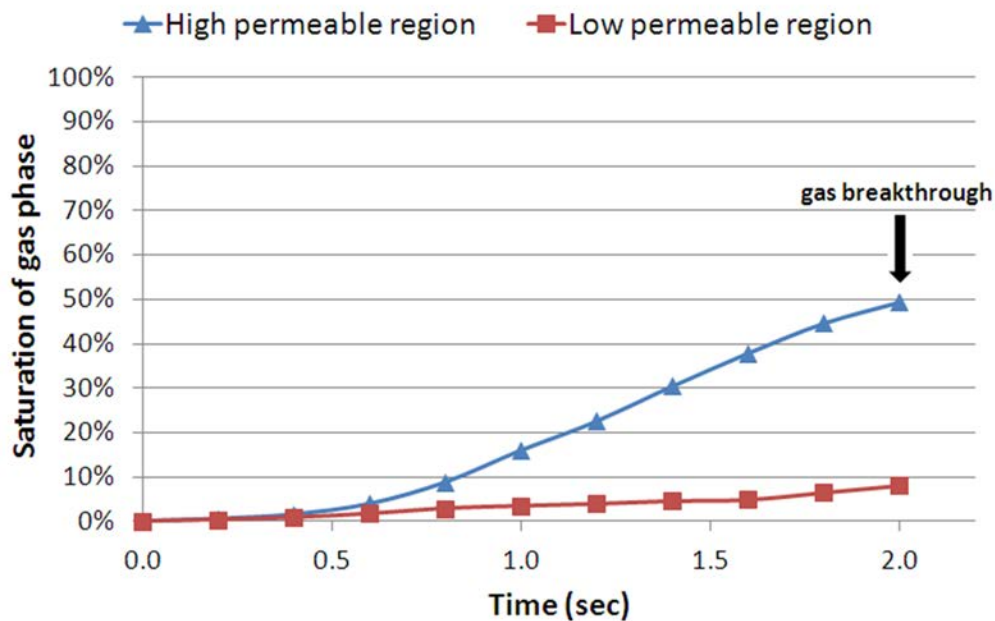
$$t_{bt} = -\frac{V_{swept} \left(\frac{C_0}{kk_{rg}} + \frac{C_1}{R^2}\right)\mu_g}{\nabla P_g A} \quad (5.14)$$

This equation indicates that, given a certain gas pressure gradient ∇P_g in our system, an increase in V_{swept} or μ_g or a decrease in k_{rg} can all lead to a delayed gas breakthrough. The presence of foam is able to decrease the relative permeability, k_{rg} , and increase the apparent viscosity, μ_g ($\mu_{g,app}$), of the gas phase, which leads to favorable mobility control and delayed gas breakthrough. The semi-empirical foam model in Eqn (5.15) (Hirasaki and Lawson 1985; Kam 2008; Chen, Gerritsen et al. 2010) shows that the gas mobility in the presence of foam depends on the bubble size and the gas saturation:

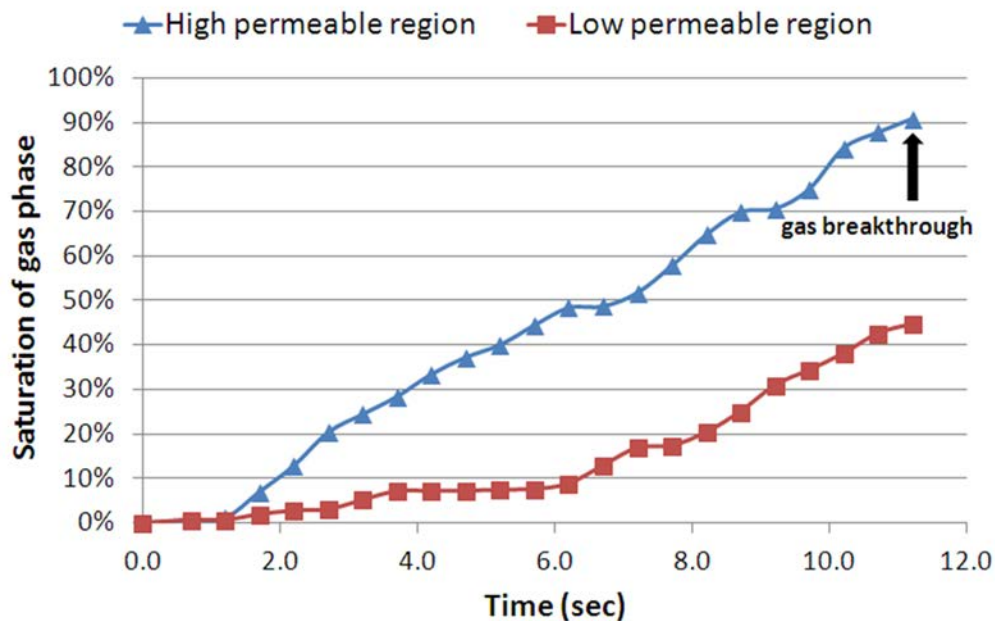
$$\mu_g^f = \mu_g^0 + \frac{C_f n_f}{[u_g / (\phi S_g)]^{1/3}} \quad (5.15)$$

In Eqn (5.15), ϕ is the porosity of the system, C_f is a model parameter characterizing foam strength, and μ_g^f and μ_g^0 are gas viscosities with and without foam, respectively. This foam model shows that an increase in the foam texture (n_f , inversely related to bubble size), an increase in the gas saturation (S_g) and a decrease in the gas superficial velocity (u_g) can all lead to an increase in the effective gas viscosity. Additionally, the presence of foam increases the volume swept, V_{swept} , by gas in the heterogeneous porous medium, which also contributes to late breakthrough of the gas phase. However, the mobility reduction by foam plays a key role in improved sweep and fluid diversion, thus V_{swept} is highly dependent on k_{rg} reduction and μ_g enhancement.

In Table 5-4, Run ID 10 shows that 100% gas injection at 400 mbar causes very early gas breakthrough (0.03 sec) as a result of poor mobility control due to the low viscosity of air. Even with a lowered gas inlet pressure of 50 mbar, the gas breakthrough is still an order of magnitude faster than the cases with pre-generated foam. By comparing the case of 100% gas in Run ID 10 with the case of late gas breakthrough in Run ID 8, the presence of pre-generated foam in Run ID 8 is able to delay the time of gas breakthrough by a factor of 373.3 in our heterogeneous porous medium, owing to the combined effect of mobility reduction and improved sweep as described in Eqn (5.14).



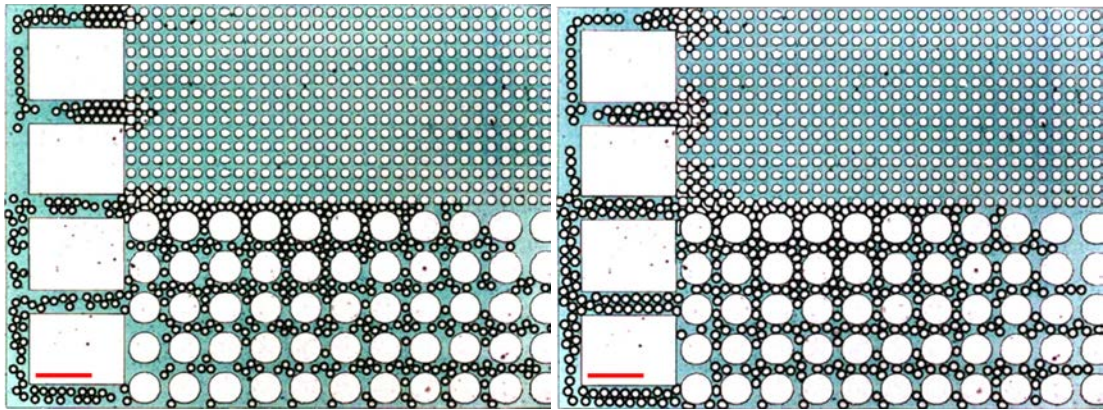
(a) $P_g = 400$ mbar and $F_l = 0.80$ ml/hr;



(b) $P_g = 400$ mbar and $F_l = 0.05$ ml/hr.

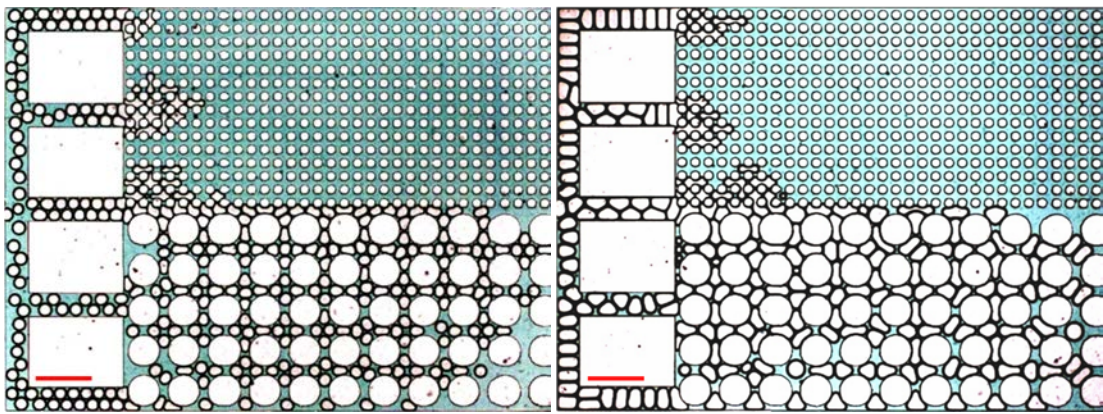
Figure 5-16. Displacement profiles in high and low permeable regions before gas breakthrough within the image captured. (a) The surfactant flow rate is 0.80 ml/hr (Run ID 1); (b) the surfactant flow rate is 0.05 ml/hr (Run ID 8). Gas inlet pressure is controlled at 400 mbar. Videos recorded by the high speed camera are available in the supplementary materials.

To demonstrate the effect of foam quality on the efficiency of fluid diversion, we compare two representative displacement profiles with surfactant flow rates of 0.80 and 0.05 ml/hr at a gas inlet pressure of 400 mbar in Figure 5-16. When the surfactant flow rate is set at 0.80 ml/hr, a wet foam is generated containing small bubbles with an average diameter of 65.5 μm dispersed in the aqueous phase (Figure 5-17(a)); when the surfactant flow rate is decreased to 0.05 ml/hr, a dry foam is generated containing large bubbles with an average hydraulic diameter of 185.2 μm separated by thin liquid lamellae (Figure 5-17(h)). Figure 5-16 shows that in both cases, a substantial amount of gas enters the low permeable region as foam sweeps through the high permeable region. The dry foam in Figure 5-16(b) exhibits a longer time for gas breakthrough than the wet foam in Figure 5-16(a), due to the thin liquid lamellae reducing the gas mobility more readily than the wet foam. Although gas saturation is affected by the aqueous fractional flow in addition to the foam strength, the dry foam in Figure 5-16(b) shows better performance in gas diversion to the low permeable region compared with the wet foam in Figure 5-16(a). At the time of gas breakthrough, the ratio of gas saturation in the high permeable region to the low permeable region is 2.04:1 for the dry foam, and 6.25:1 for the wet foam according to Figure 5-16. Qualitatively, dry foams that are separated by thin lamellae are more desirable for diversion of the gas phase in heterogeneous porous media.



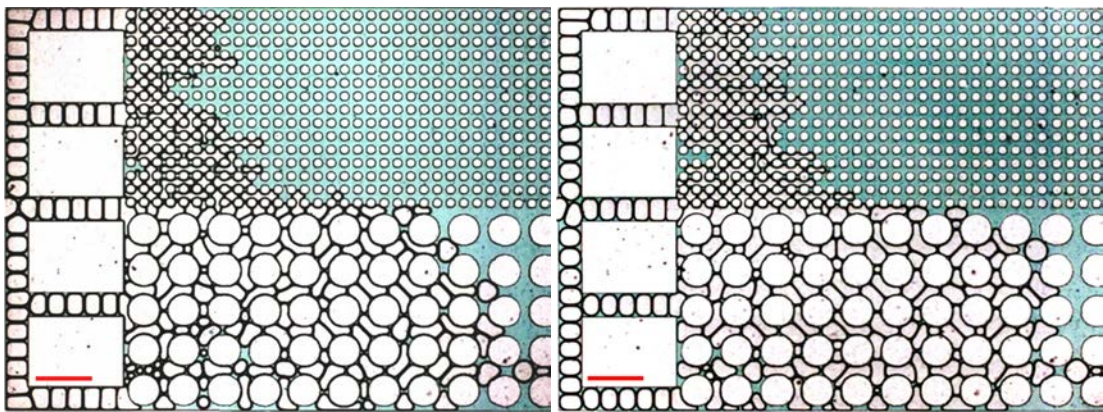
(a) $F_1 = 400$ mbar and $F_2 = 0.80$ ml/hr;

(b) $F_1 = 400$ mbar and $F_2 = 0.40$ ml/hr;



(c) $F_1 = 400$ mbar and $F_2 = 0.20$ ml/hr;

(d) $F_1 = 400$ mbar and $F_2 = 0.16$ ml/hr;



(e) $F_1 = 400$ mbar and $F_2 = 0.13$ ml/hr;

(f) $F_1 = 400$ mbar and $F_2 = 0.10$ ml/hr;

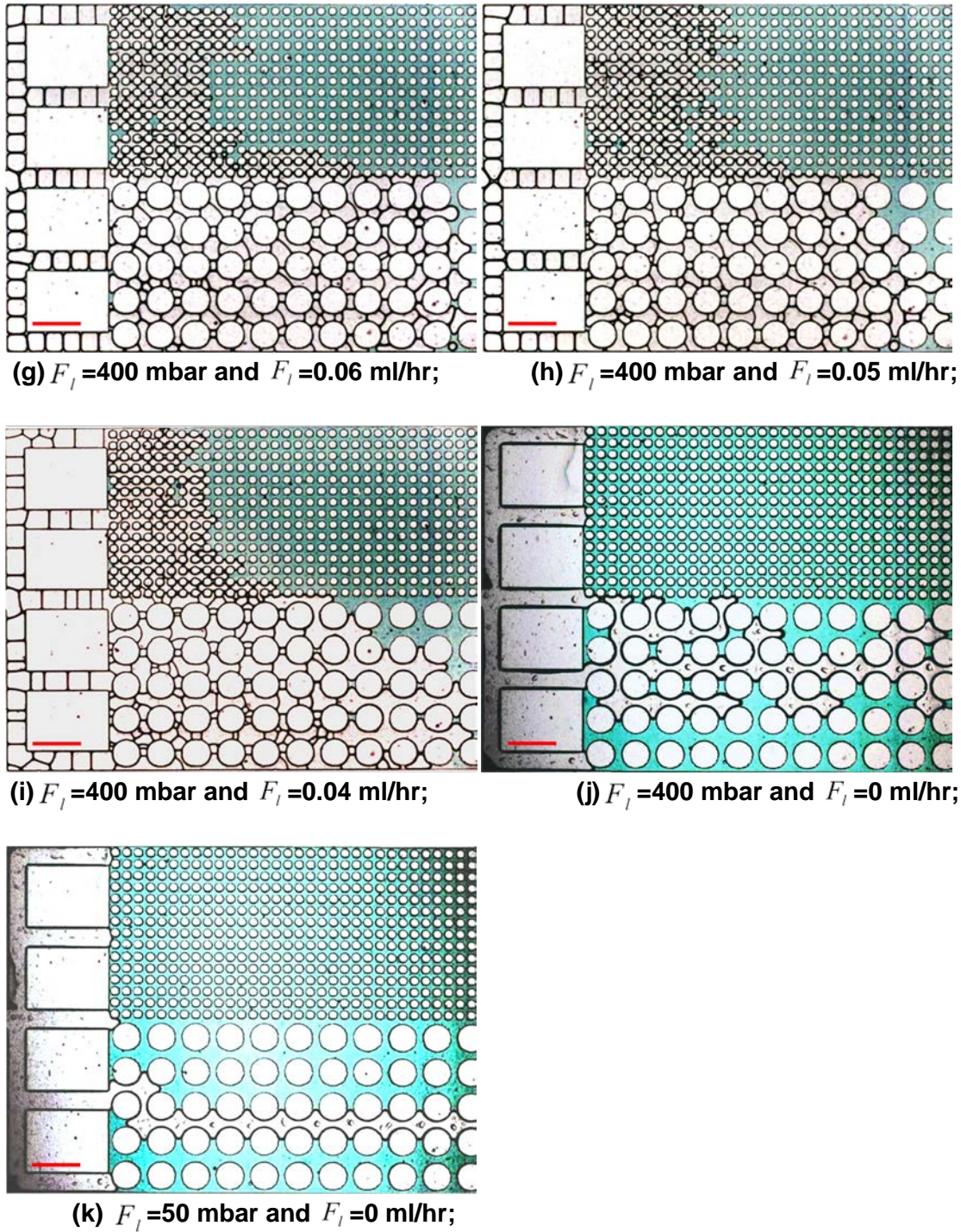


Figure 5-17. Snapshots of the porous media at gas breakthrough within the image captured. The gas inlet pressure and the flow rates of the aqueous phase are indicated underneath the images. The red scale bar at the lower left corner represents 500 μm .

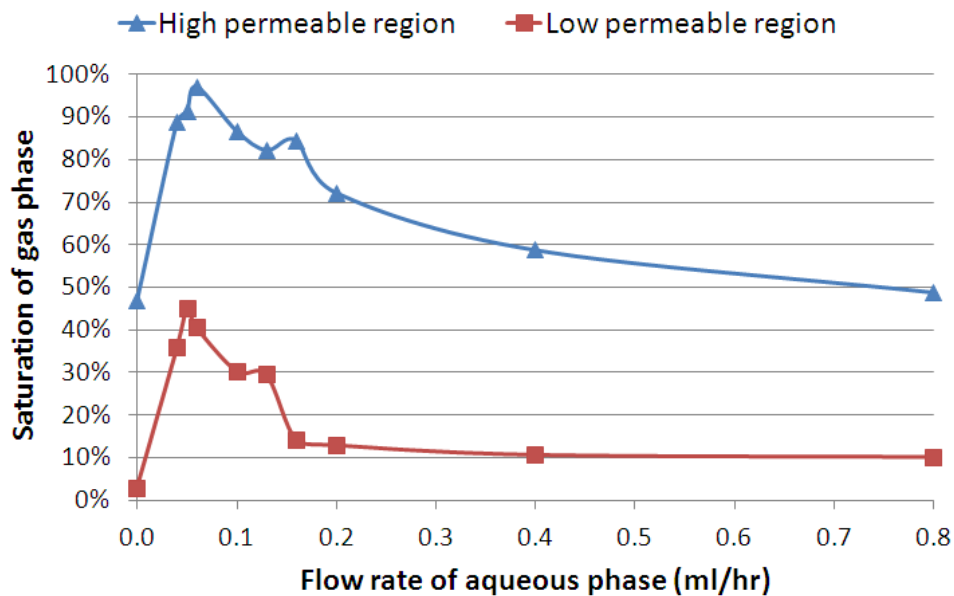
The snapshots of gas breakthrough in all experiments (Run ID 1 to 11) are compared in Figure 5-17. It is observed that at a given gas inlet pressure, as the surfactant flow rate decreases the bubble size increases, which is expected and has been well predicted in similar flow-focusing devices (Garstecki, Gitlin et al. 2004). However, after monodisperse bubbles enter the porous medium, in-situ generation and coalescence of foam occur. It is shown that in our experiments, lamella division (Kovscek and Radke 1994) is the dominating mechanism for generating bubbles with sizes smaller than those entering the porous medium (Figure 5-17(e) - (i)). When a mobilized lamella comes across a pore throat, it splits into two separate lamellae thus creating smaller bubbles. Foam texture, which is defined as the number of lamellae per unit volume present in porous media, becomes finer through the mechanism of lamella division. If the gas fraction remains unchanged, finely textured foam with small bubbles reduces gas phase mobility significantly, which contributes to fluid diversion into the low permeable region as foam propagates through the high permeable region (Figure 5-17(e) - (i)). Meanwhile, for the high permeable region in Figure 5-17(a) - (c) bubbles flow through the pore throats without splitting the liquid lamella, because the diameters of the moving gas bubbles are smaller than the pore throats.

It has been documented that two regimes exist in the case of foam flow through porous media: the high-quality regime with high gas fractional flow (dry foam) and the low-quality regime with low gas fractional flow (wet foam) (Osterloh and Jante Jr 1992). In the high-quality regime, gas bubbles are separated by thin liquid lamellae and capillary pressure controls foam behavior

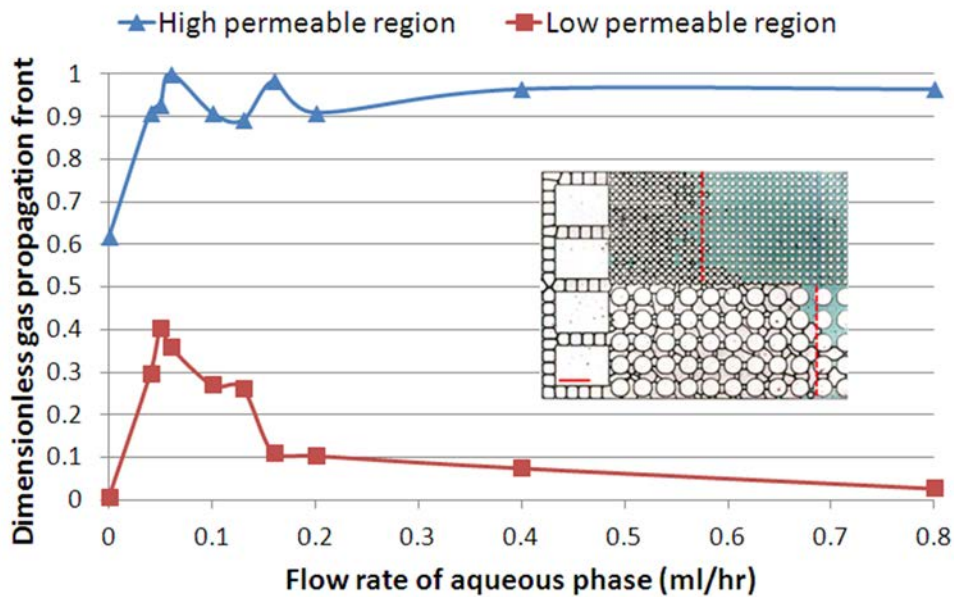
(Khatib, Hirasaki et al. 1988; Alvarez, Rivas et al. 2001) as shown in Figure 5-17(e) to (i); in the low-quality regime, the water fractions are generally high and bubble trapping and mobilization dominate foam flow (Rossen and Wang 1999) as in the case of Figure 5-17(a) and (b); Figure 5-17(c) and (d) show characteristics of both regimes and could be considered the boundary of these two foam regimes. Based on the qualitative observations in Figure 5-17, at the time of gas breakthrough, foam in the high-quality regime has a longer propagation distance through the low permeable region than foam in the low-quality regime, indicating that the high-quality regime is preferred to divert foam into the low permeable region.

Figure 5-17(j) and (k) show the snapshots of 100% air injection at the point of gas breakthrough in Run ID 10 and 11, respectively. As indicated in Figure 5-17(j), at a gas inlet pressure of 400 mbar the gas thread only penetrates the high permeable region, leaving the low permeable region unswept. When the gas inlet pressure is decreased to 50 mbar, the gas fingering effect is more significant as the gas thread follows a single path without branching, as shown in Figure 5-17(k). In both cases of 100% air injection, the volume swept V_{swept} by gas in the high permeable region is smaller than that with dry foam in Figure 5-17(h). Meanwhile, we observe polydisperse gas slugs upstream of the porous medium soon after gas breakthrough in Run ID 10 with 400 mbar gas inlet pressure (data not shown). These gas slugs enter the high permeable region and function as foam, diverting the incoming gas into the low permeable region. However, this phenomenon is not seen in Run ID 11, when the gas inlet pressure is set at 50

mbar. This behavior is closely related to the shear rate of the gas phase. High pressure increases the shear rate, which leads to a higher capillary number for the gas phase and capillary instability in the long winding channel (Figure 5-15) when the gas thread displaces the dye solution. Nevertheless, foam is still advantageous for gas diversion into the low permeable region as it significantly lowers the mass flow rate of gas given a certain gas inlet pressure, which makes the displacement process more efficient and economical.



(a)



(b)

Figure 5-18. Comparison of (a) gas phase saturation and (b) dimensionless gas propagation front at gas breakthrough within the image captured. The dimensionless gas propagation front is calculated by the arithmetic mean of the dimensionless position of gas front in all rows of pore throats, and the length of the porous medium within the image captured is treated as the unit distance for dimensionless scale. An example (Run ID 8) of how the dimensionless gas propagation front is defined is shown by vertical dashed lines in the image in Figure 5-17(b). Gas inlet pressure is controlled at 400 mbar.

A quantitative analysis of the snapshots in Figure 5-17 is shown in Figure 5-18 to understand the mechanism of foam on fluid diversion. The phase saturations from Figure 5-17 in both high and low permeable regions are analyzed in Figure 5-18(a). The results show that at the time of gas breakthrough, the saturation of gas phase increases as the flow rate of surfactant solution decreases, until reaching a critical flow rate (0.05 ml/hr), which corresponds to a specific foam quality and capillary pressure. At a specific gas inlet pressure, both the decrease in surfactant flow rate and the increase in foam strength enhance

gas saturation. Generally foam becomes more viscous as it transitions from a low lamella (sparse bubbles) regime (Figure 5-17(a)) to the lamella-dominant regime (Figure 5-17(h)). As a result, stronger foam improves the sweep efficiency and increases the gas saturation. However, below the critical surfactant flow rate, poor foam mobility control is observed and the saturation of gas in both high and low permeable regions sharply declines as indicated in Figure 5-18(a). This is in agreement with the “limiting capillary pressure (P_C^*)” in the high-quality foam regime (Khatib, Hirasaki et al. 1988), which states that capillary coalescence occurs if the foam quality is above a certain value, resulting in coarse-textured foam to maintain the capillary pressure between the gaseous and aqueous phases. In the high permeable region of Figure 5-17(i), the existence of large bubbles in the gas front demonstrates this fact due to the in situ coalescence of gas bubbles by capillary suction. The coarse-textured foam leads to reduced apparent viscosity in the gas phase and reduced sweep efficiency in the low permeable region. Since for surfactant flow rates in the range of 0 to 0.05 ml/hr the saturation of aqueous phase decreases with the increase of the surfactant flow rate, the foam strength dominates gas saturations in both high and low permeable regions in this regime.

To compare the propagation efficiency of the gas phase in the low permeable region, Figure 5-18(b) presents a quantitative analysis of the gas propagation front in both high and low permeable regions at the time of gas breakthrough. As the snapshots in Figure 5-17 are taken at gas breakthrough, a dimensionless gas propagation front greater than 0.9 in the high permeable

region is expected and observed for most cases with foam, regardless of the surfactant flow rate. However, in the case of 100% gas injection, the dimensionless gas propagation front is only 0.62 in the high permeable region, which indicates the occurrence of significant gas fingering as shown in Figure 5-17(j). Therefore in contrast to 100% gas, both high-quality foam and low-quality foam are able to overcome the gas fingering problem when flowing through the homogeneous high permeable region.

When the water content is high (wet foam), gas saturation does not necessarily indicate gas propagation. At high surfactant flow rates, comparison of Figure 5-18(a) and (b) demonstrates that in the low permeable region the gas propagation front shows consistency with gas saturation, while in the high permeable region there is inconsistency between the gas propagation front and gas saturation. Consistency is observed in the low permeable region because the small pore throats of the low permeable region cause gas bubbles to squeeze together, leading to an increase in foam quality. This observation indicates that foam tends to become drier when diverted into the low permeable region especially in the case of wet foam. In contrast, the large pore throats of the high permeable region allow wet foam to easily pass through without filling the void space so that gas saturation is much lower than the gas propagation front. This behavior can be visualized in Figure 5-17(a) and (b).

At the time of gas breakthrough, the furthest gas propagation front (40.4% in dimensionless scale) in the low permeable region occurs for Run ID 8, which also corresponds to the longest time to reach gas breakthrough as indicated in Table

5-4. These results suggest that the most effective foam for fluid diversion contains gas bubbles separated by thin liquid lamellae, where the gas pressure inside the bubbles approaches but does not exceed the limiting capillary pressure (P_c^*). P_c^* is dependent on permeability, as it has been shown that lower permeability corresponds to higher limiting capillary pressure (Khatib, Hirasaki et al. 1988; Rossen 1992). When foam is diverted into the low permeable region both P_c^* and the actual capillary pressure (P_c) among pore-spanning gas bubbles increase. The coarsen rate of the foam texture depends on relationship between P_c and P_c^* which needs further investigation.

In the future, we will investigate the performance of fluid diversion by surfactant-stabilized foam in the presence of nonaqueous phase, which also involves the study of the stability of foam with oil or organic contaminants in underground formations. In order to gain a better understanding of a real heterogeneous porous medium, we will study the effect of varying permeability ratios (including matrix/ fracture system) on foam diversion, quantify the cross flow between different permeable layers, and create heterogeneity along the flow direction. Additionally, we will attempt to independently change the gas fractional flow (foam quality) and the bubble size in our future micromodel experiments.

5.4 Conclusions

By utilizing UV-ozone oxidization approach to modify surfaces, we have successfully patterned and tuned the wettability in PDMS-based microfluidic

devices. The rate of surface hydrophilization of PDMS with UV-ozone oxidation is accelerated by extending curing time at elevated temperature. This improves the efficiency of microfluidic fabrication without losing the advantage of precise wettability tuning of this approach.

Through a one-dimensional diffusive reaction model, it is found that the initial concentration of LMW species residing in cured PDMS significantly affects the rate of surface hydrophilization during the UV-ozone oxidation process which agrees with the trend observed in our experimental results. The initial concentration of LMW species is minimized through sufficient curing time of PDMS at elevated temperature. The key issue of wettability control of UV-ozone-oxidized PDMS is to control the diffusivity of LMW species as shown by the experimental and modeling results of the hydrophobic recovery process. Low temperature and water immersion are effective ways to decrease the diffusivity of LMW species in PDMS and achieve better wettability control.

In a flow-focusing microfluidic geometry where CO₂ enters from the central channel and the aqueous phase enters from the side channels, different wettability results in different flow patterns, under the condition that the other variables are kept the same, including the flow rate of aqueous phase, the in-flow pressure of CO₂ and the channel dimensions. Various flow patterns are observed, including aqueous phase flow, dripping flow, jetting flow, stratified flow and unstable slug flow. There exists a minimum entry pressure for the CO₂ phase to enter the downstream channel. The use of the AOS 1618 surfactant lowers this pressure threshold due to the reduction of surface tension.

Pre-generated foam is found to effectively improve the sweep of gas through a heterogeneous aqueous-phase-saturated porous medium. Substantial fluid diversion is observed in the presence of foam, and the most efficient foam diversion to the low permeable region occurs with pore-spanning bubbles separated by lamellae. This work demonstrates that the use of pre-generated foam has the potential to improve the sweep efficiency in heterogeneous porous media, which is applicable to aquifer remediation and enhanced oil recovery processes.

5.5 References

- Alvarez, J. M., H. J. Rivas, et al. (2001). "Unified model for steady-state foam behavior at high and low foam qualities." SPE Journal **6**(3): 325-333.
- Andrade, J. D. (1985). Surface and interfacial aspects of biomedical polymers. New York, Plenum Press.
- Berdichevsky, Y., J. Khandurina, et al. (2004). "UV/ozone modification of poly(dimethylsiloxane) microfluidic channels." Sensors and Actuators B-Chemical **97**(2-3): 402-408.
- Bird, R. B., W. E. Stewart, et al. (2002). Transport phenomena. New York, John Wiley & Sons.
- Bretherton, F. P. (1961). "The Motion of Long Bubbles in Tubes." Journal of Fluid Mechanics **10**(2): 166-188.
- Carman, P. C. (1937). "Fluid flow through granular beds." Transactions, Institution of Chemical Engineers, London **15**: 150-166.
- Cassie, A. B. D. and S. Baxter (1944). "Wettability of porous surfaces." Transactions of the Faraday Society **40**: 0546-0550.
- Chan, V. Z. H., E. L. Thomas, et al. (1998). "Curious morphology of silicon-containing polymer films on exposure to oxygen plasma." Chemistry of Materials **10**(12): 3895-3901.
- Chen, I. J. and E. Lindner (2007). "The stability of radio-frequency plasma-treated polydimethylsiloxane surfaces." Langmuir **23**(6): 3118-3122.
- Chen, Q., M. G. Gerritsen, et al. (2010). "Modeling foam displacement with the local-equilibrium approximation: theory and experimental verification." SPE Journal **15**(1): 171-183.

- Cubaud, T. and C. M. Ho (2004). "Transport of bubbles in square microchannels." Physics of Fluids **16**(12): 4575-4585.
- Eddington, D. T., J. P. Puccinelli, et al. (2006). "Thermal aging and reduced hydrophobic recovery of polydimethylsiloxane." Sensors and Actuators B-Chemical **114**(1): 170-172.
- Efimenko, K., W. E. Wallace, et al. (2002). "Surface modification of Sylgard-184 poly(dimethyl siloxane) networks by ultraviolet and ultraviolet/ozone treatment." Journal of Colloid and Interface Science **254**(2): 306-315.
- Fu, Y. J., H. Z. Qui, et al. (2010). "Effect of UV-Ozone Treatment on Poly(dimethylsiloxane) Membranes: Surface Characterization and Gas Separation Performance." Langmuir **26**(6): 4392-4399.
- Garstecki, P., I. Gitlin, et al. (2004). "Formation of monodisperse bubbles in a microfluidic flow-focusing device." Applied Physics Letters **85**(13): 2649-2651.
- Gent, A. N. and R. H. Tobias (1982). "Diffusion and Equilibrium Swelling of Macromolecular Networks by Their Linear Homologs." Journal of Polymer Science Part B-Polymer Physics **20**(12): 2317-2327.
- Gordillo, J. M., A. M. Ganan-Calvo, et al. (2001). "Monodisperse microbubbling: Absolute instabilities in coflowing gas-liquid jets." Physics of Fluids **13**(12): 3839-3842.
- Green, D. W. and G. P. Willhite (1998). Enhanced oil recovery. Richardson, TX, Henry L. Doherty Memorial Fund of AIME, Society of Petroleum Engineers.
- Hadley, G. F. and L. L. Handy (1956). A Theoretical and Experimental Study of the Steady State Capillary End Effect. Fall Meeting of the Petroleum Branch of AIME. Los Angeles, California.
- Hirasaki, G. J. and J. B. Lawson (1985). "Mechanisms of Foam Flow in Porous-Media - Apparent Viscosity in Smooth Capillaries." Society of Petroleum Engineers Journal **25**(2): 176-190.
- Holmesfarley, S. R., R. H. Reamey, et al. (1987). "Reconstruction of the Interface of Oxidatively Functionalized Polyethylene and Derivatives on Heating." Langmuir **3**(5): 799-815.
- Jeong, S. W. and M. Y. Corapcioglu (2003). "A micromodel analysis of factors influencing NAPL removal by surfactant foam flooding." Journal of Contaminant Hydrology **60**(1-2): 77-96.
- Kam, S. I. (2008). "Improved mechanistic foam simulation with foam catastrophe theory." Colloids and Surfaces a-Physicochemical and Engineering Aspects **318**(1-3): 62-77.
- Khatib, Z. I., G. J. Hirasaki, et al. (1988). "Effects of capillary pressure on coalescence and phase mobilities in foams flowing through porous media." SPE Reservoir Engineering **3**(3): 919-926.
- Kiefer, J. (1953). "Sequential Minimax Search for a Maximum." Proceedings of the American Mathematical Society **4**(3): 502-506.
- Kim, J., M. K. Chaudhury, et al. (2006). "Modeling hydrophobic recovery of electrically discharged polydimethylsiloxane elastomers." Journal of Colloid and Interface Science **293**(2): 364-375.
- Kini, G. C., J. Lai, et al. (2010). "Microfluidic Formation of Ionically Cross-Linked Polyamine Gels." Langmuir **26**(9): 6650-6656.

- Kovscek, A. R. and C. J. Radke (1994). "Fundamentals of foam transport in porous-media." Foams: Fundamentals and Applications in the Petroleum Industry **242**: 115-163.
- Kovscek, A. R., G. Q. Tang, et al. (2007). "Verification of Roof snap off as a foam-generation mechanism in porous media at steady state." Colloids and Surfaces a-Physicochemical and Engineering Aspects **302**(1-3): 251-260.
- Landau, L. D. and E. M. Lifshietis (1959). Fluid mechanics , Pergamon Press; Addison-Wesley Pub. Co.
- Lee, J. N., C. Park, et al. (2003). "Solvent compatibility of poly(dimethylsiloxane)-based microfluidic devices." Analytical Chemistry **75**(23): 6544-6554.
- Li, R. F., G. J. Hirasaki, et al. (2012). "Wettability Alteration and Foam Mobility Control in a Layered, 2D Heterogeneous Sandpack." SPE Journal **17**(4): 1207-1220.
- Llave, F. M., F. T. H. Chung, et al. (1990). Foams as Mobility Control Agents for Oil Recovery by Gas Displacement. SPE/DOE Enhanced Oil Recovery Symposium . Tulsa, Oklahoma.
- Ma, K., J. Rivera, et al. (2011). "Wettability control and patterning of PDMS using UV-ozone and water immersion." Journal of Colloid and Interface Science **363**(1): 371-378.
- Mathison, D. E., B. Yates, et al. (1991). "Absorption of Silicone Fluid in a Silicone Elastomer." Journal of Materials Science **26**(1): 6-10.
- Mirley, C. L. and J. T. Koberstein (1995). "A Room-Temperature Method for the Preparation of Ultrathin Siox Films from Langmuir-Blodgett Layers." Langmuir **11**(4): 1049-1052.
- Olah, A., H. Hillborg, et al. (2005). "Hydrophobic recovery of UV/ozone treated poly(dimethylsiloxane): adhesion studies by contact mechanics and mechanism of surface modification." Applied Surface Science **239**(3-4): 410-423.
- Osterloh, W. T. and M. J. Jante Jr (1992). Effects of gas and liquid velocity on steady-state foam flow at high temperature. SPE/DOE Enhanced Oil Recovery Symposium . Tulsa, Oklahoma, 1992 Copyright 1992, Society of Petroleum Engineers Inc.
- Rice, S. L., A. F. Diaz, et al. (1988). "Absorption of Silicone Oil by a Dimethylsiloxane Elastomer." Rubber Chemistry and Technology **61**(2): 194-204.
- Romero-Zeron, L. and A. Kantzas (2005). "Pore-scale visualization of foamed gel propagation and trapping in a pore network micromodel." Journal of Canadian Petroleum Technology **44**(5): 44-50.
- Rossen, W. R. (1992). "Rheology of Foam in Porous-Media at the Limiting Capillary-Pressure." Revue De L Institut Francais Du Petrole **47**(1): 68-80.
- Rossen, W. R. (2008). "Comment on "Verification of Roof snap-off as a foam-generation mechanism in porous media at steady state"." Colloids and Surfaces a-Physicochemical and Engineering Aspects **322**(1-3): 261-269.
- Rossen, W. R. and M. W. Wang (1999). "Modeling Foams for Acid Diversion." SPE Journal (06).
- Spiendiani, A., C. Nicolella, et al. (2003). "A novel biphasic extractive membrane bioreactor for minimization of membrane-attached biofilms." Biotechnology and Bioengineering **83**(1): 8-19.

- Thompson, P. A., W. B. Brinckerhoff, et al. (1993). "Microscopic Studies of Static and Dynamic Contact Angles." Journal of Adhesion Science and Technology **7**(6): 535-554.
- Xia, Y. N. and G. M. Whitesides (1998). "Soft lithography." Angewandte Chemie-International Edition **37**(5): 551-575.
- Ye, H. K., Z. Y. Gu, et al. (2006). "Kinetics of ultraviolet and plasma surface modification of poly(dimethylsiloxane) probed by sum frequency vibrational spectroscopy." Langmuir **22**(4): 1863-1868.

Conclusions and future work

The previous chapters have described experimental and modeling results of foam transport and chromatographic retardation of surfactants. The understanding of foam transport in porous media is still far from complete and this chapter provides a short summary of the work performed in this thesis as well as recommendations for future directions.

6.1 Summary of main findings

6.1.1 Screening of low-adsorbing surfactants on carbonates

Surfactant adsorption experiments were performed on natural dolomite powder at room temperature. Among the nine surfactants tested, the nonionic surfactant Tergitol 15-S-30 and the ethoxylated cationic surfactant Ethomeen C/25A exhibited low adsorption in alkaline conditions, with plateau values of 0.54 mg/m² and 0.57 mg/m², respectively. The reason for low adsorption was considered to be the weak electrostatic interactions between the surfactants and the dolomite surface. Anionic (AOS 1618 and IOS 1518) and zwitterionic (cocamidopropyl hydroxysultaine and lauryl betaine) surfactants generally had moderate to high adsorption on dolomite; however, the ethoxylated anionic surfactant (STEOL CS-330) showed relatively low adsorption (1.1 mg/m²).

The reason why some cationic surfactants exhibited high adsorption on natural dolomite was found to be caused by impurities in natural dolomite. Synthetic calcite and natural limestone and dolomite were used to evaluate the adsorption behavior by comparing the anionic sodium dodecyl sulfate (SDS) and the cationic cetylpyridinium chloride (CPC). A substantial amount of silicon and aluminum was found in natural dolomite and limestone, but not in synthetic calcite using x-ray photoelectron spectroscopy. The adsorption plateau of CPC on carbonates highly depended on the silicon and aluminum composition in the carbonate samples due to the strong electrostatic interaction between CPC and negative binding sites in silica and/or clay. CPC even exhibited negative adsorption in alkaline conditions on synthetic calcite in which silicon and aluminum were negligible. Our result indicated that low adsorption of CPC on carbonates was only valid when the silicon and aluminum composition was low. Therefore, cationic surfactants could be considered as low-adsorbing EOR candidates on high-purity carbonates but not on carbonates with high silica and/clay.

6.1.2 Modeling foam flow and surfactant transport in porous media

In order to understand foam and surfactant transport in porous media, a one-dimensional simulator was established using the IMPES (implicit in pressure and explicit in saturation) formulation. The simulator modified gas relative permeability using the STARS foam model to describe the effect of foam on mobility reduction. In addition to foam transport, the transport of surfactant was

also modeled in the simulator using a convective diffusion equation. Surfactant adsorption on reservoir formation and partitioning between phases were included in the simulator. The code for finite difference simulation was verified by the method of characteristics.

Dynamic simulation of surfactant adsorption in aqueous-phase flow was performed using the simulator. The adsorption isotherms obtained from static adsorption results on dolomite were used for dynamic simulation. The simulation results indicated significant chromatographic retardation of high-adsorbing surfactants such as Mackam LAB (lauryl and myristyl betaines) compared with the tracer and low-adsorbing surfactants such as Ethomeen C/25A (15-EO cocoalkylamines). The high-adsorbing surfactants also showed undesirable behavior in simulations of finite surfactant slug injection, as a result of severe interactions of the leading shock wave at the adsorption front and the tailing spreading wave due to desorption which significantly smeared out the effluent. Thus, low-adsorbing surfactants such as Ethomeen C/25A were recommended in EOR processes.

If the surfactant was CO₂-soluble, the study on surfactant partitioning between CO₂ and water indicated that surfactant could be injected either with CO₂ or water. If the surfactant was injected with CO₂ at a certain concentration, larger partition coefficient between CO₂ and water (i.e., the surfactant favors CO₂) led to faster foam propagation. However, the foam strength depended on the surfactant concentration in aqueous phase (if this concentration was below the critical surfactant concentration, f_{msurf}) and the water saturation according to

the STARS foam model. If the partition coefficient between CO₂ and water was small (i.e., the surfactant favors water), one needed to design the injection strategy such that the surfactant concentration in aqueous phase did not significantly exceed $fmsurf$, less the portion for adsorption consumption.

6.1.3 Estimation of parameters for foam simulation in porous media

In the absence of oil in the porous medium, the foam model has three parameters to describe the foam quality dependence, $fmmob$, $fmdry$, and $epdry$. We performed laboratory experiments to estimate these three parameters. Gas and surfactant solution were co-injected into a sand pack. At steady state, saturation of the aqueous phase was shown to be relatively constant over a wide range of foam qualities, which was consistent with the STARSTM foam model using the dry-out function. In order to obtain an accurate model fit at the transition foam quality, the difference between the foam model parameter $fmdry$ and the transition water saturation S_w^t was identified and a method to precisely calculate S_w^t was developed. By superimposing contour plots of the transition foam quality and the foam apparent viscosity with a preset $epdry$, one could estimate $fmmob$ and $fmdry$ using the STARSTM foam model. The parameter $epdry$, which regulated the abruptness of the foam dry-out effect, could be estimated by a transient foam experiment in which 100% gas displaces surfactant solution at 100% water saturation. This transient scanned the entire

range of fractional flow and the values of the foam parameters that best matched the experiment could be uniquely determined.

Even for a specified value of $epdry$, two pairs of values of $fmmob$ and $fmdry$ could sometimes match the transition foam data. This non-uniqueness could be broken by limiting the solution to the one for which $fmdry$ was smaller than S_w^t . Additionally, a multi-dimensional three-parameter search was developed to estimate the parameters $fmmob$, $fmdry$, and $epdry$ simultaneously using all available experimental data points. Depending on the initial guess, the possibility of reaching a local optimal solution rather than the global optimal solution was discussed. The penalty function method for constrained optimization could be applied for a wider range of initial guesses.

Finite difference simulation for the transient foam process was consistent with the method of characteristics. The numerical artifact in finite difference simulation was revealed by local apparent viscosity profiles using the method of characteristics. Finite difference simulation led to an overestimation and oscillations in foam apparent viscosity as a result of the spike viscosity in foam displacement front. For parameter sets which matched steady-state foam data, small $epdry$ led to lower amplitude in numerical oscillation and larger apparent viscosity when foam broke through.

6.1.4 Micromodel study of foam flow in porous media

A simple method was developed to tune and pattern the wettability of polydimethylsiloxane (PDMS) to generate microfluidic mimics of heterogeneous porous media. This technique allowed one to tailor the capillary forces at different regions within the PDMS channel to mimic multi-phase flow in oil reservoirs. In this method, UV-ozone treatment was utilized to oxidize and hydrophilize the surface of PDMS. The rate of surface hydrophilization of PDMS with UV-ozone oxidation was accelerated by extending curing time at elevated temperature. This improved the efficiency of microfluidic fabrication without losing the advantage of precise wettability tuning of this approach. To maintain a stable surface wettability, the oxidized surfaces were immersed in water. Additionally, the use of a photomask made it convenient to pattern the wettability in the porous media. A one-dimensional diffusive reaction model was established to understand the UV-ozone oxidation as well as hydrophobic recovery of oxidized PDMS surfaces. The modeling results showed that during UV-ozone, surface oxidation dominated over diffusion of low-molecular-weight (LMW) species. However, the diffusivity of LMW species played an important role in wettability control of PDMS surfaces.

The effect of wettability on two-phase flow patterns in microchannels was demonstrated in a flow-focusing microfluidic device. CO₂ entered from the central channel and the aqueous phase (surfactant solution or DI water) entered from the side channels. Different wettability resulted in different flow patterns, under the condition that the other variables were kept the same, including the flow rate of aqueous phase, the in-flow pressure of CO₂ and the channel dimensions.

Various flow patterns were observed depending on the wettability of the PDMS surface, including aqueous phase flow, dripping flow, jetting flow, stratified flow and unstable slug flow. There existed a minimum entry pressure for the CO₂ phase to enter the downstream channel. The use of the AOS 1618 surfactant lowered this pressure threshold due to the reduction of surface tension.

The use of foam to divert flow from high permeable to low permeable regions was investigated in a PDMS heterogeneous porous microfluidic system. Foam was generated using a flow-focusing microfluidic device with co-flowing gas and aqueous surfactant streams. Foam quality (gas fractional flow) was modulated by adjusting the flow rate of the aqueous surfactant solution while keeping the gas inlet pressure fixed. The foam was then injected into an aqueous-solution filled heterogeneous porous media containing a high and low permeable region and sweep of the saturated aqueous phase was monitored. Compared with 100% gas injection, surfactant-stabilized foam was shown to effectively improve the sweep of the aqueous fluid in both high and low permeable regions of the porous micromodel. The best performance of foam on fluid diversion was observed in the lamella-separated foam regime, where the presence of foam could enhance gas saturation in the low permeable region up to 45.1% at the time of gas breakthrough. The presented results were useful in understanding and designing foam injection in porous underground formations for aquifer remediation and enhanced oil recovery processes.

6.2 Future work

More foaming surfactants with low adsorption on carbonates should be evaluated. According to our findings in Chapter 2, nonionic surfactants can be potentially used for low temperature carbonate reservoirs. For EOR applications in high temperature and high salinity reservoirs, the screening of ethoxylated amines is a direction for finding low-adsorbing surfactants. In addition to surfactant adsorption, one should also evaluate the surfactant's foaming capacity, thermal stability, and foam stability in the presence of crude oil at reservoir conditions. The surface chemistry of carbonate reservoir formations should be evaluated to quantify the amount of silica and clay in natural carbonates. If the silica and clay content is high, a substantial amount of adsorption on the formation may be expected for cationic surfactants (including ethoxylated amines) due to electrostatic interactions. Means to reduce cationic surfactant adsorption should be sought, and potential determining ions to alter surface charge should be identified. Specifically, the addition of divalent (such as Ca^{2+} and Mg^{2+}) and/or trivalent (such as Al^{3+}) ions, and/or potential positively-charged sacrificial agents in aqueous solution needs to be evaluated for adsorption reduction of cationic surfactants on carbonates.

The simulation for surfactant and foam transport should be expanded to two-dimensional porous media. The effect of gravity segregation in 2-D systems on foam propagation needs to be investigated. In order to have viscous forces dominate over gravitational forces, the minimum foam strength in the target 2-D system needs to be evaluated in terms of sweep efficiency. The transition foam

quality obtained in 1-D systems, which characterizes where the maximum foam strength is achieved, should be measured in 2-D systems and compared with the results in 1-D systems. The effect of limiting capillary pressure on slug size and frequency in SAG injection should also be studied in 2-D systems. The influence of surfactant adsorption on reservoir formation and partition between CO₂, brine, and oil on chromatographic retardation need be evaluated and simulated in 2-D systems. The effect of reservoir heterogeneity such as large permeability contrasts and matrix / fracture systems on foam transport should also be addressed in 2-D systems.

Parameter estimation for modeling foam flow through porous media should include the presence of oil. The effect of oil saturation and oil composition on foam stability should be investigated in both steady-state and transient foam experiments. The effect of trapped gas saturation on foam hysteresis should be carefully addressed. Laboratory co-injection experiments should be conducted to reach steady-state with different initial trapped gas saturations. This effect also needs to be evaluated in the simulation especially in the reservoir scale when the injection gas fraction is changed. For systems below the minimum pressure gradient for strong foam generation, the minimum capillary number should be determined for foam simulation. This effect needs to be combined with the typical shear-thinning effect in foam modeling to reduce the number of parameters to be estimated. Scale-up of foam modeling from 1-D to 3-D systems is needed to conduct reservoir-scale simulation. For a specific surfactant formulation under reservoir temperature and pressure, how the foam modeling parameter changes

from high permeability systems to low permeability systems, from 1-D systems to 2-D and 3-D systems needs to be understood.

In addition to investigations to the local steady-state STARSTM foam model, the mechanistic population-balance foam model should be studied. The foam generation and decay functions in various population-balance foam models should be evaluated with laboratory experiments. The differences between population-balance foam model and local steady-state foam model in simulations of SAG and co-injection of foam flow through porous media should be identified. The procedure to estimate parameters from laboratory foam experiments for the population-balance foam model should be developed. The existence and uniqueness of the solutions for modeling foam flow using the population-balance foam model should also be explored.

Foam-oil interactions should be investigated in micromodel experiments. A design for quickly evaluating foam stability in the presence of oil should be developed. The effect of oil type and surfactant formulation on foam stability needs to be studied in micromodels. The mechanisms for in situ foam generation and coalescence with and without oil should be quantitatively investigated in order to obtain a better understanding to design the population-balance foam model. Foam propagation in systems with large permeability contrast, such as fracture-matrix systems, needs to be evaluated in micromodels. The effect of foam on fluid diversion should be studied in such systems with and without oil. The design of foam generator in micromodel experiments should be improved

such that one can control foam quality (gas fraction) and bubble size independently.

The transport of foam in porous media is a complex process dependent on a number of parameters. This thesis has led to a better understanding of the role of surfactant adsorption, surface wettability, permeability contrast, and foam quality that can be input into transport models of foam. The use of foam for enhanced oil recovery requires further understanding of the interactions of foam with oil and successful field-level demonstration.

Appendix A

Nomenclature in the simulation of surfactant and foam transport in porous media

a = specific surface area

C = concentration

Ca = capillary number

$epdry$ = a parameter regulating the slope of F_2 curve near $fmdry$

f = fractional flow

f_g^t = transition foam quality where the maximum foam apparent viscosity is achieved

FM = a dimensionless foam parameter in the STARS™ foam model

$fmdry$ = critical water saturation in the STARS™ foam model

$fmmob$ = reference mobility reduction factor in the STARS™ foam model

$fmsurf$ = critical surfactant concentration in the STARS™ foam model

F_1 = a function describing the contribution of surfactant concentration in the STARS™ foam model

F_2 = a function describing the contribution of aqueous phase saturation in the STARS™ foam model

K^* = dispersion coefficient

K_{sgw} = partition coefficient of the surfactant between gas phase and aqueous phase

k = permeability of the system

k_r = relative permeability

k_{rw}^0 = end-point relative permeability of aqueous phase

k_{rg}^0 = end-point relative permeability of gas phase

L = length of the system

NX = total number of grid blocks in finite difference simulation

p = pressure

P_c = capillary pressure

P_c^* = limiting capillary pressure

Pe = Peclet number

u = superficial (Darcy) velocity

S = saturation

S_w^t = transition water saturation where the maximum foam apparent viscosity is achieved

t = time

x = distance

ρ = density

μ = viscosity

$\mu_{foam,app}$ = local foam apparent viscosity

$\bar{\mu}_{foam,app}$ = average foam apparent viscosity

$\mu_{foam,app}^t$ = maximum foam apparent viscosity obtained at the transition foam quality

ω = weighting parameter in multi-variable multi-dimensional search

Θ = penalty function in multi-variable multi-dimensional search

σ = penalty coefficient in multi-variable multi-dimensional search

λ_r = relative mobility

ϕ = porosity of the system

$\Gamma_{s,max}$ = adsorption plateau of the surfactant on solid surface

Superscripts

BC = boundary condition

nf = without foam

f = with foam

n_g = exponent in k_{rg} curve

n_w = exponent in k_{rw} curve

t = transition between high-quality and low-quality foam

Subscripts

g = gas phase

gr = residual gas

s = surfactant

sg = surfactant in gas phase

ss = surfactant adsorbed on rock surface

sw = surfactant in aqueous phase

w = aqueous phase

wc = connate water

Appendix B

MATLAB code for 1-D foam simulation

1. foam1D.m

```
%% main program for 1-D foam transport in porous media %%

clear all
clc

NX=50; %total number of grid blocks in x direction
deltax=1/NX; %step length in x direction
deltat=0.005*deltax; %step length in t direction
NT=round(5/deltat); %total number of grid blocks in t direction
TIME_TOTAL=5; %total dimensionless time

T_max=0; %surfactant adsorption plateau (mg/m^2)
Tr_max=0; %tracer (NaCl) adsorption plateau (mg/m^2)
alpha=12.2; %parameter in Langmuir isotherm (L/g)
poro=0.36; %porosity of the formation
rou_s=2.71; %density of the formation (g/cm^3)
a_s=0.1; %specific surface area of the formation (m^2/g)

Cg_inj=0;%injected surfactant concentration in CO2 phase (g/L)
Psgw=0; %partition coefficient between gas phase and aqueous phase
Cw_inj=10; %injected surfactant concentration in aqueous phase (g/L)
NaCl_w_0=1.0; %injected tracer cocentration (dimensionless)

f_g_BC=1; %injected gas fraction (foam quality)

S_wc=0.07; %connate water saturation
S_gr=0; %residual gas saturation
krw0=0.79; %end-point relative permeability for aqueous phase
krg0=1.0; %end-point relative permeability for gas phase
visw=0.001*1e3; %in cp
visg=0.00002*1e3; %in cp
nw=1.96; %exponent in water relative permeability function
ng=2.29; %exponent in gas relative permeability function
fmmob=47094; %reference mobility reduction factor
fmdry=0.1006; %critical water saturation for foam collapse
epdry=500; %dry-out parameter

S_g=zeros(1,NX); % initialize gas phase saturation (invading phase)
S_g(1,:)=S_gr; %IC for gas saturation
S_w=1-S_g; %IC for water saturation

Csw=Cw_inj*ones(1,NX); %IC for aqueous urfactant concentration(g/L)
```

```

    Css=rou_s*a_s*T_max*alpha*Csw./(1+alpha*Csw); %IC for surfactant
adsorption(g/L)

    NaCl_w=zeros(1,NX); %IC for aqueous tracer concentration
(dimensionless)
    NaCl_s=rou_s*a_s*Tr_max*alpha*NaCl_w./(1+alpha*Cw_inj*NaCl_w);

    Fwater=0.5+(atan(epdry*(S_w-fmdry)))/pi; %dry-out function
    fmsurf=10; %minimal surfactant concentration (g/L) to reach full
strength foam
    epsurf=1; %exponent in surfactant-concentration-dependent function
    Fsurf=(Csw/fmsurf).^epsurf; %contribution of surfactant to foam
stability
    FM=1./(1+fmmob*Fwater.*Fsurf); %mobility reduction factor in the
foam model

    S_nor=(S_g-S_gr)/(1-S_gr-S_wc);%normalized gas phase saturation
(invading phase)
    kri=FM.*(S_nor.^ng); %IC for invading (gas) phase relative
permeability
    krd=(1-S_nor).^nw; %IC for displaced (aqueous) phase relative
permeability
    M=krg0/visg/(krw0/visw); %end-point mobility ratio
    lamda=kri+krd/M; %IC for lamda(t,x) = kri + krd/M

    pot=zeros(1,NX); %initialize flow potential
    pc=zeros(1,NX); %initialize dimensionless capillary pressure
    Npc=0; %capillary number in capillary pressure model
    C1=0.17; %parameter C1 in capillary pressure model
    C2=0.29; %parameter C2 in capillary pressure model

    u_w=(1-f_g_BC)*ones(1,NX+1); %dimensionless aqueous phase velocity
at the WALL of each grid block
    %u_w(I-1/2) is in u_w(I) and u_w(I+1/2) is in u_w(I+1)
    u_g=f_g_BC*ones(1,NX+1); %dimensionless gas phase velocity at the
WALL of each grid block

    COUNTER=1;
    TIME=0;
    TIME_HIS(COUNTER)=TIME;
    f_g_HIS(COUNTER)=0;
    f_surf_HIS(COUNTER)=0;
    f_NaCl_HIS(COUNTER)=0;
    f_total_HIS(COUNTER)=0;
    p_drop_HIS(COUNTER)=0;
    VIS_FOAM(COUNTER)=0; %foam apparent viscosity

    Pe_w=1e100; %Define Peclect number for aqueous dispersion Pe=
L*uBC/phi/Ksw
    Pe_g=1e100; %Define Peclect number for gaseous dispersion Pe=
L*uBC/phi/Ksg

    SAG=0; %SAG=1 if Surfactant-Alternating-Gas or SAG=0 if co-
injection

%% enter the loop for caculation in the next time step
while TIME<=TIME_TOTAL

```

```

if SAG==1
    CYCLE=0.3; %SAG cycle throughput
    fg=2/3; %gas fraction per cycle
for JJJJ=1:(round(TIME_TOTAL/CYCLE)+1) %loop for SAG process
    AAAA=JJJJ*CYCLE;
    if TIME>=(AAAA-CYCLE) & TIME<(AAAA-0.0)
        if TIME>=(AAAA-CYCLE) & TIME<(AAAA-CYCLE*fg)
            f_g_BC=0;
        else
            f_g_BC=1;
        end
    end
end
u_w(1)=1-f_g_BC;
end

S_w_old=1-S_g; %water saturation in the current time step for
calculation of surfactant concentration
S_g_old=S_g; %gas saturation in the current time step for
calculation of surfactant concentration
u_w_old=u_w; %water fractional flow in the current time step for
calculation of surfactant concentration
u_g_old=u_g; %gas fractional flow in the current time step for
calculation of surfactant concentration

%% solve Tridiagonal System by LU decomposition and backward
substitution START%%
UPPER=ones(1,NX-1);
for uu=1:(NX-1)
    UPPER(uu)=lamda(uu);
end

MIDDLE=ones(1,NX);
for dd=2:(NX-1)
    MIDDLE(dd)= -(lamda(dd-1)+lamda(dd));
end
MIDDLE(1)=-lamda(1);
MIDDLE(NX)=- (lamda(NX-1)+2*lamda(NX));

if pot(NX)<0 %prevent reverse flow of invading phase
    kri(NX)=0;
    krd(NX)=1;
    lamda(NX)=kri(NX)+krd(NX)/M;
    d(NX)=- (lamda(NX-1)+2*lamda(NX));
end

LOWER=ones(1,NX-1);
for ll=1:(NX-1)
    LOWER(ll)=lamda(ll);
end
[u,d,l]=decomt(UPPER,MIDDLE,LOWER); %find LU decomposition
Tridiagonal Matrix by "decomt.m"

b=zeros(1,NX);
for k=2:(NX-1)
    b(k)=1/M*(krd(k)*(pc(k+1)-pc(k))-krd(k-1)*(pc(k)-pc(k-1)));

```

```

end
b(1)=-1/NX+1/M*(krd(1)*(pc(2)-pc(1)));
b(NX)=1/M*(krd(NX-1)*pc(NX-1)-(krd(NX-1)+2*krd(NX))*pc(NX));

pot=solvvet(u,d,l,b); %find flow potential at TIME=TIME(old)+deltat
with backward substitution by "solvvet.m"

%% solve Tridiagonal System by LU decomposition and backward
substitution END %%

S_g(1)=S_g(1)+deltat/(deltax)^2*(kri(1)*(pot(2)-
pot(1))+deltax*f_g_BC); %BC at x=0; find saturation at
TIME=TIME(old)+deltat
for i=2:(NX-1)
S_g(i)=S_g(i)+deltat/(deltax)^2*(kri(i)*(pot(i+1)-pot(i))-kri(i-
1)*(pot(i)-pot(i-1)));
end
S_g(NX)=S_g(NX)+deltat/(deltax)^2*(kri(NX)*2*(0-pot(NX))-kri(NX-
1)*(pot(NX)-pot(NX-1))); %BC at x=1

S_nor=(S_g-S_gr)/(1-S_gr-S_wc); % normalized gas saturation for
capillary pressure calculation

for kk=1:NX %%prevent the generation of complex number in krg
and/or krw by round-off errors
if S_nor(kk)<0
S_nor(kk)=0;
elseif S_nor(kk)>1
S_nor(kk)=1;
end
end

S_g=S_nor*(1-S_gr-S_wc)+S_gr;
S_w=1-S_g;
Fwater=0.5+(atan(epdry*(S_w-fmdry)))/pi;
krd=(1-S_nor).^nw; %find aqueous relative permeability at
TIME=TIME(old)+deltat

for m=1:NX %capillary pressure model using Leveret-J function for
geometrically similar systems
if S_nor(m)<=1e-3
pc(m)=Npc*C1./exp(C2./log(1e-3))*(S_nor(m)/1e-3);
else if S_nor(m)>0.999
pc(m)=Npc*C1./exp(C2./log(0.999));
else
pc(m)=Npc*C1./exp(C2./log(S_nor(m)));
end
end
end

u_w(1)=1-f_g_BC; %In-flow BC
u_w(NX+1)=-krd(NX)/M*2.*(0-pot(NX)+pc(NX))/deltax;

for iii=1:(NX-1) %find water fractional flow at grid block wall at
TIME=TIME(old)+deltat
u_w(iii+1)=-krd(iii)/M.*((pot(iii+1)-pc(iii+1))-(pot(iii)-
pc(iii)))/deltax;

```

```

end

u_g=1-u_w;
%if TIME>=1
% Cw_inj=0; %%FINITE SLUG from TIME=0 to TIME=1%%
%end

Csg=Psgw*Csw; %surfactant concentration in gas phase
for ii=1:NX
    Css(ii)=rou_s*a_s*T_max*alpha*Csw(ii)/(1+alpha*Csw(ii));
    para1= alpha*(S_w(ii)+Psgw*S_g(ii));

    if ii==1
        N_temp=(Csw(ii)*S_w_old(ii)+Csg(ii)*S_g_old(ii)+(1-
poro)/poro*Css(ii))+deltat*(1/Pe_w*(S_w_old(ii)*(Csw(ii+1)-Csw(ii))-(1-
f_g_BC)*2*(Csw(ii)-Cw_inj))/(deltax^2)+1/Pe_g*(S_g_old(ii)*(Csg(ii+1)-
Csg(ii))-f_g_BC*2*(Csg(ii)-Cg_inj))/(deltax^2)-
(Csw(ii)*u_w_old(ii+1)+Csg(ii)*u_g_old(ii+1)-Cw_inj*u_w_old(ii)-
Cg_inj*u_g_old(ii))/deltax);
    elseif ii==NX
        N_temp=(Csw(ii)*S_w_old(ii)+Csg(ii)*S_g_old(ii)+(1-
poro)/poro*Css(ii))+deltat*(1/Pe_w*(S_w_old(ii)*(Csw(ii)-Csw(ii)-
S_w_old(ii-1)*(Csw(ii)-Csw(ii-
1)))/(deltax^2)+1/Pe_g*(S_g_old(ii)*(Csg(ii)-Csg(ii)-S_g_old(ii-
1)*(Csg(ii)-Csg(ii-1)))/(deltax^2)-
(Csw(ii)*u_w_old(ii+1)+Csg(ii)*u_g_old(ii+1)-Csw(ii-1)*u_w_old(ii)-
Csg(ii-1)*u_g_old(ii))/deltax);
    else
        N_temp=(Csw(ii)*S_w_old(ii)+Csg(ii)*S_g_old(ii)+(1-
poro)/poro*Css(ii))+deltat*(1/Pe_w*(S_w_old(ii)*(Csw(ii+1)-Csw(ii)-
S_w_old(ii-1)*(Csw(ii)-Csw(ii-
1)))/(deltax^2)+1/Pe_g*(S_g_old(ii)*(Csg(ii+1)-Csg(ii)-S_g_old(ii-
1)*(Csg(ii)-Csg(ii-1)))/(deltax^2)-
(Csw(ii)*u_w_old(ii+1)+Csg(ii)*u_g_old(ii+1)-Csw(ii-1)*u_w_old(ii)-
Csg(ii-1)*u_g_old(ii))/deltax);
    end
    para2=S_w(ii)+Psgw*S_g(ii)+(1-poro)/poro*rou_s*a_s*T_max*alpha-
alpha*N_temp;
    para3=-N_temp;

    if para1==0
        Csw_NEW(ii)=-para3/para2;
    else
        Csw_NEW(ii)=(-para2+sqrt(para2^2-4*para1*para3))/(2*para1);
%find surfactant concentration at TIME=TIME(old)+deltat
%a new temporary variable Csw_NEW is used to avoid it to replace the
value C_w(ii) in the old time step of the iteration
    end

    if Csw_NEW(ii)>Cw_inj %round-off error can cause serious
oscillation
        Csw_NEW(ii)=Cw_inj;
    elseif Csw_NEW(ii)<0
        Csw_NEW(ii)=0;
    end
end
Csw=Csw_NEW; %surfactant concentration at TIME=TIME(old)+deltat

```

```

%if TIME>=1
%   NaCl_w_0=0.0; %FINITE SLUG from TIME=0 to TIME=1.0
%end

    for jj=1:NX

NaCl_s(jj)=rou_s*a_s*Tr_max*alpha*NaCl_w(jj)/(1+alpha*Cw_inj*NaCl_w(jj)
);
        para1= alpha*Cw_inj*S_w(jj)/deltat;
            if jj==1
                para2= (S_w(jj)+(1-poro)/poro*rou_s*a_s*Tr_max*alpha-
(NaCl_w(jj)*S_w_old(jj)+(1-poro)/poro*NaCl_s(jj))*alpha*Cw_inj)/deltat
+alpha*Cw_inj*((NaCl_w(jj)*u_w_old(jj+1)-NaCl_w_0*u_w_old(jj))/deltax
-1/Pe_w*(S_w_old(jj)*(NaCl_w(jj+1)-NaCl_w(jj)))-(1-
f_g_BC)*2*(NaCl_w(jj)-NaCl_w_0))/(deltax^2));
                para3= -(NaCl_w(jj)*S_w_old(jj)+(1-
poro)/poro*NaCl_s(jj))/deltat
+(NaCl_w(jj)*u_w_old(jj+1)-NaCl_w_0*u_w_old(jj))/deltax-
1/Pe_w*(S_w_old(jj)*(NaCl_w(jj+1)-NaCl_w(jj)))-(1-f_g_BC)*2*(NaCl_w(jj)-
NaCl_w_0))/(deltax^2);
                elseif jj==NX
                    para2= (S_w(jj)+(1-poro)/poro*rou_s*a_s*Tr_max*alpha-
(NaCl_w(jj)*S_w_old(jj)+(1-poro)/poro*NaCl_s(jj))*alpha*Cw_inj)/deltat
+alpha*Cw_inj*((NaCl_w(jj)*u_w_old(jj+1)-NaCl_w(jj)-
1)*u_w_old(jj))/deltax-1/Pe_w*(S_w_old(jj)*(NaCl_w(jj)-NaCl_w(jj))-
S_w_old(jj-1)*(NaCl_w(jj)-NaCl_w(jj-1)))/(deltax^2));
                    para3= -(NaCl_w(jj)*S_w_old(jj)+(1-
poro)/poro*NaCl_s(jj))/deltat
+(NaCl_w(jj)*u_w_old(jj+1)-NaCl_w(jj-1)*u_w_old(jj))/deltax...
-1/Pe_w*(S_w_old(jj)*(NaCl_w(jj)-NaCl_w(jj))-
S_w_old(jj-1)*(NaCl_w(jj)-NaCl_w(jj-1)))/(deltax^2);
                    else
                        para2= (S_w(jj)+(1-poro)/poro*rou_s*a_s*Tr_max*alpha-
(NaCl_w(jj)*S_w_old(jj)+(1-poro)/poro*NaCl_s(jj))*alpha*Cw_inj)/deltat
+ alpha*Cw_inj*((NaCl_w(jj)*u_w_old(jj+1)-NaCl_w(jj)-
1)*u_w_old(jj))/deltax-1/Pe_w*(S_w_old(jj)*(NaCl_w(jj+1)-NaCl_w(jj))-
S_w_old(jj-1)*(NaCl_w(jj)-NaCl_w(jj-1)))/(deltax^2));
                        para3= -(NaCl_w(jj)*S_w_old(jj)+(1-
poro)/poro*NaCl_s(jj))/deltat+ (NaCl_w(jj)*u_w_old(jj+1)-NaCl_w(jj)-
1)*u_w_old(jj))/deltax-1/Pe_w*(S_w_old(jj)*(NaCl_w(jj+1)-NaCl_w(jj))-
S_w_old(jj-1)*(NaCl_w(jj)-NaCl_w(jj-1)))/(deltax^2);
                        end
                    end

                if para1==0
                    NaCl_w_NEW(jj)=-para3/para2;
                else
                    NaCl_w_NEW(jj)=(-para2+sqrt(para2^2-
4*para1*para3))/(2*para1); %find NaCl concentration at
TIME=TIME(old)+deltat
                end

                if NaCl_w_NEW(jj)>1 %round-off error can cause serious
oscillation
                    NaCl_w_NEW(jj)=1;
                elseif NaCl_w_NEW(jj)<0
                    NaCl_w_NEW(jj)=0;

```

```

end
end
    NaCl_w=NaCl_w_NEW;

    for mm=1:NX
    if Csw(mm)<fmsurf
        Fsurf(mm)=(Csw(mm)/fmsurf).^epsurf;
    else
        Fsurf(mm)=1;
    end
    end

    FM=1./(1+fmmob*Fwater.*Fsurf);
    kri=FM.*(S_nor.^ng); %find gasous relative permeability at
TIME=TIME(old)+deltat
    lamda=kri+krd/M; %find lamda at TIME=TIME(old)+deltat

    COUNTER=COUNTER+1;
    TIME=TIME+deltat;
    TIME_HIS(COUNTER)=TIME;

    if (TIME-0.5)<=1e-6 & (TIME-0.5)>=-1e-6
        TIME1=TIME
        S_time1=S_g;
        C_w_time1=Csw/Cw_inj;
        NaCl_w_time1=NaCl_w;
        pot_time1=pot;
        pc_time1=pc;
        pwd_time1=pot_time1-pc_time1;
    end

    if (TIME-1.0)<=1e-6 & (TIME-1.0)>=-1e-6
        TIME2=TIME
        S_time2=S_g;
        C_w_time2=Csw/Cw_inj;
        NaCl_w_time2=NaCl_w;
        pot_time2=pot;
        pc_time2=pc;
        pwd_time2=pot_time2-pc_time2;
    end

    if (TIME-5.0)<=1e-6 & (TIME-5.0)>=-1e-6
        TIME3=TIME
        S_time3=S_g;
        C_w_time3=Csw/Cw_inj;
        NaCl_w_time3=NaCl_w;
        pot_time3=pot;
        pc_time3=pc;
        pwd_time3=pot_time3-pc_time3;
    end

    f_g_HIS(COUNTER)=kri(NX).*pot(NX)./(kri(NX).*pot(NX)+krd(NX).*(pot(NX)-
pc(NX))/M);
    f_total_HIS(COUNTER)=2*(kri(NX).*pot(NX)+krd(NX).*(pot(NX)-
pc(NX))/M)/deltax;

```

```

    f_surf_HIS(COUNTER)=Csw(NX)/Cw_inj; %surfactant effluent history in
aqueous phase (g/L)
    f_NaCl_HIS(COUNTER)=NaCl_w(NX);
    p_drop_HIS(COUNTER)=pot(1)*NX/(NX-0.5);
    VIS_FOAM(COUNTER)=p_drop_HIS(COUNTER)*visg/krq0; %foam apparent
viscosity

end

x1=deltax/2:deltax:(1-deltax/2);

prof1=[S_time1' C_w_time1' NaCl_w_time1' x1'];
prof2=[S_time2' C_w_time2' NaCl_w_time2'];
prof3=[S_time3' C_w_time3' NaCl_w_time3'];
prof4=[TIME_HIS' f_g_HIS' f_surf_HIS' f_NaCl_HIS' p_drop_HIS'
VIS_FOAM'];
prof5=[pot_time1' pot_time2' pot_time3'];
prof6=[pwd_time1' pwd_time2' pwd_time3'];

save prof1.dat prof1 /ascii
save prof2.dat prof2 /ascii
save prof3.dat prof3 /ascii
save prof4.dat prof4 /ascii
save prof5.dat prof5 /ascii
save prof6.dat prof6 /ascii

```

2. plots.m

```

%% graphical out of simulation results %%

clear

load prof1.dat
S_time1=prof1(:,1);
C_w_time1=prof1(:,2);
NaCl_w_time1=prof1(:,3);
x1=prof1(:,4);

load prof2.dat
S_time2=prof2(:,1);
C_w_time2=prof2(:,2);
NaCl_w_time2=prof2(:,3);

load prof3.dat
S_time3=prof3(:,1);
C_w_time3=prof3(:,2);
NaCl_w_time3=prof3(:,3);

load prof4.dat
TIME_HIS=prof4(:,1);
f_g_HIS=prof4(:,2);
f_surf_HIS=prof4(:,3);
f_NaCl_HIS=prof4(:,4);
p_drop_HIS=prof4(:,5);

```

```

VIS_FOAM=prof4(:,6);

load prof5.dat
pot_time1=prof5(:,1);
pot_time2=prof5(:,2);
pot_time3=prof5(:,3);

load prof6.dat
pwd_time1=prof6(:,1);
pwd_time2=prof6(:,2);
pwd_time3=prof6(:,3);

figure(1)
set(gca, 'FontSize', 25);
plot(x1,S_time1, 'r^-', x1,C_w_time1, 'bo-', x1,NaCl_w_time1, 'ks-')
xlabel('DIMENSIONLESS DISTANCE')
ylabel('COMPOSITION')
title('COMPOSITION PROFILE at t_D=0.5')
legend('gas saturation', 'surfactant concentration in aqueous phase (g/L)', 'NaCl concentration in aqueous phase')

figure(2)
set(gca, 'FontSize', 25);
plot(x1,S_time2, 'r^-', x1,C_w_time2, 'bo-', x1,NaCl_w_time2, 'ks-')
xlabel('DIMENSIONLESS DISTANCE')
ylabel('COMPOSITION')
title('COMPOSITION PROFILE at t_D=1.0')
legend('gas saturation', 'surfactant concentration in aqueous phase (g/L)', 'NaCl concentration in aqueous phase')

figure(3)
set(gca, 'FontSize', 25);
plot(x1,S_time3, 'r^-', x1,C_w_time3, 'bo-', x1,NaCl_w_time3, 'ks-')
xlabel('DIMENSIONLESS DISTANCE')
ylabel('COMPOSITION')
title('COMPOSITION PROFILE at t_D=5.0')
legend('gas saturation', 'surfactant concentration in aqueous phase (g/L)', 'NaCl concentration in aqueous phase')

figure(4)
set(gca, 'FontSize', 25);
plot(TIME_HIS, f_g_HIS, 'r-', TIME_HIS, f_surf_HIS, 'b-
.', TIME_HIS, f_NaCl_HIS, 'k--')
xlabel('Dimensionless time (TPV)')
ylabel('Dimensionless effluent history')
title('EFFLUENT HISTORY')
legend('gas cut', 'surfactant concentration in aqueous phase', 'NaCl concentration in aqueous phase')

figure(5)
set(gca, 'FontSize', 25);
plot(x1,pot_time1, 'ro-', x1,pot_time2, 'b*-', x1,pot_time3, 'gs-')
xlabel('DIMENSIONLESS DISTANCE')
ylabel('DIMENSIONLESS PRESSURE')
title('DIMENSIONLESS GAS PRESSURE PROFILE')
legend('t_D=0.5', 't_D=1.0', 't_D=5.0')

```

```

figure(6)
set(gca, 'FontSize', 25);
plot(x1,pwd_time1, 'ro-', x1,pwd_time2, 'b*-', x1,pwd_time3, 'gs-')
xlabel('DIMENSIONLESS DISTANCE')
ylabel('DIMENSIONLESS PRESSURE')
title('DIMENSIONLESS LIQUID PRESSURE PROFILE')
legend('t_D=0.5', 't_D=1.0', 't_D=5.0')

figure(7)
set(gca, 'FontSize', 25);
plot(TIME_HIS,p_drop_HIS, 'b-+')
xlim([0 5])
xlabel('DIMENSIONLESS TIME')
ylabel('DIMENSIONLESS PRESSURE DROP')
title(['GAS PHASE PRESSURE DROP HISTORY'])

figure(8)
set(gca, 'FontSize', 25);
plot(TIME_HIS,VIS_FOAM, 'b-+')
xlim([0 5])
xlabel('Dimensionless time (TPV)')
ylabel('Foam apparent viscosity(cp)')
title(['FOAM APPARENT VISCOSITY HISTORY'])

```

3. solvet.m

```

%% subroutine of backward substitution (solving Tridiagonal System) %%
function [x] = solvet(u,d,l,b)

n = length(d);
x = (1:n);
y = (1:n);

% Solve Tridiagonal system LUx=b;

% Step 1 : Solve Ly=b for y
y(1) = b(1);
for i=2:n
    y(i) = b(i) - l(i-1)*y(i-1);
end

% Step 2 : Solve Ux=y for x
x(n) = y(n)/d(n);
for i=(n-1):-1:1
    x(i) = (y(i)-u(i)*x(i+1))/d(i);
end

```

4. decomt.m

```

%% subroutine of LU decomposition (solving Tridiagonal System) %%
function [u1,d1,l1] = decomt(u,d,l)

n = length(d); % get the length of the diagonal

```

```
% initialize the output vectors
u1=u;
d1=d;
l1=1;

%Perform LU decomposition
d1(1)=d(1);
for i=2:n
    l1(i-1) = l(i-1)/d1(i-1); % Update the lower triangle vector
    d1(i) = d(i) - (l(i-1)/d1(i-1))*u(i-1); %Update the diagonal
end
```